University of Southampton

The Aerodynamics of a Diffuser Equipped Bluff Body in Ground Effect

Andrea Elizabeth Senior

School of Engineering Sciences

Doctor of Philosophy

April 2002

UNIVERSITY OF SOUTHAMPTON

ABSTRACT

SCHOOL OF ENGINEERNG SCIENCES

Doctor of Philosophy

THE AERODYNAMICS OF A DIFFUSER EQUIPPED BLUFF BODY IN GROUND EFFECT

by Andrea Elizabeth Senior

An investigation of the flow physics of a diffuser equipped bluff body in ground effect has been undertaken. Situated at the rear of a racing car undertray, the diffuser is an important component and the least understood part of the vehicle. Diffuser performance can change dramatically with vehicle ride height. This includes a significant loss in performance at low ride heights which can also be a serious vehicle safety issue. An increased understanding of the diffuser behaviour in ground effect is required to assist design improvements. An accurate experimental database of the flow field is necessary both to aid this understanding and also to provide information against which the continuing development of computational simulations may be assessed.

The present research is two-fold; experimental and computational. Model tests were conducted on a generic 3D bluff body equipped with a fixed angle diffuser representative of current racing car diffusers. Extensive experimental tests in wind tunnels equipped with moving belts included mean forces, surface pressures, oilflow visualisation, laser doppler anemometry and particle image velocimetry. The 3D diffuser flow field has been measured for the first time and the results are used to analyse the behaviour of the diffuser in ground effect. Complementary RANS simulations provide valuable insight into the modelling requirements.

It is known that the diffuser generates down-force by accelerating air underneath the model through the channel formed by the model underside and the ground. The diffuser flow is characterised by a counter rotating vortex pair. The present research presents a new understanding of the diffuser flow field and the mechanisms causing its behaviour in ground effect. It has been found that the behaviour of the vortices alters according to the model ride height and the pressure gradient inside the diffuser. Additional down-force is generated due to the low pressure zones associated with these vortices. At relatively large ground clearances, the vortices are coherent and strong with a high axial speed core. At these heights the down-force experienced by the model increases with reducing model ride height. This behaviour is terminated at lower ground clearances by the advent of a plateau in the down-force curve and the occurrence of breakdown in the vortices inside the diffuser. The vortex breakdown results in large, diffusive and weak vortices. Maximum down-force on the model occurs at the lowest ride height of this type of flow at the end of the plateau. A sharp reduction in the down-force occurs thereafter, due to the complete breakdown of one of the vortices. The resulting asymmetric flow consists of a single coherent vortex to one side of the flow and significant flow reversal at the other side. At very low ride heights the vortices are asymmetric and weak.

Down-force reduction is believed to occur as a result of the steep pressure gradient inside the diffuser which advances the vortex breakdown inside the diffuser upstream as the model ride height is reduced. At the point of down-force reduction one of the vortices breaks down completely. At very low ride heights the boundary layers at the model underside and at the moving ground are believed to merge to restrict flow through the diffuser inlet.

The experimental database is comprehensive and provides the necessary tool for validation of computational modelling. A computational simulation of the flow at a high ride height successfully predicts force and surface pressure coefficients and the main flow features.

Acknowledgements

To my family; M, D & H.

This project could not have been completed without the help and support of a large number of people.

Firstly my thanks go to British American Racing, Brackley, U.K., for funding and collaboration in the research, and in particular to Willem Toet. Also to Advantage CFD, in particular Rob, Henrik, John, Bill, Tony and Elka for all their assistance with Geomesh and Fluent.

Thanks to my supervisor, Professor Xin Zhang, for his enthusiasm, patience and unerring support; Andreas for absolutely everything; Geoff & Geoff and Mike & Mike for saving my life on several occasions; Dave Goldsworthy for helping with the model; David Jeffrey for invaluable time and assistance, particularly in the early stages of the research; Ed Rayner for equally invaluable assistance and for putting up with me in the office next door; Alan, Sonya and the other administrative staff in the Aero department for providing help when I needed it; Robert at Dantec for keeping both the LDA and PIV systems in order.

Mike Gascoyne for taking me on in the first place, and to Tyrrell F1 Team for assistance in the design and manufacture of my wind tunnel model. Bonnie and James for drawing up the Pro-E files, and many others for making the model for me.

Family and friends for helping me through the stress of writing a PhD. In the department: Zippy Zerihan, my fellow sufferer of LDA-itis, for cheering me up on many an occasion; special thanks to Ben; Paul C, Matt O, James O, Sandrine, and the Dodgy Geezers; all friends outside of the department, especially Taj and Matt B, who were bemused but very supportive through my reclusion in the last few months - I hope to see you all soon!.

Finally to the diffuser, that seemingly innocent piece of carbon fibre. Long may it live at the back of an F1 car, because it is essential to the overall downforce of the car, and as all aerodynamicists should know...that's a hell of a lot of downforce.

Contents

Appendices

List of Tables

List of Figures

Notation and Glossary

Notation

A = model frontal area, m^2
C_D = drag coefficient, $D/q_\infty A$
C_L = down-force coefficient, $L/q_\infty A$
C_p = pressure coefficient, $p - p_\infty/q_\infty$
d = model half width, m
D = drag, N
h = model height, m
h_r = ride height of model above ground or ground clearance, measured from the flat lower surface of the model, m
l = model length, m
L = down-force, N
p = pressure, N/m^2
q_∞ = freestream dynamic head, $\rho_\infty U_\infty^2/2$, kg/ms^2
Re = Reynolds Number, $\rho_\infty U_\infty l/\mu$
TKE = turbulent kinetic energy: $\frac{1}{2}\{\overline{uu} + \overline{vv} + \overline{ww}\}$, non-dimensionalized by U_∞^2
U_∞ = freestream flow speed, m/s
u, v, w = velocity components in x, y, z directions, m/s
x, y, z = cartesian co-ordinates: x +ve downstream, y +ve up, z +ve to starboard, m
$\overline{uv}$ = Reynolds shear stress, non-dimensionalised by U_∞^2
x_1 = $x - l, m$
y_1 = $y + h, m$

Greek symbols :
Ω = cross-plane vorticity, $(\partial w/\partial y - \partial v/\partial z)$, s^{-1}
ρ = density, kg/m^3
μ = dynamic viscosity, kg/ms
δ = boundary layer thickness, m
δ^* = displacement thickness, m
θ = diffuser divergence angle, *degrees*

Subscripts :
c = centre of vortex
ls = left side vortex as viewed from downstream of the model

m = maximum or peak value
rs = right side vortex as viewed from downstream of the model
∞ = freestream value

$Plane - walled\ diffuser\ geometry\ notation:$
θ = diffuser divergence angle, *degrees*
W_1 = diffuser inlet width, m
W_2 = diffuser exit width, m
b = diffuser inlet depth, m
N/W_1 = non-dimensional diffuser axis length
l_d/W_1 = non-dimensional diffuser wall length
AS = Diffuser aspect ratio, b/W_1
AR = Diffuser area ratio, W_2/W_1

Glossary

2D = two dimensional
3D = three dimensional
BSA = Burst Spectrum Analyser
CFD = Computational Fluid Dynamics
LES = Large Eddy Simulation
LDA = Laser Doppler Anemometer
NASA = National Aeronautics and Space Administration
PIV = Particle Image Velocimeter
RANS = Reynolds Averaged Navier Stokes

Flow type A,B,C,D = the flow associated with a region of the downforce curve

Overview of Thesis

The diffuser is a geometrically simple device whose complex flow field has been the subject of much published research. However, very little of this research relates to the application of a diffuser as an important aerodynamic component of a racing car. For this application the diffuser operates in ground effect. This thesis aims to redress the gap in the research and contributes significantly to the understanding of an underbody diffuser flow acting in ground effect. The research is two-fold; experimental and computational. This first research project presents an extensive database of experimental findings from various model tests. The computational modelling that has been undertaken is successful. Both sets of results provide a valuable insight into this important aerodynamic and fluid mechanical flow.

The thesis is concerned with the flow through a diffuser-equipped bluff body in ground effect. The thesis is presented with a technical history and the background to the research in Chapter 1. This is followed by the aims of the research. A description of the techniques and equipment used in conducting the research and an introduction to the structure of the research programme in Chapter 2. Chapters 3-6 present the experimental results and discuss the measurements taken. In each of these Chapters, results from different experimental techniques are discussed with reference to implications for the flow field. Chapter 7 introduces the computational aspect of the research before Chapter 8 presents the conclusions of the research. Recommendations for future research are suggested in Chapter 9.

Chapter 1

Introduction and Literature Review

An introduction to the research subject is presented in this Chapter. A definition of the diffuser is followed by a review of published diffuser research. The importance of a diffuser in the context of a racing car application is explained. Current understanding of the flow field is summarised. The chapter is concluded with the aims and objectives of the research.

1.1 The Definition of the Diffuser

A diffuser is a device which aims to decelerate a mean flow, converting its kinetic energy into a pressure rise. For subsonic flow this is achieved simply by a gradual increase in the flow cross sectional area. A simple diffuser geometry is shown in Figure 1 with some of the main design parameters. Diffusers are used widely in aircraft inlet ducts, duct components for the design of ventilation and air-conditioning systems, and as a fluid mechanical element in wind tunnels and turbomachinery. Diffusers are also utilised at the rear of a racing car underbody in order to generate down-force.

1.2 History and Application of the Diffuser

The first known reference in open literature to diffuser flow can be found in Clemens Herchel's translation from Sextus Julius Frontinius (100AD) [44], which notes the use of diffuser flow as a means of increasing pipe flow rate by flaring the outlet section of the pipe. Early experimental studies to determine the efficient operation of internal flow diffusers include those by Gibson [37, 38], and Patterson [72]. These works were undertaken with the aircraft industry in mind, as are the majority of publications concerning diffuser flow. In the case of an aircraft turbojet engine operating at a subsonic Mach Number, the inlet duct upstream of the compressor must be designed to act as a diffuser with reasonably gentle diffusion, and to prevent boundary layer separation. This is because distortions in the velocity profile at the compressor inlet can lead to failure of the compressor blades due to vibrations. A similar specification is required of the diffuser section of a closed-circuit wind tunnel, in which it is desirable to reduce the velocity level at the test section discharge so that the fluid flow can be returned to the test section inlet with as low a power loss as possible.

Power losses at any point in the tunnel can vary as the speed cubed, thus the criterion for a good diffuser is to be able to reduce the flow speed to the desired level whilst incurring minimum energy losses.

This thesis is concerned with a racing car diffuser, which in its generic configuration utilises the geometric features of an internal flow diffuser. The diffuser is seen as the characteristic upward-sloping tunnels at the rear of the car undertray in Figure 2. The diverging tunnels are placed in close proximity to the ground. When the car is driven at speed, the result is a three-dimensional flow through the tunnels that produces an increase in down-force on the car. The down-force is felt as aerodynamic grip at the rear wheels, hence allowing an increase in acceleration, braking and cornering speeds.

1.3 Diffuser Flow in Ground Effect

1.3.1 The role of the diffuser on a racing car

Underbody diffusers are used on both road and racing cars, and first appeared in Formula 1 racing. In 1978 the Lotus Formula 1 team used an idea originating at BRM Racing to pioneer extremely effective ground effects vehicles involving shaping of the underbody with venturi tunnels and the use of flexible side skirts. The idea of manipulating the air flow beneath the chassis to generate down-force was revolutionary and so successful that in 1981 sliding skirts were banned. In 1983 flat bottomed undertrays were made mandatory, allowing only a relatively small rear diffuser, an upsweep at the rear of the undertray. In 1994 the regulations were altered once more; it is currently required that a 10 mm thick 'plank' of wood be attached underneath the undertray longitudinal axis in order to force teams to run the car at a higher ride height. The total down-force experienced by the Formula 1 car as it travels at 250 kph is approximately 12 kN [62]. The diffuser can typically contribute up to one third of this total, however it also interacts with the front wing and rear wing assemblies, and effectively governs flow under the whole undertray of the car. Thus its actual contribution to the total down-force experienced by the car varies with the set-up of these and other components, and can be higher or lower than the typical value depending upon the type of circuit for which the car is to be set up.

However, problems occur as the car runs over bumps and undulations in the race track surface, changing the effective ride height of the car above the track. This causes undesirable fluctuations in the down-force levels experienced by the car, destabilizing the car and affecting its performance. In these conditions the car can be difficult to control and thus diffuser performance is also a safety issue. The introduction of the undertray plank was an attempt to reduce down-force levels on the car following the fatal accident of Ayrton Senna in 1994. Moments before the crash, Senna's car had been riding up the kerbs, effectively reducing the height of the car above the ground. The sharp decrease in rear down-force that this would have imparted on the car was thought to have contributed to the accident. In 1999 the Mercedes Le Mans cars became airborne from the track due to an imbalance of the front and rear aerodynamics as the car drove over the brow of a hill, narrowly avoiding serious injury of the driver and spectators.

The rear diffuser is acknowledged to be the least understood part of the car, however the importance of understanding its behaviour in ground effect is clear from both the performance and safety points of view.

1.4 Diffuser Literature

The diffuser literature can be sectioned into studies of internal flow and ground effect diffusers, where an internal flow is defined as being enclosed by the diffuser, excepting the inlet and outflow. This is to be contrasted with a diffuser in ground effect in which the fluid is not completely bound by the geometry of the diffuser, as is the case on a racing car. Little has been published in open literature about racing car or automotive diffuser applications. However, strong parallels may be drawn with internal diffuser flow as the factors affecting their performance are closely related to those affecting a diffuser in ground effect.

1.4.1 Internal Flow Diffusers

Much experimental, analytical and computational research has been devoted to the subject of internal diffuser flow. However, even the simplest 2D turbulent diffuser flow is complicated, and general understanding of the details of energy transfer and dissipative losses inside a diffuser remains incomplete. Since the 1950s experimental/analytical studies have been conducted on two dimensional diffusers of various geometries, including high aspect ratio plane-walled [53, 76, 77], low aspect ratio plane-walled [63], curved and conical shapes [13, 51, 61, 65, 87, 89, 96], annular [85], rectangular [35], square pyramidal [31], and S-shaped [75]. The plane-walled diffusers are of most relevance to diffuser in ground effect flows and are reviewed here.

Plane-walled diffusers

Flow Regimes The performance of plane walled diffusers such as that of Figure 1 can depend on a number of factors. Diffuser geometry (area ratio (AR), aspect ratio (AS), non-dimensional diffuser length (n/W_1), included angle (2θ)), Reynolds Number, inlet conditions, exit conditions and Mach Number can all affect a diffuser's performance. The conversion of energy from kinetic to static pressure rise is not a simple one-dimensional process, due to the adverse pressure gradient which develops along the diffuser walls, and the resulting complicated flow patterns in the diffuser. These flow patterns are dependent upon many combinations of variables that early researchers often reported contradicting performance data.

Stephen Kline and his co-workers at Stanford University were the first to coherently classify plane-walled diffuser flow as a function of geometry ([52, 53, 67, 77, 92]). Figure 3 is a reproduction of a map of flow regimes inside a plane-walled 2D diffuser constructed by Kline *et al* [77] from their experimental data and flow visualisations, and is a reasonable guide to the different stages of flow diffusion under the conditions of a thin inlet boundary layer, low Mach number, high Reynolds number and downstream tailpipe (see Table 1).

Geometries lying below line a-a (Figure 3), having small angles and area ratios, were found to produce a flow which was, in the main, apparently unseparated and well behaved.

As the area ratio increases for a constant n/W_1, regions of large transitory stall occur, usually originating in one of the diffuser corners, in which the separation varies in position, size and intensity with time. At larger area ratios, the flow becomes fully stalled, and the greater portion of the diffuser is occupied by a large turbulent re-circulation region. The separated flow occupies one diverging wall whilst the main flow follows along the other wall continuously and reasonably smoothly. Finally, above line c-c in Figure 3, a jet flow exists with flow separation from both diverging walls. The transition between modes is gradual in some places and sudden at others, and a hysteresis zone exists between lines c-c and d-d.

Diffuser Performance Parameters Diffuser performance is often measured by the criterion of pressure recovery coefficient, C_{pr}; $C_{pr} = (p_2 - p_1)/q_1$, where p_1 and p_2 are the static pressures measured at the inlet and exit stations along the diffuser, and q_1 is the dynamic pressure at the inlet.

The pressure recovery coefficient relates the pressure rise in the diffuser to the maximum that would be attainable at the same flow rate with one-dimensional flow. When designed to optimum efficiency, a diffuser can regulate a flow, giving it uniformity and stability. The pressure rise associated with this type of flow produces unseparated, well behaved flow with minimum loss of total pressure and a high pressure recovery. In flows with an adverse pressure gradient, non-uniformities in the flow become amplified; the magnitude of the velocity reductions of diffusing flows is largest where the local velocity is smallest, thus velocity differences across the stream are accentuated [84]. Above small diffuser angles, the adverse pressure gradient at the diffuser wall causes stall and flow separation, with an appreciable reversed flow inside the diffuser. The pressure recovery is then far less than its ideal value, which would be achievable from the same geometry with frictionless flow at the same flow rate.

The pressure recovery of an internal flow diffuser may be affected by several factors, but most importantly the geometry of the diffuser and conditions at the diffuser inlet.

Geometry Diffuser performance depends on factors other than flow regime, and was found by Reneau *et al* [77] to be dominated by different geometrical parameters in different regimes. Area ratio was found to control the pressure recovery of unstalled flow, divergence angle was the dominating factor in the transitory stall regime, and no geometric parameter was observed to dominate the 2D-stall and jet flows. The area ratio is one of the main parameters controlling the level of attainable pressure recovery, as are divergence angle (2θ), non-dimensional wall length l_d/W_1 (or n/W_1) and aspect ratio (AS) (Figure 1). Peak pressure recovery for a constant l_d/W_1 has been found to occur for area ratios at, or slightly above, the limit of the unstalled flow regime [53] (see line a-a, Figure 3).

The effects of aspect ratio ($0.25 \leq AS \leq 4$) were investigated by Johnston & Powars [49] for thin, uniform inlet boundary layers, and diffusers of low aspect ratio (AS=0.1) were studied by McMillan & Johnston [63] for fully developed turbulent inlet flows. Johnston & Powars defined their inlet blockage factor as a function of AS and held all other variables constant in an attempt to isolate the effects of aspect ratio. They found that for unstalled flow diffusers, up to and including peak pressure recovery for a constant l_d/W_1, that C_{pr} increased with increasing aspect ratio. This was a consequence of the inlet blockage ratio decrease with increasing AS, (from 0.067 at AS=0.25 to 0.017 at AS=4). However, in diffuser flows exhibiting transitory stall, C_{pr} was observed to increase with increasing inlet blockage ratio (decreasing AS). The authors could not account for this trend, stating that it was an aspect ratio effect which could not be fully explained by the blockage concept. McMillan & Johnston noted that the transition between flow regimes occurred at lower area ratios in their low aspect ratio diffusers (AS=0.1), indicating a dependence of the flow regime on a combination of aspect ratio and boundary layer thickness. The latter may have been the primary cause of this difference since Waitman *et al* [92] observed the same trend when they increased the boundary layer thickness in high aspect ratio diffusers. Runstadler *et al* [81] and Dighe [23] concluded that the optimum aspect ratio for obtaining maximum pressure recovery was slightly greater than 1.

Reneau *et al* [77] found that for unstalled diffusers, a long thin diffuser produced a slightly lower pressure recovery than a short wide angle diffuser, since the thicker boundary layer that develops over the longer wall creates a greater blockage to the flow. Peak recoveries for various geometries and inlet conditions were found by Kline *et al* [53] to be around n/W_1=20-28. As the inlet boundary layer thickness increases the optimum n/W_1 decreases. Waitman *et al* [92] found an optimum l_d/W_1 of around 20-25, finding no real gain in recovery with large l_d/W_1 ratios.

Inlet conditions A reduction in diffuser pressure recovery was found by Waitman *et al* [92] when increasing the thickness of the turbulent inlet boundary layer. McMillan & Johnston [63] observed that fully developed turbulent inlet flows were Reynolds Number dependent for low aspect ratio diffuser geometries lying below the line of appreciable stall. This is in contrast to the findings of Kline *et al* [53], and later Reneau *et al* [77], who reported no Reynolds Number effect for high aspect ratio diffusers with thin turbulent boundary layers of $2\delta^*/W_1 \leq 0.05$. Kline *et al* found that although the profiles of thin inlet boundary layers showed no bearing on the flow regime, they had a large effect on pressure recovery performance and losses.

Sovran & Klomp [85] developed a performance correlation for optimum geometry diffusers of rectangular, conical and annular cross-sections, based upon the area blockage due to the non-uniformities in velocity profile across the flow stream. The correlation was validated for high aspect ratio diffusers with a low blockage ratio, however it seems less useful for predicting low aspect ratio diffuser flow with a larger blockage ratio [63].

Asymmetric plane-walled diffusers

Asymmetric plane-walled diffusers having only one diverging wall have been studied experimentally by Tults [90], Reid [76], and more recently by Obi *et al* [70] and Buice & Eaton [10]. This type of diffuser has also been modelled using RANS simulations [41, 97] and by large eddy simulation (LES) [27, 50].

An early study by Tults [90] discussed experiments conducted in very large aspect ratio diffusers having only one diverging wall varied from 0 degrees to 20 degrees. Maximum pressure recovery was recorded at an 8 degree divergence angle.

Large area ratio ($AR \geq 3$) asymmetric diffusers performed badly in comparison to their symmetric equivalents [76], however in the same study it was found that a central splitter plate dividing a symmetric diffuser into two asymmetric diffusers resulted in improved maximum pressure coefficient over the plain diffuser for large area ratio diffusers. The divided diffuser achieved the performance of a longer diffuser of the same area ratio.

The asymmetric internal flow diffuser has received further attention in the last decade as the need for reliable data for validation of CFD simulations has increased. As a complex turbulent flow, the asymmetric diffuser provides a geometrically simple benchmark case for the development of turbulence models and large eddy simulation methods. The experiments of Obi *et al* and later Buice & Eaton were conducted with such data validation in mind. The diffuser channels used in each case had a divergence angle of 10 degrees with an inlet channel and exit plenum. Fully developed channel flow was established at the diffuser inlet. The diffuser of Obi *et al* [70] had an inlet aspect ratio of 35, and detailed LDA measurements of the separation at the diverging wall were provided. However, later inspection of the data revealed an increase in the mass flow along the core section of the diffuser that was attributed to flow separation from the end walls, compromising the two-dimensionality of the flow. Buice & Eaton [10] re-created the experiments, ensuring flow two dimensionality by the use of a very high inlet aspect ratio and active boundary layer control at the end walls. Separation at the diverging wall was found to occur at a streamwise location equivalent to six inlet channel heights downstream of the inlet, with re-attachment occurring only in the exit plenum.

Computational and analytical studies of internal flow diffusers

The majority of research concerning diffuser flows has been conducted experimentally. However the cost, practical limitations and time constraints associated with experimental research have resulted in an increasingly large number of computational studies.

Early methods of predicting subsonic diffuser flow were based on boundary layer approximations of the governing equations, the solutions to which were obtained by solving the integral equations [4, 16, 36, 88]. The Unified Integral Method (UIM) developed at Stanford University is zonal, utilising a one-dimensional, inviscid model at the core and the linear momentum equation for the boundary layer zone plus an equation for the rate of entrainment of core fluid into the boundary layers [48]. For unseparated and slightly stalled flow the method is able to predict overall and local pressure recovery to within ±10 percent of measured values. However, the method is too simple for full representation of the flow physics of transitory stall.

Integral methods are parabolic in nature, that is the downstream effects on the upstream flow are not accounted for, thus the complicated pressure gradient effects in diffuser flows can not be accounted for correctly. The methods are also based on the assumption of turbulent local equilibrium, however the turbulent field near the diffuser wall is anisotropic [65, 71].

Computational methods based on the Reynolds Averaged Navier-Stokes (RANS) equations have emerged as tools for predicting diffuser flow. Several turbulence models have been used to close the RANS with varying degrees of success in simulating the turbulent flow field. The standard $k-\epsilon$ model [56] overpredicts wall shear stress for these complex flows. The Baldwin-Lomax, Chien low Reynolds number $k-\epsilon$ [15] and Wilcox $k-\omega$ [95] models tested in the NASA NPARC CFD code all failed to respond to an adverse pressure gradient or to indicate separated flow [24]. The Baldwin-Barth one-equation model [3] fared considerably better, though results remained quantitatively inaccurate. Xu *et al* [97] found the standard $k-\epsilon$ and the Launder & Sharma low Reynolds number $k-\epsilon$ models to predict flow separation positions too early and to underpredict reattachment locations along a diffuser wall, whereas a high Reynolds number $k-\epsilon$ model with one transport equation gave a significantly better performance. Lai *et al* [54] applied a low Reynolds number $k-\epsilon$ model incorporating severe adverse pressure gradient effects to non-separating diffuser flow, whilst Cho & Fletcher [17] achieved accurate results with an algebraic Reynolds stress model. Hah [40] also produced fairly accurate results using an algebraic Reynolds Stress model with a correction for the effect of streamline curvature incorporated into the transport equation for energy dissipation. The correction accounted for the anisotropy of the Reynolds stresses. More recently, Rothe [80] used the commercial RANS solver FLUENT®to predict flow in Ashjaee's 8 degree diffuser, finding that the wall-function he used did not represent the physics of the turbulent wall layers in detaching and detached flow.

Obi *et al* [70] conducted RANS simulations of their experiment using the standard wall function approach with several turbulence models including the $k - \epsilon$ model at the wall, and an SMC (second moment closure) model modified with a wall reflection term. None of the models adequately predicted the flow separation in the diffuser, however the SMC was the only model to predict separation at all, indicating the need for representation of the anisotropy of the Reynolds stress tensor.

Large Eddy Simulation with a dynamic subgrid-scale model was utilised to simulate the experiments of Obi ([70]) and Buice & Eaton ([10]) [50]. Predicted mean flow and pressure coefficients agreed well with the experiments, however velocity fluctuations and shear stress were less well predicted. It was suggested that to successfully capture the details of the flow reattachment downstream of the diffuser, the flow entering the diffuser would need to be accurately simulated. This would involve a fine mesh resolution, small time steps and an increase in the domain width. The use of zonal meshes was recommended in order to decrease the 'prohibitively expensive' [50] cost of these requirements.

Implication of Internal Diffuser Flow to a Diffuser in Ground Effect

In two dimensions, the diffuser in ground effect is geometrically similar to an asymmetric internal diffuser flow, however with a moving ground boundary condition it is more similar to one half of a symmetric diffuser. Each of these flows are subjected to adverse pressure gradients and it is possible that a similar pattern of flow regimes exists for a diffuser in ground effect. Internal diffuser flow is very much dependent upon area ratio, aspect ratio and the boundary layers at the diffuser inlet. Although the diffuser of the present research generates a three dimensional flow, these key parameters could also have a significant effect on a diffuser flow in ground effect. The internal flow diffuser literature gives an initial indication of the parameters involved and also draws attention to the issue of stall inside the diffuser and its causes. Accordingly, a test structure was devised to incorporate these relevant issues, and experimental results were interpreted with the internal diffuser flow in mind.

1.4.2 Ground Effect

The effect of ground proximity on a lift producing body has been a subject of aerodynamic research since the early twentieth century and the first powered flights. Theoretically, the presence of the ground may be represented by an image flow system in which the influence of a ground plane boundary on an object at a distance above the ground is the same as that of the inverted body placed at an equal distance 'below' the ground boundary. Early aircraft wing tests employed the principle by using two identical models, one mounted inversely to the other. However this method of ground representation requires great accuracy in the symmetry between the models and also in the positioning of the models relative to each other. The increase in model costs and in wind tunnel test section size make this approach unpopular. Fixed ground boards have been used in many automotive tests. The disadvantage of this representation is that a boundary layer builds up along the length of the test section floor, altering the velocity profile between a test model and the ground from that which would occur in a real road test. The boundary layer introduces a velocity deficit at the ground that is fundamentally incorrect. Various solutions to this problem have included the introduction of an elevated ground plane above the wind tunnel floor, the idea being to avoid the thick boundary layer on the tunnel floor and placing the model in a much thinner boundary layer formed on the elevated plane. An alternative is to introduce a spanwise suction slot ahead of the model to remove a large percentage of the boundary layer upstream of the model. This approach can be effective in testing at the relatively large ground clearances used in production car tests and is used in many full scale wind tunnels, however it remains incorrect. Suction slots or tangential blowing at the tunnel floor are effective methods of boundary layer removal, however its implementation is complex and expensive. The system is used in the Porsche wind tunnel.

However the only correct method of reproducing the ground boundary condition is to employ a moving belt travelling at the same velocity as the freestream, thus removing the velocity deficit at the ground plane. This method is used by racing car teams in current ground effects research [11, 19, 32].

1.4.3 Diffuser in Ground Effect Research

Experimental studies

Studies of 3D underbody diffuser flows have been undertaken by Carr [14], George [33, 34], Frost [29], Howell [46], and more recently by Cooper *et al* [19, 20]. It is well established that diffusers are capable of generating down-force in ground effect. A summary of the fluid dynamic mechanisms which combine to produce down-force on a three-dimensional diffuser equipped model is given by Cooper *et al* [19], comprising of the underbody upsweep, the interaction with the ground, and a concept proposed by Sovran [84] known as 'diffuser pumping.' The 'diffuser pumping' idea suggests that as the diffuser delivers flow to a fixed exit pressure such as the base pressure of a vehicle, its pressure recovery appears as a depression in pressure at the diffuser inlet. The diffuser has 'pumped down' the underbody pressures below that which would occur on a flat bottomed model, the underbody flow rate increases and the result is greater down-force.

The down-force trend of a diffuser equipped bluff model is given by Cooper *et al* [19], who found that for any one diffuser angle, the down-force exerted on the model increases as the model is lowered from a freestream ride height towards the ground until a maximum is reached. Below this ride height the down-force reduces sharply. They surmised that at this critical height the boundary layers under the body and over the ground merge and become a substantial fraction of the ride height. They also documented a difference in the down-force curves between smaller and larger angles of diffuser below a certain ride height, the latter showing a reversal in the consistent trend in down-force seen in all the curves above this ride height. No explanation was given for this finding.

George [33] observed a leeside vortex pair on the upsweep surface of his model which appeared to keep the flow attached to the diffuser surface at angles where it would be expected to detach, and thus maintain down-force. In later tests on a venturi-type model George & Donis [34] found that flow entrainment underneath the side-skirts resulted in a separated shear layer from which a vortex pair formed. They observed loss of down-force and asymmetric diffuser surface patterns when the model skirts were sealed to the fixed ground plane, attributing the phenomena to the absence of the vortices originating from the skirt edges. At low ride heights an unsteady vertical oscillation of the model led to their suspicion of either vortex breakdown inside the diffuser or an association with a small separated region of fluid found on the ground plane. This was thought to be a flow away from the ground up towards the model, induced by the vortices. Due to the broad nature of the study these findings were not probed further. Both of these tests were conducted using a fixed ground plane, and as such the observations made cannot necessarily be applied to the present test conditions using a moving ground.

Computational studies

Computational simulation of diffuser flow in ground effect was conducted as part of the research of Cooper *et al* [19]. The 3D model with a 9.17 degree and a 13.5 degree diffuser was simulated as a symmetry half-model and without the side-plates. The commercial flow solver CFD-ACE was employed with the SIMPLEC pressure-correction algorithm and the $k - \omega$ turbulence model. A near-wall grid spacing allowed resolution to the diverging wall. Adequate lift and pressure predictions were obtained for the 9.17 degree diffuser, however the simulation was less successful for the 13.5 degree diffuser. The simulated flow field was not presented. The results of these and similar computations for different diffuser lengths were used in their analytical model [20]. Details of the solutions are not presented, however the results were utilised in providing certain input data for the model. The model calculated the total underbody mean-effective pressure coefficient from a correlation based upon the CFD data for different diffuser lengths and on the experimental data of [19]. Predictions of the underbody mean-effective pressure coefficient calculated for diffusers of various lengths in proportion to model length (n/L) were given for several area ratio parameters ($AR - 1$). Whilst acknowledging the shortcomings of the model, for example that it was based upon only model centreline data and on certain assumptions of data applicability, the authors provided a useful insight into the design of underbody diffusers, concluding an optimum area ratio parameter of approximately $AR - 1$ =2 and a diffuser of approximately half the length of the vehicle itself.

1.5 Motivation for Research

It is clear that whilst internal diffuser flows have been well researched over the past few decades, ground effect diffuser flow, particularly in the context of a racing car, has received little attention.

Published work focuses on parametric studies and time averaged forces and pressures. For a given ramp angle, fluid flow in a diffuser appears to operate in several different modes in ground effect. Investigations of the actual flow field are limited to surface flow visualisation taken over a fixed ground board. No off-surface flow measurements have been made. Thus the structure of the flow inside a diffuser operating in ground effect is to a large extent unknown.

It is clear that there are many large gaps in the current understanding of this important flow, in particular with regard to the flow field and the major flow physics affecting the down-force reduction. It is by no means clear that boundary layer merging is the dominant factor.

1.6 Importance of Research Topic

The 3D diffuser in ground effect is particularly relevant to the motor racing and automotive industries. However, it is believed that flow features generated by the diffuser such as 3D vortex flow and bluff body in ground effect aerodynamics are of general applicability to aerodynamics and fluid mechanics.

1.7 Objectives of Research Programme

This research project is the first study of the flow of external underbody diffusers in ground effect. Bearing this in mind, the research has been conducted with the aim of fulfilling the following objectives;

- Investigation of the flow field around/inside a fixed angle diffuser in ground effect.

- Establishment of an experimental database for the flow field.
- Modelling of the 3D flow field using a RANS CFD code.
- Development of an explanation for the diffuser behaviour in ground effect, in particular the force reduction phenomenon.

1.8 Research Strategy

In order to investigate the flow physics of the diffuser in ground effect, it was concluded that model testing in a wind tunnel facility with a moving ground was the most reliable and useful method of conducting the research. A wind tunnel model was designed, manufactured and tested using a variety of experimental techniques. Complementary computational simulations of the model tests were conducted. The following chapters describe the tests and simulations in detail.

	inlet conditions	main findings
Moore & Kline, 1958		flow regimes reported
Kline, 1959 [52]	thin turb. b.l.	classifications of stall regimes
Waitman *et al*, 1961	varied b.l. thickness	reduction in pressure recovery with increased b.l. thickness
Kline *et al*, 1959	thin turb. b.l.	performance map established
Sovran & Klomp, 1967 [85]		performance correlation
Johnston & Powars, 1969	thin turb b.l.	effects of aspect ratio
Reneau *et al*, 1973 [77]	thin turb. b.l	different parameters affect different flow regimes
McMillan/Johnston, 1973 [63]	fully turb.	low AS flow characteristics
Runstadler *et al*1975	various	comprehensive design data
Ashjaee & Johnston, 1980	thin turb. b.l.	transitory stall investigation

	AS	l_d or n/W_1	$2\theta, deg.$ or AR	Re. No.
Moore & Kline, 1958	high	1-30	2θ =0-30	6-20000
Kline, 1959 [52]	high	1-40	2θ =1-200	various
Waitman *et al*, 1961	high	8,12,48	2.5-40,2θ =2.5-40°	10^4
Kline *et al*, 1959	high	1-40	2θ =1-60	various
Sovran & Klomp, 1967 [85]				
Johnston & Powars, 1969	0.25-4	6	AR =1.5-3	2×10^5
Reneau *et al*, 1973 [77]	high	1-60	2θ=0-100	$\geq 5 \times 10^4$
McMillan/Johnston, 1973 [63]	0.1	6	AR =1.5-8.0	2.1×10^4-6.8×10^4
Runstadler *et al.* 1975	various	various	various	various
Ashjaee & Johnston, 1980	4	L 15	2θ=0-26°	2.2×10^5

Table 1: Landmarks of 2D plane wall diffuser research

	Investigation	Model	Ground Condition	*Re*	Comment
Carr,1968 [14]	experimental	saloon car	fixed	3.2×10^6	force/pressures
Howell,1994 [46]	experimental	bluff body	fixed/moving		force/pressures
George,1981 [33]	experimental	bluff body	fixed		force, pressures, oil flow
George/Donis,1983 [34]	experimental	various	fixed/moving		force/oil flow
Sovran,1994 [84]	review	N/A	N/A	N/A	N/A
Cooper *et al*,1998 [19]	exp./CFD	bluff body	fixed/moving	8.3×10^5	force/pressures
Cooper *et al*,1999 [20]	analytical	N/A	N/A	N/A	N/A

	Main Findings
Carr,1968 [14]	rear diffuser found to increase aerodynamic performance
Howell,1994 [46]	fixed/moving ground comparison
George,1981 [33]	counter-rotating vortex pair
George/Donis,1983 [34]	occurrence of an optimum ride height, flow asymmetry at low ride height
Sovran,1994 [84]	diffuser pump
Cooper *et al*,1998 [19]	performance map, analysis of components of down-force production
Cooper *et al*,1999 [20]	

Table 2: Diffuser in ground effect research.

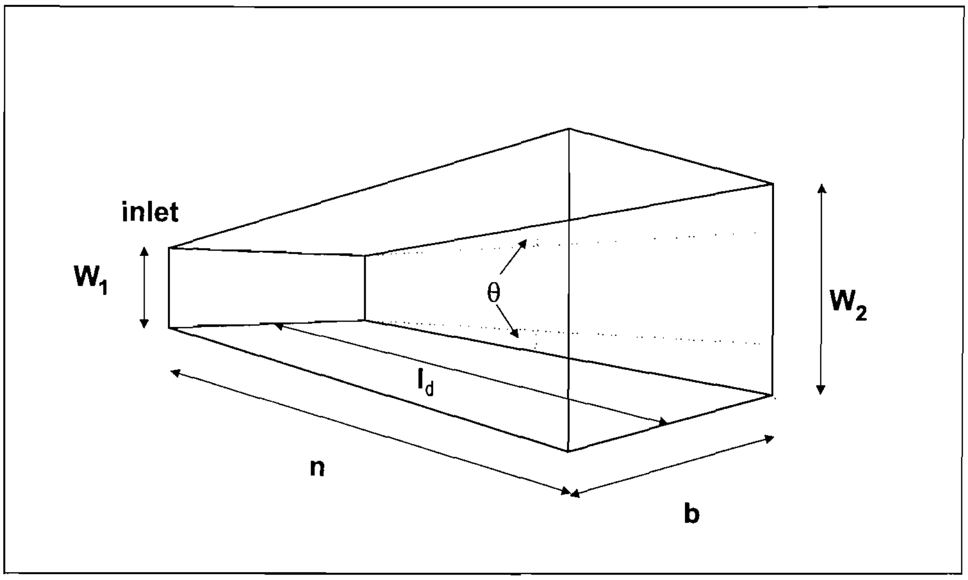

Figure 1: Schematic representation of an internal flow plane-walled diffuser.

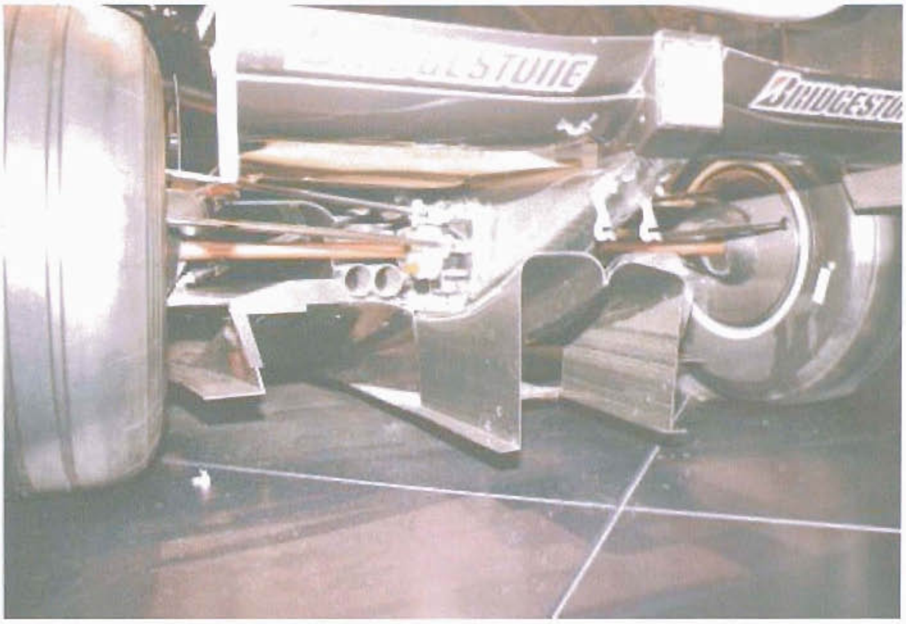

Figure 2: The rear diffuser of a Formula 1 racing car.

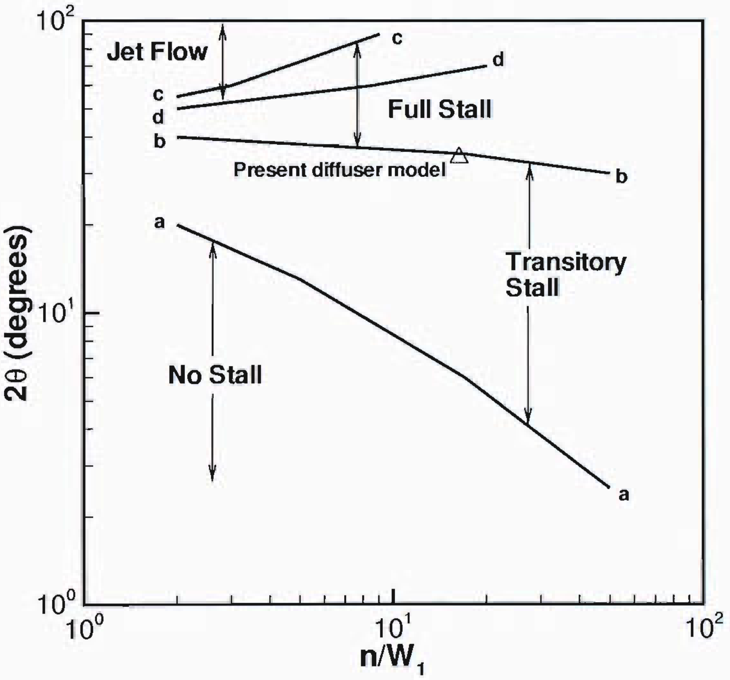

Figure 3: Plane-walled diffuser flow regimes for a high aspect ratio, thin inlet boundary layer, high Reynolds Number, low Mach Number flow. Reneau*et al* [77].

Chapter 2

Test Models and Experimental Techniques

The wind tunnel model and test techniques are outlined in this Chapter. A description of the experimental facilities is included. Details of the measurement uncertainties and repeatability are given in Appendices A and B respectively.

2.1 Introduction

It was decided from the outset that the diffuser should be investigated in isolation from the other components of the racing car. The reason for this was that the flow around the diffuser as positioned on the car was expected to be too complicated to analyse. It made more sense to attempt to understand the diffuser in isolation before adding additional complexities. The basic design requirements of the model were that it consisted of the necessary features of a racing car diffuser. These were considered to be a diffusing section: an upswept surface, preferably with side-plates; a flat-bottomed surface upstream of the diffusing section to replicate the undertray of the car, a bluff base and a means of preventing flow separation at the leading edge of the model so that air from upstream of the model was permitted a clear pathway to the diffusing section. Further criteria were to produce a sufficiently large Reynolds Number based on the model length and the wind speed in the wind tunnel to produce the flow characteristics, the facility to access the flow inside the diffuser with a laser, and access to the upper side of the diffuser surface for installation of pressure tappings. Installation of the model in the wind tunnels required that the model ride height above the ground be adjustable. For certain tests, it was advantageous to be able to lift the model from its installation in order to view the model underside more easily. The wind tunnel model design is discussed in Section 2.2. Using this model, an experimental database for the flow field has been established, and it provides the basis for the discussions presented in the thesis. The database has also been used for the validation of a complementary CFD simulation that provides a more detailed understanding of the flow.

2.2 Test Models

In order to study the effects of a diffuser in isolation from the rest of the car, a generic model was designed with the aim of incorporating the salient features of a diffuser in ground effect and to generate the major flow physics. The model was a 3D bluff body whose length upstream of the diffusing section was sufficient to ensure that the upstream flow did not interact with the diffuser flow. In this way the flow phenomena encountered could be attributed to the effects of the diffuser. The model is shown schematically in Figure 4 together with the co-ordinate system used in presenting the results. The model length is l =1.315 m, the width is $2d$ =0.314 m, and the height is h =0.326 m. The diffuser has a 17 degree ramp angle, its length is 0.538 m and the height of the rear bluff base is 0.159 m. The diffuser angle was chosen as being representative of current racing car diffuser angles, and also keeping in mind the possibility of controlling flow separation inside the diffuser in later tests. The inlet to the upswept surface of the diffuser is faired at a radius of 0.0785 m.

2.2.1 Transition fixing

The transition to turbulent flow over the model nose was fixed by a length of 0.4 mm diameter piano wire attached around the nose by thin aluminium foil tape. The location of transition was fixed to avoid a laminar separation bubble developing over the nose top surface, and also so that computational simulations could be designed to transition at a fixed location at the model nose.

2.2.2 Pressure Tapped Model

A second model was manufactured, identical to the first model. The second model was fitted with pressure tappings located along the underbody centreline and in a spanwise direction across the diffuser ramp at four measurement stations. A schematic of the measurement locations is shown in Figure 5 (b). The bluff base of the model was also tapped. See Tables 10-12. There were 111 tappings on the model.

2.2.3 Transparent side-plate

PIV tests inside the diffuser required optical access to the diffuser. In order that the laser sheet could be shone through the flow a transparent perspex side-plate was employed to replace the aluminium side-plate on the starboard side of the model. The transparent side-plate was of the same thickness as the aluminium side-plate so as to preserve replication of the lower edge. As such, it required reinforcement with a 1 mm thick carbon fibre plate towards its trailing edge to avoid bending in the wind. The plate was faired around its edges to minimise alteration to the flow. It was considered that the added thickness of the plate should not significantly alter the flow, and indeed no indication was given throughout the tests that it did so.

2.3 Model Installation in wind tunnel

Installation of the model in the 3.5 $m \times$ 2.6 m wind tunnel is shown in Figure 7. The model was hung from the overhead balance by two struts, faired near the model, which were attached to a circular rod placed through the model. The distance between the model and the struts was 0.140 m at each side. The rear of the model was attached via a pin in the top of the model to a pitch rod, located along the model centreline and also attached to the overhead balance. The installation was adjustable allowing the model to be placed above the moving ground plane at heights varying from 0.01 m (h_r/d=0.064) to 0.199 m (h_r/d= 1.268), (0.65 m (h_r/d=4.14) in the 3.5 $m \times$ 2.6 m wind tunnel). The model was positioned in the centre of the tunnel span.

2.4 Setting of Model Ride Height

The ride height of the model above the ground belt was determined using aluminium blocks and spacers of pre-determined size. The height was measured at four model locations in order to ensure the height was even along the length and the span of the model. These were at either side of the model underneath the front struts, and at the rear corner of each side-plate. The model incidence was checked with a digital inclinometer. Care was also taken to ensure the yaw angle of the model was maintained to within 0.3 degrees of zero by measuring the distance from the model to the edge of the ground platen at two locations, under the front struts and at the rear corner of the side-plate. Checks of the model position were made before and after each run.

2.5 Blockage

In the 2.1 $m \times 1.5$ m wind tunnel the blockage caused by the model cross sectional area in the flow direction was 2.86%, whilst in the 3.5 $m \times$ 2.6 m tunnel it was 1.12%. No corrections were made to the measurements for blockage as it was considered to be unnecessary.

2.6 Test Facilities and Operating Conditions

Experiments were conducted in the University of Southampton's two low-speed wind tunnels. The wind tunnels are of a closed circuit design and are each equipped with a moving ground belt system. The R.J. Mitchell wind tunnel has a test section of 3.5 m × 2.6 m whilst the smaller of the two tunnels has a test section cross sectional area of 2.1 m × 1.5 m . A schematic of the moving belt system of the 3.5 m × 2.6 m wind tunnel is shown in Figure 8. The belt is 4 m long and 2 m wide. The belt is driven at the rear driven roller. The boundary layer is removed ahead of the moving belt by a large suction slot. Any residual boundary layer is then sucked out through a perforated plate directly upstream of the belt. A tension roller keeps the belt tight, and suction holes in the platen on which the belt lies ensure that the belt does not lift. Belt suction is regulated to the required level. Water cooling underneath the platen regulates the temperature of the belt and platen. The flow speed is 100% of the freestream at 2 mm above the moving ground, and the freestream turbulence level is 0.25%. In the 2.1 m × 1.5 m the flow speed is 99.4% of the freestream at 2 mm above the ground and the freestream turbulence is 0.2%.

All measurements presented were taken in the 2.1 m × 1.5 m wind tunnel with the exception of the LDA measurements, which were taken in the 3.5 m × 2.6 m wind tunnel. This was due to the fixed nature of the LDA apparatus in the 3.5 m × 2.6 m wind tunnel and the more limited access to use of this tunnel. Various checks were undertaken to ensure that flows in the two tunnels were similar. Oil flow visualisation of the model at salient ride heights was conducted in each tunnel. Force measurements were attempted in the 3.5 m × 2.6 m wind tunnel using its overhead balance, however a problem with the calibration of the balance prevented a meaningful comparison of the force results between the two tunnels. A comparison of LDA measurements taken in the 3.5 m × 2.6 m wind tunnel with PIV measurements taken at the same plane but in the 2.1 m × 1.5 m wind tunnel are presented in Figure 83.

The majority of the experiments were conducted at a Reynolds Number of 1.8×10^6 based on the model length, equating to a freestream velocity of 20 m/s. Force measurements were also taken at three other Reynolds Numbers of 0.7×10^6, 1.3×10^6 and 2.3×10^6. Formula 1 teams testing in a tunnel the size of the 3.5 m × 2.6 m wind tunnel would conduct tests at wind speeds up to 40 m/s, on a model of length 2.4 m, equating to a test Reynolds Number of 6.6×10^6.

2.7 Experimental Techniques

Techniques employed in investigating the flow were force measurements, surface pressure measurements, oil flow visualisation, LDA and PIV.

2.7.1 Force measurements

Force measurements were taken using overhead force balances. Taking a set of force measurements involved setting all balance components to zero with the wind turned off. The tunnel was then run up to the required freestream dynamic pressure and the measurements were taken. A set of 8 measurements were recorded in a run, each with 75 samples, and then the wind was turned off. After a short settling period, the balance components returned to zero force reading, indicating that the results were valid. The results presented in Chapter 3 are averaged from these datasets. In this way, the forces measured are due only to the effect of the air flowing around the model. The wind tunnel was stopped in-between force measurements at different ride heights. The measurements were corrected to free-air wind-axes coefficients, and the values given were also corrected for installation tares. In discussing the results the term down-force or suction will be used rather than negative lift or pressure to avoid confusion. The uncertainties in C_L and C_D measurements were calculated as ± 0.0280 and ± 0.0038 respectively. An account of the uncertainty estimates can be found in Appendix A.1.

2.7.2 Surface pressure tappings

Surface pressure measurements were obtained using hypodermic tubes mounted flush with the model surface. The tubes were 0.85 mm inner diameter and 1.5 mm outer diameter, and 25 mm long. Plastic tubing attached the tubes to either a ZOC (Zero, Operate, Calibrate) or a Scanivalve pressure transducer. Tappings connected to the ZOC transducer are measured simultaneously, whilst the Scanivalve transducer measures each port in turn, spending 2 seconds at each port. A further description of the transducers may be found in Reference [5]. The Scanivalve was calibrated by setting two ports, one at the beginning and one at the end of the run, to measure total pressure. In this way, any drifting of the transducer was immediately apparent. The ZOC was calibrated by setting each port to zero before the start of a run and checking that the ports returned to zero after the run. The data was output in the form of a pressure coefficient, C_p, which was calculated by the PI Research data acquisition software from the measured values of static pressure, total pressure and dynamic pressure. Dynamic pressure was measured by a diaphragm in the transducer which was connected to the pitot tube in the wind tunnel and subjected to total pressure (p_{tot}) on one side and freestream static pressure (p_s) on the other side. The difference in pressure across the diaphragm was therefore the dynamic pressure, q. The tappings record local static pressure at the surface, p, and the pressure coefficient is calculated to be $C_p = p - p_\infty / q_\infty$. Each set of readings was repeated several times in order to ensure repeatability, and the results presented in Chapter 3 are the pressure coefficients averaged from these datasets. The uncertainty in the results was calculated as $C_p = \pm 0.0656$. An account of the uncertainty estimate can be found in Appendix A.2.

2.7.3 Oil flow visualisation

Surface flow was visualised using an oil streak method with a mixture of titanium dioxide and light oil [60]. The technique involves spraying the mixture over all outer surfaces of the model. Running the wind tunnel for several minutes at the freestream velocity evaporates the oil in the mixture, leaving the titanium dioxide to mark time-averaged streaklines on the model surface.

2.7.4 Laser doppler anemometry

LDA is a non-intrusive method of measuring ensemble averaged off-surface velocities. The technique is based upon the principle that at the intersection of two laser beams, a pattern of interference fringes can occur, forming fringes of high and low intensity. A seed or tracer particle passing through the intersection scatters light through the bright fringes but not from the dark. The scattered light contains components of both beams and fluctuates in intensity with a frequency proportional to the velocity perpendicular to the bisector of the two beams. This additional frequency is known as the Doppler shift. Directional ambiguity of the velocity is resolved by shifting the frequency of one beam relative to the other by a fixed amount; the interference fringes appear to move at the shift frequency and negative velocities may thus be distinguished. In LDA tests, two or more laser beams are aligned to create the intersection or focus of the beams, the tracer particles are small droplets of oil seeded into the flow, and as they pass through the focus the scattered light is received by a photo-optical sensor. The signals are processed to calculate the velocity of each tracer particle.

A Dantec three-component system with 5W Ar-ion laser generator was employed. The system was operated in an off-axis back-scatter (coincident) mode, which means that a particle must pass through the focus of all three beam pairs to be counted as a valid measurement. The reflected signals were analyzed using three DANTEC Burst Spectrum Analyzers. A comprehensive description of the LDA apparatus and calibration method is given in Jeffrey [47]. In the present tests, three component velocities were obtained using two optical probe heads. Movement of the beam focus through the measurement plane was achieved by mounting the probe heads on an automated three directional traverse, thus allowing measurements to be taken at a specified array of points in space.

Three component measurements of flow velocity (u, v, w) can be obtained at a single point in a flow field. At each point, the instantaneous velocity is ensemble averaged to obtain the mean velocity. Corresponding mean squares of the perturbation velocities $(\overline{uu}, \overline{vv}, \overline{ww})$, and Reynolds stresses $(\overline{uv}, \overline{vw}, \overline{wu})$ are then calculated.

LDA test cases are listed in Table 7. Measurement planes are shown schematically in Figure 5 (a). The LDA measurements were made at several stations on the model surface along the centreline ($z = 0$) to capture boundary layer profiles above and below the model. Surveys were also performed in streamwise cross-planes downstream of the model. A description of the velocity resolution can be found in Zhang [99]. The velocities measured in the beam axes were resolved into the tunnel coordinate system (x, y, z) using a matrix transformation [47]. In these tests, the green beam was used to resolve the streamwise velocity component, u, the blue beam the transverse component, v, and the violet beam the spanwise component, w. The oil based seeding particles were $3 \mu m$ in diameter, and were provided by two seeding generators: one released seed particles downstream of the model and the other from inside the front of the model.

Typically, over 1000 particle samples were collected at each measurement point and the number of data points in a plane ranged from 421 to 822. The measurement grid spacing varied, being finer near the centre of the vortex. The positioning of the measurement points was chosen based upon an initial coarse grid survey of the area to be measured, in order to ascertain the whereabouts of the main flow features. Refinements were then made in specific areas of interest, such as the vortex regions. The final measurement grid resolution thus varied from 2 mm to 20 mm between adjacent grid points. 95% confidence level uncertainties in the measurements were estimated to be $\pm 0.09\ m/s$, $\pm 0.09\ m/s$, and $\pm 0.31\ m/s$ for u, v, w respectively at a freestream speed of 20 m/s. An account of the uncertainty estimate can be found in Appendix A.3.

2.7.5 Particle image velocimetry

PIV is a non-intrusive technique for obtaining instantaneous whole field velocities. The property measured is the distance travelled by particles in the flow within a known time interval. The flow is seeded as with LDA, and in order to detect the movement of the seeding particles, an area of the flow field is illuminated by a light sheet of approximately 1 mm thickness. The light sheet, which is generated by a laser and a system of optical components, is pulsed to produce a stroboscopic effect, freezing the movement of the seeding particles.

A CCD (Charge Coupled Device) camera is positioned at right angles to the light sheet to detect the position of the illuminated seeding particles. Camera images are synchronized with the light pulses of the laser so that the positions of the particles at light pulse 1 are registered on camera frame 1, and positions at light pulse 2 appear on camera frame 2. The camera images are divided into rectangular interrogation areas. For each of these areas the images from the first and second light-sheet pulses are cross-correlated to produce an average particle displacement vector. Dividing by the time between the two images captured, the displacement vectors are converted into a map of velocity vectors.

A number of two-component PIV tests were conducted in the 2.1 $m \times 1.5$ m wind tunnel. A Dantec PIV system was employed, consisting of a FlowMap 1100 Processor, a Gemini PIV 15 Nd:YAG laser (class 4, 120 mJ at 532 nm) and a Dantec HiSense Camera (type 13 gain 4) producing images of 1290×1024 pixels. Flow was seeded by smoke particles of 0.1-5 μm in diameter. The use of a single camera allows the measurement of velocity components in two dimensions in the plane of the laser light-sheet. The camera was operated at a rate of 2Hz.

PIV can be used to produce either a time-averaged flow field, by averaging over a large number of instantaneous flow fields, or may be used to obtain instantaneous flow field data. At a sampling rate of 2Hz, full resolution of turbulent flow features is not realistic, however the instantaneous snapshots of a flow field that are obtained can provide a useful insight into the unsteady nature of a flow.

Measurements were taken in cross-flow planes both inside the diffuser to coincide with those of the spanwise pressure distributions and at x_1/d=0.096 aft of the diffuser exit. Additional measurements were taken for certain cases in the streamwise flow exiting the diffuser and at the diffuser inlet. Test cases and conditions are listed in Table 8. The physical resolution between measured velocity vectors is 3.2 mm in each direction of the measurement plane for the majority of results shown. This resolution is determined by the size of the actual measurement plane, and a user determined level of resolution during processing of the raw data. The uncertainty in the measurements is estimated to be $\approx$ 10% on average. An account of the measurement uncertainty can be found in Appendix A.4.

2.8 Experimental Programme

In this Section, the types of wind tunnel experiments conducted during the course of the research are presented with the conditions under which they were performed.

Force and pressure measurements were conducted at a constant dynamic pressure of 25 mmH_20, equating to a Reynolds Number of 1.8×10^6. Certain force measurements were taken in both wind tunnels to ensure there was no significant difference in the flows for each tunnel. Force measurement test cases are listed in Tables 3. Surface pressure measurement test cases are listed in Table 4. Surface flow visualisation tests were conducted mainly in the 2.1 $m \times 1.5$ m wind tunnel at a constant dynamic pressure of 25 mmH_20. Test cases are listed in Table 5. LDA and PIV measurements were carried out at a constant freestream velocity of 20 m/s. LDA measurements were conducted in the 3.5 $m \times$ 2.6 m wind tunnel, whilst PIV measurements were conducted in the 2.1 $m \times 1.5$ m tunnel. Tables 6 and 7 list the LDA test cases and Tables 8 and 9 list PIV measurement cases.

h_r/d	wind tunnel	Re	Ground Condition	Transition
0.064	2.1 m × 1.5 m	1.3×10^6,	moving	fixed
0.064	2.1 m × 1.5 m	1.8×10^6,	moving/fixed	fixed/free
0.064	2.1 m × 1.5 m	1.8×10^6,	moving	fixed
0.096	2.1 m × 1.5 m	1.3×10^6	moving	fixed
0.096	2.1 m × 1.5 m	1.8×10^6	moving/fixed	fixed/free
0.096	2.1 m × 1.5 m	2.3×10^6	moving	fixed
0.127	2.1 m × 1.5 m	1.3×10^6	moving	fixed
0.127	2.1 m × 1.5 m	1.8×10^6	moving/fixed	fixed/free
0.127	2.1 m × 1.5 m	2.3×10^6	moving	fixed
0.127	3.5 m × 2.6 m	1.8×10^6	moving	fixed
0.159	2.1 m × 1.5 m	1.3×10^6	moving	fixed
0.159	2.1 m × 1.5 m	1.8×10^6	moving/fixed	fixed/free
0.159	2.1 m × 1.5 m	2.3×10^6	moving	fixed
0.159	3.5 m × 2.6 m	1.8×10^6	moving	fixed
0.166	2.1 m × 1.5 m	1.8×10^6	moving/fixed	fixed
0.178	2.1 m × 1.5 m	1.8×10^6	fixed	fixed
0.191	2.1 m × 1.5 m	1.3×10^6	moving	fixed
0.191	2.1 m × 1.5 m	1.8×10^6	moving/fixed	fixed/free
0.191	2.1 m × 1.5 m	2.3×10^6	moving	fixed
0.191	3.5 m × 2.6 m	1.8×10^6	moving	fixed
0.197	2.1 m × 1.5 m	1.3×10^6	moving	fixed
0.197	2.1 m × 1.5 m	1.8×10^6	moving	fixed
0.197	2.1 m × 1.5 m	2.3×10^6	moving	fixed
0.197	3.5 m × 2.6 m	1.8×10^6	moving	fixed
0.204	2.1 m × 1.5 m	1.3×10^6	moving	fixed
0.204	2.1 m × 1.5 m	1.8×10^6	moving/fixed	fixed/free
0.204	2.1 m × 1.5 m	2.3×10^6	moving	fixed
0.204	3.5 m × 2.6 m	1.8×10^6	moving	fixed
0.210	2.1 m × 1.5 m	1.3×10^6	moving	fixed
0.210	2.1 m × 1.5 m	1.8×10^6	moving/fixed	fixed/free
0.210	2.1 m × 1.5 m	2.3×10^6	moving	fixed
0.210	3.5 m × 2.6 m	1.8×10^6	moving	fixed
0.217	2.1 m × 1.5 m	1.8×10^6	moving/fixed	fixed/free
0.223	2.1 m × 1.5 m	1.3×10^6	moving	fixed
0.223	2.1 m × 1.5 m	1.8×10^6	moving/fixed	fixed/free
0.223	2.1 m × 1.5 m	2.3×10^6	moving	fixed
0.223	3.5 m × 2.6 m	1.8×10^6	moving	fixed

h_r/d	wind tunnel	Re	Ground Condition	Transition
0.229	2.1 $m \times$ 1.5 m	1.8×10^6	moving	fixed
0.236	2.1 $m \times$ 1.5 m	1.8×10^6	moving	fixed
0.242	2.1 $m \times$ 1.5 m	1.8×10^6	moving	fixed
0.248	2.1 $m \times$ 1.5 m	1.8×10^6	moving	fixed
0.255	2.1 $m \times$ 1.5 m	1.3×10^6	moving	fixed
0.255	2.1 $m \times$ 1.5 m	1.8×10^6	moving/fixed	fixed/free
0.255	2.1 $m \times$ 1.5 m	2.3×10^6	moving	fixed
0.255	3.5 $m \times$ 2.6 m	1.8×10^6	moving	fixed
0.287	2.1 $m \times$ 1.5 m	1.3×10^6	moving	fixed
0.287	2.1 $m \times$ 1.5 m	1.8×10^6	moving/free	fixed/free
0.287	2.1 $m \times$ 1.5 m	2.3×10^6	moving	fixed
0.318	2.1 $m \times$ 1.5 m	1.3×10^6	moving	fixed
0.318	2.1 $m \times$ 1.5 m	1.8×10^6	moving/free	fixed/free
0.318	2.1 $m \times$ 1.5 m	2.3×10^6	moving	fixed
0.318	3.5 $m \times$ 2.6 m	1.8×10^6	moving	fixed
0.382	2.1 $m \times$ 1.5 m	1.3×10^6	moving	fixed
0.382	2.1 $m \times$ 1.5 m	1.8×10^6	moving/free	fixed/free
0.382	2.1 $m \times$ 1.5 m	2.3×10^6	moving	fixed
0.382	3.5 $m \times$ 2.6 m	1.8×10^6	moving	fixed
0.446	2.1 $m \times$ 1.5 m	1.3×10^6	moving	fixed
0.446	2.1 $m \times$ 1.5 m	1.8×10^6	moving	fixed
0.446	2.1 $m \times$ 1.5 m	2.3×10^6	moving	fixed
0.510	2.1 $m \times$ 1.5 m	1.3×10^6	moving	fixed
0.510	2.1 $m \times$ 1.5 m	1.8×10^6	moving	fixed
0.510	2.1 $m \times$ 1.5 m	2.3×10^6	moving	fixed
0.573	2.1 $m \times$ 1.5 m	1.3×10^6	moving	fixed
0.573	2.1 $m \times$ 1.5 m	1.8×10^6	moving	fixed
0.573	2.1 $m \times$ 1.5 m	2.3×10^6	moving	fixed
0.573	3.5 $m \times$ 2.6 m	1.8×10^6	moving	fixed
0.637	2.1 $m \times$ 1.5 m	1.3×10^6	moving	fixed
0.637	2.1 $m \times$ 1.5 m	1.8×10^6	moving	fixed
0.637	2.1 $m \times$ 1.5 m	2.3×10^6	moving	fixed
0.764	2.1 $m \times$ 1.5 m	1.3×10^6	moving	fixed
0.764	2.1 $m \times$ 1.5 m	1.8×10^6	moving/fixed	fixed/free
0.764	2.1 $m \times$ 1.5 m	2.3×10^6	moving	fixed
0.764	3.5 $m \times$ 2.6 m	1.8×10^6	moving	fixed

Table 3: Force measurement cases.

h_r/d	wind tunnel	Re	Ground Condition	Transition
0.064	2.1 $m \times$ 1.5 m	1.8×10^6	moving	fixed
0.127	2.1 $m \times$ 1.5 m	1.8×10^6	moving	fixed
0.159	2.1 $m \times$ 1.5 m	1.8×10^6	moving	fixed
0.191	2.1 $m \times$ 1.5 m	1.8×10^6	moving	fixed
0.204	2.1 $m \times$ 1.5 m	1.8×10^6	moving	fixed
0.210	2.1 $m \times$ 1.5 m	1.8×10^6	moving	fixed
0.217	2.1 $m \times$ 1.5 m	1.8×10^6	moving	fixed
0.223	2.1 $m \times$ 1.5 m	1.8×10^6	moving	fixed
0.255	2.1 $m \times$ 1.5 m	1.8×10^6	moving	fixed
0.318	2.1 $m \times$ 1.5 m	1.8×10^6	moving	fixed
0.382	2.1 $m \times$ 1.5 m	1.8×10^6	moving	fixed
0.446	2.1 $m \times$ 1.5 m	1.8×10^6	moving	fixed
0.573	2.1 $m \times$ 1.5 m	1.8×10^6	moving	fixed
0.764	2.1 $m \times$ 1.5 m	1.8×10^6	moving	fixed
1.268	2.1 $m \times$ 1.5 m	1.8×10^6	moving	fixed

Table 4: Surface pressure measurement cases.

h_r/d	wind tunnel	Re	Ground Condition	Transition
0.064	2.1 $m \times$ 1.5 m	1.8×10^6	moving	fixed
0.127	2.1 $m \times$ 1.5 m	1.8×10^6	moving	fixed
0.159	2.1 $m \times$ 1.5 m	1.8×10^6	moving	fixed
0.159	3.5 $m \times$ 2.6 m	1.8×10^6	moving	fixed
0.191	2.1 $m \times$ 1.5 m	1.8×10^6	moving	fixed
0.204	2.1 $m \times$ 1.5 m	1.8×10^6	moving	fixed
0.210	2.1 $m \times$ 1.5 m	1.8×10^6	moving	fixed
0.217	2.1 $m \times$ 1.5 m	1.8×10^6	moving	fixed
0.223	2.1 $m \times$ 1.5 m	1.8×10^6	moving	fixed
0.223	3.5 $m \times$ 2.6 m	1.8×10^6	moving	fixed
0.255	2.1 $m \times$ 1.5 m	1.8×10^6	moving	fixed
0.318	2.1 $m \times$ 1.5 m	1.8×10^6	moving	fixed
0.382	2.1 $m \times$ 1.5 m	1.8×10^6	moving	fixed
0.446	2.1 $m \times$ 1.5 m	1.8×10^6	moving	fixed
0.510	2.1 $m \times$ 1.5 m	1.8×10^6	moving	fixed
0.764	2.1 $m \times$ 1.5 m	1.8×10^6	moving	fixed

Table 5: Surface flow visualisation cases.

h_r/d	Measurement planes			
top of model	x/d=2.3	x/d=3.5	x/d=4.5	x/d=5.5
underneath model	x/d=3.0	x/d=4.0	x/d=4.5	x/d=4.9

Table 6: LDA boundary layer profile cases at h_r/d=4.14.

h_r/d	Measurement planes			
0.064		x_1/d=0.096	x_1/d=1.051	x_1/d=2.006
0.159		x_1/d=0.096	x_1/d=1.051	x_1/d=2.006
0.204		x_1/d=0.096		x_1/d=2.006
0.210		x_1/d=0.096		x_1/d=2.006
0.255		x_1/d=0.096	x_1/d=1.051	x_1/d=2.006
0.318		x_1/d=0.096		x_1/d=2.006
0.382		x_1/d=0.096	x_1/d=1.051	x_1/d=2.006
0.764		x_1/d=0.096	x_1/d=1.051	x_1/d=2.006
4.14	x/d =4.95	x_1/d=0.096		

Table 7: Cross-flow LDA cases.

h_r/d	Measurement planes						
0.064					x/d=6.83	x/d=7.74	x_1/d=0.096
0.204	x/d=4.95	x/d=5.44	x/d=5.91		x/d=6.83	x/d=7.74	x_1/d=0.096
0.255	x/d=4.95	x/d=5.44	x/d=5.91	x/d=6.37	x/d=6.83	x/d=7.74	x_1/d=0.096
0.382		x/d=5.44	x/d=5.91	x/d=6.37	x/d=6.83	x/d=7.74	x_1/d=0.096
0.764		x/d=5.44	x/d=5.91		x/d=6.83	x/d=7.74	x_1/d=0.096

Table 8: Cross-flow PIV cases.

h_r/d	Measurement planes		
0.204	z/d=-0.936	z/d=0	z/d=0.936
0.255	z/d=-0.936	z/d=0	z/d=0.936

Table 9: Streamwise PIV cases.

Port	x/d	Port	x/d
1	0.032	22	5.518
2	1.146	23	5.595
3	2.293	24	5.673
4	3.185	25	5.750
5	4.625	26	5.828
6	4.706	27	5.905
7	4.747	28	5.982
8	4.787	29	6.060
9	4.828	30	6.137
10	4.868	31	6.214
11	4.909	32	6.292
12	4.949	33	6.369
13	4.988	34	6.524
14	5.054	35	6.678
15	5.093	36	6.833
16	5.131	37	7.065
17	5.170	38	7.297
18	5.209	39	7.529
19	5.286	40	7.761
20	5.363	41	7.994
21	5.441	42	8.226

Table 10: Surface pressure tapping locations at model centreline, z/d =0.

Port	x/d	z/d	Port	x/d	z/d	Port	x/d	z/d	Port	x/d	z/d
43	5.44	-0.89	64	5.91	-0.89						
44	5.44	-0.809	65	5.91	-0.809	86	6.83	-0.809	94	7.76	-0.809
45	5.44	-0.728	66	5.91	-0.728						
46	5.44	-0.647	67	5.91	-0.647						
46	5.44	-0.566	68	5.91	-0.566	87	6.83	-0.566	95	7.76	-0.566
47	5.44	-0.485	69	5.91	-0.485						
48	5.44	-0.404	70	5.91	-0.404						
49	5.44	-0.324	71	5.91	-0.324	88	6.83	-0.324	96	7.76	-0.324
50	5.44	-0.243	72	5.91	-0.243						
51	5.44	-0.162	73	5.91	-0.162	89	6.83	-0.162	97	7.76	-0.162
52	5.44	-0.081	74	5.91	-0.081						
21	5.44	0	27	5.91	0	36	6.83	0	40	7.76	0
53	5.44	0.081	75	5.91	0.081						
54	5.44	0.162	76	5.91	0.162	90	6.83	0.162	98	7.76	0.162
55	5.44	0.243	77	5.91	0.243						
56	5.44	0.324	78	5.91	0.324	91	6.83	0.324	99	7.76	0.324
57	5.44	0.404	79	5.91	0.404						
58	5.44	0.485	80	5.91	0.485						
59	5.44	0.566	81	5.91	0.566	92	6.83	0.566	100	7.76	0.566
60	5.44	0.647	82	5.91	0.647						
61	5.44	0.728	83	5.91	0.728						
62	5.44	0.809	84	5.91	0.809	93	6.83	0.809	101	7.76	0.809
63	5.44	0.89	85	5.91	0.89						

Table 11: Spanwise pressure tapping distributions.

Port	x/d	y/d	z/d
102	8.38	0.524	-0.955
103	8.38	0.524	-0.637
104	8.38	0.524	-0.318
105	5.44	0.524	0
106	8.38	0.524	0.318
107	8.38	0.524	0.637
108	8.38	0.524	0.955

Table 12: Distribution of pressure tappings across model base.

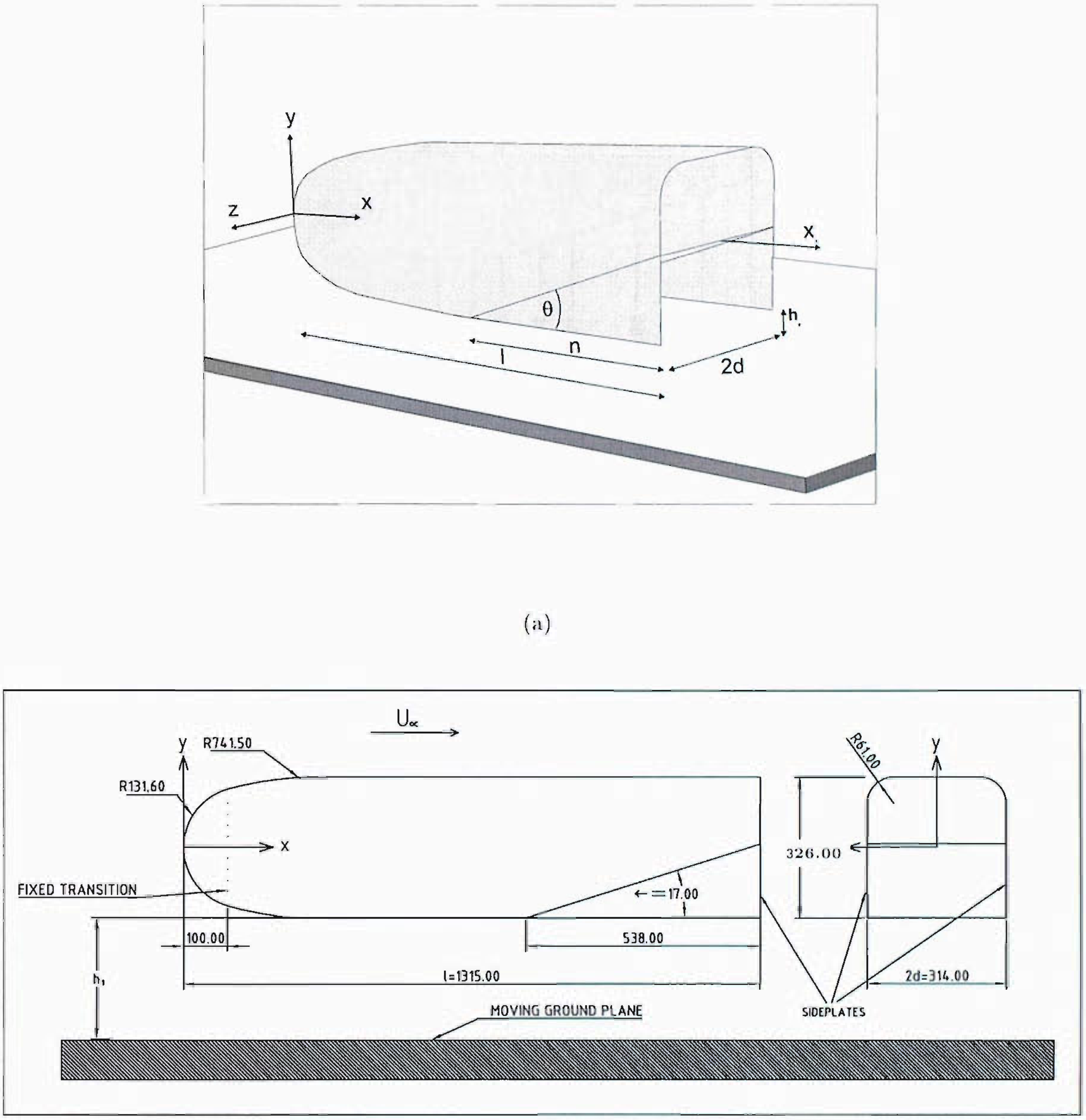

(a)

(b)

Figure 4: Schematics of model and co-ordinate system. Dimensions in mm.

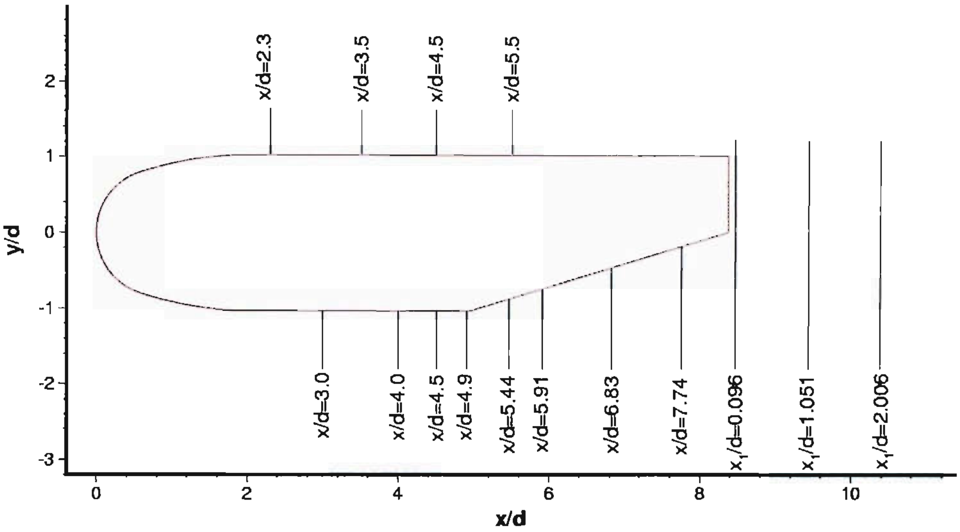

(a) Schematic of LDA and PIV measurement planes

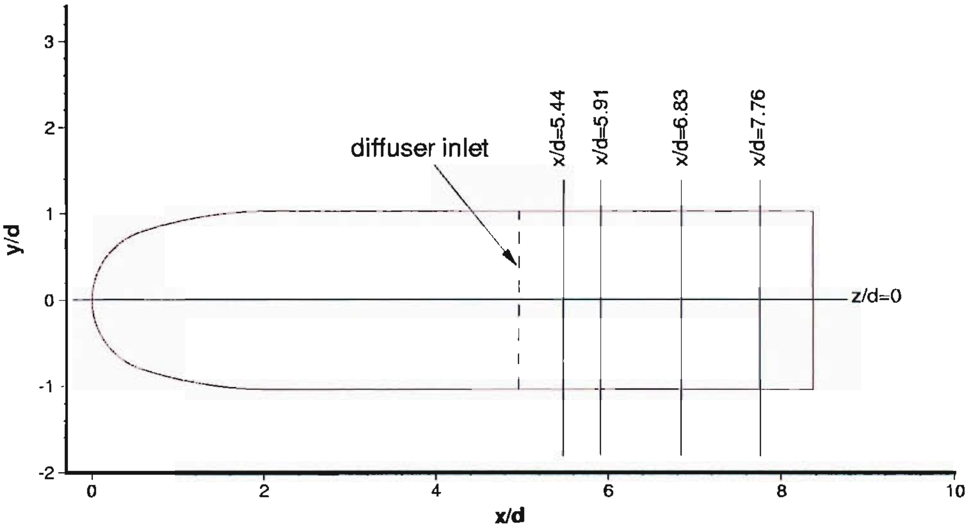

(b) Schematic of pressure tapping measurement planes

Figure 5: Schematic of measurement locations

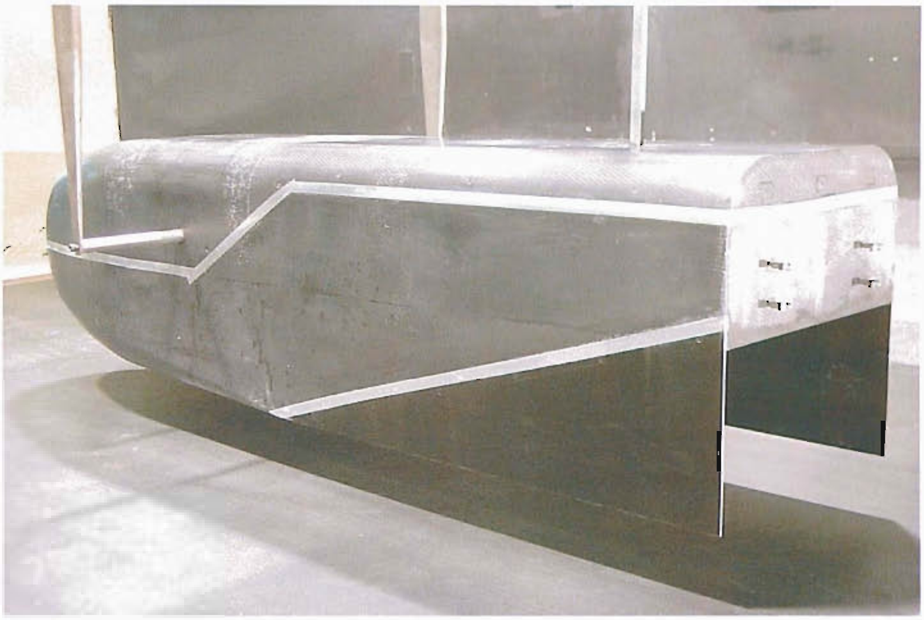

Figure 6: Model in the 2.1 $m \times 1.5$ m wind tunnel.

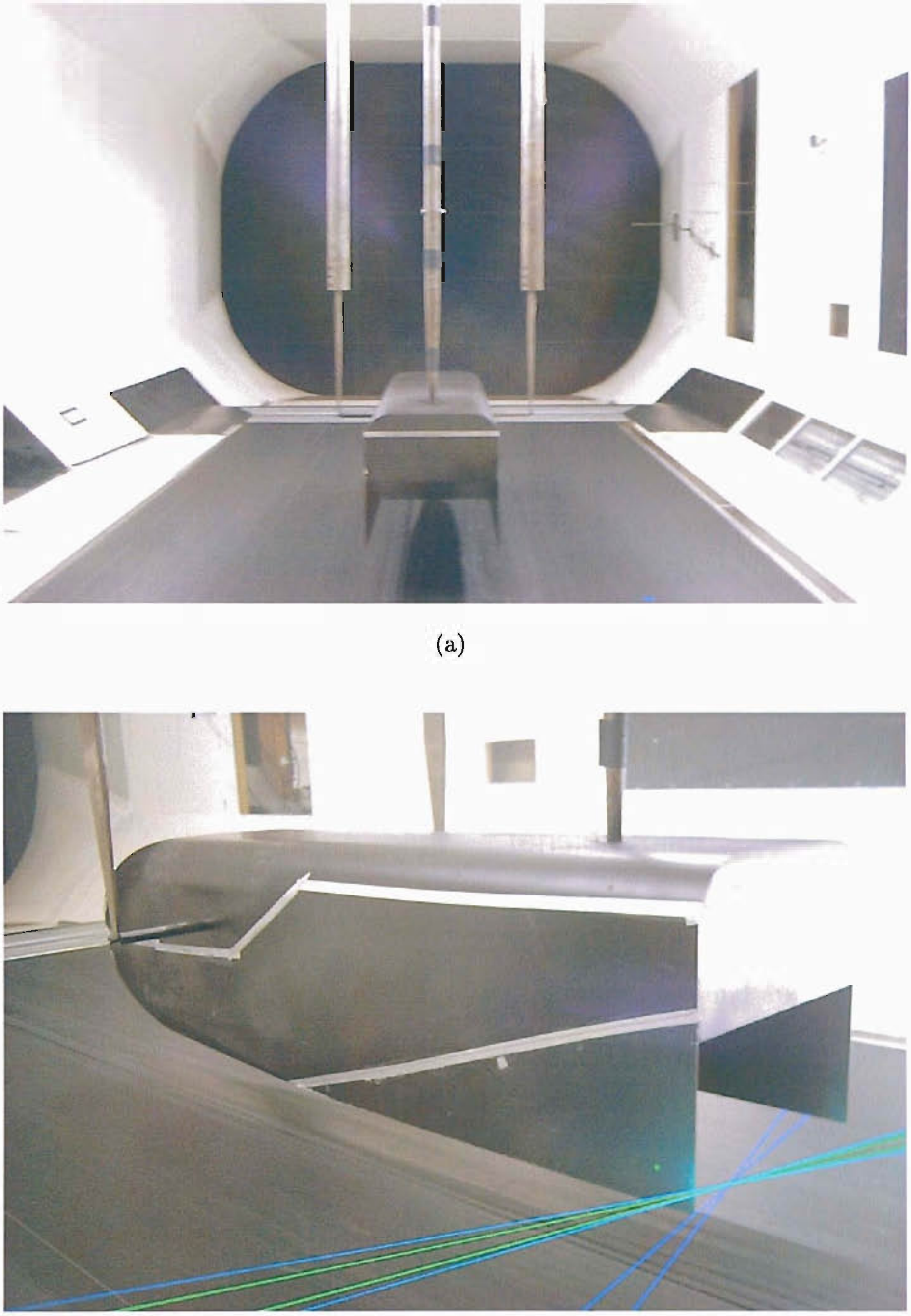

(a)

(b)

Figure 7: (a) Model installed in the 3.5 $m \times$ 2.6 m wind tunnel; (b) LDA beams focused behind the model.

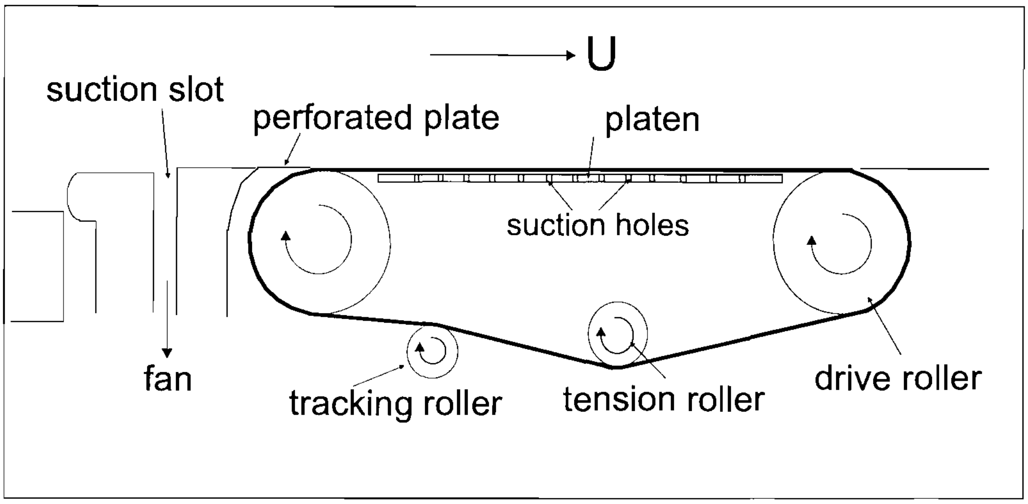

Figure 8: Schematic of the 3.5 $m \times$ 2.6 m moving ground apparatus.

Chapter 3

Force and Pressure Characteristics

The force and surface pressure characteristics of the diffuser model in proximity to a moving ground plane were deduced from forces, surface pressures and oil flow visualisation. The aerodynamic behaviour is described in terms of four distinct flow types according to ground proximity. An initial discussion presents the possible causes of the flow behaviour.

3.1 General Flow Behaviour

Four distinct types of flow may be identified along the down-force curve, each characterised by the curve gradient (Figure 9 (a)); A: down-force enhancement, B: maximum down-force, C: down-force reduction, and D: constant low level down-force. The down-force in the type A region is relatively weak at h_r/d=0.764, increasing smoothly with decreasing height until h_r/d=0.382. A noticeable change in the gradient of the lift curve at h_r/d=0.318 signifies the introduction of new flow physics due to the proximity of the ground. Between this height and h_r/d=0.210 is the type B region, a 'plateau' in the down-force in which the gradient of the lift curve between measurement points is small, and in which the air flow around the model appears to maintain a constant character. A maximum down-force occurs at h_r/d=0.210-0.217. The plateau is terminated by a sharp drop in the down-force which continues to fall steeply in the type C region before levelling once more at low ground clearances (type D). The drag force maximum occurs at the same ride height as the maximum down-force, and tends to fall with a similar trend to the down-force either side of the drag maximum (Figure 9 (b)). Centreline pressure coefficients at six salient model heights are shown in Figure 10. The first tapping just aft of the nose tip is in the near vicinity of the nose stagnation point, then as the flow is accelerated under the nose the pressure decreases to a suction peak at the beginning of the flat bottom. Along the flat bottom the pressure increases slightly before dropping steeply to the suction peak at the diffuser inlet. Inside the diffuser the pressure increases sharply before maintaining a gentle gradient towards the exit pressure, which is slightly negative due to a separated flow at the bluff base of the model. At h_r/d=0.217 and above, the curves are mainly smooth throughout the diffuser, however at the heights below the height of maximum down-force the curves show distinct undulations. The flow visualisation tests revealed that at all heights, air is entrained underneath the model from the sides by the low pressure on the bottom surface. Although there is evidence of a slight flow convergence towards the centreline on the surface immediately upstream of the diffuser inlet, the flow appears to be relatively uniform across the span of the model. Flow is also entrained underneath the side-plates. Separation occurs along the plate edges forming longitudinal vortices [34].

3.2 Classification of Flow Types

The results of the force, surface pressure and surface flow visualisation tests are presented in terms of flow type. Type A region of the down-force curve is denoted as the down-force enhancement region, type B as the maximum down-force region, type C as the force reduction region, and type D as the region of low down-force.

3.3 Down-force Enhancement

During force enhancement the flow is symmetric about the centre-plane (z = 0) of the diffuser. The symmetric flow is illustrated in Figure 11 where the spanwise pressure distributions along the diffuser ramp at h_r/d = 0.764 and 0.382 are plotted. At h_r/d=0.764 the presence of two longitudinal vortices at the location of x/d = 5.91, z/d = ±0.8 can just be identified by the points of low pressure, which increase again slightly at z/d = ±0.89. At x/d = 5.44 the pressures are even lower at the sides of the ramp, the maximum C_p=-1.048, indicating that the vortices are more than likely present in this part of the ramp as well, however the suction peak of the vortex is possibly beyond the tapping at z/d = 0.89.

By two and three model half-widths down the ramp the presence of the vortex pair is no longer apparent, leaving an almost flat pressure distribution across the ramp surface. Figure 11 also indicates how the vortices have developed at h_r/d = 0.382. The pressures at the diffuser surface have decreased, the peak is now C_p =-2.131 at x/d = 5.44, z/d = 0.89. Once again, the suction peaks appear to be at z/d > ±0.89, x/d = 5.44 and at z/d=0.8, x/d = 5.91. The vortices are still apparent at x/d = 6.83 albeit somewhat weakened, but are not a feature of the flow at the ramp surface at x/d = 7.76.

Oil flow visualisation reveals more of the flow features. Figure 12 shows the oil flow patterns over the diffuser ramp at h_r/d = 0.764. The patterns are symmetric about the model centreline. A small separation bubble is seen to occur across the inlet to the ramp except at the sides. This is in agreement with the behaviour of internal plane wall diffusers which were found to exhibit inlet separation at an included angle (2θ) of approximately 30-40 degrees depending upon the diffuser length ratio N/W_t [67], giving a wall divergence angle of between 15-20 degrees. Counter-rotating longitudinal vortices are detectable at either side of the ramp in the upper third of the photograph as weak 'S' shaped lines. The spanwise location of the suction peak of each vortex lies close to the point of inflexion of these S-lines [60]. The suction peak can be seen to move slightly towards the centreline as the flow proceeds along the diffuser. The curvature of the lines weakens as the flow decelerates to the base of the model, confirming the loss of vorticity on the ramp surface towards the exit. However as the pattern on the inner side-plate in Figure 12(b) shows, the vortices actually become detached from the surface. Secondary separations are apparent at the sides of the ramp in Figures 12 (a) and (b). As the ride height is lowered to $h_r/d = 0.382$, Figure 13 shows that the S-lines of the vortices are more defined, indicating increased vortex strength, and they extend much further down the ramp. The curvature ends at $x/d \approx 7$, at which point the vortices detach from the ramp surface. This is confirmed later by an LDA wake survey at 15mm downstream of the diffuser exit, which shows that flow is entrained from the model sides to flow through the gap under the side-plates, and the vortex is seen at the lower part of the side-plate (see Chapter 4). It spans most of the model half-width. From Figure 13 it may be seen that after the vortices have detached, the central flow lines along the diffuser surface remain attached to the ramp surface yet are still induced into the sides of the ramp by the relatively low pressures.

3.4 Maximum Down-force

Flow patterns typical of type B are shown in Figures 14 and 15. Again, the pattern is symmetric to a large extent. The defining characteristic of type B flow and a possible cause of the sudden decrease in the down-force gradient at these heights is the bubble occurring in the centre of the diffuser. The main flow features are similar to those found by Morel [68] in his work on base-slant flows. This separation is also a possible explanation for the difference in down-force curves between smaller and larger angle diffusers, below a certain ride height, found by Cooper *et al* [19].

Figure 60 shows the moving ground plane after a flow visualisation run at h_r/d=0.255. The flow direction is from left to right. The tracks of what is likely to be a longitudinal vortex pair are seen running across the figure. Out board of these tracks the fluid appears to be well behaved and flowing uniformly in one direction. The fluid in between the tracks seems to be more turbulent. The large coagulation of fluid which occurs between the tracks is thought to be fluid from the surface separation bubble which, towards the beginning of the diffuser, touches the ground belt. The fluid appeared as such at periodic intervals along the moving belt, indicating that the bubble pulsated in an unsteady manner.

The first clear sign of the separation in these tests appears at h_r/d=0.318 (Figure 14).

Its presence is governed by the limiting pressure at the diffuser exit and the consequential low pressure in the diffuser. At the larger ground clearances typical of the down-force enhancement flow, there is little acceleration beneath the model and the underbody flow rates do not increase greatly, thus the suction remains low and the pressure gradient between the diffuser inlet and exit remains weak. Although the flow deceleration and loss of momentum occur immediately downstream of the inlet, the pressure gradient is weak enough for the flow to remain attached over the ramp surface. However, as the model is lowered towards the ground, the underbody flow rate increases and the pressure recovery of the diffuser is seen as a stronger suction at the inlet. The pressure gradient along the diffuser becomes increasingly steep with reducing ride height, until at a critical height boundary layer separation occurs, producing the bubble and primary separation line seen in Figure 15. With a reduction in ride height, the primary separation line of the Type B flow moves forward up the ramp as the down-force increases and the pressure gradient becomes steeper. The spanwise pressure distributions across the diffuser at these heights exhibit similar characteristics to each other, the pressures staying almost constant at ride heights between $h_r/d = 0.217$ and 0.318 over the majority of the ramp. The down-force increase for the Type B flow is created by the larger levels of suction experienced at the inlet and at the sides of the diffuser where the maximum suction was measured on the model, due to the longitudinal vortices attached to the surface. The C_p at $h_r/d = 0.318$ is -2.332 at $x/d = 5.44$, $z/d = 0.89$, reducing to C_p=-1.282 at $x/d = 5.91$, $z/d = 0.89$. At $h_r/d = 0.217$, the C_p is -2.66 at $x/d = 5.44$, reducing to -1.429 at $x/d = 5.91$ (Figure 16). The increase in suction is reflected in the increased curvature of the surface flow, the curvature being greatest at the height of maximum down-force (Figure 15). The maximum suction measured on the model surface occurs at this ride height and is due to the suction induced by the streamwise vortex in the first part of the diffuser.

From the surface flow it appears that the streamwise primary vortex flow meets the secondary separated flow at junctions either side of the ramp centreline. The primary separation line includes the separation line of the bubble. The line is then seen to run towards the secondary separation line, after which the primary vortex flow is no longer present on the ramp surface. It appears that the vortex has detached from the surface. The flow patterns downstream of the primary separation line are the result of re-circulating fluid from the bubble reattaching to the diffuser surface then being entrained out-board towards the low pressure associated with the presence of the near-surface primary vortices.

3.5 Down-force Reduction and Low Down-force

The maximum down-force occurs between $h_r/d = 0.21$ and 0.217. During the model tests it was found that the height at which the maximum down-force occurred varied between these two heights. The switch between the maximum down-force and the onset of the loss of down-force appeared in a random fashion, and on occasion the flow switched between a type B flow (maximum force) and a type C flow (force reduction) between wind tunnel runs without apparent variation in model setting.

Figure 17 (a) gives surface pressure distributions on the diffuser surface typical of flows in the force reduction region (type C). The measurements in Figure 17 (a) were taken at $h_r/d = 0.204$, and show the flow at a point where the down-force experiences a rapid reduction. Figure 17 (b) gives spanwise pressures at $h_r/d = 0.064$, which is a type D flow. The loss of down-force is accompanied by the appearance of an asymmetric flow in the diffuser. The flow is now separated at the inlet on one side (see Figure 18 (a) and (b)). The separation bubble has collapsed and the primary separation line is now difficult to identify from the surface flow visualization. In Figure 18, the surface flow is no longer symmetric about the diffuser centre-plane. Instead, it runs from the top left corner of the ramp diagonally towards the centre-plane, where the boundary layer separation coincides with the vortex detachment from the surface on the top side, as in the maximum force region. Although the right side vortex rolls up as normal, the left side flow has begun to reverse back up the ramp, indicating a separated flow and the collapse of the vortex at that side of the diffuser.

This asymmetry was unlikely to be caused by errors in setting the model height. Its appearance occurs at random, during pressure measurement tests a switching of the side of the reverse flow occurred, as seen in the two different spanwise distributions of Figure 17. The cause could be slight imperfections in the model surface, as found in slender body and missile aerodynamics.

A slight mis-alignment in the zero yaw angle could also cause the asymmetry. Researchers of delta wing vortex flows have found flow asymmetry with yaw angles as little as 0.1 degrees [73]. Asymmetric flow is, however, a fundamental flow feature of internal plane walled diffusers operating in the large transitory stall/2D stall flow regimes (see Chapter 1). The surface flow patterns and pressures of flow types B and C are highly reminiscent of the large transitory stall and 2D separation flow regimes found in 2D plane-walled diffusers. In internal flow diffusers, the large transitory stall regime occurs in the vicinity of, and just beyond, the geometry of peak pressure. Ashjaee and Johnston, in their study of the transitory stall regime of a 2D plane-walled diffuser [2], found slightly asymmetric static pressure distributions near the walls at diffuser geometries just beyond peak pressure recovery. Pressure recovery was found to increase in the transitory stall regime, as in type B of the present diffuser flow, and started to decrease as soon as a zone of strong reverse flow was found to occur on one wall, as in type C of the current flow. The asymmetric stall of an internal flow diffuser originates near the diffuser inlet and blocks a significant fraction of the available flow area, accounting for the low performance in this flow. The stall has been found to be stable to small disturbances but can be switched from one diverging wall to the other by a large disturbance. Once it has been switched, the stall remains fixed if undisturbed [77].

3.6 Further Discussion of Flow Physics

From the perspective of classical internal flow diffuser physics, the parameter W_1 transposes as the ride height of the model above the ground and as such is variable. The current diffuser therefore has a non-dimensional length, n/W_1 of 16.3 at the height of maximum down-force, taken as h_r/d=0.210. The aspect ratio of the diffuser ranges from low, AS = 2.62 at h_r/d=0.764 to high, AS = 31.4 at 0.064. At the height of maximum down-force, the aspect ratio is 9.52. In the flow regime map of Reneau *et al* [77], the diffuser would be on the borderline between the regimes of large transitory stall and full stall at the height of maximum down-force, where the included angle 2θ of the present model is taken to be 34 degrees. Thus the comparison is effectively made by considering the present diffuser as one half of an internal flow diffuser.

As the model is lowered to the ground, the suction at the inlet increases, leading to increasing flow entrainment from both sides of the model. The boundary layer on the surface underneath of the model is therefore 3D in nature. This 3D effect is increased as the ride height is reduced. Another factor in determining the diffuser flow is the boundary layer approaching the inlet, the thickness of which has been measured to be in the order of 15 *mm* immediately upstream of the diffuser inlet with the model at a freestream ride height (Figure 22(b)).

Although it will not create a 'blockage' effect at a height in the maximum force flow type, the boundary layer does enhance the suction at the inlet as the effective ride height is reduced, leading to a high adverse pressure gradient in the diffuser. The pressure gradient in the diffuser produces a thickening of the boundary layer at the diverging wall, reducing the effective area of the diffuser as found in the transitory stall regime of 2D diffusers before the pressure recovery decrease begins. At a limiting height (h_r/d = 0.21 for the present flow), the separation eventually occurs at the inlet. The asymmetric nature of the 3D boundary layer separation produces the apparent collapse of one of the counter-rotating vortices.

The asymmetry found with the skirts sealed to a *fixed ground* by George and Donis [34] was attributed to the absence of the vortices, however it seems possible that, as in these tests, the pressure gradient over the diffuser surface was too large to be contained by a separation bubble, and the separation has instead occurred at the inlet. Support for this argument for the present diffuser flow comes from the down-force measurements at various Reynolds Numbers (Figure 19). Down-force characteristics are similar for each curve. At Re of 1.8×10^6 and 2.7×10^6 maximum down-force occurs at the same ride height, whilst at 1.3×10^6 it occurs at a slightly lower ride height (a difference of 1 *mm*). The boundary layer thickness at a lower Re is expected to be larger than that at a higher Re. If the maximum down-force and subsequent stall depended upon a blockage across the inlet of the diffuser, caused by a merging of the boundary layers, stall at a lower Re would be expected to occur at a higher ride height. The seemingly negligible effect of Re on the overall flow characteristics implies that the down-force reduction is not a phenomenon caused by boundary layer merging at the inlet, and that the inlet flow could be comparable to that of high aspect ratio internal plane-walled diffusers, in which there is a core flow that is relatively unaffected by viscosity [77].

The cause of the one-sided separation at the inlet merits further investigation. The remaining vortex occupies a smaller and smaller fraction of the diffuser surface with reducing ride height and its point of detachment continues to move forward until at h_r/d=0.064 (type D) it is no longer apparent. A vertical oscillation of the model has also been observed in the current tests, indicating the likelihood of unsteady flow in type C. A similar observation in racing cars, whereby coupled suspension and aerodynamic oscillation occurs, is known as 'porpoising'.

3.7 Base Pressures

Surface pressures measured on the model base at several ride heights are shown in Figure 20. The bluff base of the test model creates a negative base pressure at all ride heights tested, creating a drag force. From well researched bluff body flows ([1, 7, 68, 69]) it is expected that there is a separation bubble at the base of the model. The diffuser upsweep and the presence of longitudinal vortices would ensure that the base pressures are low, producing a high drag force. In all cases where the flow field exiting the diffuser is symmetric, the base pressures show a 'w' shaped distribution across the model span, the two most negative dips being associated with the low pressure cores of the vortices exiting the diffuser at these spanwise locations. Throughout type A flow and just entering the type B section of the down-force curve, from h_r/d=0.573 to h_r/d=0.318, the base pressure values and distributions do not alter much. The pressure coefficients at these ride heights are slightly negative. (C_p =-0.144 at the base centreline, h_r/d=0.382) corresponding to the lower drag forces occurring in the type A flow. At the locations of the vortices the pressures drop to the vicinity of $C_p \simeq$-2. At h_r/d=0.217, however, there is a marked decrease in the base pressures across the model span, the centreline pressure is C_p =-0.188 and above the vortices drops to C_p =-2.51 and -2.49. These localised points of low pressure contribute significantly to the drag force on the model, which increases significantly through type B flow. The distribution remains symmetric. The most negative pressure measured on the base occurs in the type C flow at h_r/d=0.159, where the surface pressure above the right side vortex drops to C_p =-0.346. Oil flow visualisation points to a single large vortex to one side of the diffuser at this ride height. At the other side the base pressures are much less negative, in keeping with the re-circulating flow or weaker vortex inside the diffuser. At the lowest ride heights the base pressures are less negative, and more uniform across the model span, indicating that the influence of any vortex inside the diffuser is weak at these heights.

3.8 Ground Simulation

Figure 21 shows the results of taking force measurements with a fixed ground plane with boundary layer control in comparison with the results taken with a moving belt, shown previously in Figure 9 (a). At each stage of the curves, a greater down-force is measured with a moving ground than with a fixed ground plane due to the influence of the moving ground in assisting the pumping of the flow through the diffuser. This increased pumping of the fluid causes the flow to accelerate more than would occur with a fixed ground plane, and hence creates a greater down-force. The characteristics of the fixed ground curve are altered in comparison to the moving-ground curve near to the point of maximum down-force; the flow appears to remain attached at the inlet at ride heights where the diffuser has stalled with a moving belt. The fixed ground down-force level falls slowly between h_r/d=0.255 and h_r/d=0.178 before eventually reaching a sharp stall. This confirms that observations made with a fixed ground plane should not be applied to flows with a moving ground. The ground boundary condition becomes increasingly important as ride height is reduced and correct simulation is necessary at lower ride heights in order to capture the force reduction flow physics.

3.9 Summary

The mean flow behaviour exhibits different characteristics in the four main flow regimes over the ride heights tested. For flow types A and B, surface flow visualisation and pressure measurements indicate that the majority of the down-force is produced across the diffuser inlet due to the 'diffuser pumping' mechanism and at the sides of the diffuser where the suction is created by the vortices at the diffuser surface. At a critical height near to the ground the pressure gradient between the diffuser inlet and the fixed exit pressure becomes too large to prevent the boundary layer separation at the diffuser surface. Even so, in type B flow the down-force increases in the presence of the separated flow as the model ride height is lowered. Although the region of separated flow inside the diffuser becomes larger, the underbody pressures become increasingly negative in localised parts of the diffuser before the vortex pair detach from the surface. This is sufficient to continue the production of an overall increasing down-force on the model. The increase in down-force is terminated at low model ride heights, when the balance between the down-force mechanisms and increasingly adverse pressure gradient changes in favour of the latter. The 3D flow separation occurs at the inlet, causing the collapse of one of the vortices.

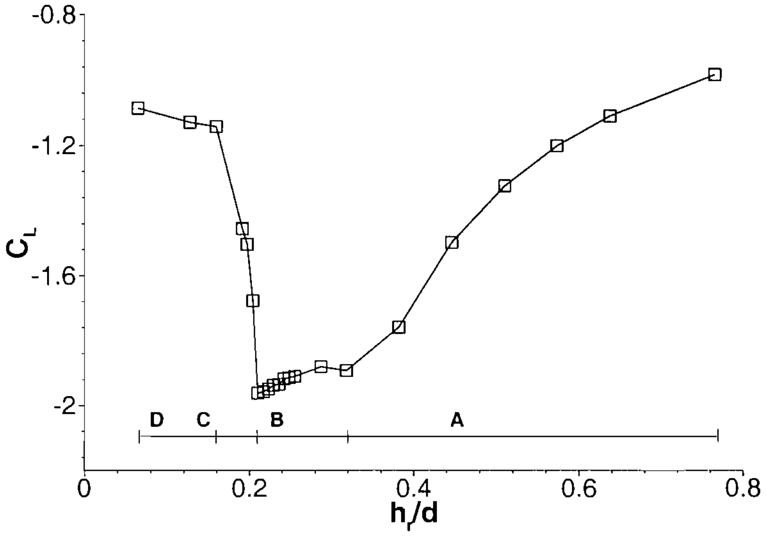

(a) Lift Coefficient

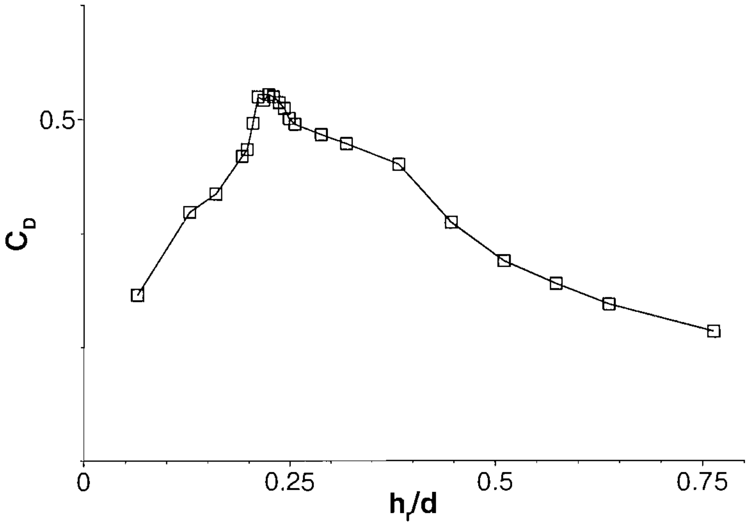

(b) Drag Coefficient

Figure 9: Force measurements vs non-dimensionalized ride height: (a) Down-force (b) Drag.

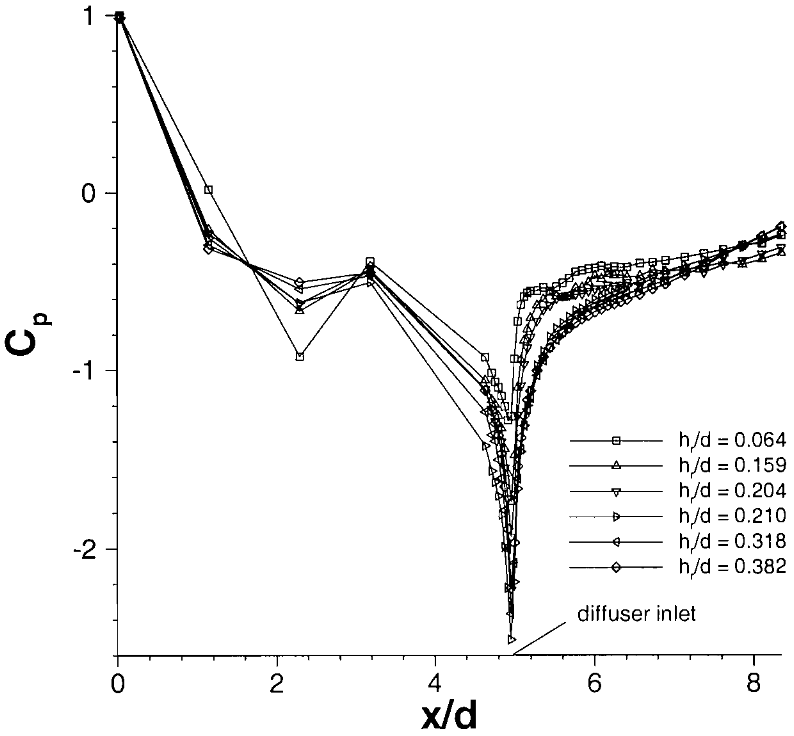

Figure 10: Underbody centreline pressure coefficients.

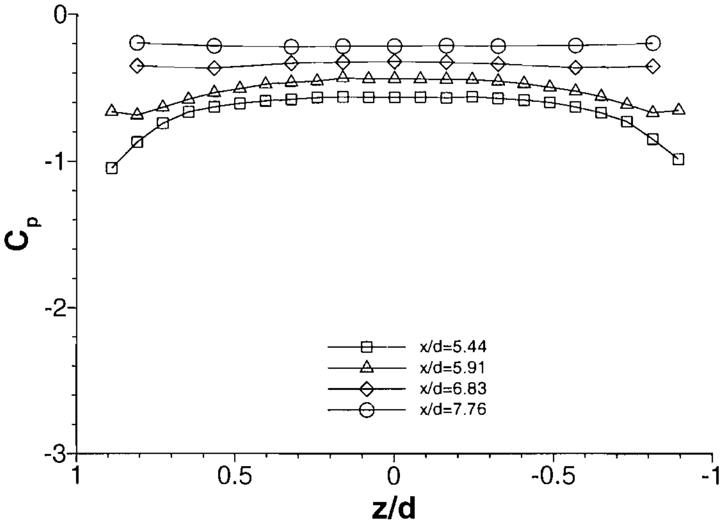

(a) h_r/d=0.764

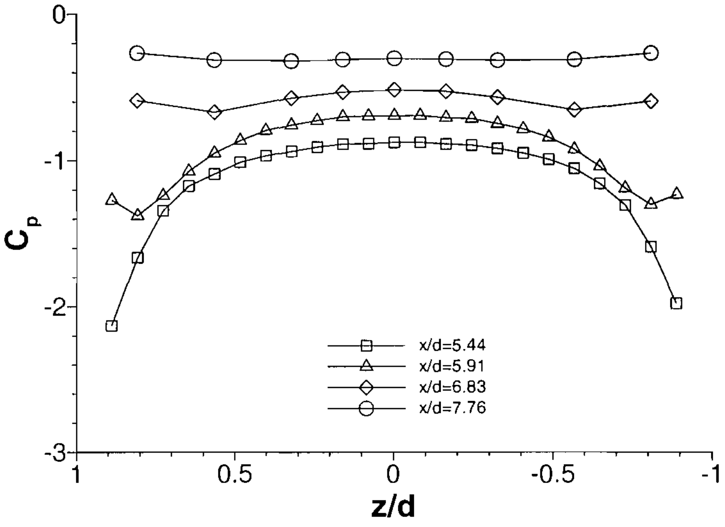

(b) h_r/d=0.382

Figure 11: spanwise pressure distributions on the diffuser surface in a Type A flow: (a) $h_r/d = 0.764$, (b) $h_r/d = 0.382$.

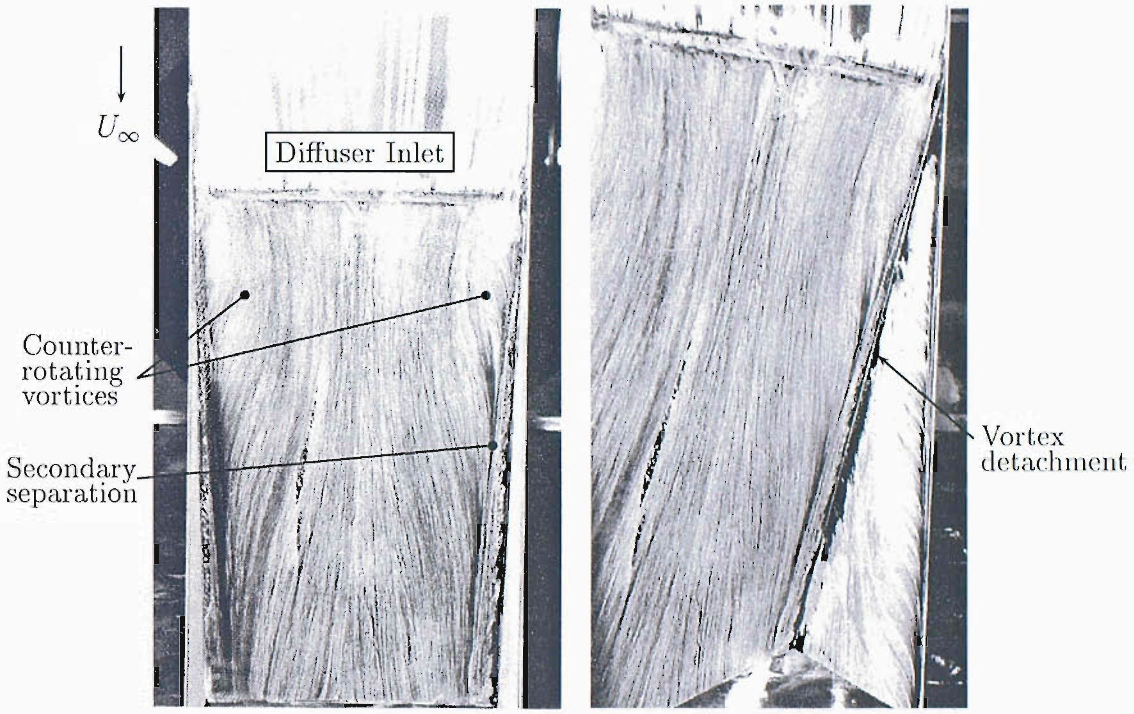

(a) h_r/d=0.764

(b) h_r/d=0.764 inner sideplate

Figure 12: Oil flow visualisation on the diffuser surface for a Type A flow: h_r/d=0.764. Flow direction from top to bottom.

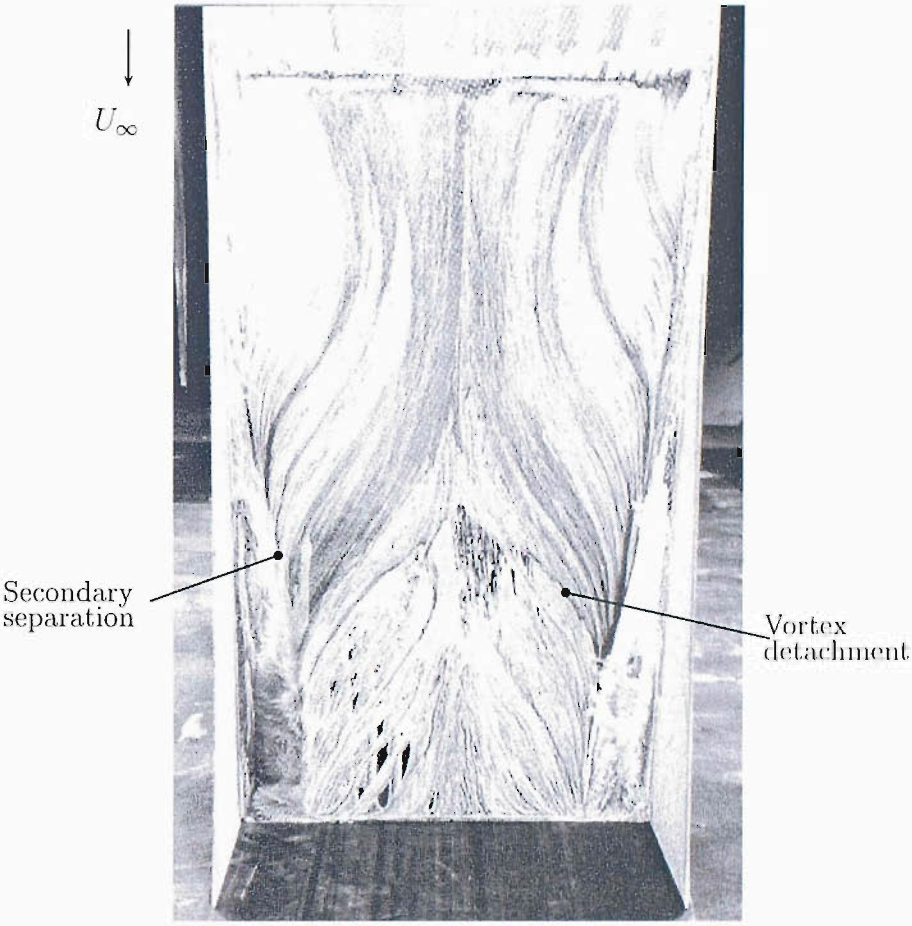

Figure 13: Oil flow visualisation on the diffuser surface for a Type A flow: $h_r/d = 0.382$. Flow direction from top to bottom.

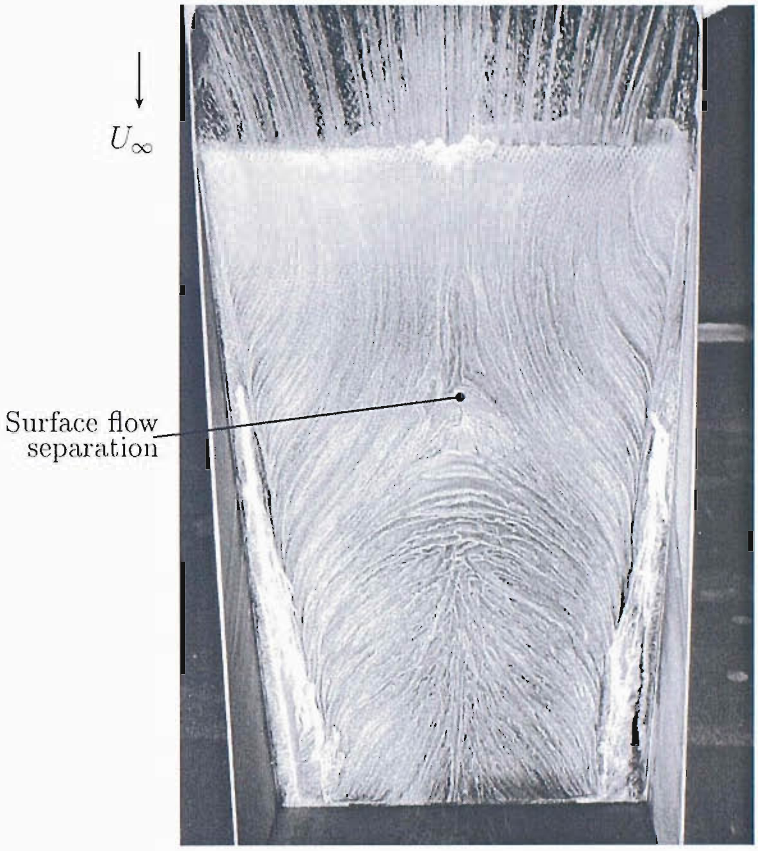

Figure 14: Oil flow visualisation on the diffuser surface in a Type B flow: h_r/d = 0.318. Flow direction from top to bottom.

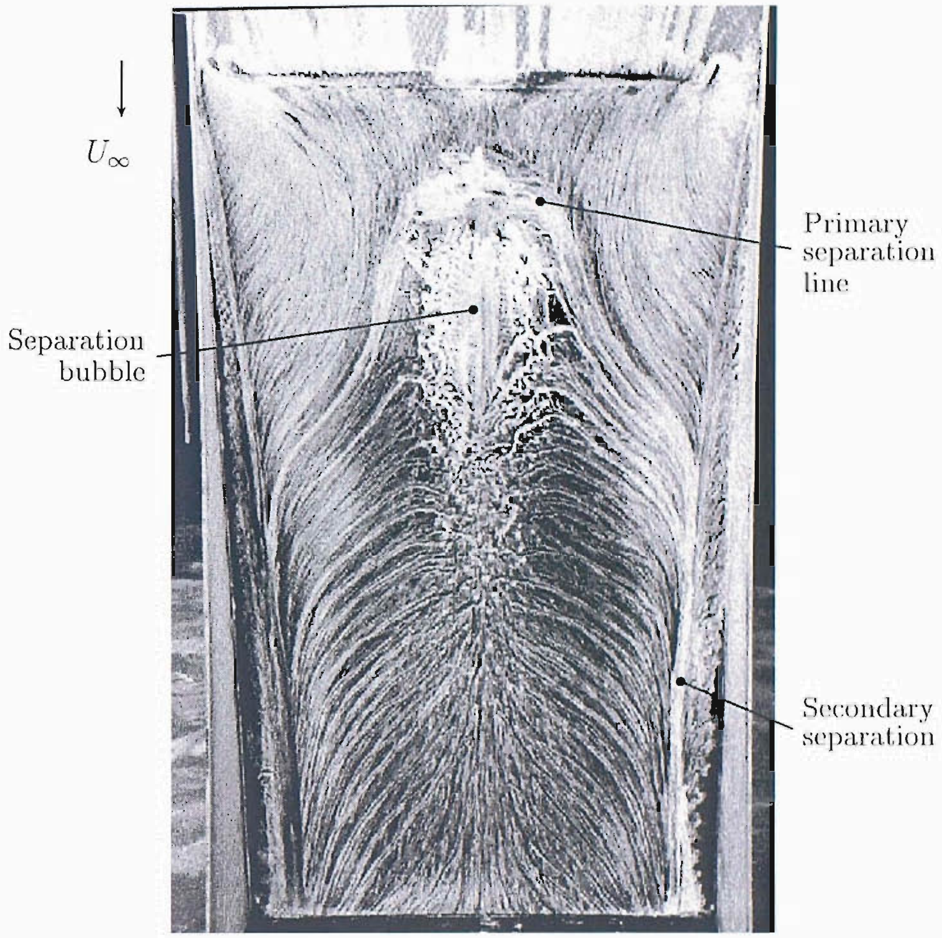

Figure 15: Oil flow visualisation on the diffuser surface in a Type B flow: $h_r/d = 0.217$. Flow direction from top to bottom.

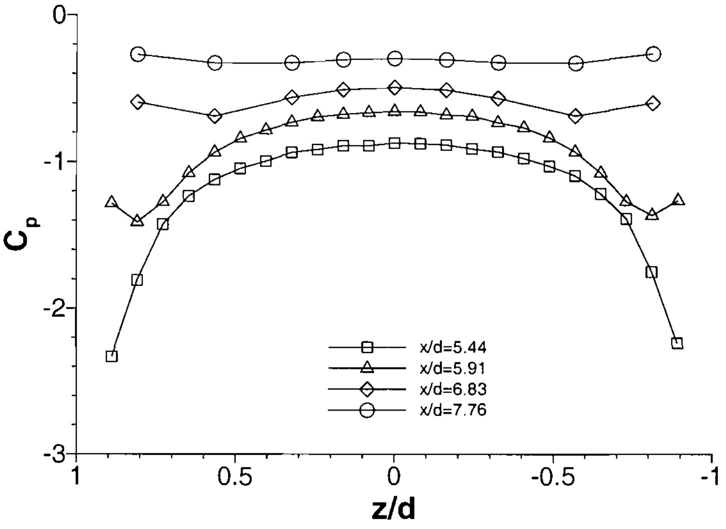

(a) h_r/d=0.318

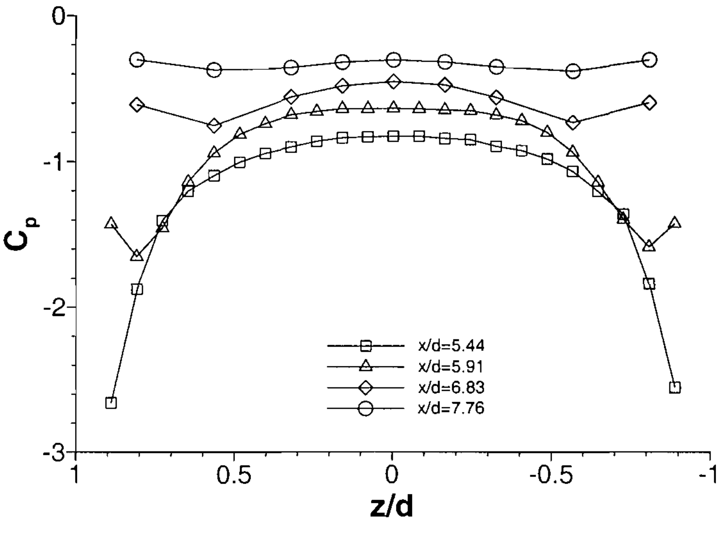

(b) h_r/d=0.217

Figure 16: Spanwise pressure distributions on the diffuser surface in a Type B flow: (a) $h_r/d = 0.318$, (b) $h_r/d = 0.217$.

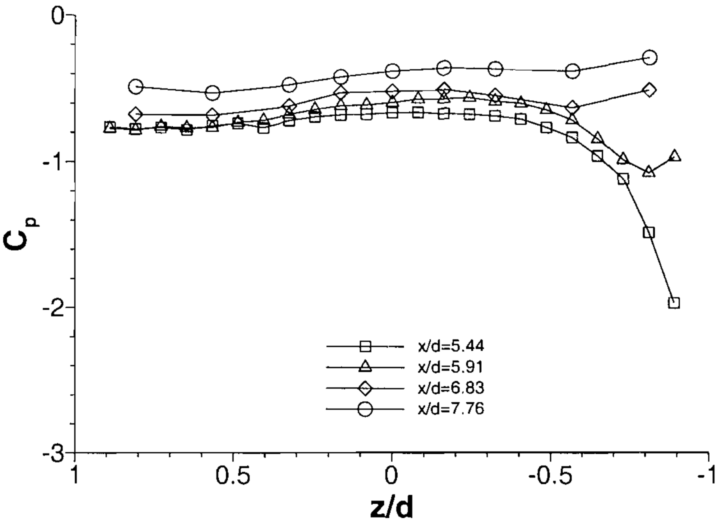

(a) h_r/d=0.204

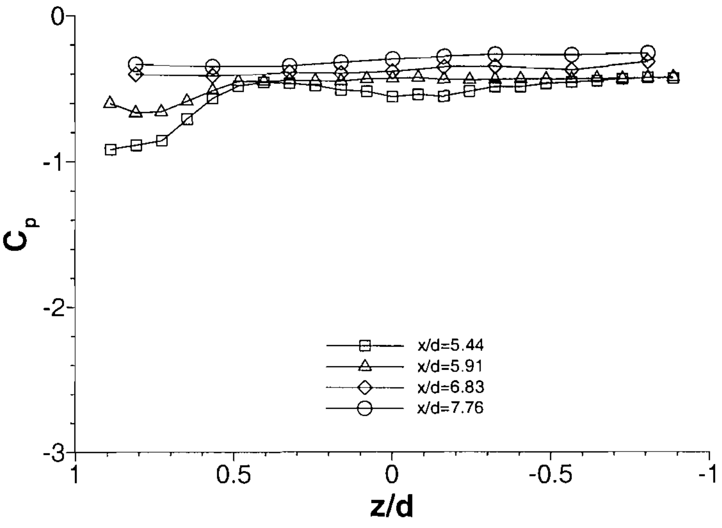

(b) h_r/d=0.064

Figure 17: Spanwise pressure distributions on the diffuser surface in a Type C and Type D flow: (a) $h_r/d = 0.204$, (b) $h_r/d = 0.064$.

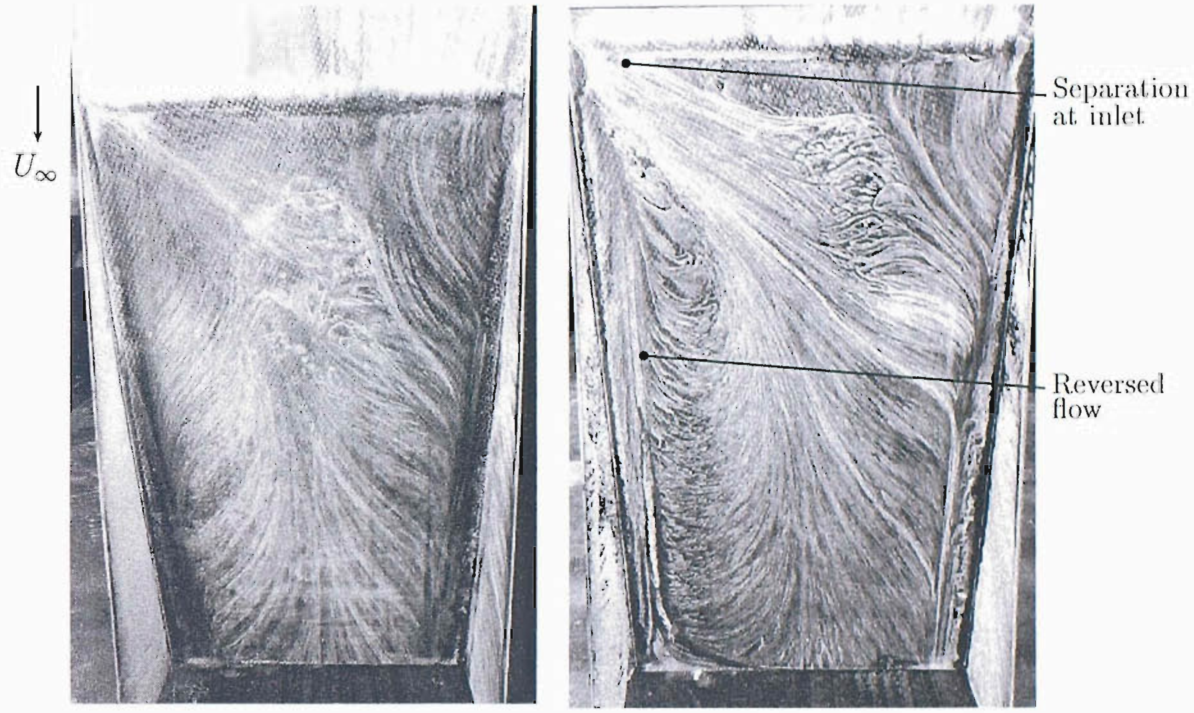

(a) h_r/d=0.210 (b) h_r/d=0.204

Figure 18: Oil flow visualisation on the diffuser surface in a Type C flow. Flow direction from top to bottom.

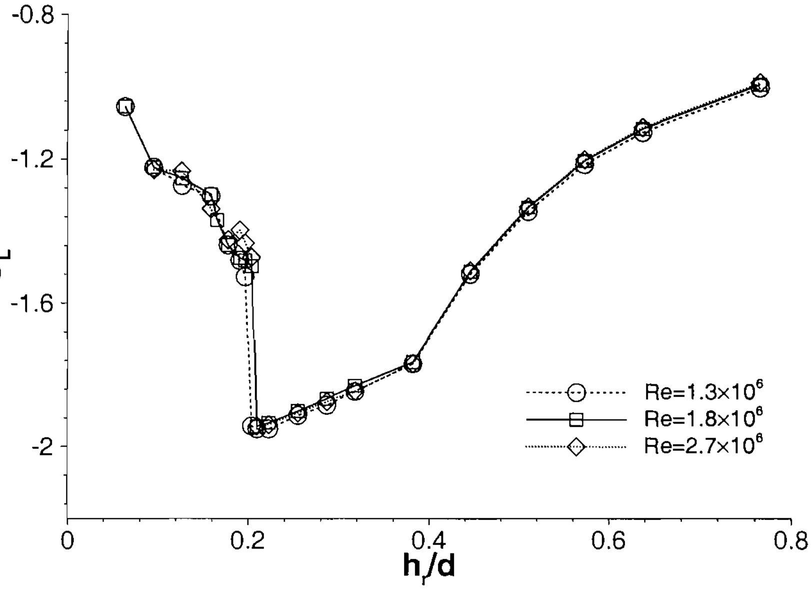

Figure 19: Reynolds Number effects on the down-force characteristics.

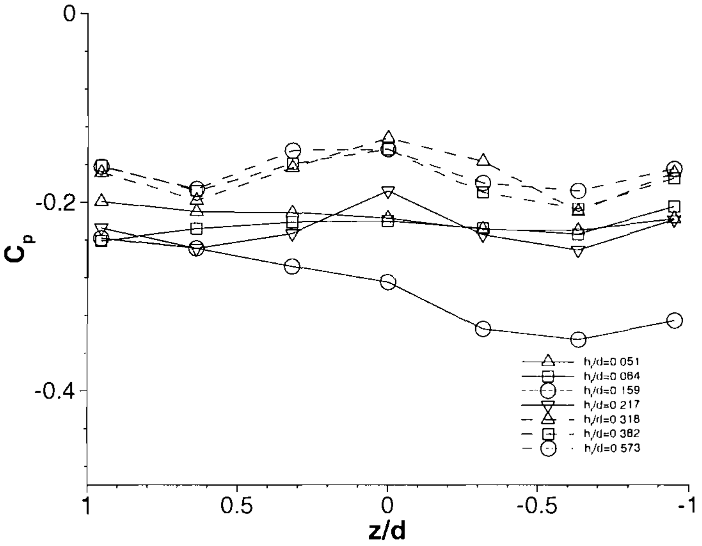

Figure 20: Surface pressure coefficients on the diffuser base.

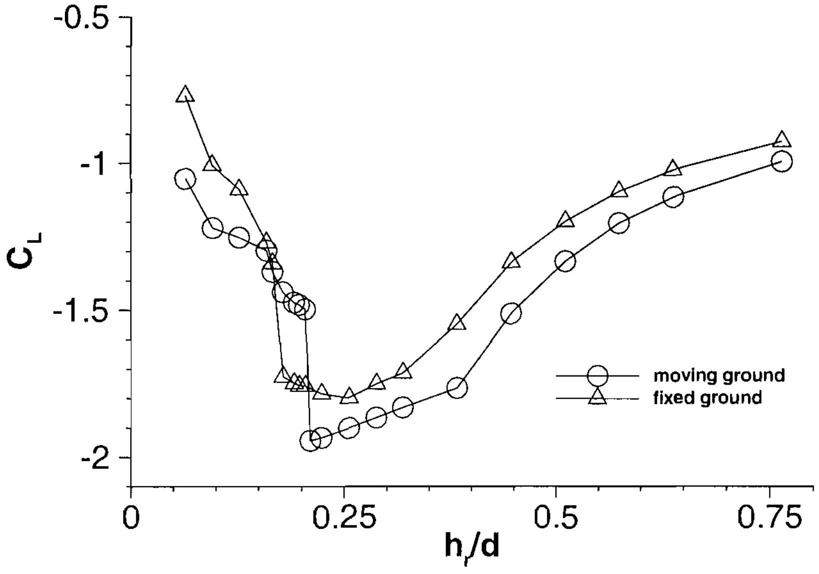

Figure 21: Down-force coefficients with a fixed ground and a moving ground.

Chapter 4

Time-Averaged Vortex Flow

In order to clarify the force reduction and asymmetric flow phenomena, the time averaged vortex flows inside and exiting the diffuser were investigated using LDA and PIV. Preliminary LDA measurements of the model centreline boundary layer, inlet boundary layer and of the flow exiting the diffuser were made with the model in freestream (at 650 *mm* above the ground). The LDA measurements conducted in ground effect confirmed four different vortex flow types at the diffuser exit. The characteristics of each vortex type explained aspects of the diffuser behaviour and revealed further insights into the diffuser flow physics. The mechanisms creating these different flows were investigated further using PIV inside the diffuser.

4.1 Diffuser Model Measurements in Freestream

The model was placed at a height of 650 *mm* (h_r/d=4.44) above the moving ground to gain an understanding of the flow around the diffuser out of ground effect. Boundary layer profiles at the upper and lower surfaces of the model are given in Figure 22. The profiles in Figure 22 (a) were taken at four stations over the top of the model centreline and illustrate the increase in the turbulent boundary layer thickness over a distance of 0.5 *m*. The non-dimensional parameter y_1/d is plotted as the normal distance variable away from the surface. At x/d = 2.3, just beyond the nose, δ = 6.8 *mm*, rising to δ = 15.3 *mm* at x/d =5.5. Boundary layer thickness is taken to be δ_{99}. Underneath the model the flow accelerates along the flat bottom (Figure 22 (b)). The boundary layer thickness increases from 11.9 *mm* at x/d =3.0 to 15.4 *mm* at x/d =4.5. The profile measured at x/d =4.9 is immediately upstream of the diffuser inlet, and shows a large flow acceleration, reaching a speed of u/U_∞ =1.374. Although not fully apparent from this figure, the profiles indicate that the flow speed does not return to freestream quickly beneath the model: at y_1/d =-1 the streamwise velocity is still falling, and continues to fall at y_1/d =-1.59.

The high streamwise velocities are confirmed in Figure 23, which shows the flow underneath the model span immediately upstream of the diffuser inlet. The 3D nature of the inlet flow is apparent, and the flow entrainment underneath the sides is clear. The streamwise velocity is highest under the model centreline, however the cross-flow velocities are highest underneath the model sides. Figure 24 shows the flow exiting the diffuser at x_1/d = 0.096. Oil flow visualisation tests at high model heights from the ground revealed that the flow is broadly symmetrical about the model x-axis, and so only one half of the exit flow was measured in detail. The streamwise flow is above the freestream velocity for the majority of the exit flow (Figure 24 (a)). A noticeable feature of the results in the freestream and type A flow is the absence of data at the vortex cores. The absence is due to a visible lack of seeding in the LDA measurement volume, and at h_r/d=0.764 and h_r/d=0.382 was accompanied by zero signals on all three BSA channels. The phenomenon was also reported by Payne *et al* [74] in their smoke flow visualisation of delta wing vortices, and also recently by Yeung & Lee [98] in their PIV study of the cross flow of a wing-tip vortex. At the vortex centre, seeding was scarce due to either centrifugal effects in which the seeding particles were induced outwards from the core as the vortex travelled downstream, or to the possibility that the core flow consisted of air entrained from the less-seeded freestream. In this case, centrifugal effects are the most likely possibility given the strength of the vortex, for although the tunnel was heavily seeded in an attempt to capture the flow at the vortex core, no meaningful velocity measurements could be obtained at the core. The flow surrounding the core is of a higher speed than the freestream in the streamwise and cross-flow directions, and the vortex is strong and concentrated (Figure 24 (b)). High axial speed vortex cores are a feature of the longitudinal vortices found in delta wing flows at moderate angle of attack [91]. Flow is entrained underneath the side-plates and is wound into the vortices, the directions of the induced flows of the two vortices being diametrically opposite to each other. The flow between them forms an upwash towards the diffuser ramp. The flow at the diffuser ramp remains attached across the span of the model, and in the corner regions of the diffuser the boundary layer appears to be thicker (Figure 24 (a)). This distribution is typical of rectangular channel flows [9]. The shear stress contours (Figure 24 (c)), show a uniform yet low distribution near the diffuser ramp, as expected of an attached flow, whilst the TKE contours (Figure 24 (d)) indicate a low turbulent energy flow exiting the diffuser, excepting the shear layer rolled up into the vortex.

4.2 Vortex Flow Exiting the Diffuser (LDA)

The flow exiting the diffuser, over a cross-plane at x_1/d = 0.096 has been measured at eight model heights above the ground. For each flow property presented as a contour plot, a single contour range is used at the different ride heights in order to present the flow development with ride height in a comparable manner.

Results are presented in Figures 25 to 29, in which each flow property is taken in turn for immediate comparison between ride heights. For each flow property, there are two figures. In the first figure are measurements taken at h_r/d=0.764, 0.382, 0.318 and 0.255 (types A and B). In the second figure are measurements for h_r/d=0.217, 0.204, 0.159 and 0.064 (types B, C and D). Flow properties are tabulated in Table 13. In discussing the vortex flow, the centre of the vortex is determined as being the point at which both cross-stream and vertical velocity components are zero.

4.2.1 Vortex Flow Exiting the Diffuser in Type A

The flow exiting the diffuser in type A has been measured at two model heights, h_r/d=0.764 and 0.382, seen in Figures 25 to 29 (a) and (b). Measurements taken at h_r/d=0.764 are mirrored from a half span measurement grid since the flow is symmetric, however the flow at h_r/d=0.382 was measured across the entire model span. Observation of the u/U_∞ contours of Figure 26 (a) reveals that there is little difference in the flow from that at h_r/d=4.14 (Figure 24). The flow trends remain the same, although the cross-flow velocities entrained under the side-plate are higher. The flow remains attached at the diffuser ramp and the u component of the exit velocity is freestream velocity or higher outside the vortex. The vortex is larger in diameter than at h_r/d=4.14, and the cross-flow velocities in it are higher. Once again the core flow could not be measured, however the streamwise flow surrounding the core is greater than freestream and is of a higher velocity than at h_r/d=4.14. The shear stress at the diffuser ramp has increased (Figure 29 (a)), and the TKE remains very low (Figure 28 (a)).

At h_r/d=0.382, the streamwise velocity surrounding the cores has increased to u/U_∞=1.3 and the vortices now occupy a far greater proportion of the span of the diffuser. Figure 27 (b) indicates a rotational cross-flow in the ground boundary layer that was not present at h_r/d=0.764. For each of the type A vortices, the maximum vorticity appears to be central to the vortex core, although caution must be exercised in interpreting the results due to the absence of core flow measurements. Figure 28 (b) shows negligible amounts of turbulent energy at the diffuser exit plane. The shear layer leaving the diffuser ramp surface is apparent and is considerably thicker in the corners at h_r/d=0.382 (Figure 28 (b)) than at h_r/d=0.764 (Figure 28 (a)). The roll up of the shear layer separating from the side-plate edge can just be seen, and small regions of TKE concentration appear above the ground plane at either side of the centreline, confirming a new flow feature in the ground boundary layer. This aspect of the flow is discussed in Section 4.4.6. Figures 29 (a) and (b) indicate that the shear stress levels in the flow exiting the diffuser in flow type A are also low, except in the ramp surface boundary layer. The shear layer separating from the side-plate edge is identifiable from the pockets of negative shear stress.

4.2.2 Vortex Flow Exiting the Diffuser in Type B

In type B a new flow feature is introduced. Figure 26(c)-(e) show a pair of larger, diffused vortices. The centre of each vortex is occupied by a low-speed axial-flow core. The streamwise velocity at the centre of the vortex is lower than the freestream velocity (Table 13). For example, at the beginning of type B ($h_r/d = 0.318$), u_c/U_∞ is 0.229; at the end of the type, $h_r/d = 0.217$, u_c/U_∞ is 0.064. The vorticity at the vortex centre is also reduced substantially (Table 13, Figure 27 (c)-(e)). The location of maximum vorticity has moved from appearing to be at or near the core in the type A flow to occurring in the lower part of the vortex: Ω_m=4.79, at y/d =-0.78, z/d =0.478.

Figures 28 (c)-(e) show that there now exists a highly turbulent core at the centres of the vortices. For type B flows, TKE values at the centre of the vortex could be doubled compared with those in a type A flow. However, the region of high turbulence in the exit flow at h_r/d=0.255 (Figure 28 (d)) and h_r/d=0.217 (Figure 28 (e)) is in the upwash flow between the two counter-rotating vortices. Figures 29 (c) and (d) show clearly the increasing shear stress in the vortex flow as the ride height is lowered from flow type A to type B. The shear stress distribution in the vortex is quite distinctly sectioned into negative and positive regions, which increase in size as the ride height is lowered through flow type B. At h_r/d=0.255 the negative shear stress regions have expanded to double the size of the positive shear stress regions, although the positive shear stress is much stronger, see Figure 29 (d).

A low axial speed core and vortex dilation are two of the signs of 'vortex breakdown' [22]. Vortex breakdown is a well known phenomenon found in the vortices over a delta wing at high angle of attack and other flows in which a vortex is subjected to a steep adverse pressure gradient [21, 26, 42, 55, 57, 58, 64, 82, 83, 94]. Vortex breakdown or vortex bursting is associated with a rapid deceleration of the vortex core, sudden vortex core dilation and the occurrence of large scale velocity fluctuations. A vortex may be said to have 'broken down' if its axial velocity is zero or reversed at the core [91]. Measurements in the type B flow reveal that the core velocity decreases as the model ride height is lowered through type B flow. At h_r/d=0.255, reverse flow is recorded at the core. The possibility of vortex breakdown occurring inside the diffuser is discussed further in Chapter 5.

A pair of small secondary vortices in the flow immediately above the ground plane in the type B flow vorticity contours (Figures 27 (c)-(e)) is thought to be induced by the primary vortex pair in accordance with the findings of Harvey & Perry [43] and Ersoy & Walker [25]. Whenever a vortex pair is close to a wall, the vortices induce a region of adverse pressure gradient near the wall and boundary layer separation will occur. At h_r/d=0.255, the vortex induces flow from the freestream under the gap between the side-plate and the ground. This flow accelerates until it is at its strongest directly beneath the vortex. As the flow progresses further inside the diffuser toward the centre-plane the flow decelerates due to the adverse pressure gradient. Separation of the ground boundary layer occurs. Explosive boundary layer growth occurs locally to the separation and moves toward an interaction with the outer inviscid flow. Air is ejected from the boundary layer and secondary vortices are produced.

These secondary vortices are not present in the type A flow because the vortices are far away from the ground and although separation is induced in the ground boundary layer, an interaction with the outer flow does not occur.

4.2.3 Vortex Flow Exiting the Diffuser in Type C

A prominent feature of this flow regime is the appearance of asymmetric vortices (Figure 17). Instead of two broadly symmetric, counter-rotating vortices, the flow in the cross-plane is now dominated by a single vortex and a re-circulating flow with flow reversal. The vortex now occupies a large cross-plane area (Figure 26 (f) and (g)). On the other side the flow is characterised by flow reversal. The appearance of the dominant vortex is random and was found in the model tests to be influenced by minute changes in model settings. In Table 13 the dominant vortex is seen to switch from one side to another when the ride height is changed from h_r/d = 0.204 to 0.159. In Table 13 the measured vorticities at the centre of the dominant vortex are listed. The peak vorticity occurs at the centre of the vortex (Figure 27 (f) and (g)). The maximum induced spanwise and transverse velocities are comparable to that in the maximum force region (Figure 25(f)), and the vortex is less diffuse than the type B vortices, leading to a high suction level on one side of the diffuser near the base of the diffuser. This feature is indicated in the spanwise pressures shown in Figure 30. However, this suction enhancement mechanism only exists in a small area towards the base of the diffuser. On the other side, flow reversal is the result of 3D flow separation at the inlet of the diffuser. Once this occurs, a loss of suction is inevitable to this side of the diffuser. This is clearly indicated in Figure 30. *TKE* concentrations occur in the vortex and in the shear layer separating from the opposite side-plate (Figure 28 (f) and (g). A large region of *TKE* in the centre of the exit area at h_r/d=0.204 (Figure 28 (f)) disappears by h_r/d=0.159 (Figure 28 (g)), indicating that the flow becomes less turbulent towards the lower reaches of type C flow. Overall, the suction loss caused by the flow separation at the diffuser inlet and the apparent break-down of the streamwise vortex (with the subsequent loss of vortex force) now dominate the force production mechanism.

4.2.4 Vortex Flow Exiting Diffuser in Type D

As the ride height is further reduced, the vortex flow is considerably weakened. In the cross-plane immediately downstream of the diffuser (Figure 25 (h)), a single large vortex is present. The vorticity at the centre of the vortex is much lower than those observed at higher ride heights ($\Omega d/U_\infty$=-2.30). The mass flow entering the diffuser from the inlet is now reduced substantially (Figure 26 (h)). Unlike the flow types A, B, and C, where a strong flow entrainment or an attached diffuser flow led to a high speed diffuser flow, measurements suggest a generally low diffuser through-flow and the presence of large scale flow reversal at both sides of the diffuser. Flow entrainment between the side-plates and the ground is greatly reduced, spanwise velocities under the side-plate are w/U_∞ ≈0.05. At this height, the gap between the model and the ground is rather small. Measurements at a freestream ride height suggest that the thickness of the boundary layer underneath the model approaches 15 *mm* before the diffuser inlet (see Figure 22). Therefore, the viscous effects should certainly be prominent at this ride height. The *Re* based on the ride height and the free-stream flow conditions is in the order of 13,000, and for a channel flow, the flow would be fully developed. It is therefore anticipated that the boundary layers underneath the model and over the ground plane have merged at the diffuser inlet at this ride height.

4.3 Discussion of Down-force Production

The LDA measurements give a useful insight into the fluid mechanics. The diffuser performs the task of decreasing the kinetic energy of the fluid and decreasing the velocity at the higher ride heights of the type A flow (Figure 28 (a) and (b)). This is a consequence of the flow remaining attached at the diffuser ramp. Lowering the diffuser to h_r/d=0.318, where separation first appears on the ramp in these tests, results in a significant increase in the TKE levels of the exit flow and the larger, more diffused vortex pair seen in Figures 28 (c).

The contour plots of u/U_∞ shown in Figures 26 reveal that at all heights between freestream and the height of maximum down-force there is a large area of flow below the diffuser surface which is of freestream velocity or higher. This indicates a passage of high speed flow from upstream of the diffuser inlet through to the outlet. The area of freestream velocity at the exit plane decreases as the vortices expand with decreasing ride height in type B, however at the diffuser ramp there remains a strong flow through the diffuser downstream of the separation bubble. It appears that the separation bubble is thin, allowing fluid to flow to the end of the diffuser without creating too much blockage. At the inception of stall (Figure 26 (f)), a large zone of re-circulating and reversed fluid is present. At the other side of the flow there is still a large region of higher speed fluid reaching the diffuser exit. This feature suggests that a straightforward boundary layer merge at the inlet may not be the cause of the diffuser stall.

The occurrence of the maximum force is associated with the onset of flow separation in the diffuser. The down-force production is mainly influenced by two contributing factors: pressure recovery and vortex flow. Whilst the onset of the separation changes the pressure recovery, at the inlet of the diffuser the flow stays attached. Hence the flow acceleration and the pressure drop mechanism still dominates the pressure recovery as the ride height is reduced, leading to an overall higher suction force. In this flow type, the vortex flow remains basically symmetric about the centreline of the model as both vortices are able to form without inlet separation introducing asymmetry. Hence the force enhancement effects of both of the vortices are still present, and the overall effect produces the maximum down-force.

4.4 Vortex Flow Inside the Diffuser (PIV)

The cross-flow inside the diffuser was measured using PIV. Measurement planes were chosen to coincide with the spanwise surface pressure measurements. However, the plane x/d =7.76 could not be measured as the carbon fibre reinforcement of the transparent side-plate did not permit laser access at this plane, and x/d =7.74 was measured instead.

4.4.1 Vortex Flow Inside the Diffuser in Type A

The evolution of the vortex flow in type A can be traced through Figures 31 and 32. As the flow features in this flow type are essentially symmetric, the discussion is presented in terms of one vortex. At x/d =5.44 , the roll up of the shear layer separating from the side-plate edge is evident from the vorticity contours (Figure 31 (a)). The shear layer rolls up into a vortex that is small in size and is concentrated and strong. The vortex lies adjacent to the side-plate, in agreement with the surface flow patterns on the inner side-plate (Figure 12 (b)). Acceleration of the freestream flow underneath the side-plates is observed. Whilst the flow separating from the side-plate edge appears to be wound into the vortex, the air entrained through the gap between the side-plates and the ground flows around the vortex and up towards the diffuser ramp.

At x/d =5.91, the vortices remain concentrated and have a larger diameter. The vectors show that the cross-flow velocities in the vortex remain high speed, i.e. freestream velocity or higher (Figure 31 (b)). The presence of the model above the ground induces a ground shear layer, visible in the vorticity contours (Figure 31 (b)) as a region of vorticity of the opposite sense to the vortex above it. The flow separating from the side-plate again appears to be wound into the vortex. Along the length of the diffuser the vortex expands, in the same way as a conical vortex expands along a delta wing. As the diffuser cross sectional area increases, the vortex centre moves inboard and slightly upwards towards the diffuser centreline (Table 14). At x/d =6.37, a new feature is observed in the vortex flow (Figure 31 (c)). The shear layer rolls up into small individual pockets of vorticity as the main vortex rolls up. These small scale vortices are co-rotating and in the same sense as the main vortex. The occurrence of the small scale vortices in the shear layer is thought to be what is described by Gursul & Xie [39] and Riley & Lowson [79] as a 'steady shear layer instability', previously found in the vortex shear layer of delta wings at incidence [12, 59, 79, 73, 74, 78, 93].

This flow phenomenon is seen more clearly in the vortex flow towards the diffuser exit, and will be discussed separately in Section 4.4.6.

The close proximity of the vortices to the side-plates at x/d =6.37 indicates that the vortex flow is still influential on the surface flow patterns; the flow separating from the side-plates is induced in to the vortices adjacent to the ramp surface (Figure 31 (c)). At x/d =6.83 the diffuser area is considerably larger in height. The vortex has expanded but no longer occupies such a large proportion of the diffuser cross-sectional area. It remains positioned at the base of the side-plate. The vectors in Figure 32 show flow separation at the inner side-plate, at approximately y/d =-0.66. Here, the flow emanating from the outwardly spiralling vortex divides, some flowing downwards and back into the vortex, some flowing upwards away from the vortex. The oil flow pattern of the diffuser surface and inner side-plate at h_r/d=0.382 confirms that the separation exists, and is the point at which the vortex detaches from the upswept surface (Figure 33). In the figure this occurrence is seen as the point at which the side-plate becomes devoid of any oil mixture. Beyond this streamwise location, the separating flow from the side-plate flows towards the diffuser ramp, and not into the vortex. This flow behaviour is also consistent with measured surface pressures at this plane, which indicate a much lesser influence of the vortex on the ramp surface flow. The strength of the vortex is gradually decreasing as the flow decelerates through the diffuser (Figure 31 (e)), however the cross-flow velocities continue to remain high (Figure 32). By x/d =7.74, the separation at the inner side-plate occurs at y/d of approximately -0.55. The ground shear layer has increased in thickness along the length of the diffuser. The gap between the shear layers of the vortex and the ground has reduced to approximately 15 mm. At either side of the centreline z/d =0, the ground boundary layer begins to be induced upwards by the vortex flow as noticed in the LDA results. A small part of the boundary layer appears to be about to shed an eddy. By x_1/d =0.096 the gap between the shear layers has reduced further and the flow has been shed, however at this model ride height the vortex flow inducement is not yet strong enough to cause the shed flow to roll up into a smaller vortex (Figure 31 (f)).

4.4.2 Vortex Flow Inside the Diffuser in Type B

The vortex flow through the diffuser at h_r/d=0.255 is presented in Figures 34 and 35. The type B flow features remain essentially symmetric. The flow velocities accelerating underneath the side-plate have increased due to the reduction in the gap through which it flows. As with the type A flow, the vortex is strong and concentrated at x/d =5.44 (Figure 34 (a)), and its core is present in the PIV images (Figure 36 (a)). The flow separating from the side-plate appears to wind into the vortex. The vortex remains concentrated at x/d =5.91 (Figure 34 (b)), although its core is no longer visible in the PIV images. The ground boundary layer is observed in the vorticity contours of Figure 34 (b). However, at x/d =6.37 a noticeable change occurs. The vortex is visibly much larger and seemingly more diffused; the vorticity at the centre has decreased to less than half that at x/d =5.91 (Figure 34 (c)). The vectors indicate flow separation at the inner side-plate at approximately y/d =-0.7 (Figure 35 (a)). The separation is similar to that which occurred in the type A flow, although it has occurred further upstream in the diffuser at this ride height. Thus the vortex detaches from the diffuser surface earlier as the ride height is lowered through the type A and type B flows. The vortex size gradually increases throughout the remainder of the diffuser, and the core locations move in-board towards the centreline (Figures 34 (d) - (f)). The PIV images in Figure 36 emphasise the transition of the type B vortex from a tightly wound and concentrated vortex at x/d =5.44 (Figure 36 (a)) to a larger, more diffused and weaker vortex at x/d =6.83 (Figure 36 (b)). Flow visualisation has revealed that the vortices separate from the diffuser surface at approximately x/d =6.7, coinciding with the diffusion of the vortex between x/d =6.37 and 6.83. The vortex and the ground boundary layer become closer to each other as they develop through the diffuser. At x/d =6.83, the gap between the shear layers is small. The ground boundary layer has thickened and is induced upwards by the vortices at $z/d = \pm 0.35$ (Figure 34 (d)). By x/d =7.74, the induction has caused the boundary layer to separate from the ground and follow the vortex shear layer upwards (Figure 34 (e)). The appearance of two small scale vortices beneath the main vortices indicates that the induction of the ground shear layer by the main vortices, discussed in Section 4.2.2, first occurs towards the end of the diffuser. On exiting the diffuser, each vortex occupies almost a full half-width of the exit cross-sectional area. The ground boundary layer interacts with the vortex across the span of the diffuser as increasing amounts of the ground shear layer are entrained upwards.

Figure 37 shows profiles of w/U_∞ extracted from the mean flow data at h_r/d=0.255. Each profile passes through the centre of the left side vortex and extends to the ground plane. Whilst the large velocities and steep gradients of the curve at x/d =5.91 emphasise the coherence and strength of the vortex at the start of the diffuser, the smaller velocities and gentler gradients of the curve at x_1/d =0.096 are indicative of the large, diffuse vortex flow at the diffuser exit.

The figure also clarifies the extent of the vortex and ground shear layer interaction at different streamwise locations in the diffuser. It may be seen that at x/d =5.91 and 6.37 there is a discontinuity in the curve between the two shear layers. At x/d =6.83 there is a small gap between the change in curve gradients, whilst at planes x/d =7.74, and x_1/d =0.096 there is no discontinuity in the curves, indicating a merging of the shear layers at these locations.

4.4.3 Vortex Flow Inside the Diffuser in Type C

Type C flow is characterised by force reduction and asymmetric vortex flow. One of the vortices is collapsed from the inlet and, at x/d =5.44 the region of low speed fluid is apparent (Figure 39 (a)). The shear layer separating from the left side-plate does not roll up into a vortex, but flows around the separated flow and upwards to the diffuser surface.

The vortex that rolls up is weaker than that at h_r/d=0.255 (Table 14 and Figure 38 (a)). It is also smaller in size than the type B vortex, and the gap between the vortex and the ground boundary layer is reduced. At x/d =5.91 the region of separated fluid at the left side of the diffuser has increased in size and the cross-flow velocities in the vortex have decreased (Figure 39 (b)). The ground boundary layer at the unstalled side of the flow is thicker than that at the stalled side. Although h_r/d has reduced, and less fluid may be entrained through the gap, there is still a channel between the shear layers through which freestream fluid accelerates and is then induced into the vortex. By x/d =6.83 (Figure 38 (c)), the vortex is still compact and retains its strength, $\Omega d/U_\infty$=-18 at the vortex centre (Table 14), compared with $\Omega d/U_\infty$=-20 at x/d =5.91, and especially in comparison with the type B vortex, the vorticity of which was $\Omega d/U_\infty$=-8 at x/d =6.83. Thus the type C vortex appears to be less diffused than the type B flow. The vortex centre follows a similar path to that of the type B vortex flow (Table 14), however it is smaller in size than the vortex at h_r/d=0.255, and is detached from the side-plate. The gap between the shear layers has almost disappeared, and it may be surmised that they merge at an earlier streamwise location in the type C flow than in the type B flow. The ground boundary layer underneath the unstalled flow has separated from the ground by x/d =7.74 (Figure 38 (d)), whilst the boundary layer beneath the stalled flow remains relatively thin and attached to the ground. Upon exiting the diffuser the vortex is diffused, detached from the side-plate and greatly reduced in strength (Figure 38 (e)). The ground boundary layer thickness has decreased since x/d =7.74, and is now reattached to the ground underneath the vortex. This is most likely due to the fact there is no side-plate to cause acceleration of fluid entering the diffuser from the sides. Although the fluid would accelerate as it flows through the gap between the ground and the vortex, the vortex strength is greatly reduced and therefore the cross-stream fluid remains at a low speed. The pressure gradient across the shear layer as the fluid then decelerates towards the centre-plane is not large enough to cause the shear layer to separate. The area of stalled flow at the left side of the diffuser occupies more than half the span of the exit area and appears as a weakly circulating flow.

4.4.4 Vortex Flow Inside the Diffuser in Type D

Only three planes were measured at h_r/d=0.064, since the area inside the diffuser became too small to capture meaningful results further upstream in the diffuser. Cross flow velocities inside the diffuser are low (Figure 41). Little flow is entrained through the gap between the side-plate and the ground. At x/d =6.83 the shear layer separating from the edge of the side-plate remains close to the ground plane, and does not roll up as at higher ride heights (Figure 40 (a)). At both sides of the diffuser, the shear layers at the side-plate and at the ground appear to merge to effectively prevent more flow entering the diffuser from the sides.

The inside of the diffuser is occupied by a weak vortex and re-circulating and reversed flow. Surface pressure measurements at this ride height indicated a single weak vortex in the front half of the diffuser, becoming almost undetectable at the surface by this streamwise location (Figure 17 (b)). Further downstream in the flow at x/d =7.74, the flow characteristics are essentially unchanged and the vortex is large, weak and low speed (Figure 40 (b)). The flow at the exit plane x_1/d =0.096 (Figure 40 (c)) confirms the LDA measurements at the same plane, revealing a single low speed vortex to the right of the flow and a stalled flow to the left. The significance of the results at this ride height lies in the fact that no high speed flow occurs inside the diffuser. It is surmised that the flow at the diffuser inlet is 'choked', that the boundary layers beneath the flat bottom of the model and over the ground merge upstream of the diffuser inlet to effectively prevent the through-flow from entering the diffuser.

4.4.5 Boundary Layer Flow Underneath the Diffuser

PIV measurements were taken in the flow beneath the model in order to elucidate the boundary layer states at the inlet to the diffuser and their possible impact upon the down-force reduction behaviour at low model ride heights. Figures 42 and 43 present boundary layer profiles, u/U_∞, at two model heights, h_r/d=0.255 and h_r/d=0.204. The first is a type B flow approaching maximum down-force, the second is a type C flow, just beyond down-force reduction. For each model height, the streamwise flow underneath the model was measured at the centreline, and at 10 mm inboard of each side-plate, i.e. $z/d = \pm 0.936$.

At h_r/d=0.255, the flow underneath the flat part of the model is high speed for each spanwise location, reaching velocities of up to U_∞ =1.6 along the model centreline (Figure 42). Boundary layers are evident both underneath the model and over the moving ground. At the centreline, high speed fluid flows through the channel between the boundary layers, decelerating gradually on entering the diffuser. Once inside the diffuser, the boundary layer thickness at the model surface increases. In each profile, there is a region of almost constant velocity between the boundary layers. Although the boundary layers cannot be fully resolved from these measurements, it is evident that the gap is over 25 mm (y/d =0.159) in each profile. This casts some doubt upon a stall caused by boundary layer interaction at the diffuser inlet. Figure 44 (a) supports this deduction. The regions of vorticity in the contours are the shear layers beneath the model and over the ground. The shear layer beneath the model is seen to thicken underneath the corner of the model. A blockage in the camera image caused by the side-plate means that part of the flow in this region is obscured. It is estimated from the paths of the surrounding vectors and from the curvature of the shear layer that the boundary layer in this region does not extend below y/d =-1.12.

Profiles of u/U_∞ underneath the model centreline at h_r/d=0.204 are shown in Figure 43. At the model centre-plane z/d =0. (Figure 43 (a)) there is a high speed flow through the channel between the model and the ground. The profiles indicate that there is a gap of approximately 15 *mm* (y/d =0.096) between the two boundary layers. The flow accelerates in the approach to the diffuser inlet, and decelerates to below u/U_∞=1.202 at x/d = 5.5. At the unstalled side of the model at z/d =0.936 (Figure 43 (c)), there is a region of high speed fluid at the diffuser inlet, although the fluid approaching the inlet from upstream is slower than at the centre-plane. This is to be expected, as the pressure would not be as low at the sides of the flat bottom as it is under the centre-plane. The flow accelerates at the inlet where the pressure is most negative, before decelerating at a faster rate than at the centre-plane (Figure 43 (c)). The velocity reduces to $u/U_\infty \leq$1.202 by x/d = 5.15. Figure 43 (b) shows the streamwise flow through the channel at the stalled side of the flow, z/d =-0.936. The streamwise flow is slower at the diffuser inlet and immediately beyond than in either of the previous figures, the maximum velocity being 15% slower than that at the left side unstalled flow. However, there remains a definite region of high speed flow. The gap between the two boundary layers indicates that there is no boundary layer merge at the stalled side of the diffuser inlet.

Figure 44 (b) shows the flow in the cross stream at the diffuser inlet at h_r/d=0.204. The velocity vectors indicate that the flow at this side of the diffuser is unstalled, and the gap of at least 15 *mm* (y/d =-1.1 to -1.2) between the boundary layers is apparent, bearing in mind that the same camera angle problem of the side-plate protruding into the flow occurs in this result as occurred at h_r/d=0.255. Although the boundary layer is not resolvable from these measurements, the figure confirms that the boundary layer thickness underneath the model inlet at h_r/d=0.204 has not increased significantly from the boundary layer thickness measured with the LDA at a freestream ride height (Figure 44).

It may be deduced from these measurements that the stall at low ride heights for this diffuser angle does not appear to occur due to a merging of the boundary layers at the diffuser inlet.

4.4.6 Steady Shear-Layer Instability

In Section 4.4.1 the observation of co-rotating small scale vortices within the main vortex shear layer was documented and is thought to be a 'steady' shear layer instability. The small vortices are of the same sense as the main vortex around which they exist, and are seen most clearly in the vorticity contours of Figure 31 (f) around the main vortex. They are less clear but visible in Figures 31 (c) - (e). The appearance of the small vortices in the flow indicates that they are a steady phenomenon, and that they are stationary in position. The time-dependent flow measurements presented in Chapter 5 confirm that this is so. In Figure 31 (f), there are seven small vortices around each main vortex. A finer resolution is required to measure these vortices in detail, however it can be seen that each has a non-dimensionalised vorticity at its estimated centre of $\Omega d/U_\infty$ = ±4-5, although the vortices around the right side vortex are of slightly higher vorticity than those around the left side vortex. It is expected that the small scale vortices also exist in the shear layer rolling up from the side-plates at h_r/d=0.255 in the early part of the diffuser. The PIV did not capture sufficient resolution in the vortices at h_r/d=0.255, x/d =5.91 (Figure 34 (b)) to show whether or not this is the case, however at x/d =6.37 (Figure 34 (c)) there is evidence to suggest that they are present but becoming obscured from view by the diffused vortex core.

The instability has been found in delta wing vortex flows at high incidence and low *Re* [59, 73, 74, 78] and also in higher *Re* delta wing flows [79, 93]. Campbell *et al* [12] found evidence that the instability also exists under flight conditions in the vortex flow over fighter aircraft. The occurrence of the instability over such a large range of *Re* suggests that it is an inviscid phenomenon. Its cause was investigated by Riley & Lowson [79] and was thought to be a local three-dimensional Kelvin-Helmholtz instability of the free shear layer.

4.5 Discussion

The LDA and time-averaged PIV data confirm the initial postulations made in Chapter 3, and also reveal important flow physics that contribute to the understanding of the diffuser behaviour in ground effect. In Chapter 3 it was surmised that the flow was characterised by a counter rotating vortex pair. The vortices, along with diffuser pumping, were thought to dominate down-force production. The measurements presented in this Chapter have proven this to be correct. In addition, the down-force reduction has been proven not to be due to boundary layer merging at the diffuser inlet.

Four different types of vortex flow corresponding to each region of the down-force curve have been identified and described, and they provide an explanation for the four regions of the down-force curve (Figure 9 (a)). The vortex characteristics provide greater understanding of the changes occurring inside the diffuser as a consequence of an increase or reduction in model ride height.

Type A vortices are similar to those found on a delta wing at moderate angle of attack: strong, coherent and characterised by a high axial speed core. Measurement of the type B flow in the early part of the diffuser reveals a vortex pair exhibiting type A vortex characteristics, however a transformation occurs part way along the diffuser to cause the vortices to become large, diffuse nature and with a low speed axial core. The transformation is illustrated in Figure 36. At h_r/d=0.255, the coherent vortex shown in (a) becomes the large, weak vortex shown in (b) over a distance of less than 100 *mm*. The vortex core disappears from the PIV camera image in all planes downstream of x/d =5.91. This is indicative of either the core no longer staying in one position or of a core dilation. The vortex core could be wandering and causing the apparent diffuse nature of the mean vortex flow. However, there are several other possibilities that could cause the vortex to be diffuse, for instance a merging of the shear layer at the side-plate with the unsteady separating flow from the ground shear layer.

The vortex could also be breaking down inside the diffuser to cause the core dilation seen in the images.

Vortex wandering is often found in delta wing vortices and tip vortices from a rectangular wing, and is thought to be caused by the Kelvin-Helmholtz instability known to exist in the shear layers of these flows [39]. Vortex breakdown is found in conditions of steep adverse pressure gradient and large swirl velocity, and is also often found in delta wing vortices at high angles of attack. The steady state instability seen in the type A flow cannot be responsible for an unsteady flow phenomenon such as vortex wandering because it does not travel round the shear layer, unlike the unsteady Kelvin-Helmholtz instability [39]. The diffuse nature of the vortex in the type B flow could be due to a number of reasons, the most likely of which are thought to be as follows.

- The vortex core wanders due to the Kelvin-Helmholtz instability in the shear layer
- Fluid from the ramp surface separation bubble is induced into the vortex cores
- The shear layers of the vortex and the ground interact to produce an unstable vortex
- The vortex breaks down inside the diffuser

The cause of the vortex becoming diffuse becomes clearer on investigation of the time-dependent vortex flow, to be discussed in Chapter 5.

In type C flow, the stronger vortex appears to behave in a manner similar to a type B vortex, being coherent and strong in the early part of the diffuser and becoming large and diffuse towards the diffuser exit. However, the type C vortex remains coherent for longer than the type B vortex. Thus, the mechanism that causes the type B flow diffusiveness also appears to affect type C flow, but at a later stage in the diffuser.

4.6 Summary

Measurements of the flow inside and exiting the diffuser have revealed four different types of vortex flow. A pair of counter-rotating vortices characterises the type A (down-force enhancement) diffuser flow. The vortices are symmetric about the model centre-line and are coherent with a high axial speed core. The type A flow appears to be steady. The type B flow vortices are similar to the type A vortices in the early part of the diffuser, however they become large and diffuse. The core axial speed reduces and the vortex strength is reduced as this occurs. The type C vortex flow is asymmetric, and characterised by a vortex and weakly re-circulating and reversed flow that is stalled from the diffuser inlet. The type C vortex is similar to a type B vortex. The type D flow vortex is also asymmetric, consisting of a weakly circulating and reversed flow and a vortex that is weak throughout the diffuser.

The ground boundary layer is induced upward by the vortex positioned above it, giving rise to separation of the cross-flow in the ground boundary layer. In some cases the boundary layer sheds pockets of vorticity into the main vortex shear layer and outer flow.

Boundary layer merging occurs inside the diffuser but only in type B flow towards the end of the diffuser (x/d =7.74), and in type C flow from x/d =6.83 as measured. Type D flow is surmised to be 'choked' at the inlet.

Boundary layer merging does not occur at the inlet at either h_r/d=0.255 (type B) or 0.204 (type C) and is therefore not the cause of the force reduction seen at low model ride heights.

A shear layer instability is present in the vortex flows of type A and possibly in early type B flow. The occurrence of the small vortices in the time averaged flow indicates that the phenomenon is steady and also that the main vortex retains a steady position and does not meander.

h/d	u_c/U_∞		TKE_c/U_∞^2		y_c/d		z_c/d		$\Omega_c d/U_\infty$		Γ_{ls}/dU_∞
	ls	rs	ls	rs	ls	rs	ls	rs	ls	rs	
0.064	-0.058	-	.0266	-	-0.797	-	-	-0.529	-	-0.230	-
0.159	-0.161	0.459	.0498	.0731	-0.632	-0.541	0.690	-0.285	4.97	-1.08	-
0.204	0.186	-0.261	.0841	.0347	-0.688	-0.746	0.490	-0.584	1.15	-8.10	-
0.217	0.064	0.081	.0924	.0743	-0.750	-0.692	0.532	-0.54	3.25	-3.76	0.161
0.255	0.036	0.029	.0772	0.081	-0.752	-0.727	0.493	-0.510	4.22	-3.636	0.339
0.318	0.096	0.229	0.062	0.050	-0.801	-0.820	0.545	-0.557	7.362	-10.231	0.224

Table 13: LDA Cross-plane vortex flow at x_1/d =0.096.

h/d	x/d	y_c/d		z_c/d		$\Omega_c d/U_\infty$	
		ls	rs	ls	rs	ls	rs
0.064	6.83	-0.873	-0.709	0.645	-0.529	1.937	-1.363
0.064	7.74	-0.607	-0.663	0.601	-0.58	0.780	-0.879
0.064	x_1/d=0.096	-0.398	-0.761	0.476	-0.583	0.386	-0.955
0.204	4.95	-	-	-	-	-	-
0.204	5.44	-0.919	-1.004		-0.929	0.649	-38.918
0.204	5.91	-0.843	-0.981	0.636	-0.858	0.844	-20.847
0.204	6.83	-0.849	-0.941	0.651	-0.724	0.700	-18.258
0.204	7.74	-0.759	-0.829	0.604	-0.596	0.769	-7.348
0.204	x_1/d=0.096	-0.838	-0.674	0.543	-0.570	0.880	-3.356
0.255	4.95	-	-	-	-	-	
0.255	5.44	-1.014	-1.003	0.920	-0.932	30.984	-65.006
0.255	5.91	-0.977	-0.978	-0.866	0.858	23.674	-24.268
0.255	6.37	-0.952	-0.957	0.774	-0.743	10.865	-13.957
0.255	6.83	-0.920	-0.923	0.699	-0.717	7.089	-7.938
0.255	7.74	-0.839	-0.8547	0.5794	-0.592	3.963	-4.267
0.255	x_1/d=0.096	-0.749	-0.7475	0.501	-0.496	3.593	-4.422
0.382	5.91	-0.9807	-0.974	0.8312	-0.8905	43.117	-49.4331
0.382	6.83	-0.9618	-0.94434	0.7605	-0.7864	50.264	-46.1595
0.382	7.74	-0.8845	-0.8668	0.6886	-0.683	37.527	-34.932
0.382	x_1/d=0.096	-0.851	-0.848	0.549	-0.603	44.647	-34.420
0.764	x_1/d=0.096	-0.812	-0.869	0.703	-0.766	27.4	-27.8

Table 14: PIV Cross-plane vortex flow inside diffuser.

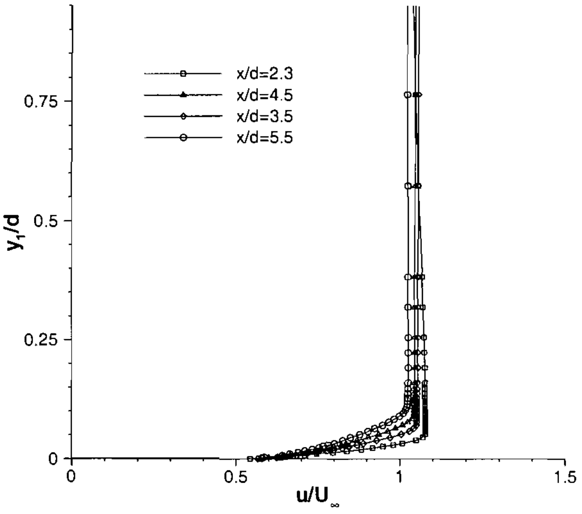

(a) Boundary layer profiles over top of model

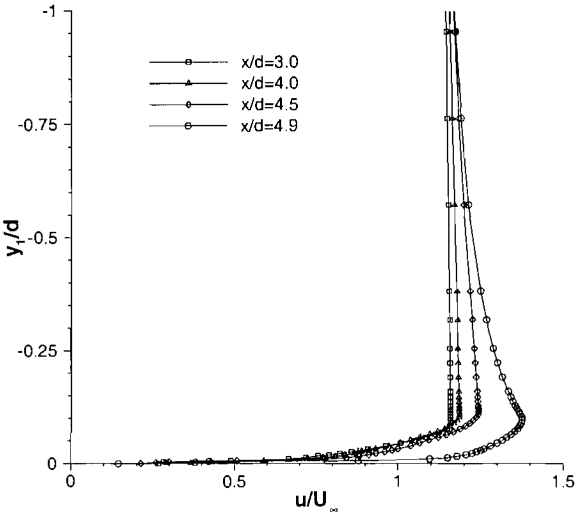

(b) Boundary layer profiles underneath model

Figure 22: Boundary layer profiles in freestream (LDA)

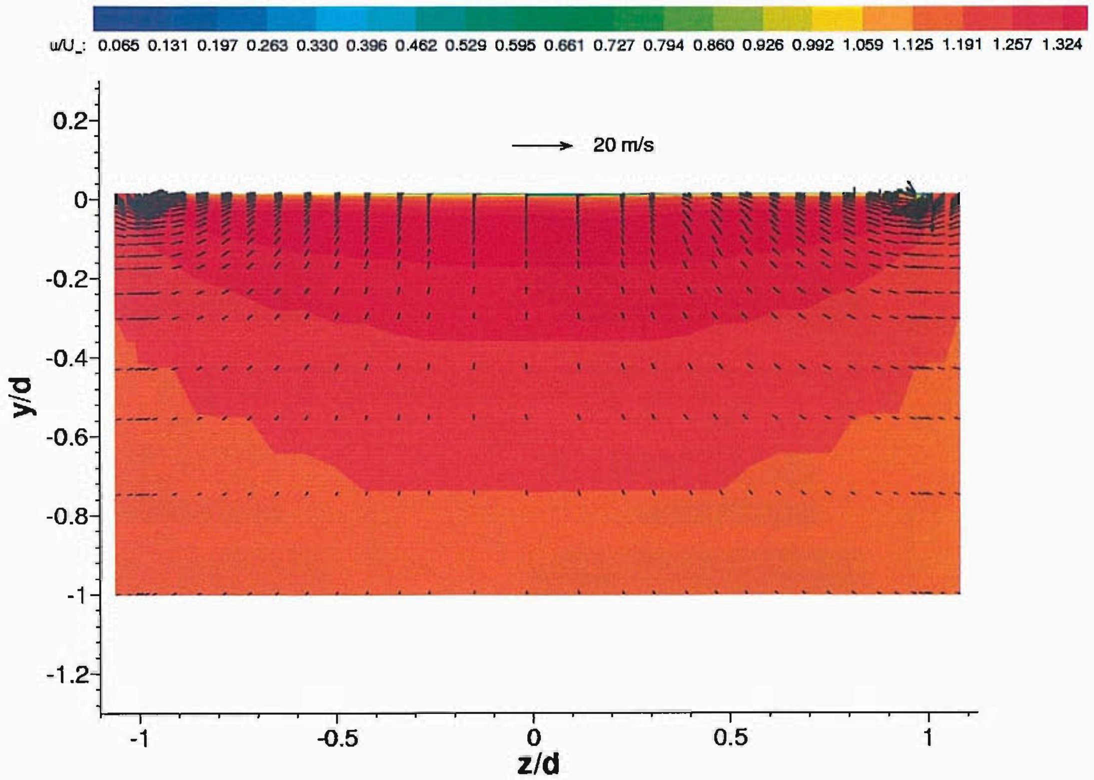

Figure 23: LDA measurements underneath the model in freestream at x/d =4.9.

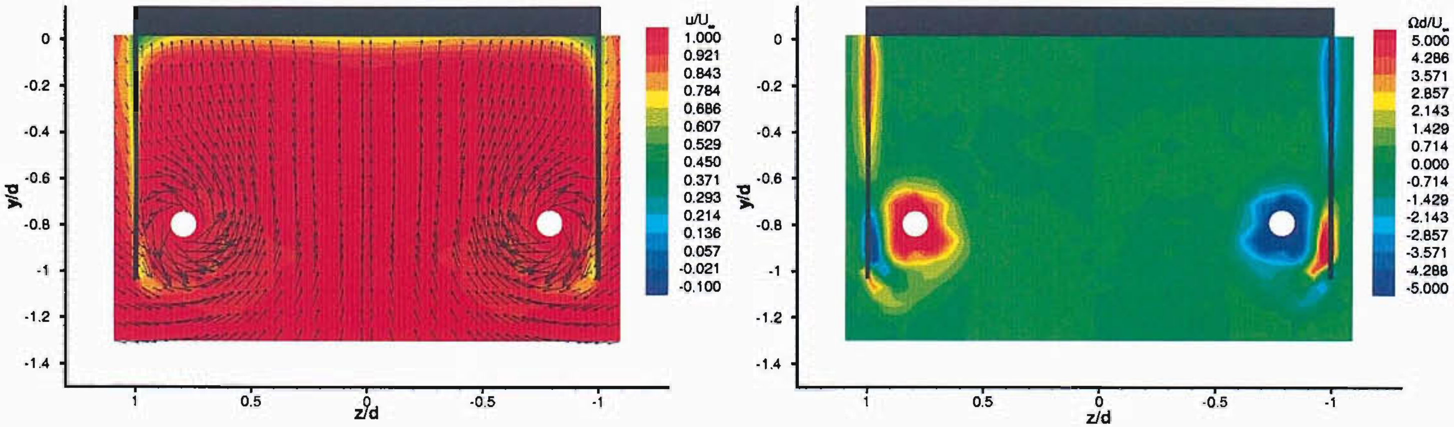

(a) u/U_∞ (b) $\Omega d/U_\infty$

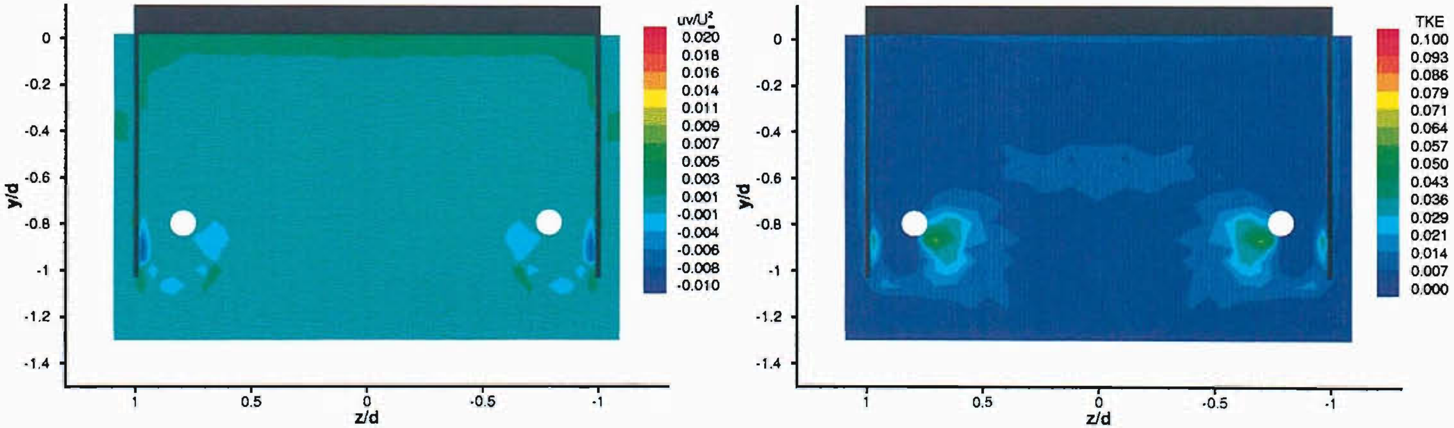

(c) $\overline{uv}/U_\infty^2$ (d) tke

Figure 24: Time averaged vortex flow exiting the diffuser in freestream, h_r/d=4.14 (LDA).

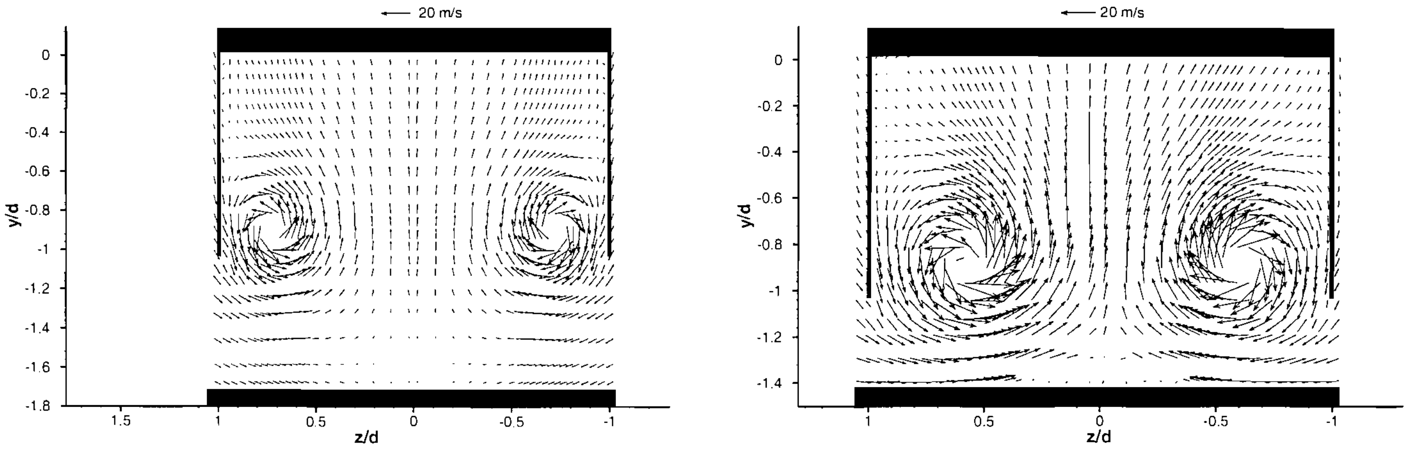

(a) h_r/d=0.764 (b) h_r/d=0.382

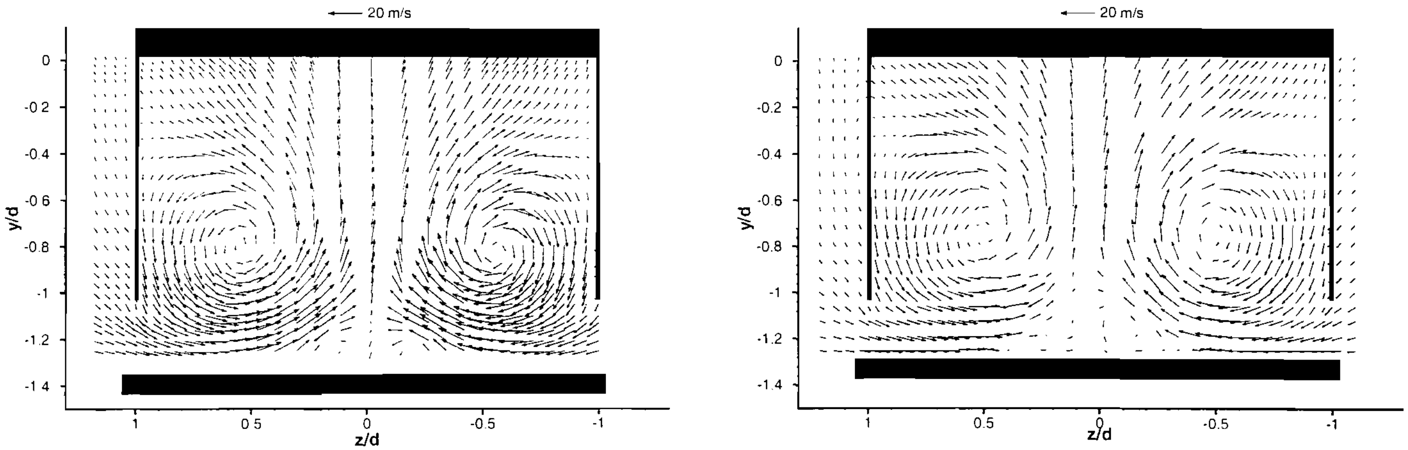

(c) h_r/d=0.318 (d) h_r/d=0.255

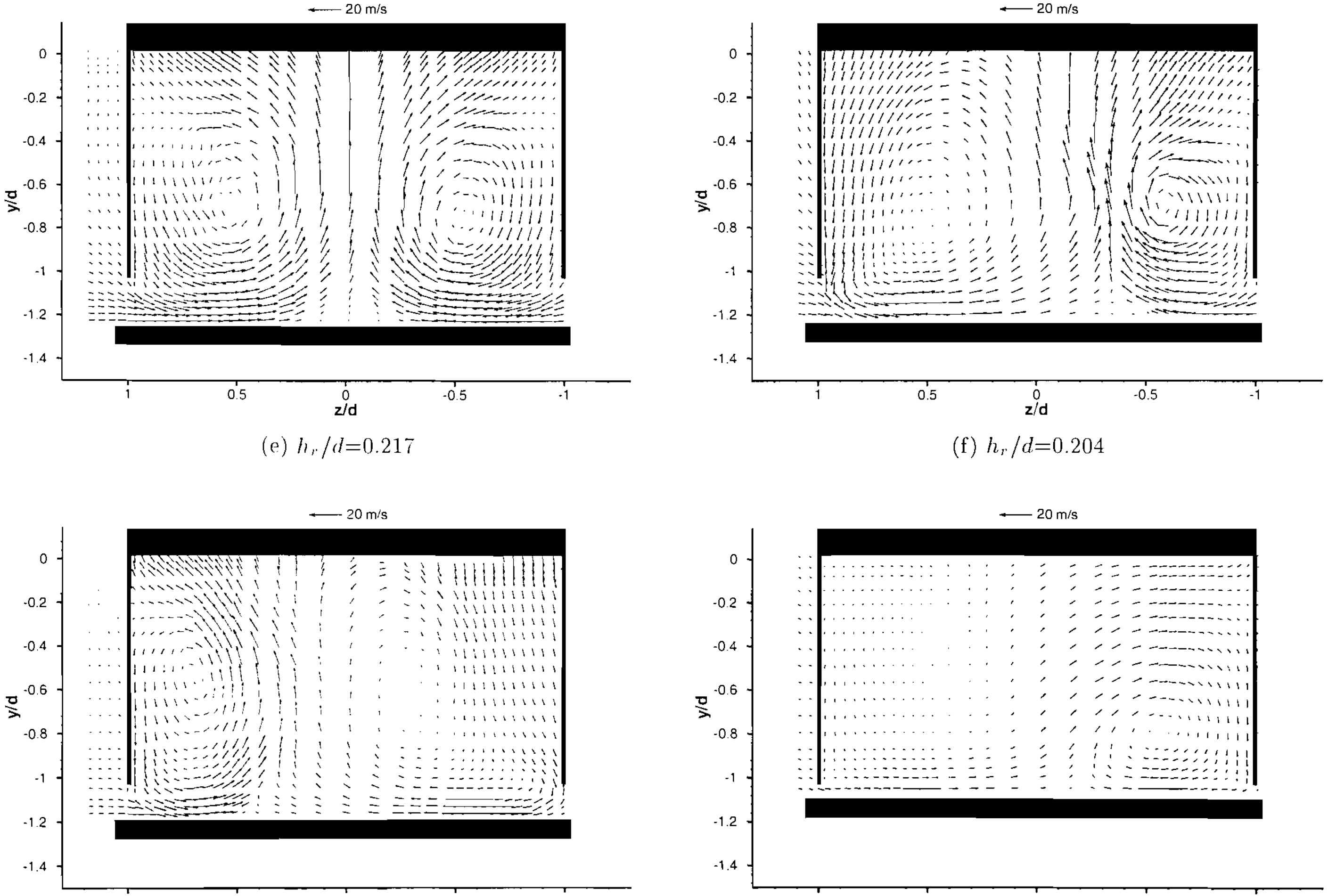

(e) h_r/d=0.217

(f) h_r/d=0.204

(g) h_r/d=0.159

(h) h_r/d=0.064

Figure 25: Time-averaged velocity vectors of flow exiting the diffuser (LDA).

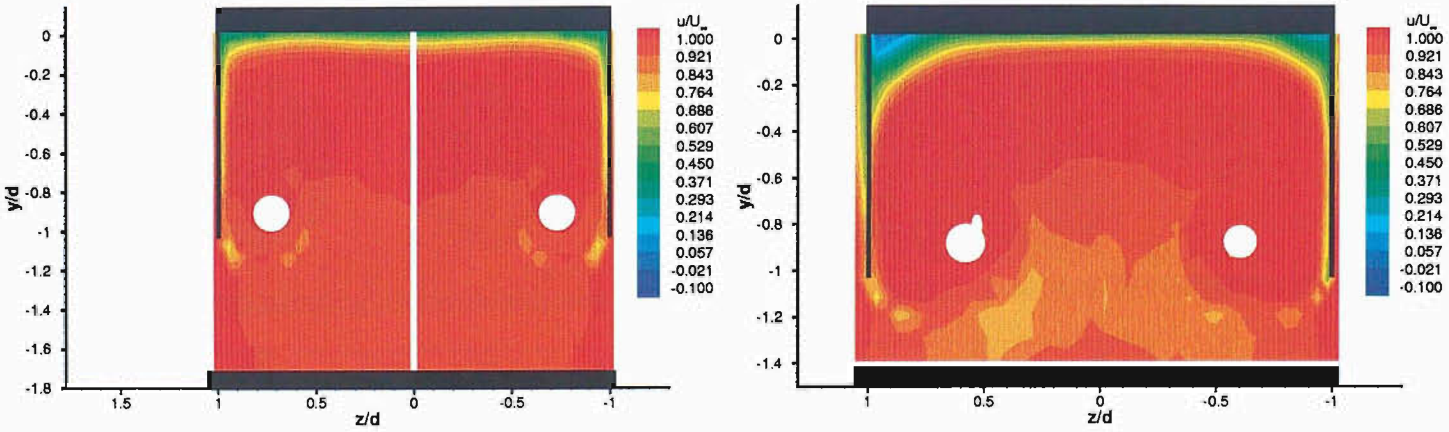

(a) h_r/d=0.764 (b) h_r/d=0.382

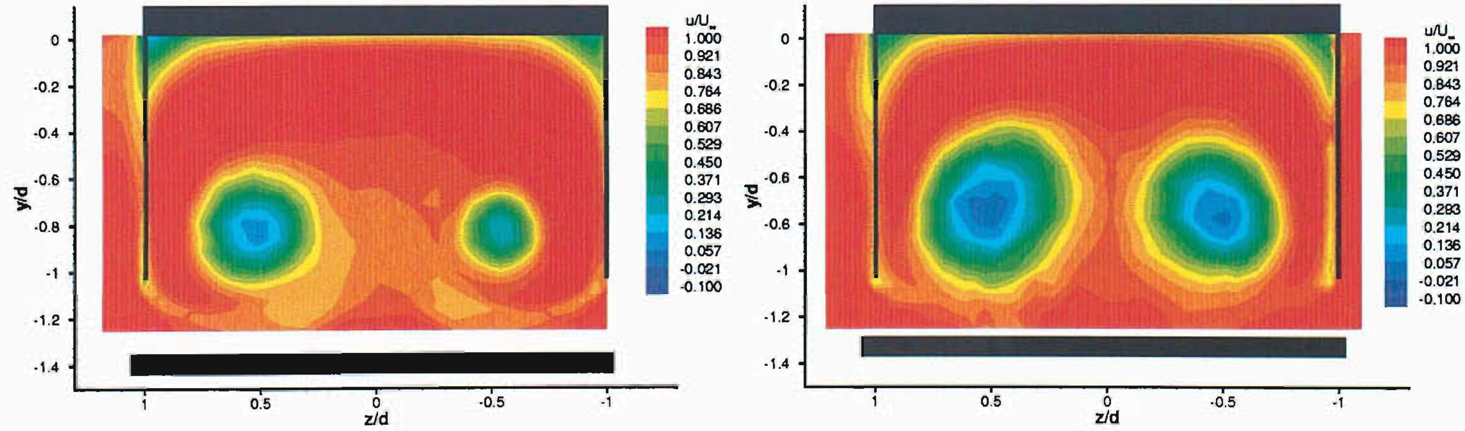

(c) h_r/d=0.318 (d) h_r/d=0.255

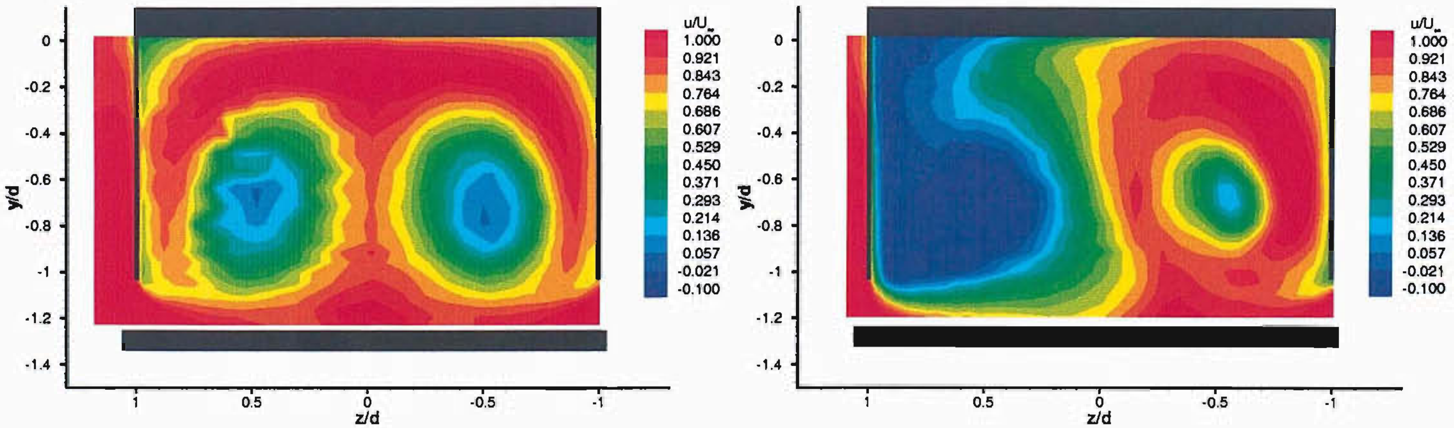

(e) h_r/d=0.217 (f) h_r/d=0.204

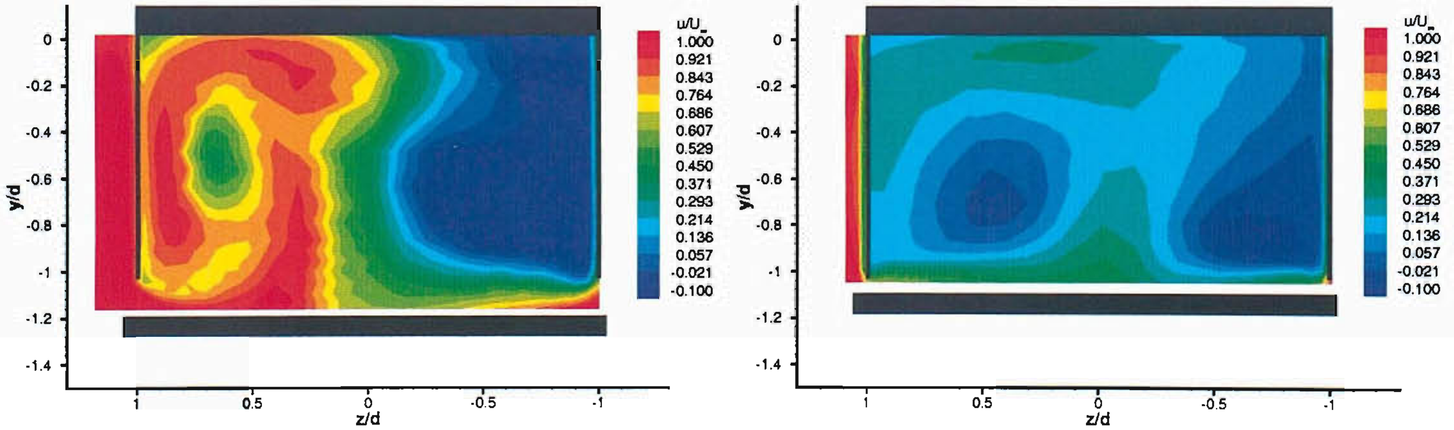

(g) h_r/d=0.159 (h) h_r/d=0.064

Figure 26: Time-averaged streamwise velocity u/U_∞ contours of flow exiting the diffuser (LDA).

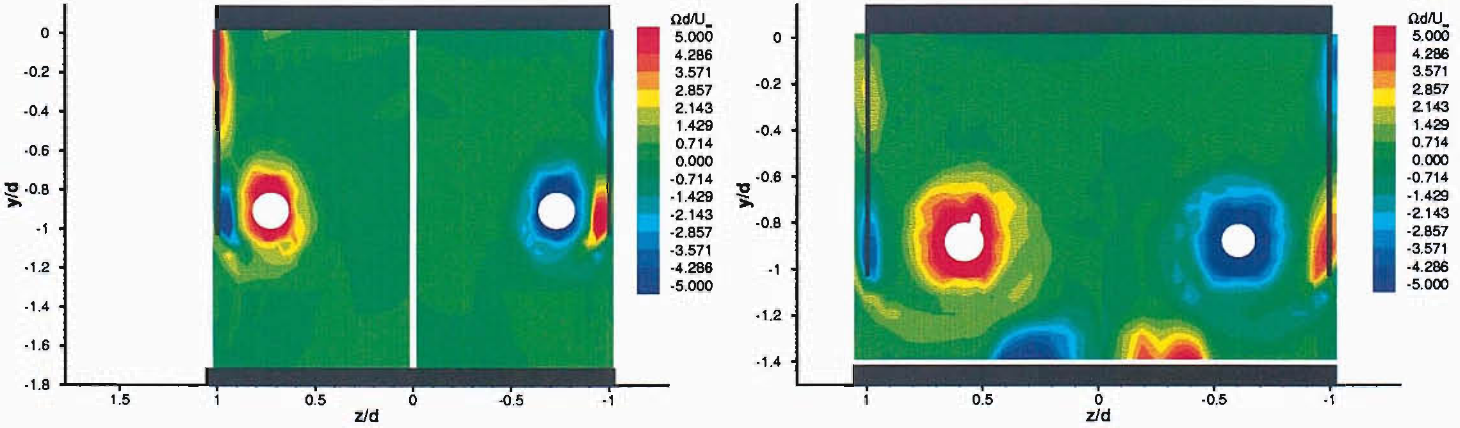

(a) h_r/d=0.764

(b) h_r/d=0.382

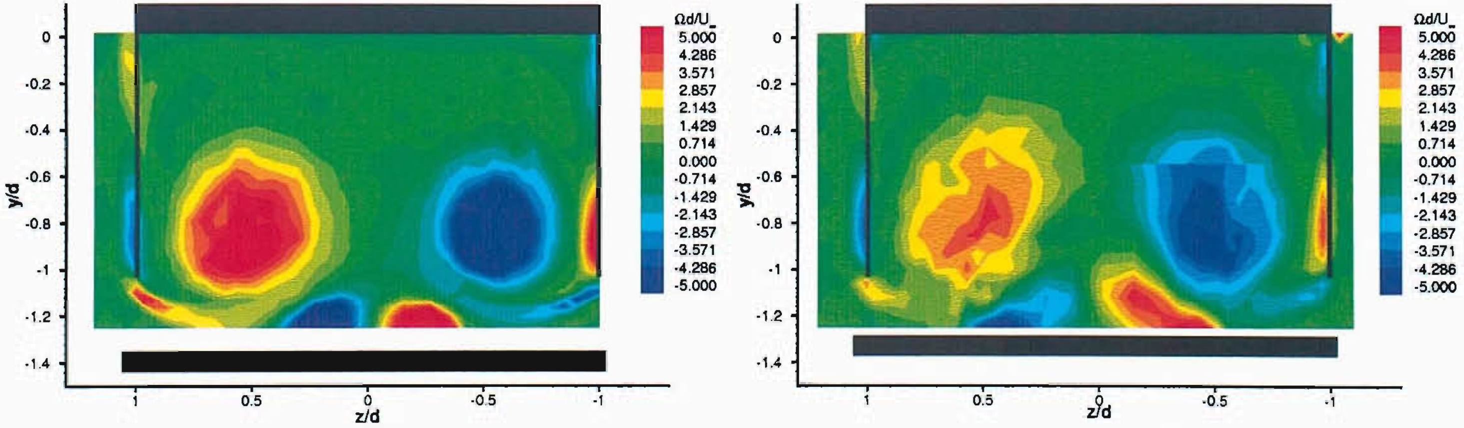

(c) h_r/d=0.318

(d) h_r/d=0.255

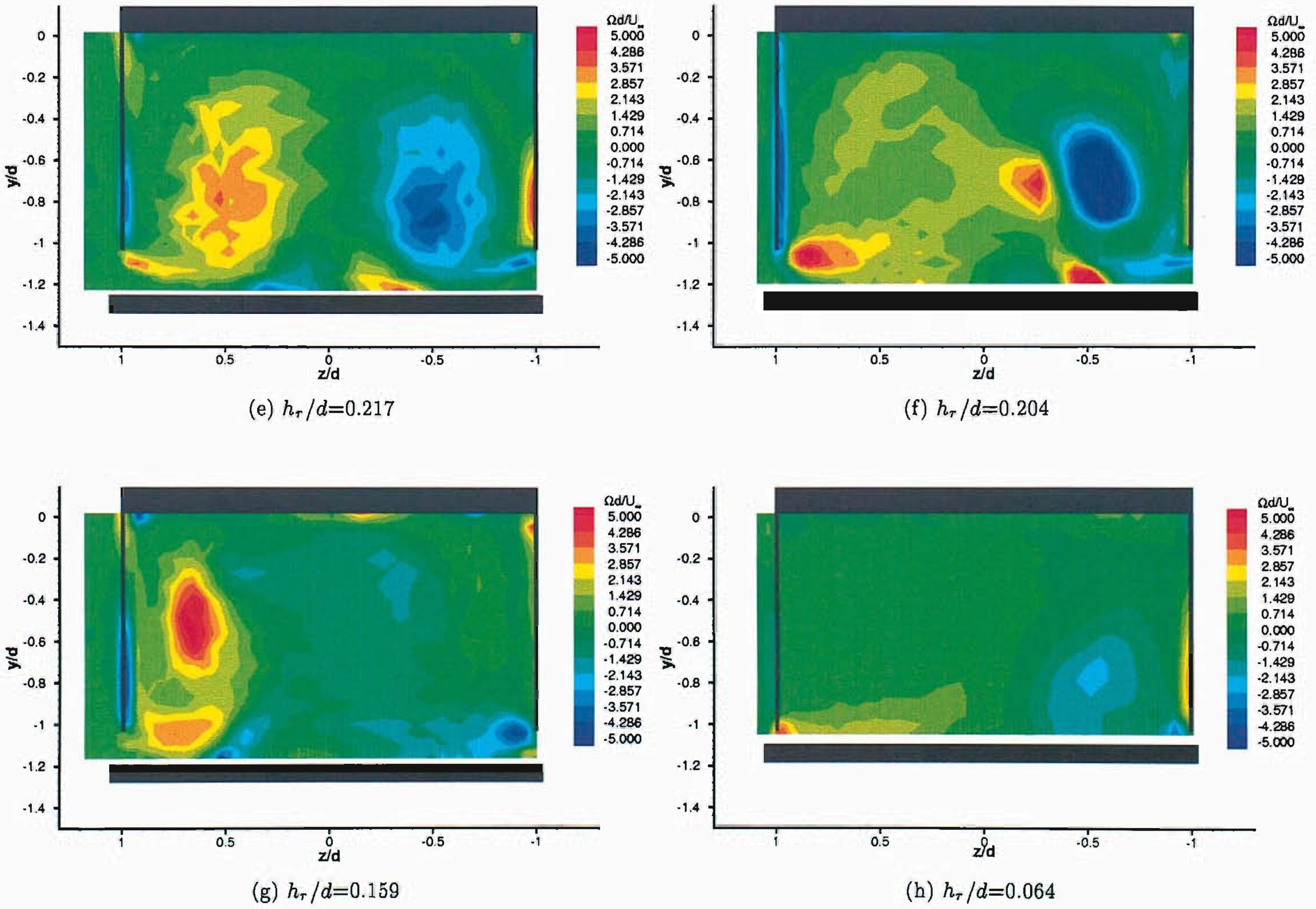

(e) h_r/d=0.217

(f) h_r/d=0.204

(g) h_r/d=0.159

(h) h_r/d=0.064

Figure 27: Time-averaged streamwise vorticity ($\Omega d/U_\infty$) of flow exiting the diffuser (LDA).

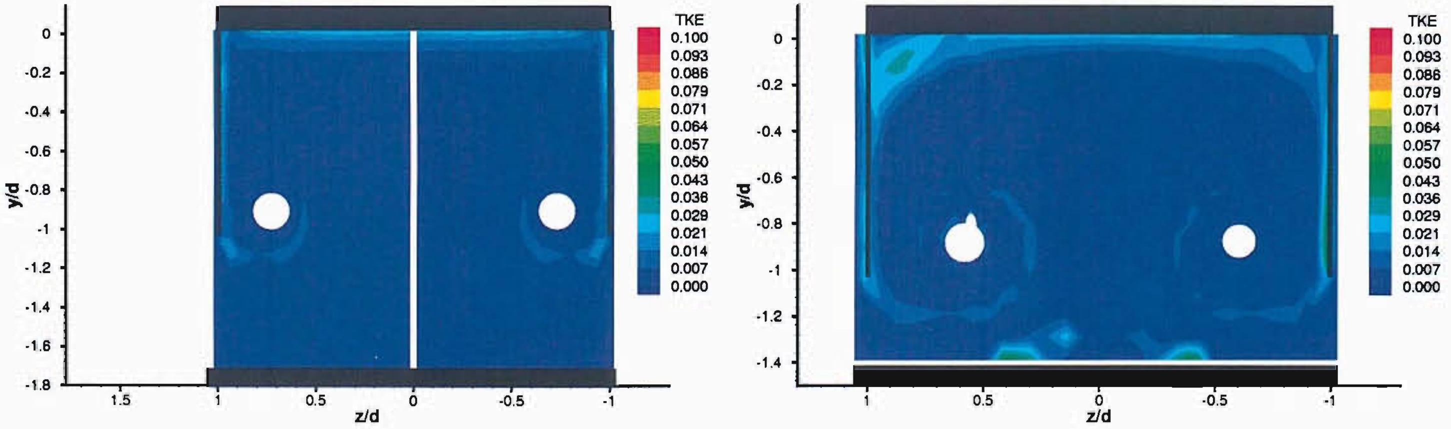

(a) h_r/d=0.764

(b) h_r/d=0.382

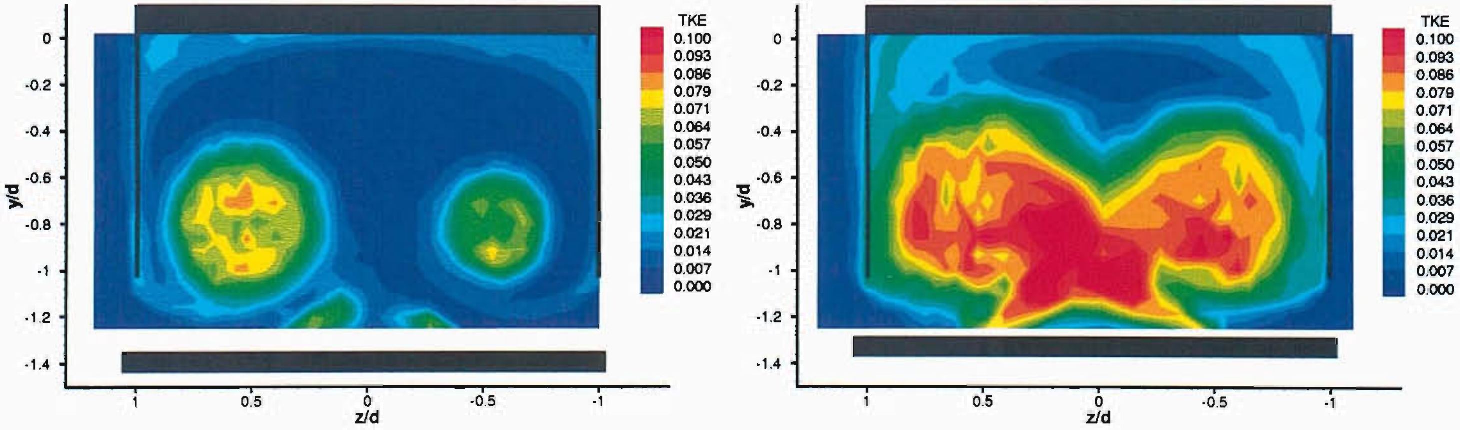

(c) h_r/d=0.318

(d) h_r/d=0.255

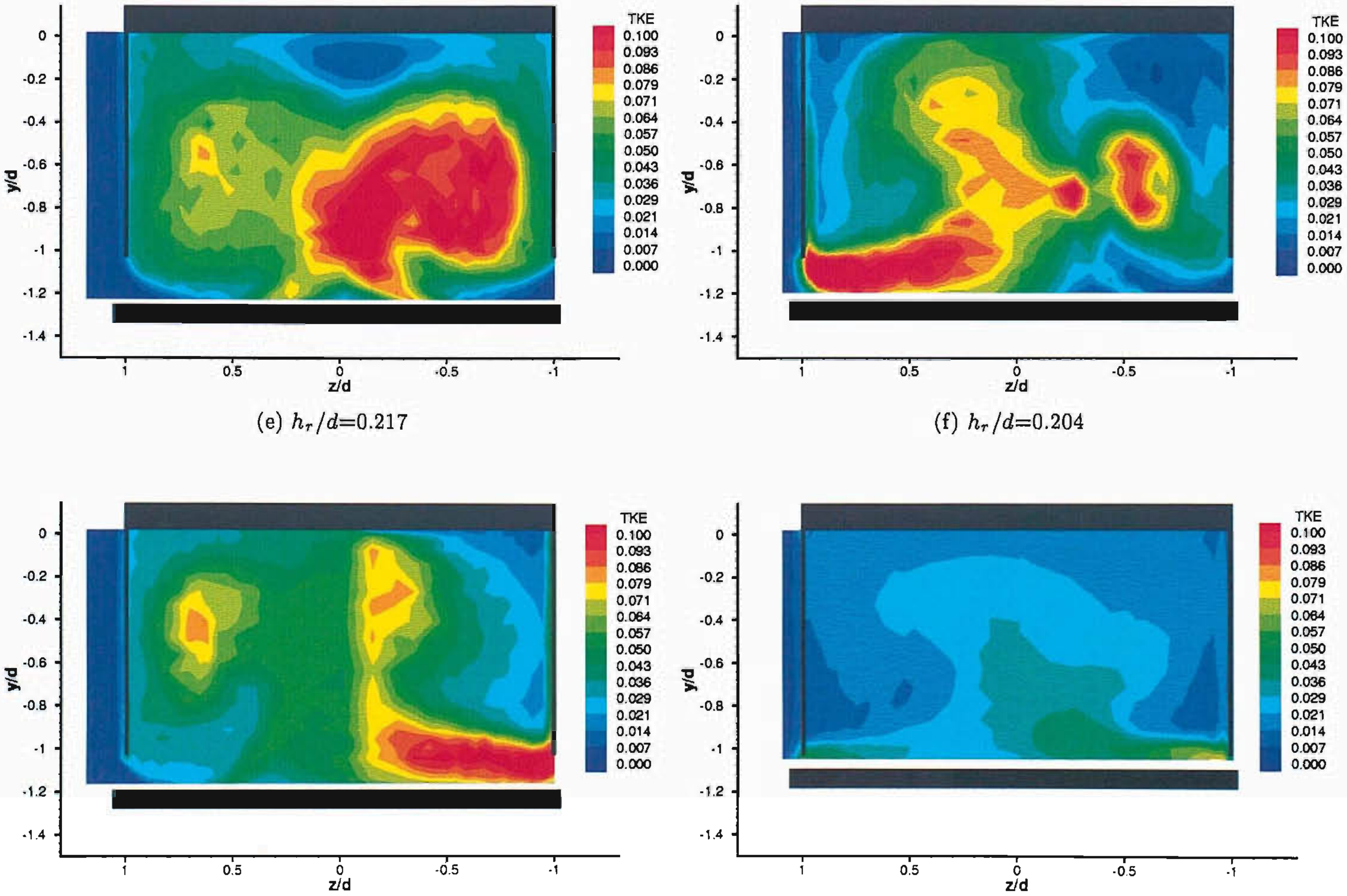

(e) h_r/d=0.217

(f) h_r/d=0.204

(g) h_r/d=0.159

(h) h_r/d=0.064

Figure 28: TKE contours of flow exiting the diffuser (LDA).

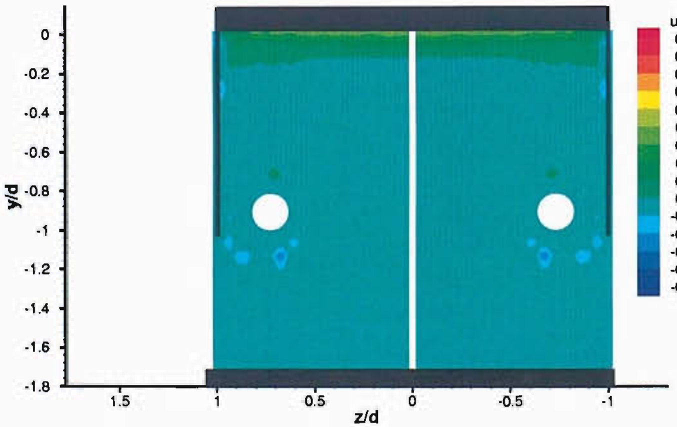

(a) h_r/d=0.764 (Region A)

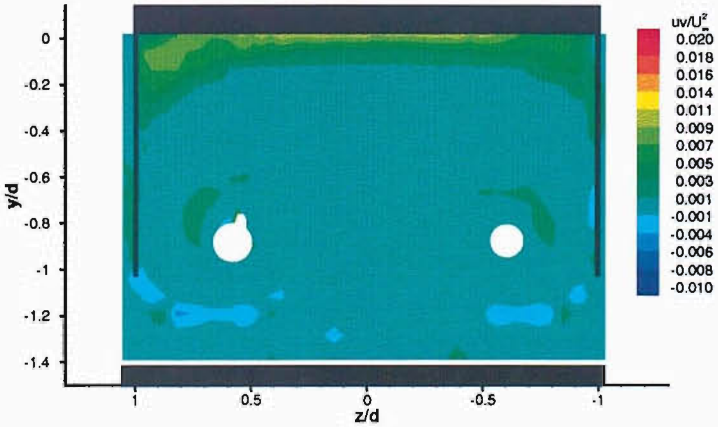

(b) h_r/d=0.382 (Region A)

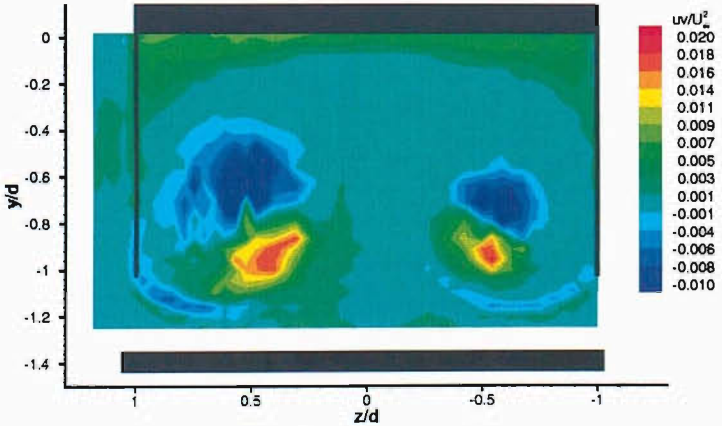

(c) h_r/d=0.318

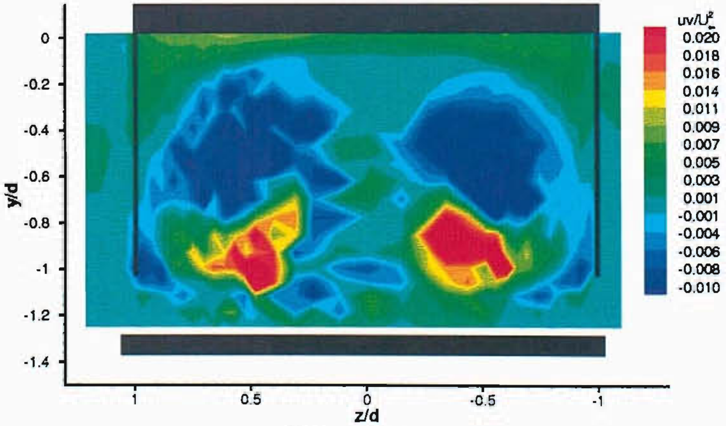

(d) h_r/d=0.255

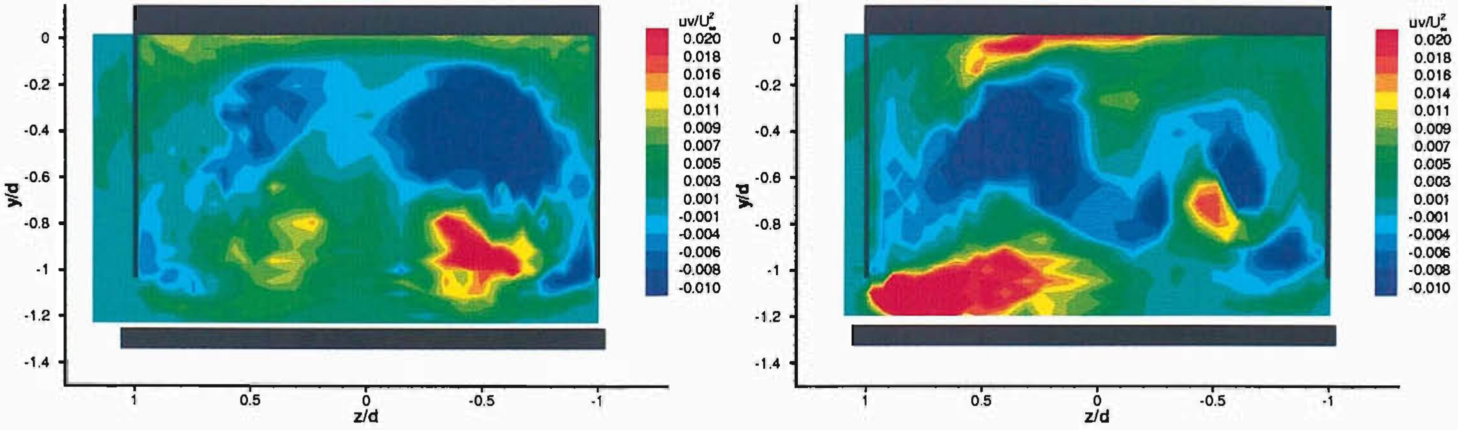

(e) h_r/d=0.217 (f) h_r/d=0.204

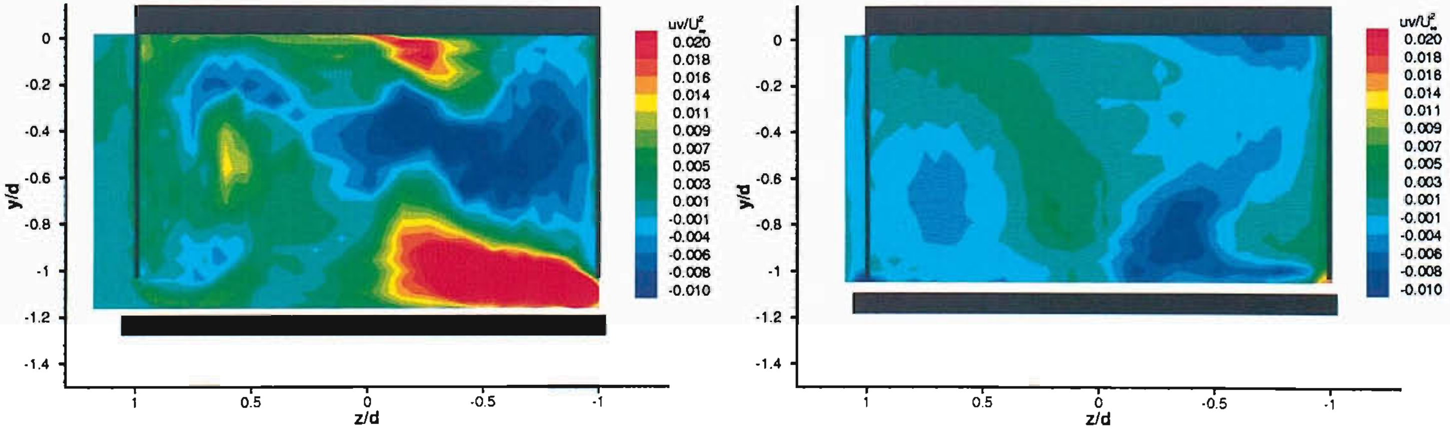

(g) h_r/d=0.159 (h) h_r/d=0.064

Figure 29: $\overline{uv}/U_\infty$ contours of flow exiting the diffuser (LDA).

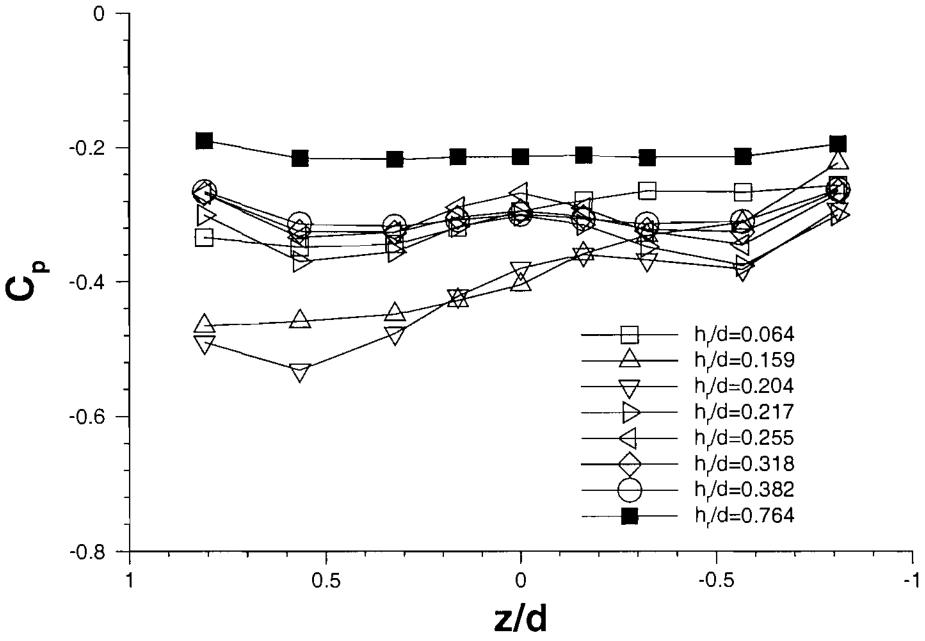

Figure 30: Surface pressure coefficients towards the exit of the diffuser surface ($x/d = 7.76$).

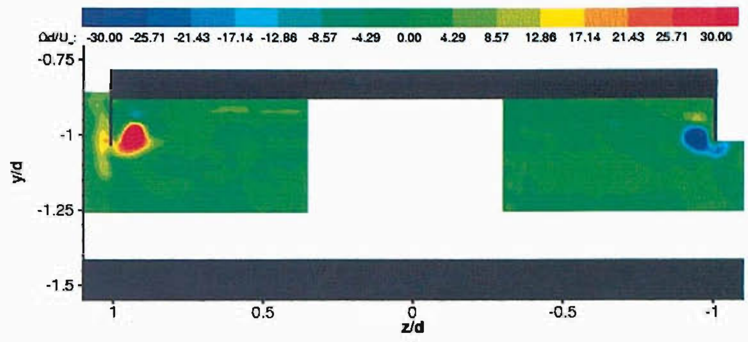

(a) x/d=5.44

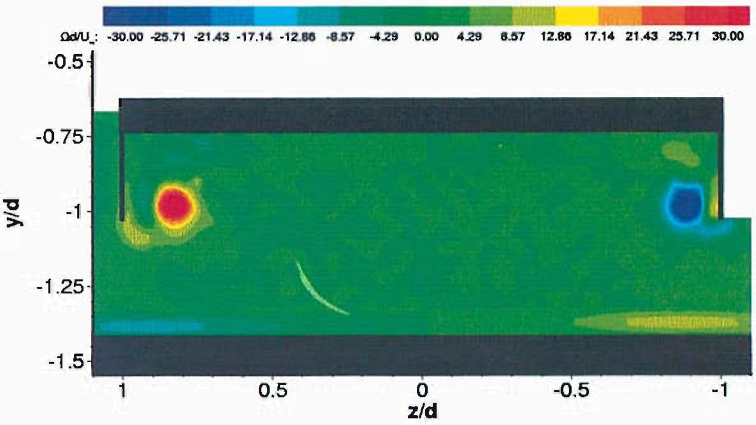

(b) x/d=5.91

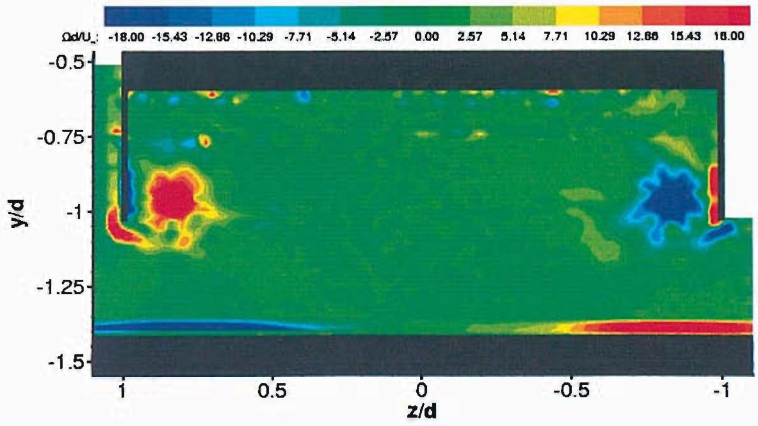

(c) x/d=6.37

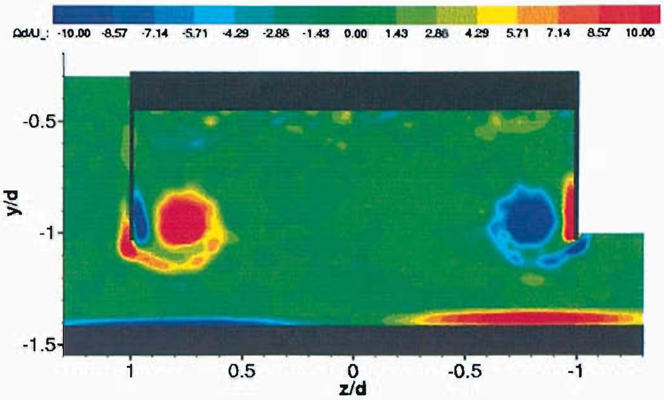

(d) x/d=6.83

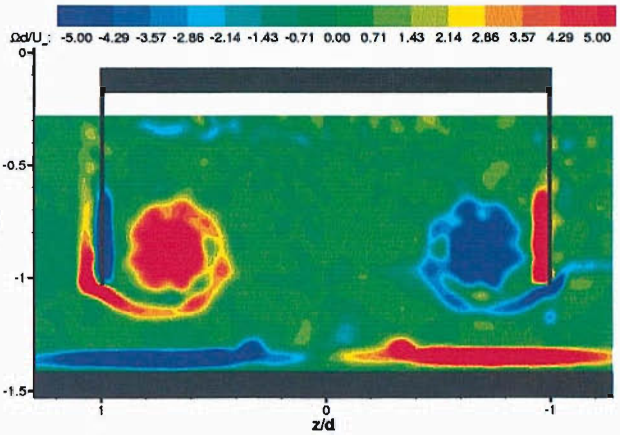

(e) x/d=7.74

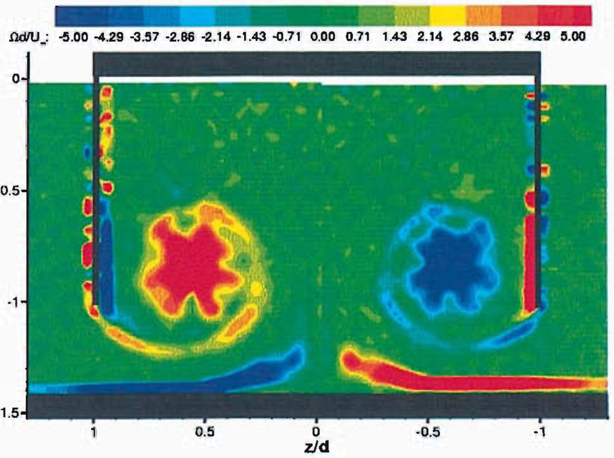

(f) x_1/d=0.096

Figure 31: Type A mean vortex flow: h_r/d=0.382 (PIV).

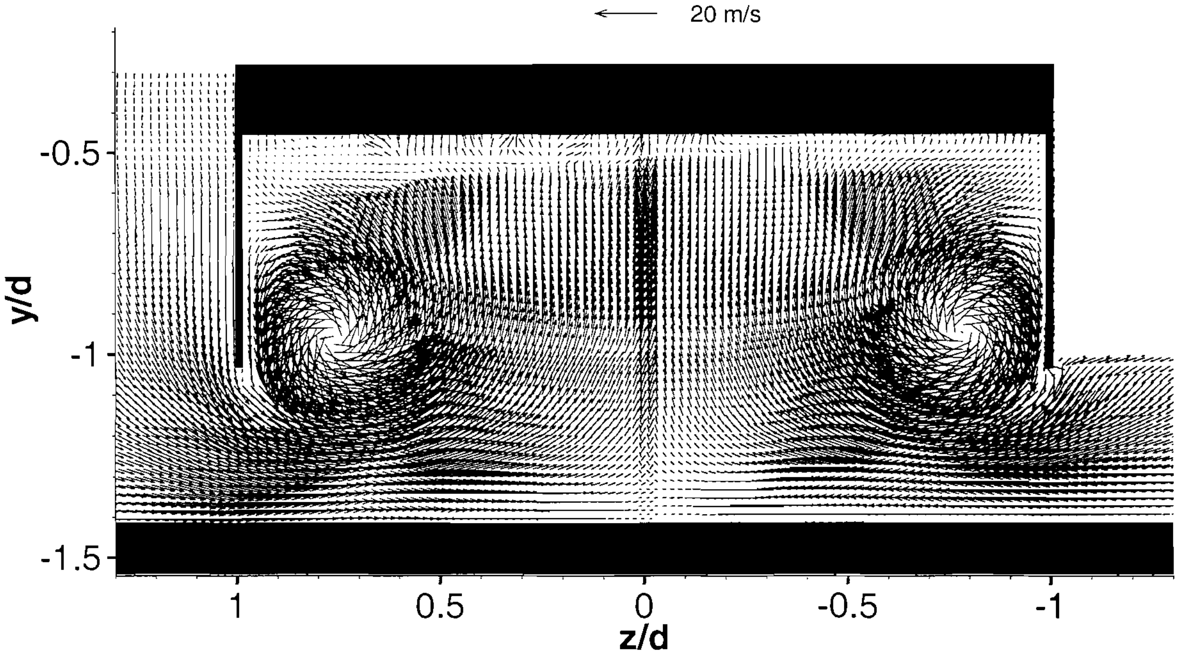

Figure 32: Type A cross-flow velocity vectors: h_r/d=0.382, x/d=6.83.

Figure 33: Type A surface flow at inner side-plate, h_r/d=0.382. Flow direction from top to bottom.

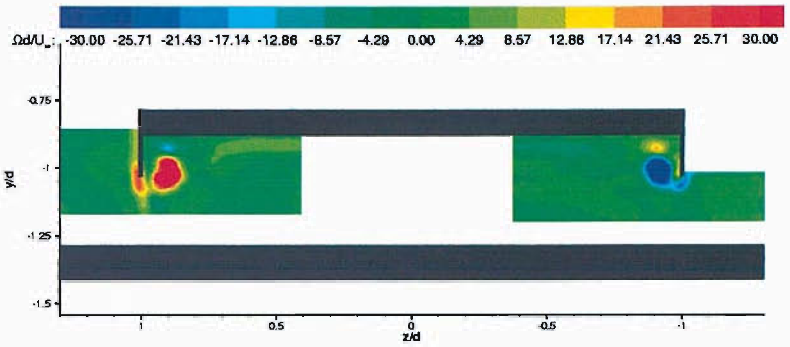

(a) x/d=5.44

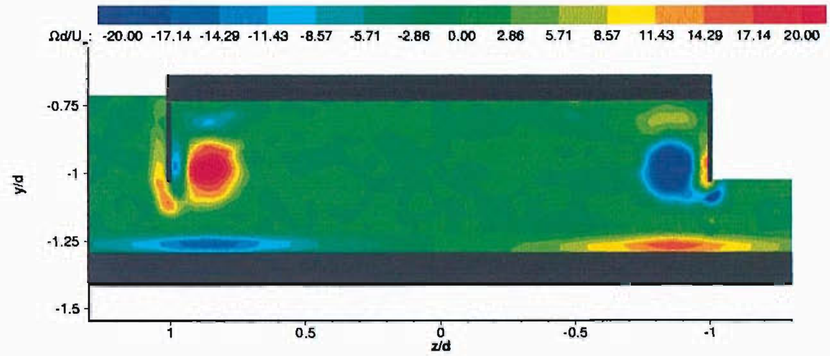

(b) x/d=5.91

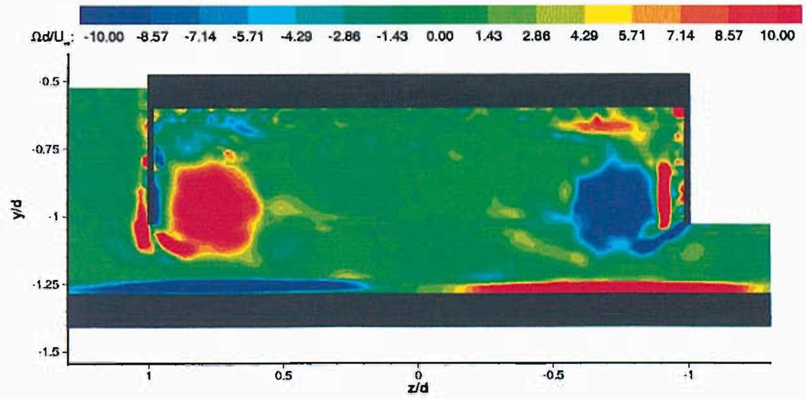

(c) x/d=6.37

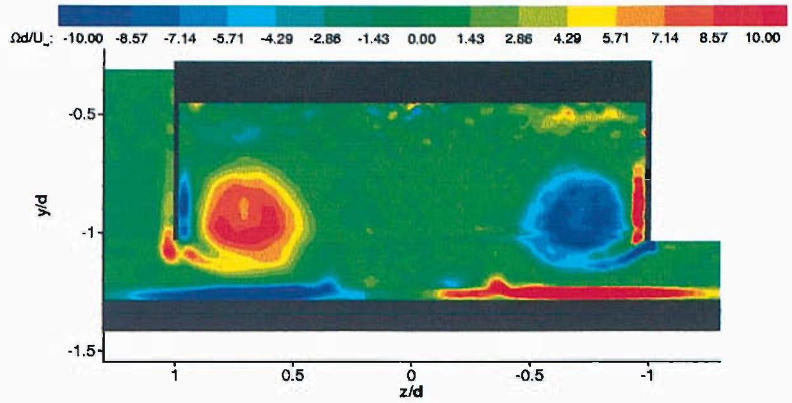

(d) x/d=6.83

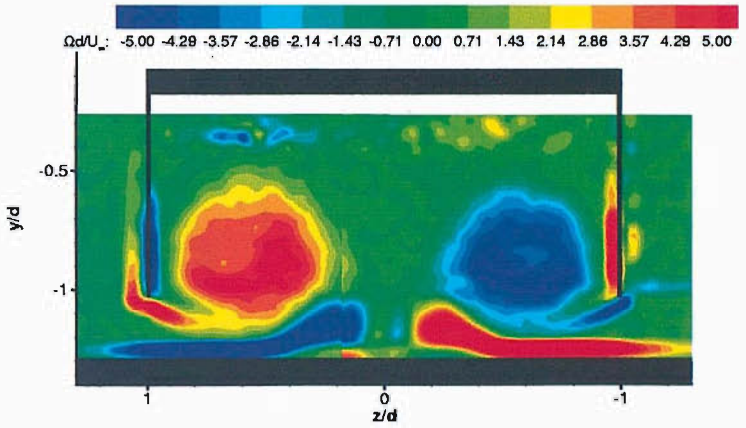

(e) x/d=7.74

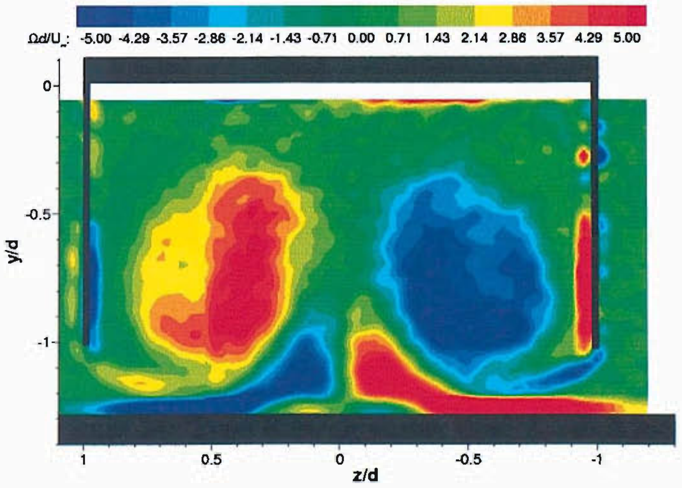

(f) x_1/d=0.096

Figure 34: Type B mean vortex flow: h_r/d=0.255 (PIV).

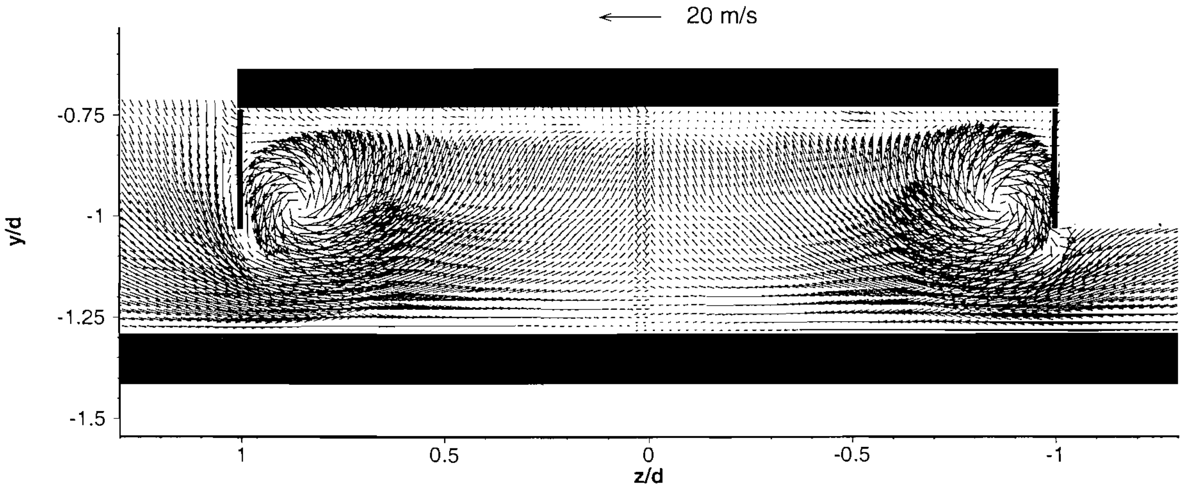

Figure 35: Type B cross-flow velocity vectors: h_r/d=0.255, x/d=5.91 (PIV).

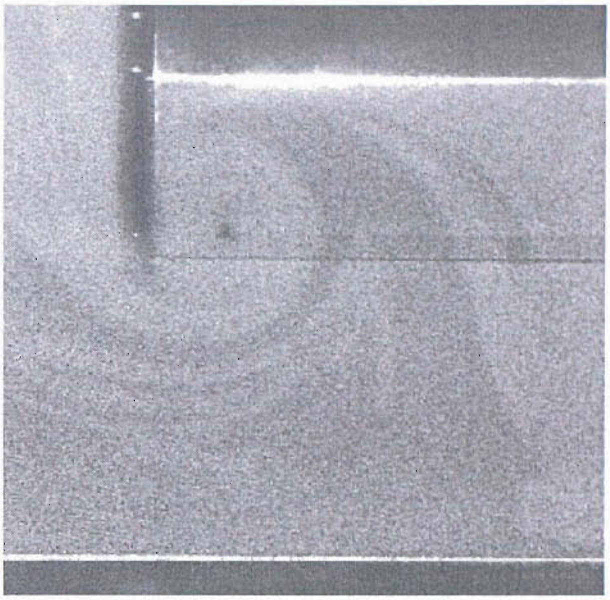

(a) x/d =5.44

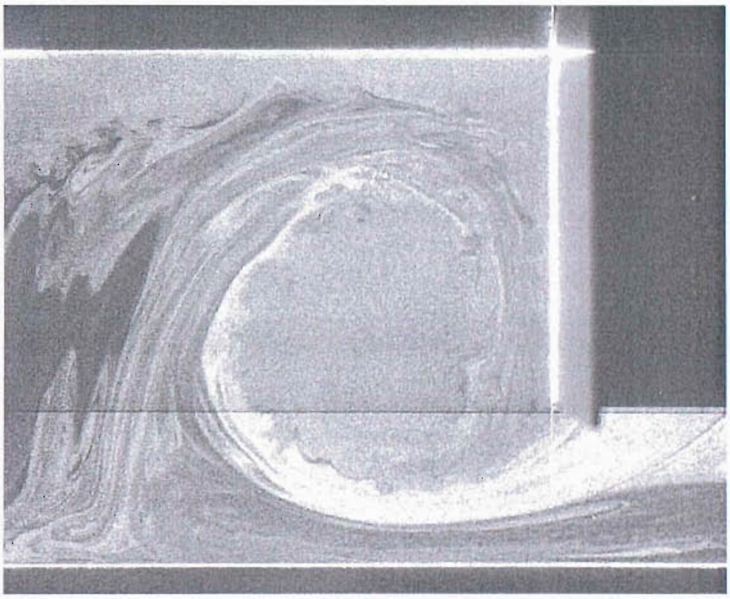

(b) x/d =6.83

Figure 36: Images of vortex flow inside diffuser.

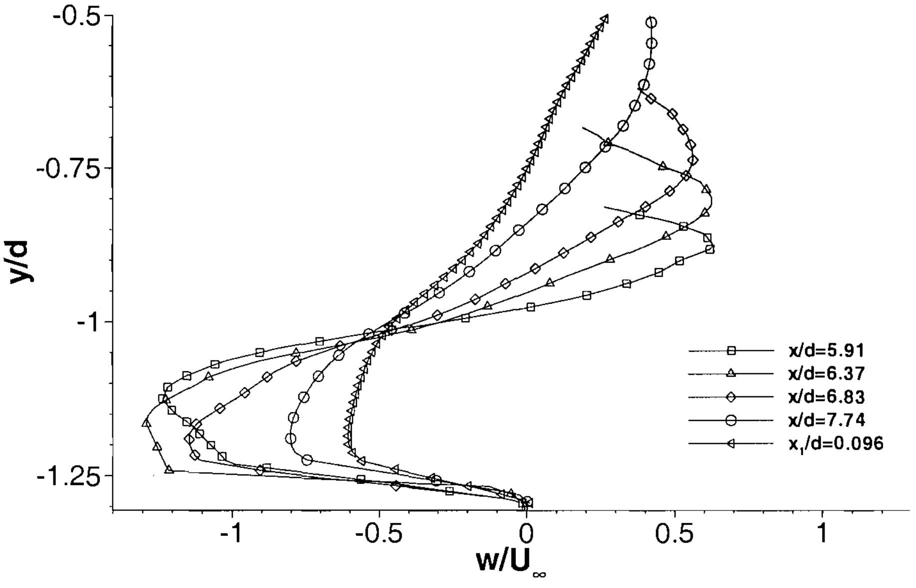

Figure 37: Spanwise velocity profiles at y/d position of lhs vortex centre (PIV).

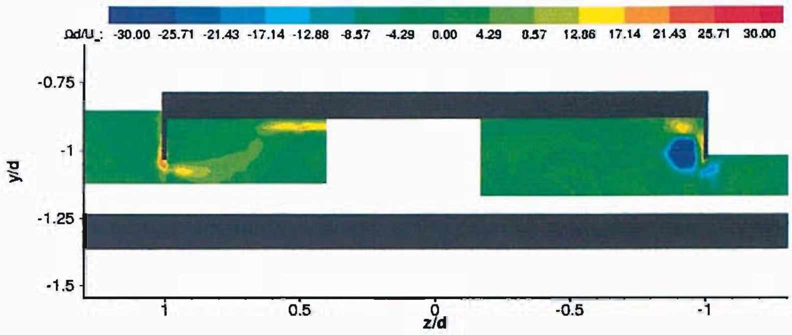

(a) x/d=5.44

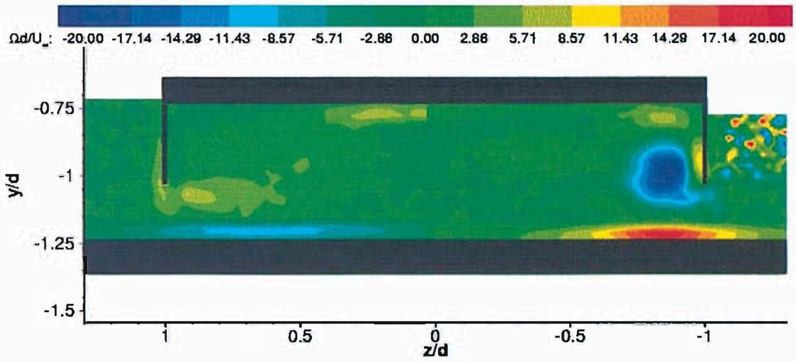

(b) x/d=5.91

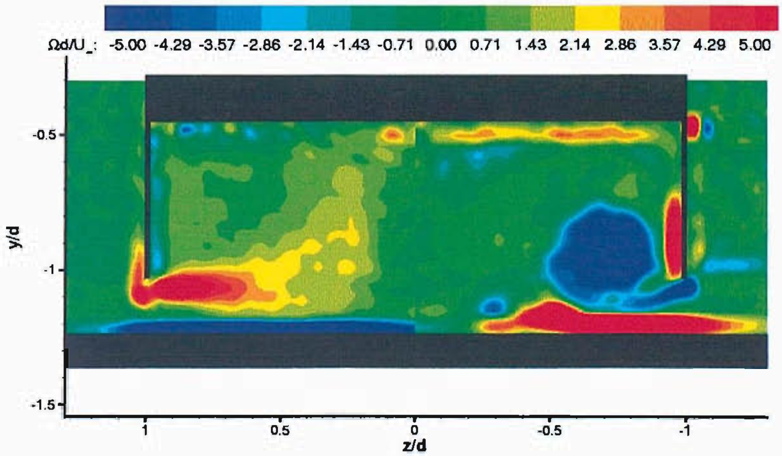

(c) x/d=6.83

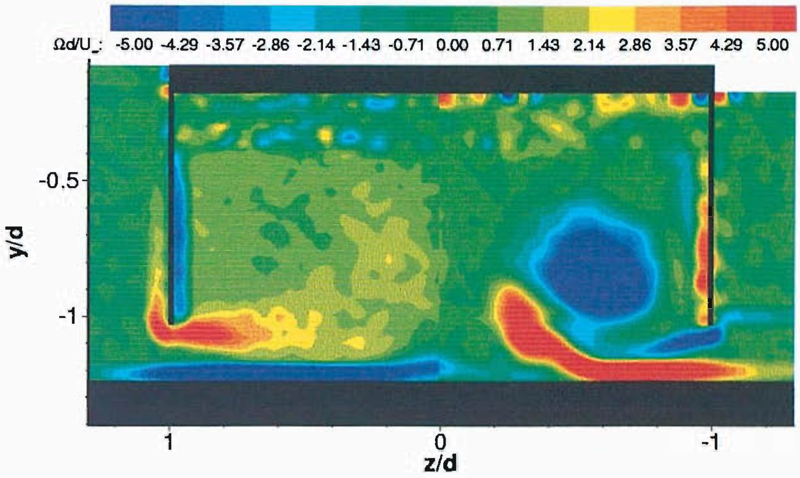

(d) x/d=7.74

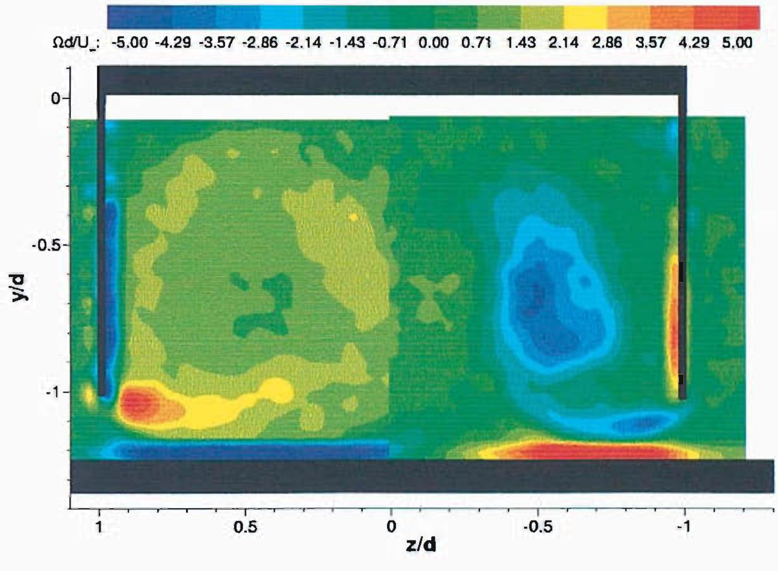

(e) x_1/d=0.096

Figure 38: Type C mean vortex flow: h_r/d=0.204 (PIV).

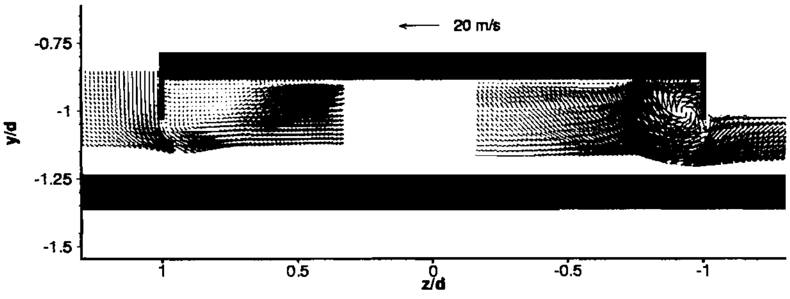

(a) x/d=5.44

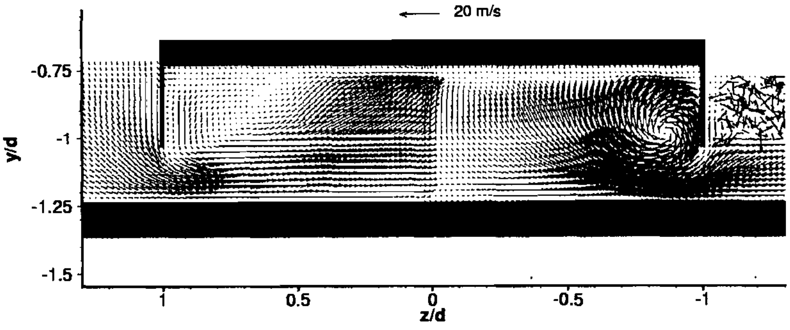

(b) x/d=5.91

Figure 39: Type C cross-flow velocity vectors: h_r/d=0.204 (PIV) .

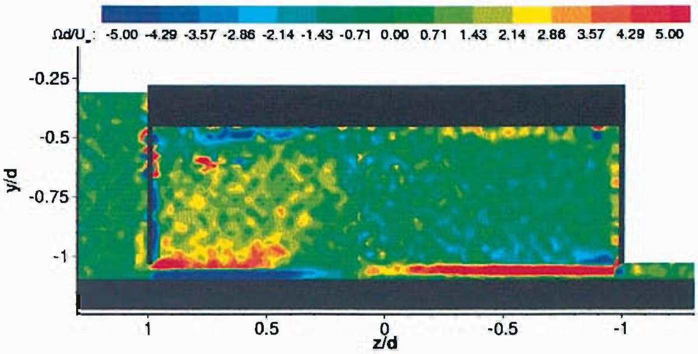

(a) x/d=6.83

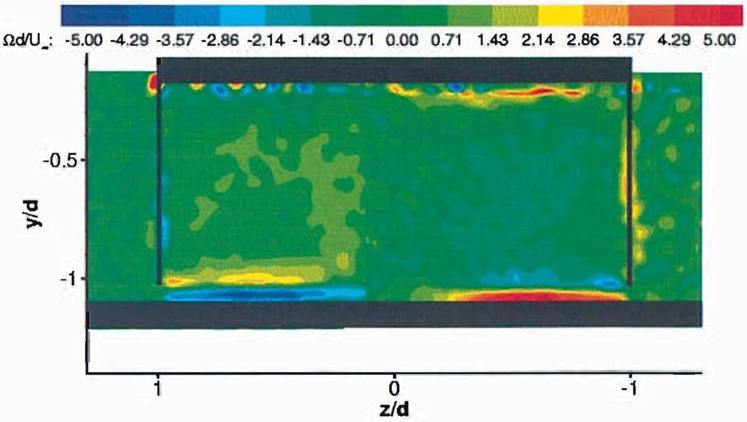

(b) x/d=7.74

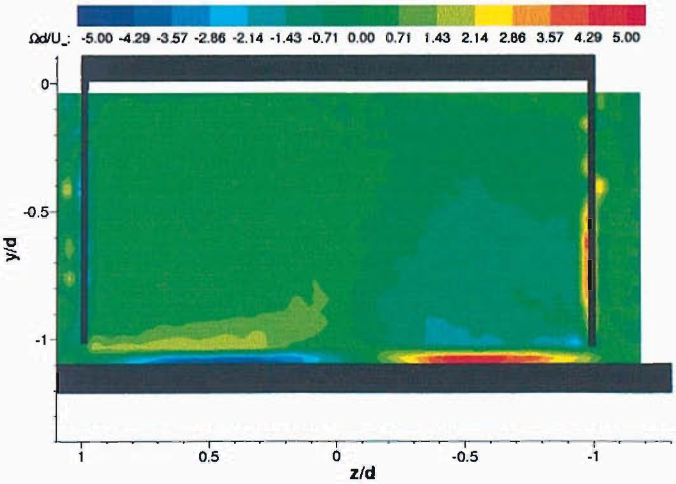

(c) x_1/d=0.096

Figure 40: Type D mean vortex flow: h_r/d=0.064 (PIV).

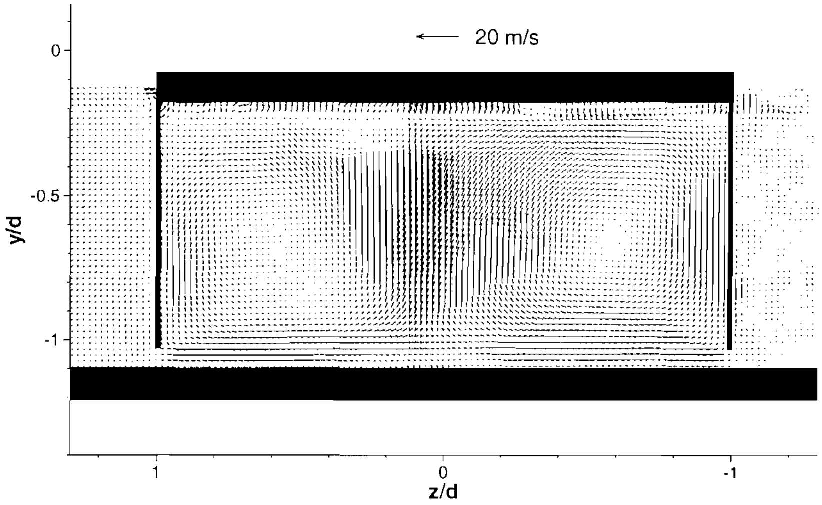

(a) x/d =7.74

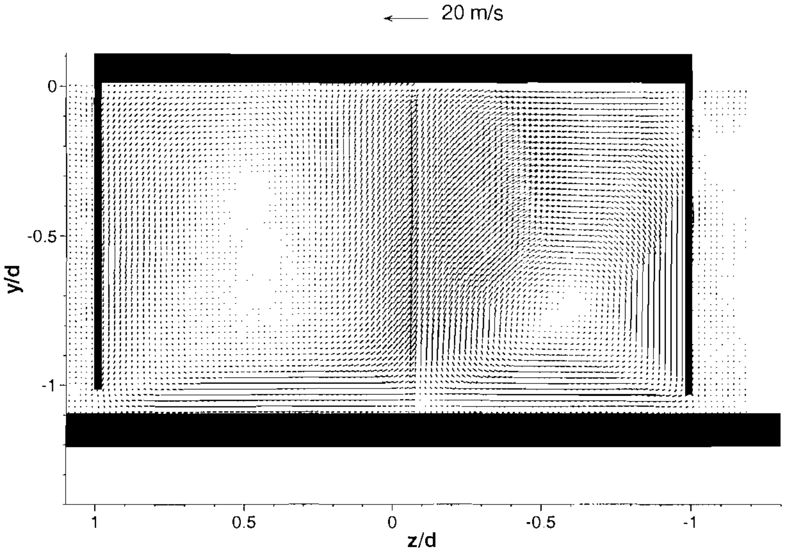

(b) x_1/d =0.096

Figure 41: Type D cross-flow velocity vectors: h_r/d=0.064 (PIV).

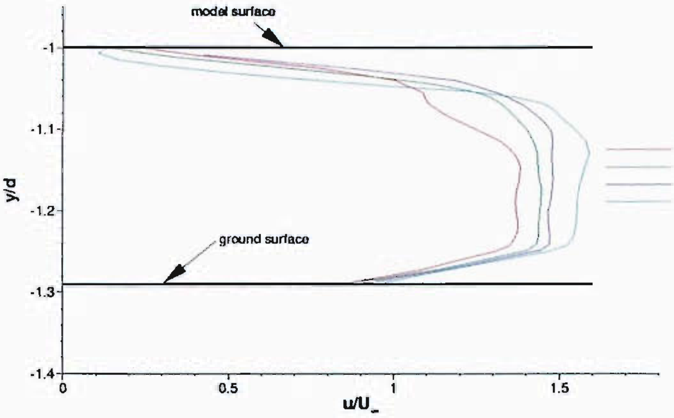

(a) z/d =0

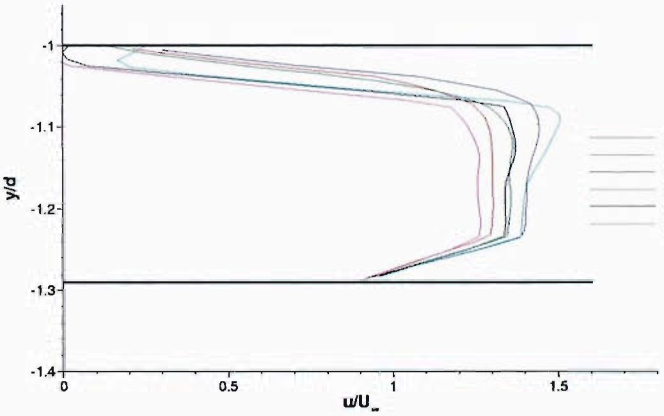

(b) z/d =-0.936

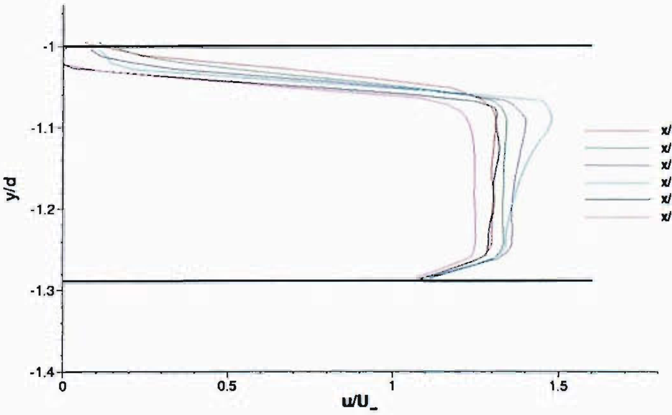

(c) z/d =0.936

Figure 42: Boundary layer flow underneath model: h_r/d=0.255 (PIV).

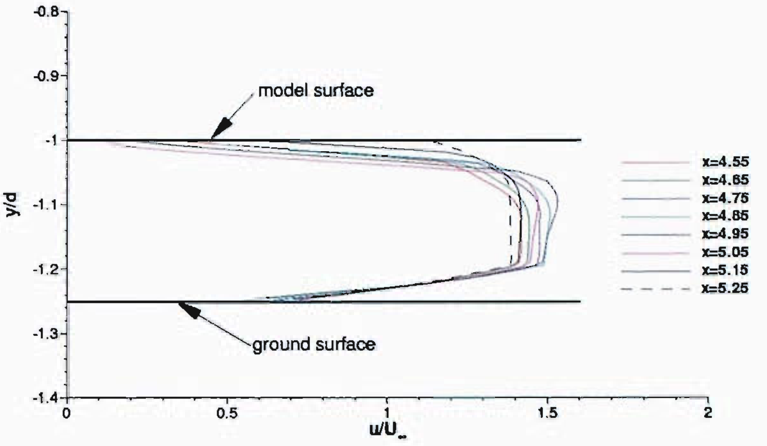

(a) z/d =0

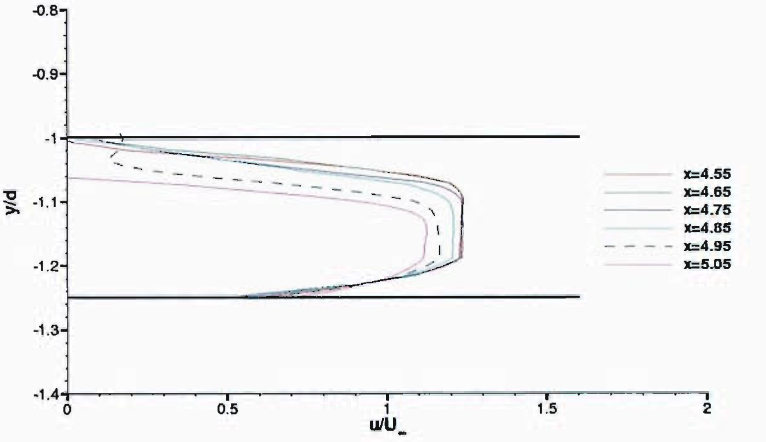

(b) z/d =-0.936

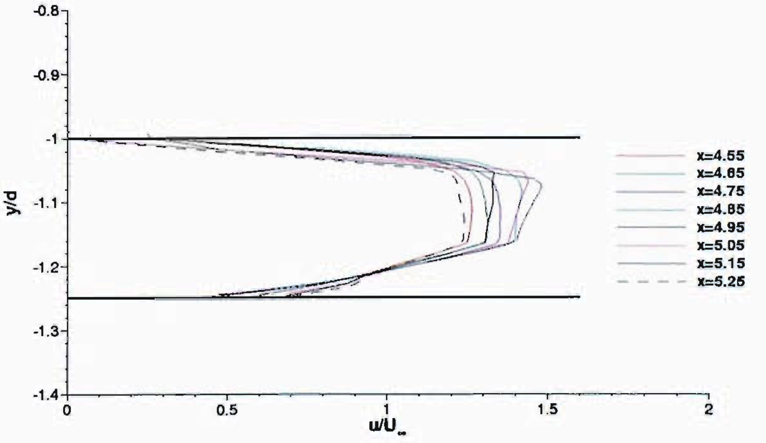

(c) z/d =0.936

Figure 43: Boundary layer flow underneath model: h_r/d=0.204 (PIV).

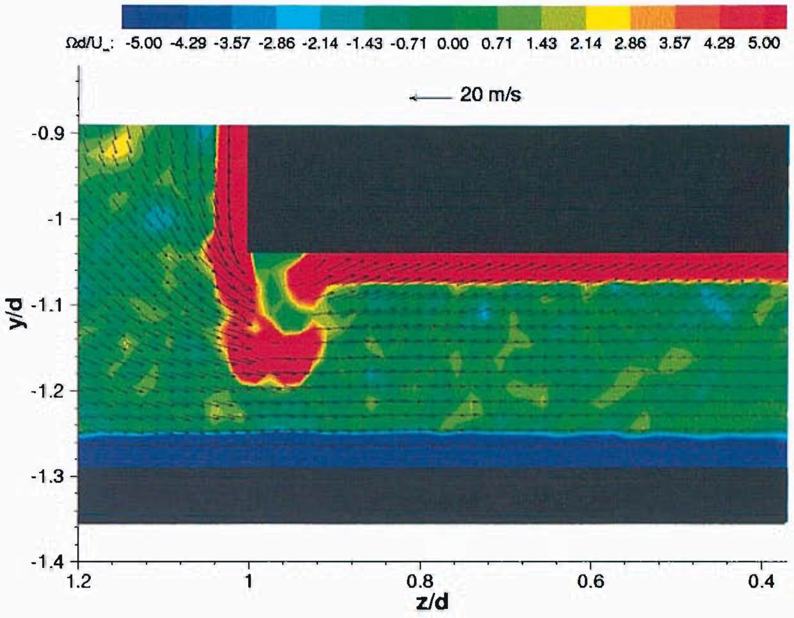

(a) h_r/d=0.255, x/d =4.95

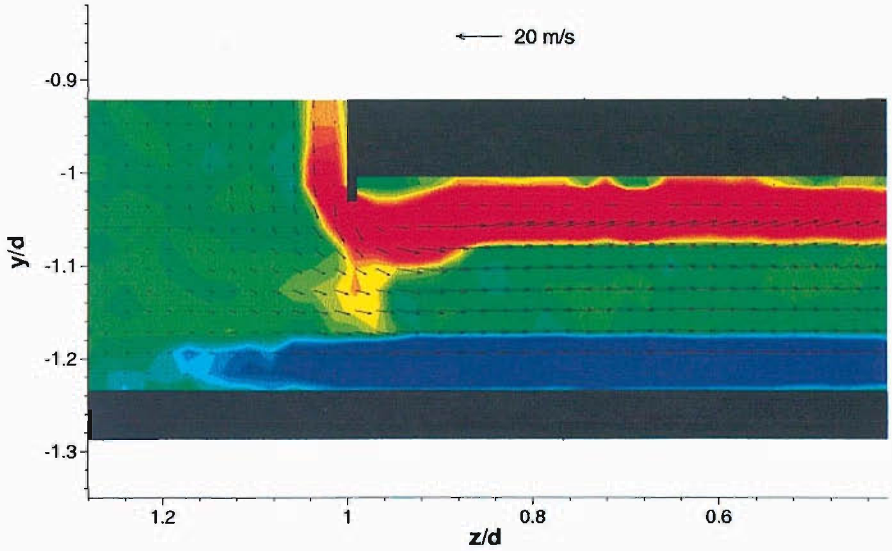

(b) h_r/d=0.204, x/d =5.064

Figure 44: Boundary layer flow at diffuser inlet (PIV)

Chapter 5

Time-Dependent Vortex Flow

The possibility of unsteady flow inside the diffuser was further investigated using PIV. The findings and their impact upon the performance of the diffuser are discussed in this Chapter. Results for each flow type are presented, before a discussion with regard to the possible causes of the mean flow diffusiveness. The consequences of these findings for the overall diffuser behaviour are discussed in Section 5.6.

5.1 Possible Causes of Vortex Diffusiveness

A correlation is sought between the diffusiveness of the mean vortex flow of flow types B and C and other features of the flow which may provide an understanding as to the behaviour of the diffuser at low ride heights. Several possible causes have been identified and are discussed below.

5.1.1 Kelvin-Helmholtz Instability

Two parallel flow streams of different velocities are susceptible to perturbations and, at a certain frequency may become unstable. Discrete vortices are shed from the streams and the vortices become paired. The mechanism is known as the Kelvin-Helmholtz instability. The instability was observed in the free shear layer of a delta wing as a series of discrete small vortices travelling in the shear layer around the main vortex [30]. The vortices were shed at a well defined frequency. During their convection through the shear layer, two vortices appear to roll around each other and merge into a single vortex, a process which is repeated, culminating in the main vortex. Any occurrence of the Kelvin-Helmholtz instability in the vortex shear layer will be apparent only in time-dependent data, and will be seen as a pairing of positive and negative sub-vortices within the vortex shear layer in the type B flow [91]. If the instability exists around the vortex it could contribute to the vortex unsteadiness.

5.1.2 Surface separation bubble

The oil flow visualisation of the type B surface flow revealed a separation bubble on the ramp surface. A correlation of the flow visualisation and the PIV data at h_r/d=0.255 shows that the bubble would be present in the flow at x/d =5.91 and x/d =6.37. The bubble is not apparent in the PIV data at the diffuser surface at either measurement plane. This is to be expected if the bubble is very thin; the resolution of the PIV measurements would not be sufficient to capture it.

However, the bubble at the surface is an unsteady flow separation since the point of separation from the surface is not fixed. The flow emanating from the bubble is therefore likely to be unsteady, giving rise to the possibility that it could affect the vortex flow. Flow from inside the bubble could cause a disturbance in the vortex core.

5.1.3 Shear layer interaction

An interaction of the shear layers at the base of the side-plate and at the ground could instigate a disturbance to the vortex, although the vortex diffusiveness begins some distance upstream of the shear layer merging. However the time-averaged flow could be masking instances of shear layer interaction further upstream of this location. Investigation of the instantaneous flow will confirm whether it is possible that shear layer interaction is a cause of the vortex diffusiveness.

5.1.4 Vortex breakdown

Although a definite criterion for the onset of vortex breakdown remains elusive, its presence is known to depend upon certain key factors; principally the ratio of the magnitude of the swirl and axial velocities (the Rossby number), and the pressure gradient imparted to the flow. Related factors include the confining geometry and boundary layer development along the geometry, and the upstream conditions. The steep pressure gradient imparted to the vortex inside the diffuser would cause a deceleration of the axial velocity. Lowering the model ride height increases the acceleration of flow entrainment underneath the side-plates and thus subsequently increases the swirl velocity component of the vortex. The combination would lead to a vortex core with a high swirl ratio that would be susceptible to breakdown [83].

5.2 Time Dependent Flow Inside the Diffuser: Type A

Figure 45 shows the left side vortex flow at three instances in time alongside the mean flow vorticity contours. The vortex core is coherent and concentrated in each of the instantaneous pictures. The vorticity levels at the core are 78.3, 62.9 and 65.2 in (a), (b) and (c) respectively (Table 15). These levels are higher than the mean flow vorticity of 50.3 (Table 14). Although the data contains a certain amount of noise, the small vortices of the shear layer are apparent as small concentrations of positive vorticity around the main vortex, and within the shear layer rolling up from the side-plate edge. The positions of the small-scale vortices appear to be consistent in each picture, indicating their steady presence within the flow. The main vortex core location is generally steady for the three instances, and compares well with the mean flow core location. The instantaneous values are within $z/d = \pm 0.0065$, and $y/d = \pm 0.043$ of the mean core location. The scatter in the y/d locations, although only amounting to a small movement of the vortex centre, is believed to account for the higher instantaneous vorticities compared to the mean vorticity.

Immediately downstream of the diffuser exit at $x_1/d = 0.096$, the vortex is still coherent, and the velocity vectors of Figure 46 illustrate how steady the vortex flow is in time. The shear layer instability remains visible in the instantaneous flow. Figure 47 (a) and (c) show seven identifiable secondary vortices around the main vortex core in similar positions to those shown in the mean flow contours, and Figure 47 (b) shows six secondary vortices. The six secondary vortices correlate spatially to the positions of the secondary vortices in figures 47 (a) and (c), and so it may be that the seventh vortex has been obscured in the data. With the exception of this discrepancy in the results, the consistent positions of the vortices in each figure confirms the spatially steady nature of the shear layer instability. The non-dimensional vorticity at the vortex core ranges between $\Omega d/U_\infty$=30.221 and $\Omega d/U_\infty$=37.718 for the results presented. The instantaneous vortex core locations are within $z/d = \pm 0.008$ and $y/d = \pm 0.008$ of the mean flow core position.

The shear layer separation at the ground however, appears to be an unsteady phenomenon. The spanwise flow of the ground boundary layer at x_1/d =0.096 (Figure 47) separates from the ground towards the centre plane of the diffuser, and in Figure 47 (c) an eddy has been shed from the shear layer. The point of separation from the ground changes at each time instant, indicating an unsteady separation. This is to be expected since there is no fixed point on the ground from which the boundary layer could separate, unlike at the side-plate edge which provides a definite point of separation for the shear layer.

Thus, in the type A diffuser flow, the instantaneous vortex flow is similar to the mean flow, and is generally steady. Unsteadiness appears in the shear layer flow at the ground towards the diffuser exit, however at this ride height the model is far enough away from the ground for the unsteadiness to have no tangible effect on the main vortex flow.

5.3 Time Dependent Flow Inside the Diffuser: Type B

At x/d =5.91 the vortex is coherent and concentrated (Figure 49). The instantaneous velocity vectors (Figure 48) indicate that the flow is mainly steady, and the locations of the vortex cores are consistent to within $z/d = \pm 0.01$ and $y/d = \pm 0.06$ of the mean flow core location.

However, this is more of a movement of the core than was measured in the type A flow, and signs of impending unsteadiness are visible in the vorticity contours (Figure 49). The value of instantaneous vorticity is slightly higher than the time-averaged value in Figure 49 (a), and is approximately 25% higher than the mean flow vorticity in Figures 49 (b) and (c). At x/d =6.37, the vortex has lost a considerable amount of its coherence. The vortex in Figure 50 (a) has become larger. The mean vorticity concentration of the vortex has diminished by over a third in a distance of only 80 mm from x/d =5.91 (Table 15). Accordingly, the levels of instantaneous vorticity in Figure 51 (a) are considerably weaker than they were at the previous measurement plane. This new feature in the vortex flow is an indication of unsteady flow in the vortex itself, and the effect is a reduction in the vortex concentration. The positions of the vortex cores presented in Figure 51 wander more on average than at x/d =5.91, ranging within $z/d = \pm 0.045$ and $y/d = \pm 0.047$ of the mean flow core location. The ground boundary layer is, at this stage of the diffuser, attached to the ground, and there is a distinct gap between the shear layer at the ground and that of the vortex flow (Figure 37).

At x/d =6.83, the mean flow vortex is large and diffusive, and this is borne out in the instantaneous data. The cross-flow velocity vectors are low speed and lacking a coherent form (Figure 52). The extent of the core displacements has increased to a range of $z/d = \pm 0.043$ and $y/d = \pm 0.105$ from the mean flow core location. The cores are dilated even further, indicating decreasing axial velocity at the core. Twin cores are present at some instants. The vortex concentration of the twin cores is variable, and the levels may be similar between the two cores or highly uneven; in Figure 53 (a) the vorticity of the primary core is 20.9, the level at the secondary core is only 5.9, however in Figure 53 (b) the vorticity levels are 15.8 and 14.1 respectively. Figure 53 (c) has a single core with a vorticity level greatly reduced from the previous measurement plane at x/d =6.37, see Table 15. In each of the instantaneous results presented, the vorticity levels are significantly higher than that of the time-averaged vortex flow, however the concentrations are in pockets with regions of low vorticity or vorticity of opposite sign in between. The small scale concentrations of instantaneous vorticity bear a distinct resemblence to the instantaneous vorticity contours downstream of vortex breakdown on a delta wing [18]. The boundary layer at the ground is thicker than at x/d =6.37, and the spanwise flow has begun to separate from the ground. From Figure 53 it is evident that the boundary layer separation is unsteady as at h_r/d=0.382, and gives rise to the shedding of pockets of fluid at periodic intervals.

Towards the diffuser exit, at x/d =7.74, the time dependent vortex flow is chaotic and diffuse. Cross-stream velocities in the flow are low (Figure 54), and the concentrations of vorticity are more sparsely scattered (Figure 55). The vortex core structure may be either single or twin core (Figure 54), and core locations are within $z/d = \pm 0.083$ and $y/d = \pm 0.134$ of the mean flow core position, thus the level of vortex core displacement is far higher than at

h_r/d=0.382. The ground shear layer is separated from the ground and sheds pockets of fluid into the shear layer rolling up to form the vortex. As seen in the time-averaged flow results, the ground and vortex shear layers have merged at this measurement plane and interact with each other.

5.4 Time Dependent Flow Inside the Diffuser: Type C

From the mean flow results it is evident that in the asymmetric type C flow, the remaining vortex is reduced in size as compared to that in the type B flow, and that at x/d = 6.83 the vortex appeared to retain its coherence and strength, in contrast to the vortex at h_r/d=0.255 which was large and diffuse at this stage of the diffuser. The velocity vectors of the instantaneous flow at h_r/d=0.204, x/d =6.83 (Figure 56) confirm that the vortex maintains its structure at this plane, however in some instances the core is beginning to show signs of unsteadiness (Figure 56 (b)). For the instants presented, the core locations differed by $z/d = \pm 0.022$ and $y/d = \pm 0.0133$ from the mean core position. The vorticity contours of Figure 57 give a clearer indication that the flow is becoming unsteady. The vorticity levels at the cores are at a similar level to the time-averaged value, however the vortex is distorted. The vorticity levels are much higher than in the type B flow measured at h_r/d=0.255 at this particular plane, indicating that whatever causes the vortex diffusiveness in the type B flow does not affect the type C flow until at least further downstream in the diffuser. Sarpkaya [83] suggested that if the boundary layer on a wall in close proximity to a vortex has separated, then the actual adverse pressure gradient seen by the vortex core is less than that which would have existed had there been no separation. The decrease in pressure gradient at the wall is reflected in a decrease in pressure gradient along the vortex core, therefore decreasing the tendency for the occurrence of vortex breakdown. Thus, the fact that there is a region of separated flow at the diffuser surface may relieve the pressure gradient imparted to the vortex and hence the type C vortex maintains its coherence where the type B vortex does not.

The ground boundary layer near the diffuser centre-plane is induced up toward the vortex near the centre-plane of the diffuser, and a pocket of vorticity is shed. It can be seen that the shear layers interact with each other at this plane, at an earlier stage than in the type B flow, probably due to the reduced ride height.

By x/d =7.74, the diffuser flow is more unsteady, although the vortex remains coherent to a large extent (Figure 58). The unsteadiness of the vortex makes it appear to be large in the mean flow velocity vectors (Figure 58 (d)), however the vorticity contours reveal that the vortex, although now slightly unstructured in the instantaneous flow, remains much smaller than at h_r/d=0.255. The concentrations of negative streamwise vorticity in Figure 59 are interspersed with pockets of much lower vorticity, and values at the cores are reduced significantly from the levels at x/d =6.83 (Table 15). The ground shear layer is separated and the secondary vortex created in the ground shear layer is visible at each time instant.

5.5 Discussion

The PIV data presented in this Chapter has helped to illuminate the reasons for the vortex diffusiveness of the type B diffuser flow. Unsteadiness in the flow is apparent from the high level of core displacement, particularly in comparison with the type A flow. Of the four possible causes identified for the vortex diffusiveness, three may be analysed through the use of the instantaneous data; the possibility of the unsteady Kelvin-Helmholtz (K-H) instability in the vortex shear layer, the extent of the interaction between the vortex and ground shear layers, and the possible vortex breakdown inside the diffuser.

The K-H instability would be identifiable by the occurrence of secondary vortex pairing within the vortex shear layer of positive and negative regions of vorticity [91]. Based upon the present data, there is no evidence in the results at h_r/d=0.255 to support the presence of the instability.

Separation of the ground boundary layer occurs with an inherently moving, unsteady point of separation. Thus part of the shear layer at the ground becomes unsteady. For the ride height of h_r/d=0.204, the vortex unsteadiness begins to appear as the shear layers springing from the side-plates and the ground begin to merge. The boundary layers are merging at x/d = 6.83 at h_r/d=0.204, however at h_r/d=0.255, merging does not occur until x/d =7.74. The exact location of the merging is at a plane in between the measurement planes presented, however it is evident that boundary layer merging occurs earlier in the diffuser at h_r/d=0.204 than at 0.255. At h_r/d=0.255, separation of the ground boundary layer has occurred at x/d =6.83, an unsteady point of separation. Thus the part of the ground shear layer that continues to be induced upwards around the vortex is unsteady, and will interact with the vortex shear layer. The vortex unsteadiness is first measured at x/d =6.37, up to 80 mm upstream of the first measured sign of shear layer separation and even further upstream of shear layer merging. It is for this reason that shear layer interaction is thought not to be the main cause of the vortex diffusiveness. However, it is possible that it makes a contribution to the flow unsteadiness in the later part of the diffuser.

The separation bubble at the diffuser surface in the type B flow is also an unsteady separation, having no fixed point of separation or reattachment. Although it is expected that the bubble is quite thin, the region of fluid seen periodically on the moving ground during oil flow visualisation experiments appears to be fluid from the bubble touching the belt (Figure 60). The fluid lies between the vortex tracks and has a similar size and shape to the bubble as seen on the diffuser surface. If the fluid in Figure 60 is from the surface bubble, then it is possible that unsteady fluid emanating from the bubble is induced into the vortex flow, contributing towards the flow unsteadiness.

The vortex unsteadiness is most likely to be caused by vortex breakdown occurring inside the diffuser. The pressure gradient imparted to the vortex pair increases through flow type A as the model is lowered to the ground. The pressure gradient decelerates the axial velocities inside the diffuser whilst, at the same time, flow is increasingly accelerating underneath the side-plates due to the low pressure inside the diffuser created by 'diffuser pumping'. At the onset of type B flow, the balance between the strong swirl component of the vortex, the reducing axial component and the pressure gradient imparted to the vortex reaches a critical level, and breakdown of the vortex core occurs. The breakdown appears to occur in both vortices simultaneously or at least close together. At h_r/d=0.318 (Figure 26 (c)), the position of breakdown is possibly downstream of the diffuser exit, as the pair of vortices are not dilated to the extent that they are at h_r/d=0.255 (Figure 26 (d)). In the early stage of vortex development at h_r/d=0.255 the vortex is similar to a type A vortex, strong and coherent. The development of the vortex at h_r/d=0.255 reveals a sudden dilation of the vortex core at x/d =6.37, and it is only then and thereafter that the flow is unsteady, and that the vortex is greatly reduced in concentration. The streamwise velocities measured at the core in the flow exiting the diffuser decrease through flow type B, and at h_r/d=0.255 reverse flow is recorded (Figure 26 (d)). The combination of this pronounced axial velocity deficit, sudden vortex dilation and unsteady flow occurring in a vortex flow governed by steep adverse pressure gradients and high swirl velocities provides the basis for the conclusion that the vortex diffusiveness seen in the type B flows is due to a breakdown of the counter-rotating vortices inside the diffuser. The occurrence of vortex breakdown would explain the apparent displacement of the maximum vorticity from the vortex centre in type A vortices to a position within the shear layer in type B flow 34 (d)-(f). Once the vortex has broken down it loses so much strength that the vorticity in the bounding shear layer is of a higher concentration than that in the burst vortex.

For the type C vortex, the streamwise velocities at the core are higher than those of the type B vortices (Table 13). The core velocities at h_r/d=0.204 and 0.159 are low but are not as close to stagnation as at h_r/d=0.255 and 0.217. The vortex at h_r/d=0.204 is unsteady towards the diffuser exit, yet it maintains its coherence through the diffuser. Surface pressure coefficients at the ramp surface above the remaining vortex have indicated a stronger suction in type C flow than occurs in either type B or type A flow (Figure 17). Thus it may be surmised that vortex breakdown does not occur inside the diffuser in the type C vortex at h_r/d=0.204. It may occur further downstream of the diffuser exit. This possibility is considered in Chapter 6.

5.6 Further Discussion of Diffuser Behaviour

In Chapter 3, the four types of flow in ground effect were identified, each type distinguished by the gradient of the down-force curve. The diffuser flow field was found to be characterised by vortex flow, the nature of which altered for each flow type. The characteristics of the vortex flow and hence the flow type is determined by the pressure gradient inside the diffuser, and this in turn is dependent upon the proximity of the diffuser to the ground and upon the angle of the diffuser; i.e. the flow type is largely determined by the area ratio of the diffuser.

As model ride height is reduced within flow types A and B, the down-force on the model is enhanced by the increased pumping of air through the diffuser and, for flow type A and early type B by the strength of the vortices. In type A flow the vortices lie near the side-plate lower edge and occupy a limited fraction of the diffuser exit area. Thus the flow through the diffuser is unobstructed from the inlet to the exit. The result is down-force enhancement through type A, and the diffuser functions well to convert kinetic energy into static pressure rise.

In type B flow, vortex breakdown was established at the exit and also inside the diffuser (as evident in the PIV measurements at h_r/d=0.255). Based upon the low core velocities in the exit flow at h_r/d=0.318 (Figure 26 (c)) it is surmised that the vortex breakdown first occurs in the vortices at the onset of type B flow, as the down-force curve gradient reduces.

The adverse pressure gradient inside the diffuser becomes steeper as the model ride height is reduced. Accordingly, it is expected that breakdown creeps further upstream inside the diffuser as the model ride height is reduced through type B flow. Thus it is likely that the vortex breakdown at h_r/d=0.255 occurs further upstream in the diffuser than it does at h_r/d=0.318.

Once the vortices have broken down or are heading towards breakdown, they dilate and they occupy a much larger fraction of the diffuser cross section. This reduces the effective area ratio of the diffuser, and consequently less flow is drawn through the diffuser. As a result, the down-force continues to increase through type B flow albeit at a much slower rate than in type A flow (Figure 9 (a)).

Type B flow is terminated by the breakdown at the diffuser inlet of one of the vortices. The data and discussion of Chapters 3 and 4 show that boundary layer merging is not the cause of the diffuser stall. It is surmised that the location of vortex breakdown moves towards the inlet as ride height is reduced through type B flow, and that at the critical ride height one of the vortices breaks down at the inlet. The reason for the asymmetry of the vortex breakdown at the inlet may also be surmised. Through type B flow, one vortex was found to be slightly stronger than the other (Table 13). It is expected that the weaker vortex breaks down fractionally ahead of the stronger vortex, and that this trend persists until the point of breakdown in this vortex reaches the inlet. Such asymmetry in a symmetric flow is also a characteristic of the stall regimes of internal diffuser flows, in which stall first occurs at one diverging wall only [52]. With the breakdown of one vortex at the inlet, the pressure gradient in the remainder of the diffuser is relieved, and thus the remaining type C vortex retains its strength and coherence. The coherence of the vortex reduces obstruction of the flow through one side of the diffuser, and the localised down-force that this produces is evident in Figure 17. However, the large scale separation of the remainder of the inlet flow causes an obstruction to the through flow. Consequently, overall down-force levels on the diffuser reduce sharply.

Through type C flow, the inlet separation becomes larger and the type C vortex retains its coherence to a large extent at h_r/d=0.204. With reducing ride height the vortex occupies a smaller fraction of the diffuser cross section. The presence of the vortex is not sufficient to offset the reduction in flow from the inlet to the exit and hence down-force reduces.

It must be noted that the angle of divergence of the present diffuser is steep. Down-force reduction is caused by a pressure gradient mechanism, however it may be that for diffusers of a lower angle in which the pressure gradient is lower, that the loss of down-force is caused by a different mechanism, and could therefore be due to boundary layer merging at the inlet.

5.7 Summary

Measurements of the instantaneous flow inside and exiting the diffuser revealed further characteristics of the vortex flow. The symmetric type A flow (down-force enhancement) is steady. Type B flow (maximum down-force) becomes diffuse and unsteady at an early stage inside the diffuser. The type C vortex becomes unsteady towards the diffuser exit although it retains its coherence through most of the diffuser. Type D instantaneous flow was not measured. The vortex diffusiveness and unsteadiness in type B flow is most likely to be caused by vortex breakdown occurring in the vortices inside the diffuser. Minor contributions occur from the ground boundary layer separation and consequent merging of the ground and vortex shear layers, and perhaps to a lesser extent from the unsteady surface separation bubble. No vortex breakdown is thought to occur inside the diffuser in the type C flow at h_r/d=0.204. The down-force reduction on the model is thought to be caused by the breakdown of one vortex at the inlet of the diffuser, the result of which is a large zone of reversed flow causing a blockage inside the diffuser.

h/d	x/d	y_c/d		z_c/d		$\Omega_c d/U_\infty$	
		ls	rs	ls	rs	ls	rs
0.204	6.83		-0.943		-0.738		-24.2
0.204	6.83		-0.942		-0.747		-28.2
0.204	6.83		-0.952		-0.739		-27.3
0.204	7.74		-0.829		-0.519		-8.8
0.204	7.74		-0.837		-0.617		-16.1
0.204	7.74		-0.831		-0.566		-16.3
0.255	5.91		-0.994		-0.876		-25.0
0.255	5.91		-0.980		-0.871		-31.0
0.255	5.91		-0.989		-0.862		-31.1
0.255	6.37	-0.967		0.808		18.9	
0.255	6.37	-0.905		0.770		12.6	
0.255	6.37	-0.947		0.819		26.9	
0.255	6.37	-0.970		0.729		31.6	
0.255	6.83	-0.924		0.709		5.9	
0.255	6.83	-1.025		0.609		20.9	
0.255	6.83	-0.875		0.670		15.8	
0.255	6.83	-0.984		0.604		14.1	
0.255	6.83	-0.934		0.742		17.5	
0.255	7.74	-0.922		0.548		9.9	
0.255	7.74	-0.842		0.554		4.5	
0.255	7.74	-0.859		0.599		8.2	
0.255	7.74	-0.4491		0.713		14.0	
0.255	7.74	-0.823		0.638		12.9	
0.382	6.83	-0.939		0.755		78.3	
0.382	6.83	-0.950		0.767		62.9	
0.382	6.83	-0.948		0.762		65.2	
0.382	x_1=0.096	-0.852		0.557		33.4	
0.382	x_1=0.096	-0.846		0.556		30.2	
0.382	x_1=0.096	-0.843		0.554		37.7	

Table 15: PIV Cross-plane instantaneous vortex flow inside diffuser.

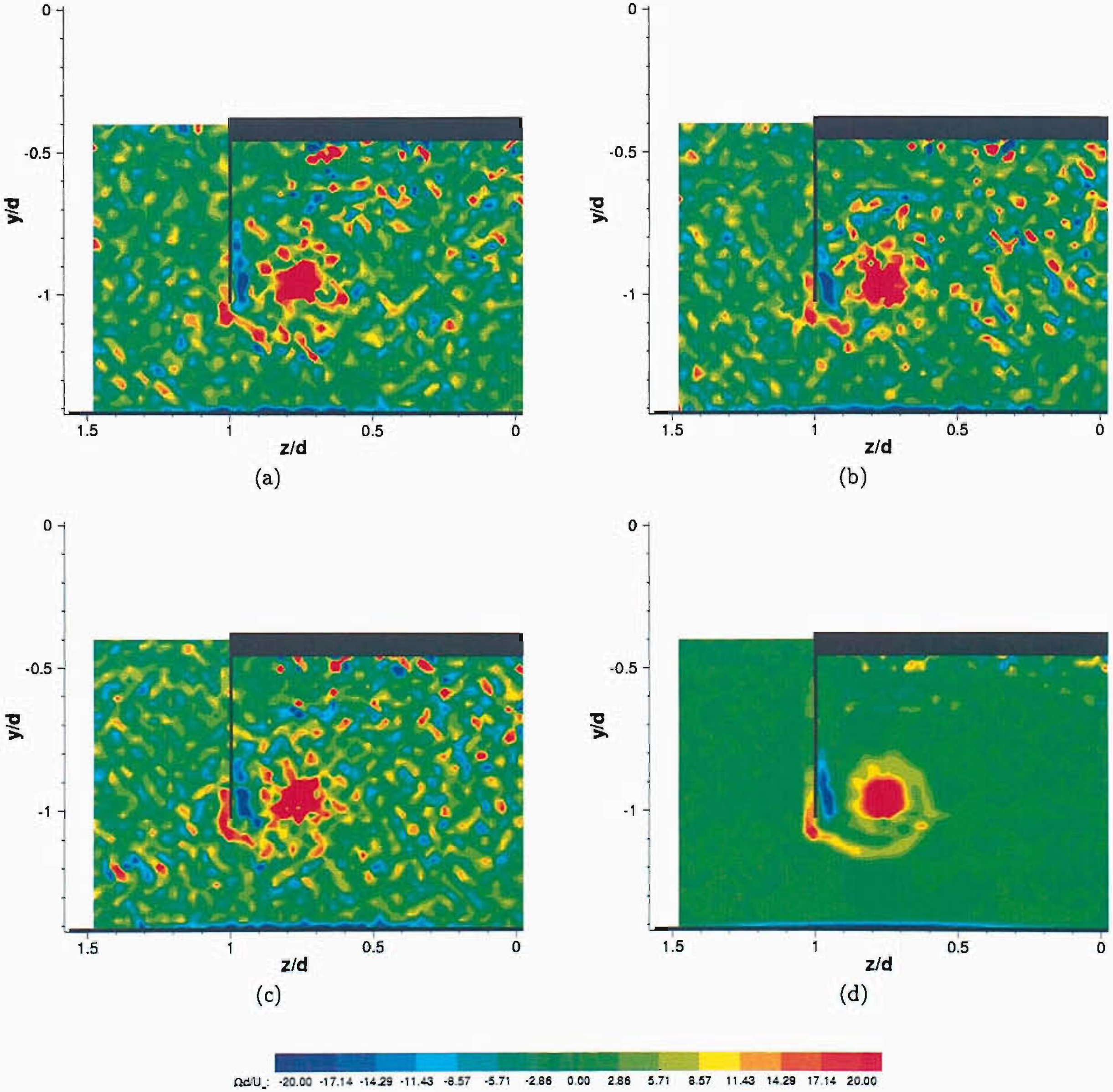

Figure 45: Instantaneous vorticity contours at x/d =6.83 in a Type A flow, h_r/d=0.382 (PIV).

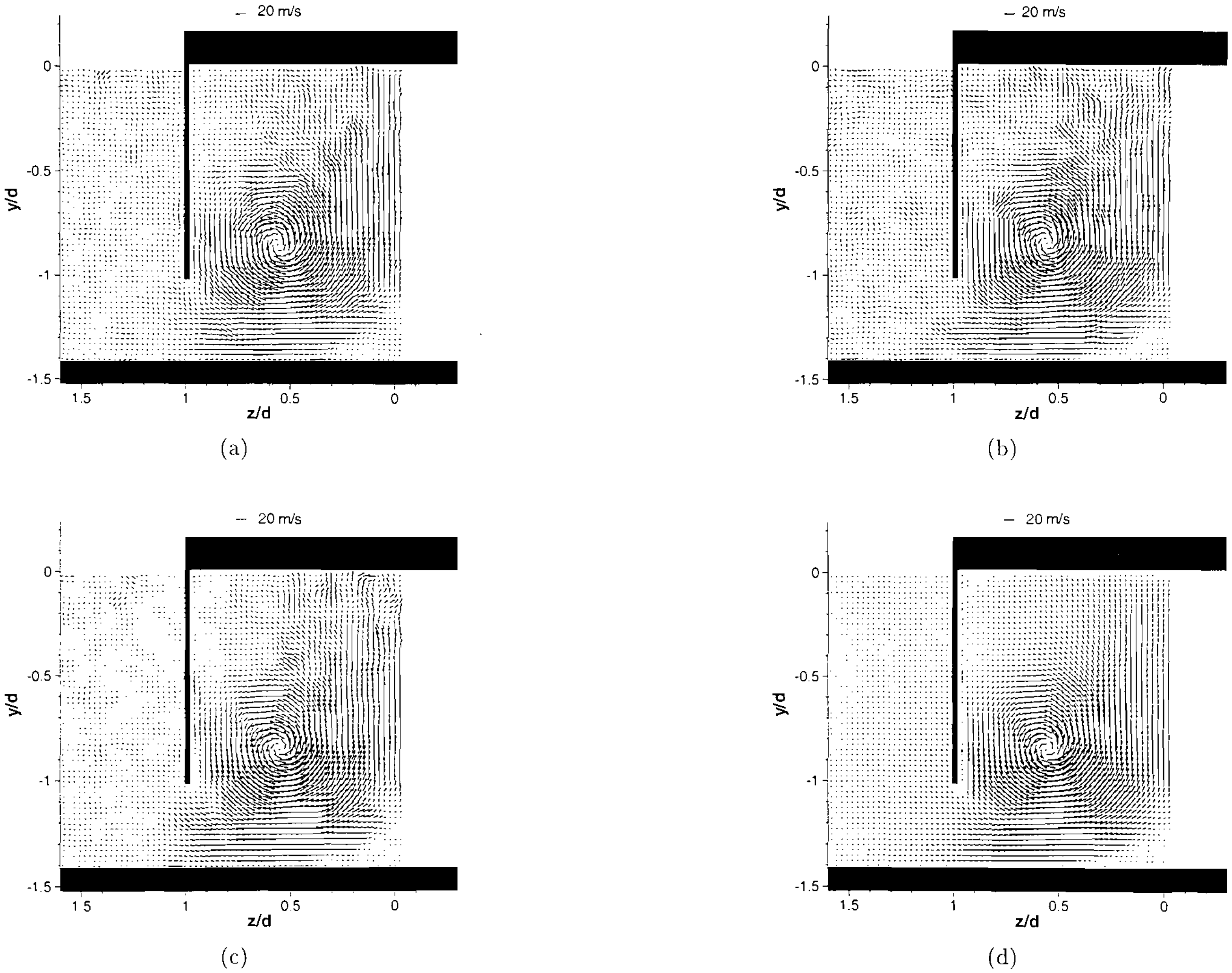

(a)

(b)

(c)

(d)

Figure 46: Instantaneous velocity vectors at x_1/d =0.096 in a Type A flow, h_r/d=0.382 (PIV).

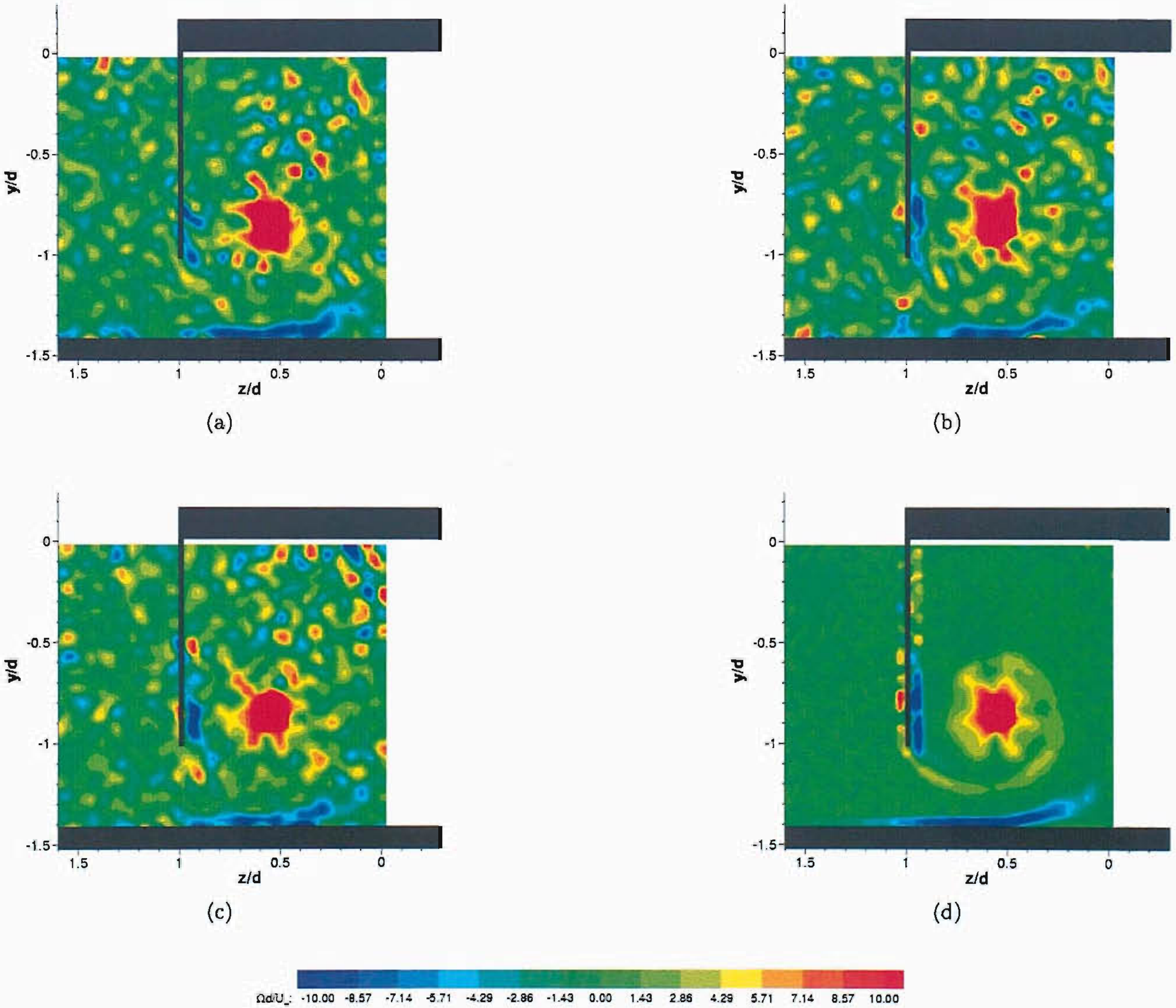

Figure 47: Instantaneous vorticity contours at x_1/d =0.096 in a Type A flow, h_r/d=0.382 (PIV).

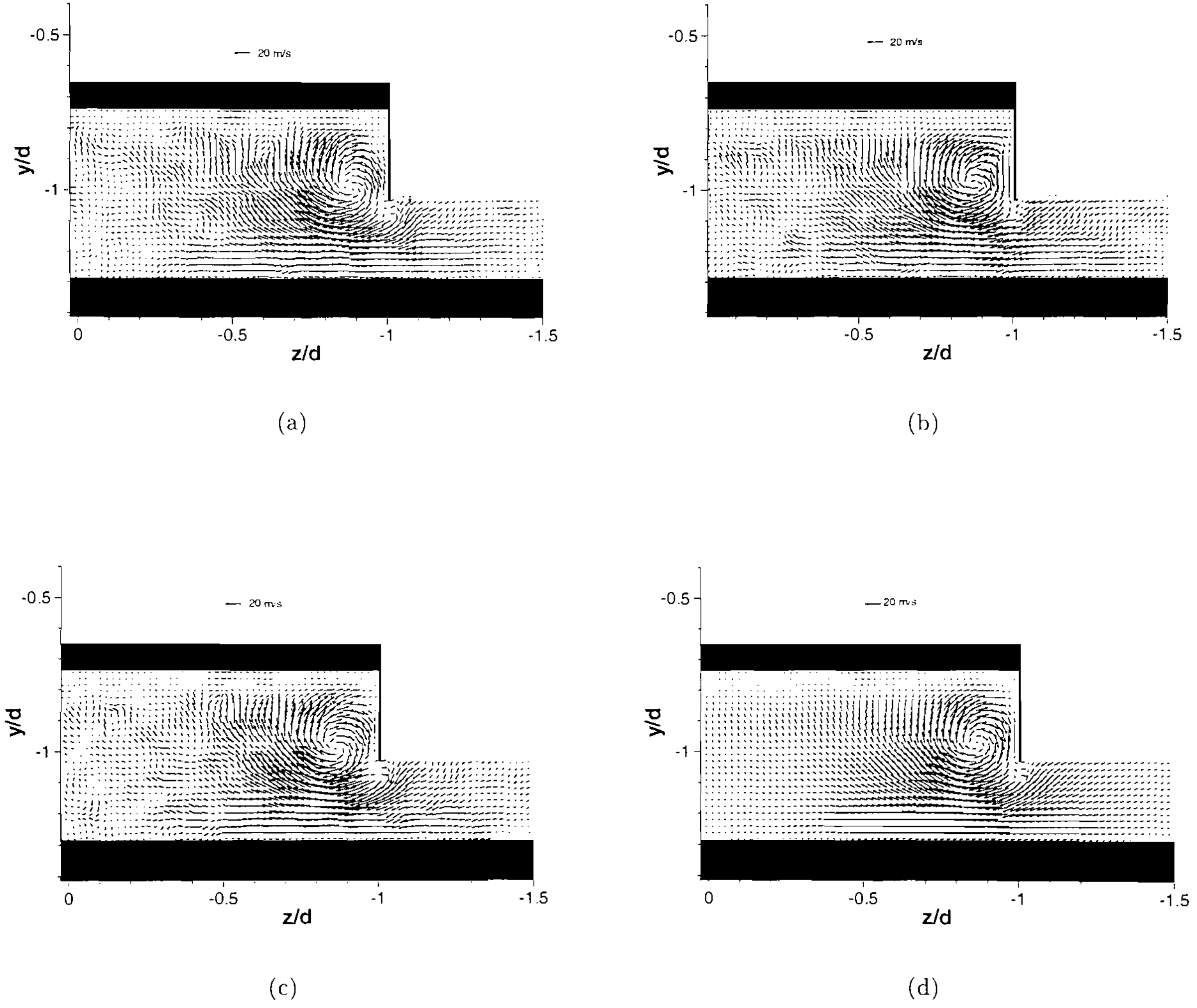

(a)

(b)

(c)

(d)

Figure 48: Instantaneous velocity vectors at x/d =5.91 in a Type B flow, h_r/d=0.255 (PIV).

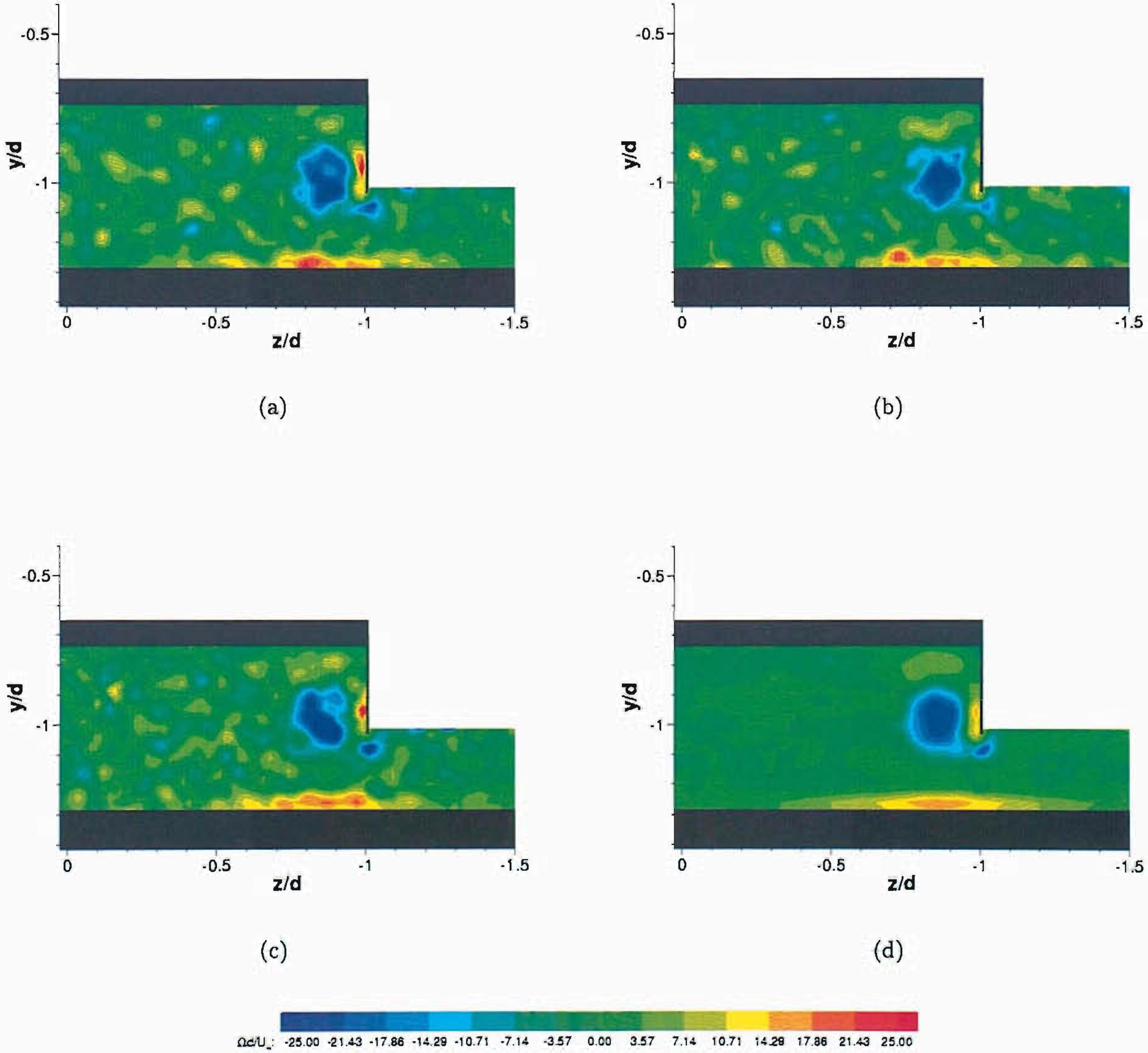

(a) (b)

(c) (d)

Figure 49: Instantaneous vorticity contours at x/d =5.91 in a Type B flow, h_r/d=0.255 (PIV).

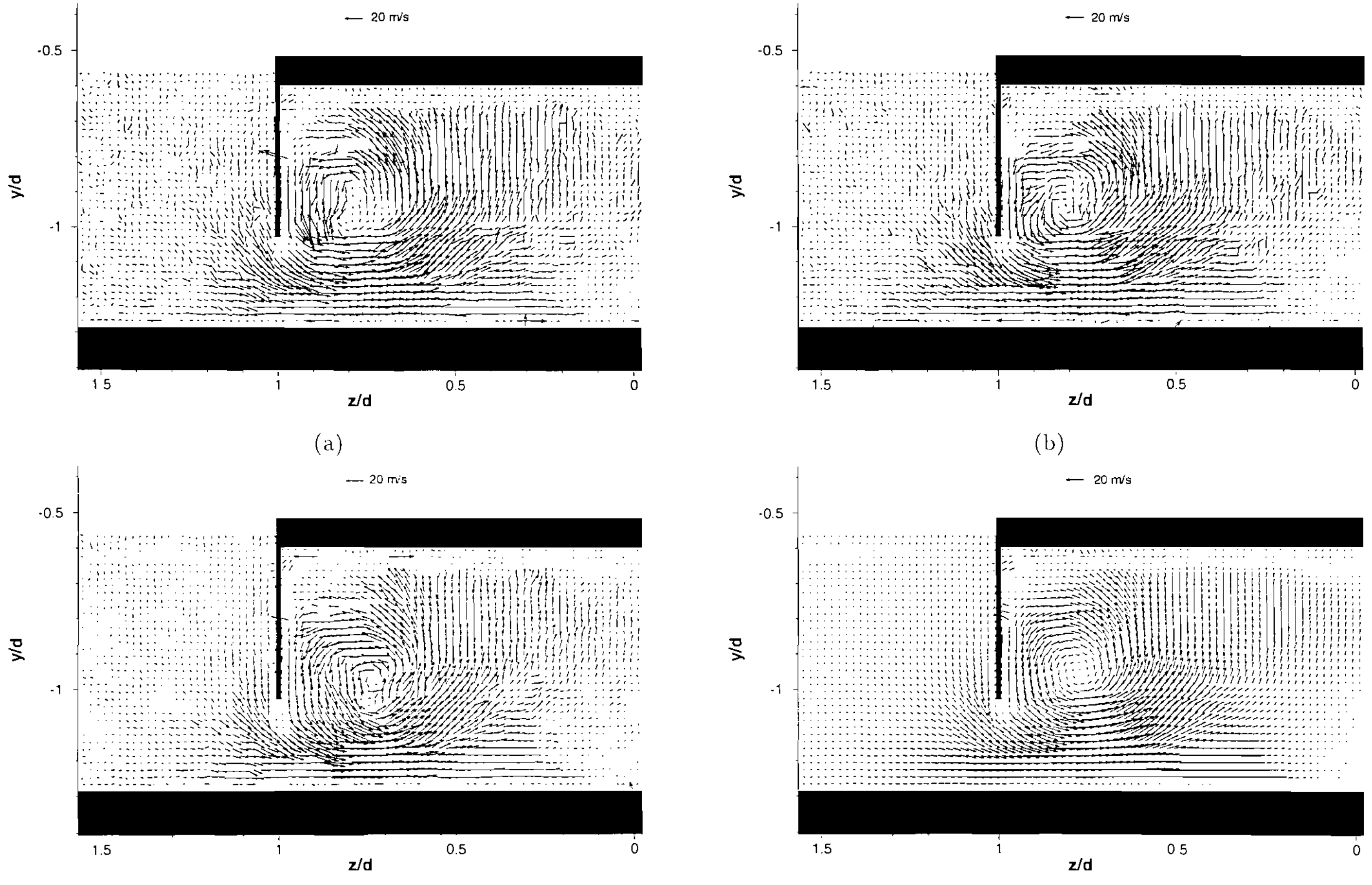

(a)

(b)

(c)

(d)

Figure 50: Instantaneous velocity vectors at x/d =6.37 in a Type B flow, h_r/d=0.255 (PIV).

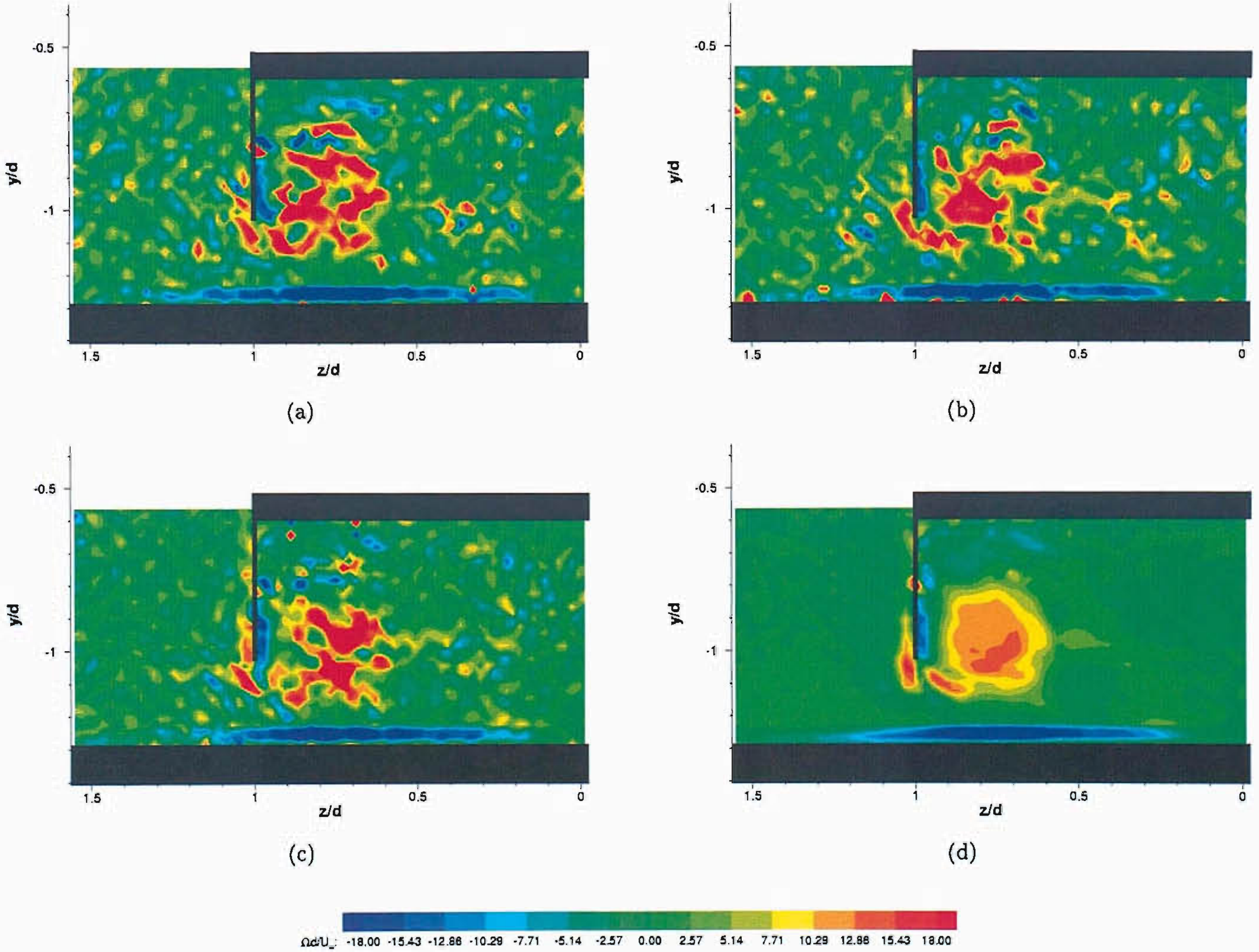

(a)

(b)

(c)

(d)

Figure 51: Instantaneous vorticity contours at x/d =6.37 in a Type B flow, h_r/d=0.255 (PIV).

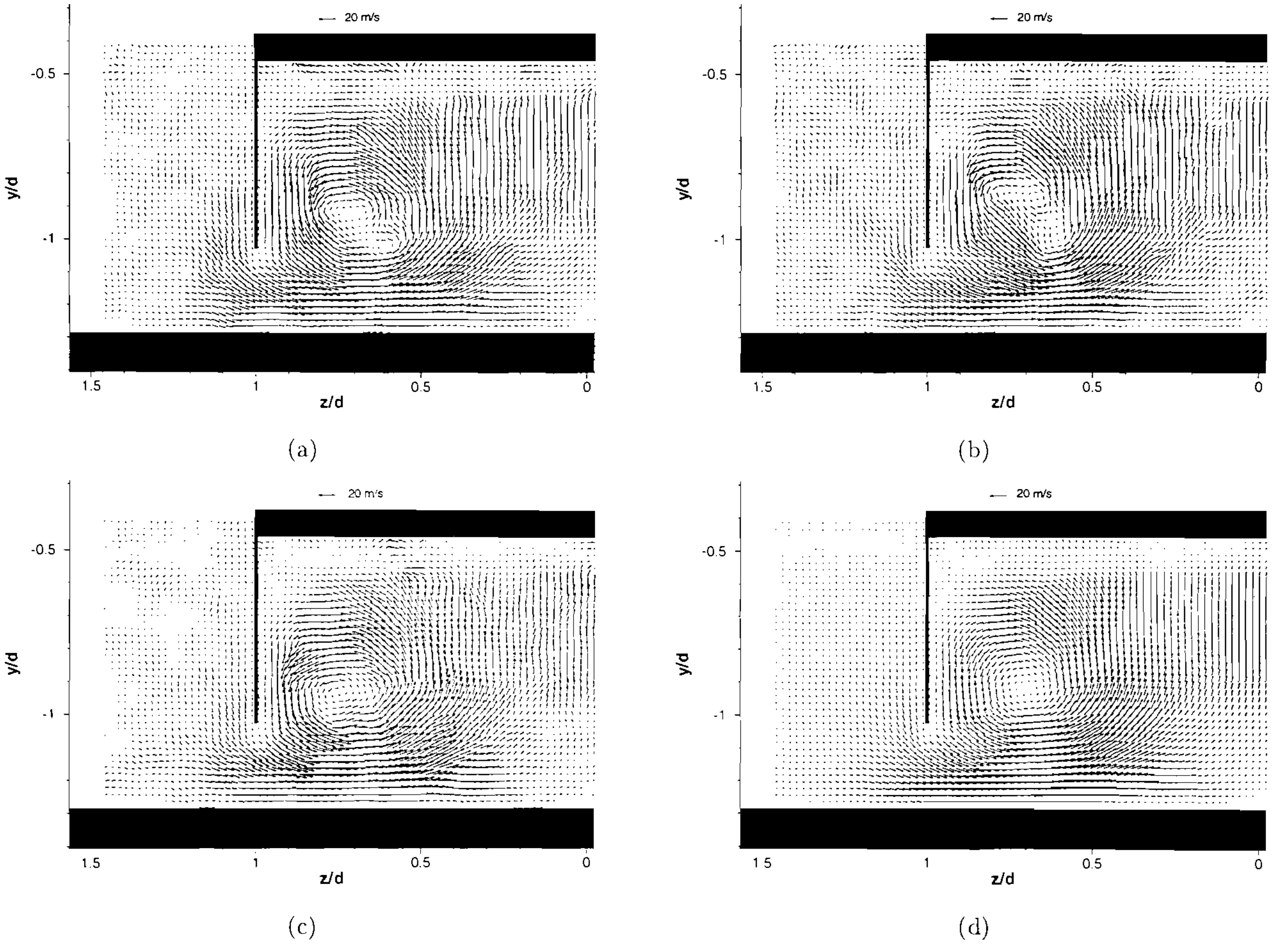

(a) (b) (c) (d)

Figure 52: Instantaneous velocity vectors at x/d =6.83 in a Type B flow, h_r/d=0.255 (PIV).

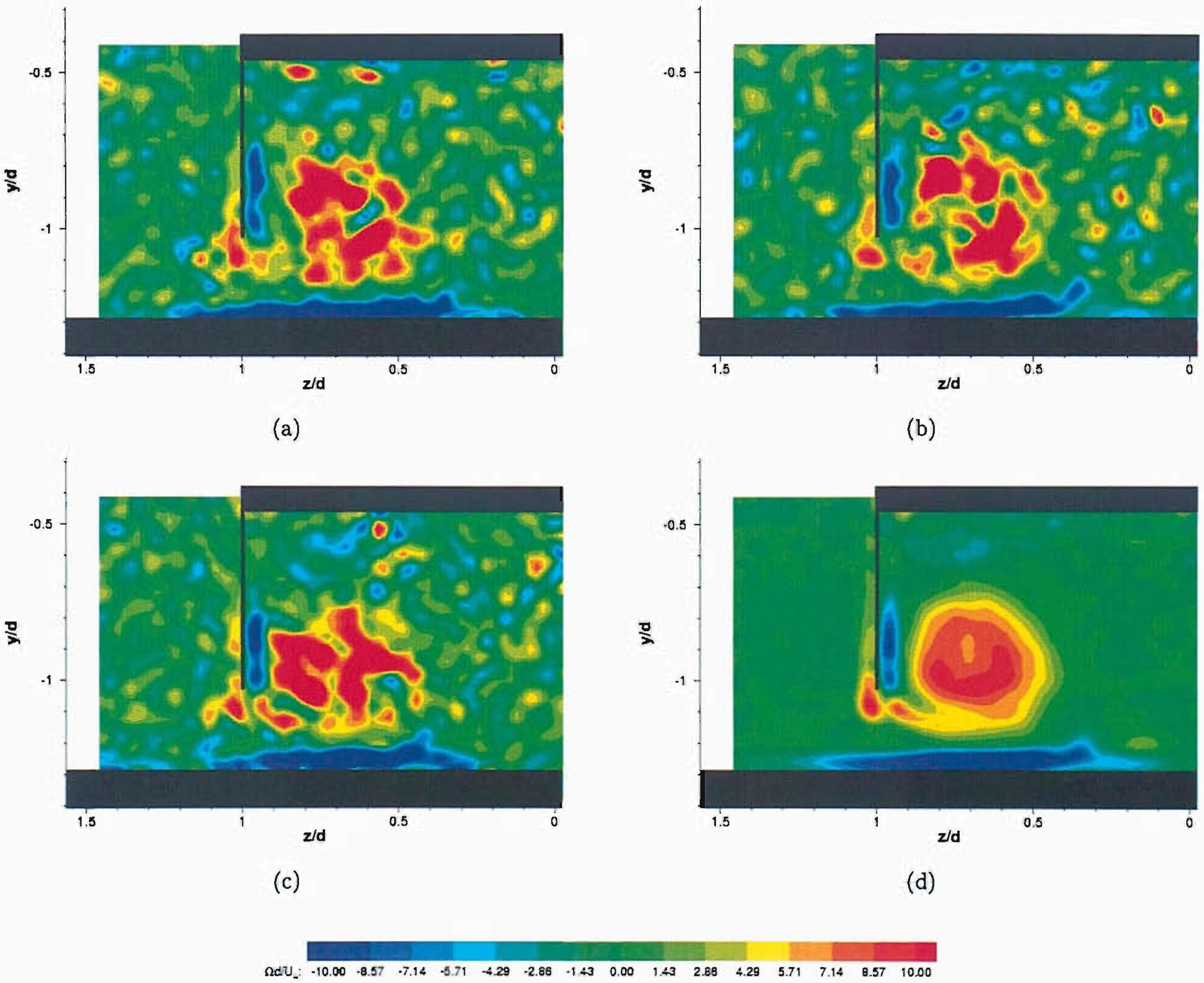

Figure 53: Instantaneous vorticity contours at x/d =6.83 in a Type B flow, h_r/d=0.255 (PIV).

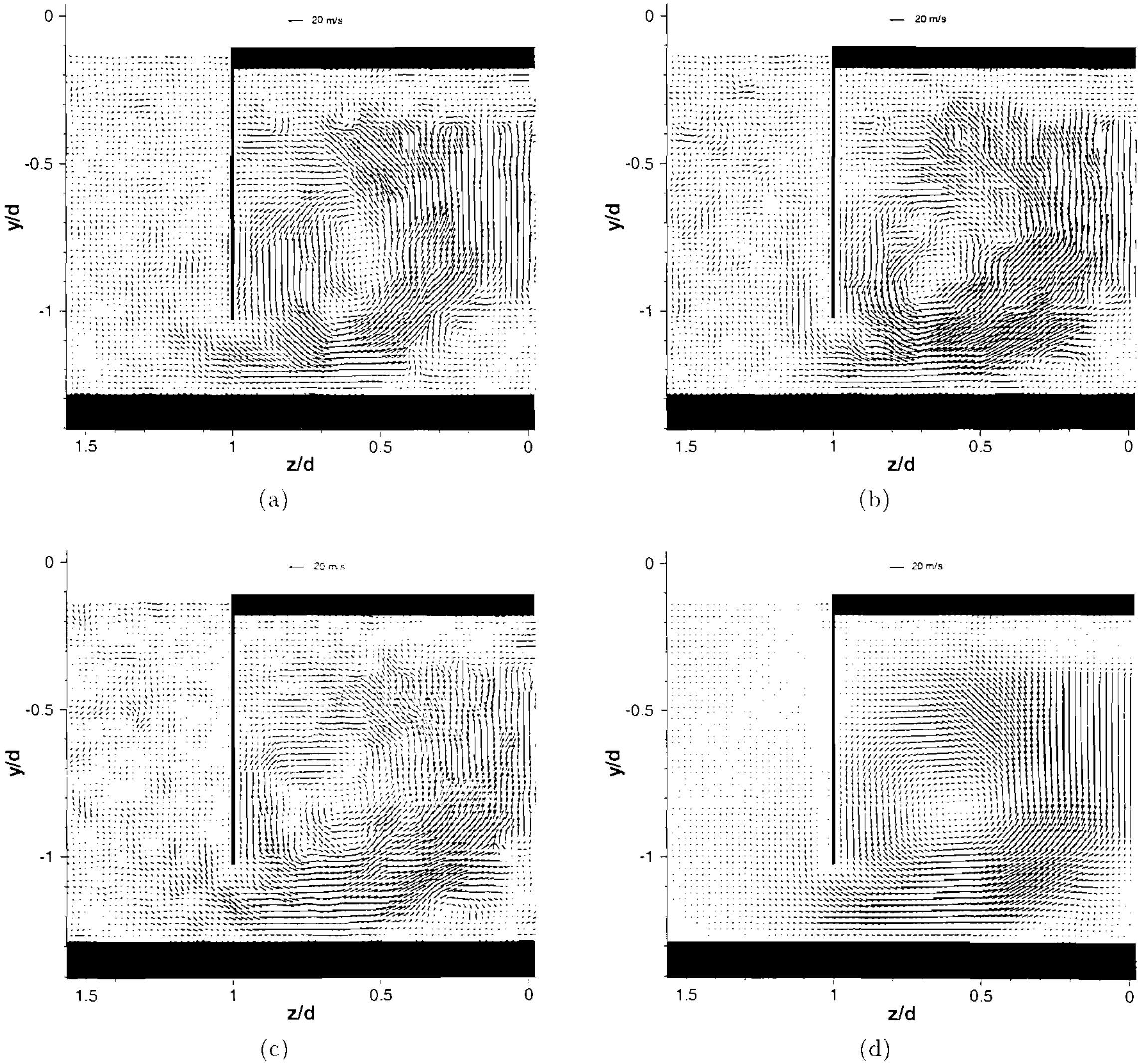

(a) (b)

(c) (d)

Figure 54: Instantaneous velocity vectors at x/d =7.74 in a Type B flow. h_r/d=0.255 (PIV).

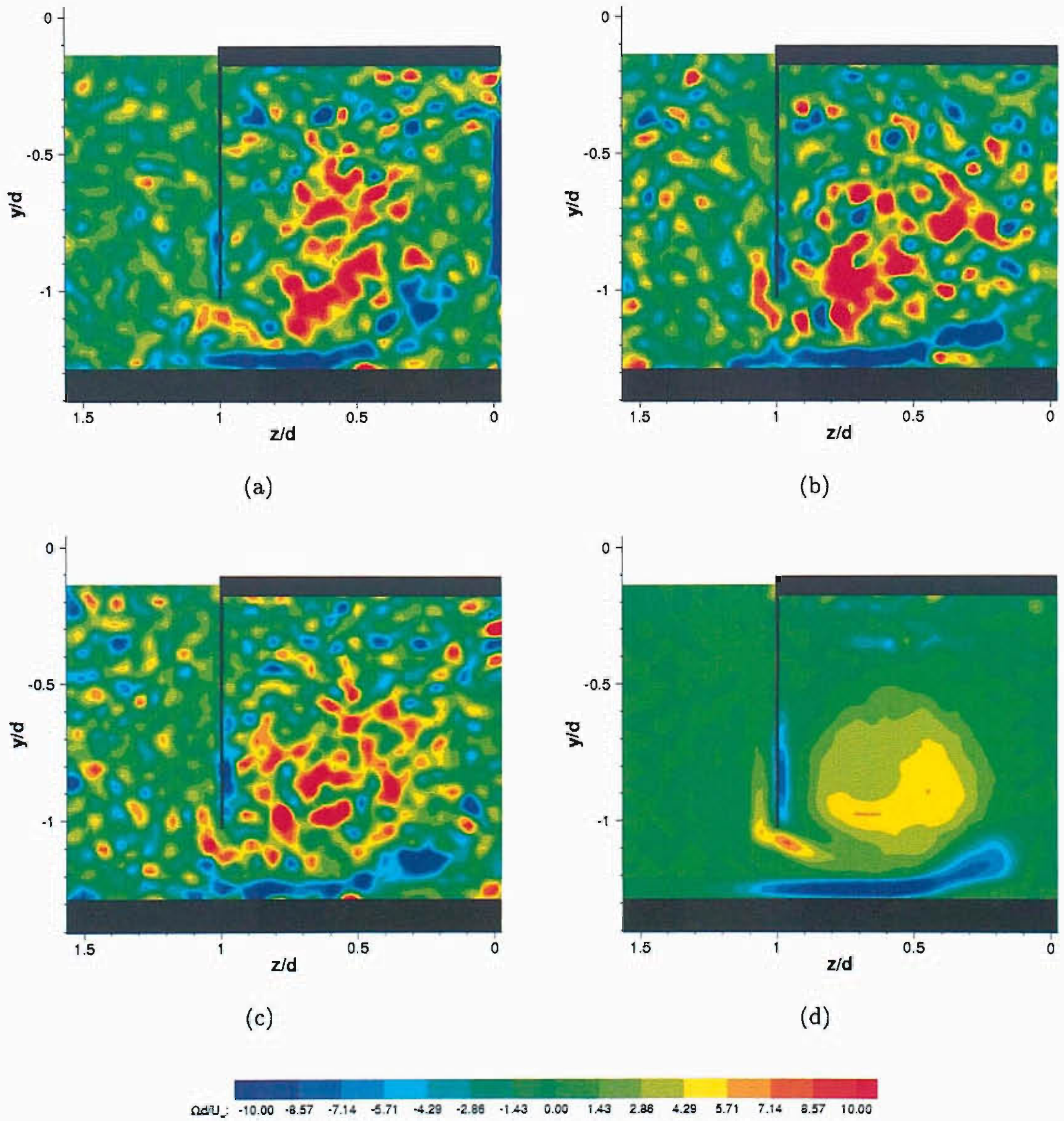

Figure 55: Instantaneous vorticity contours at x/d =7.74 in a Type B flow, h_r/d=0.255 (PIV).

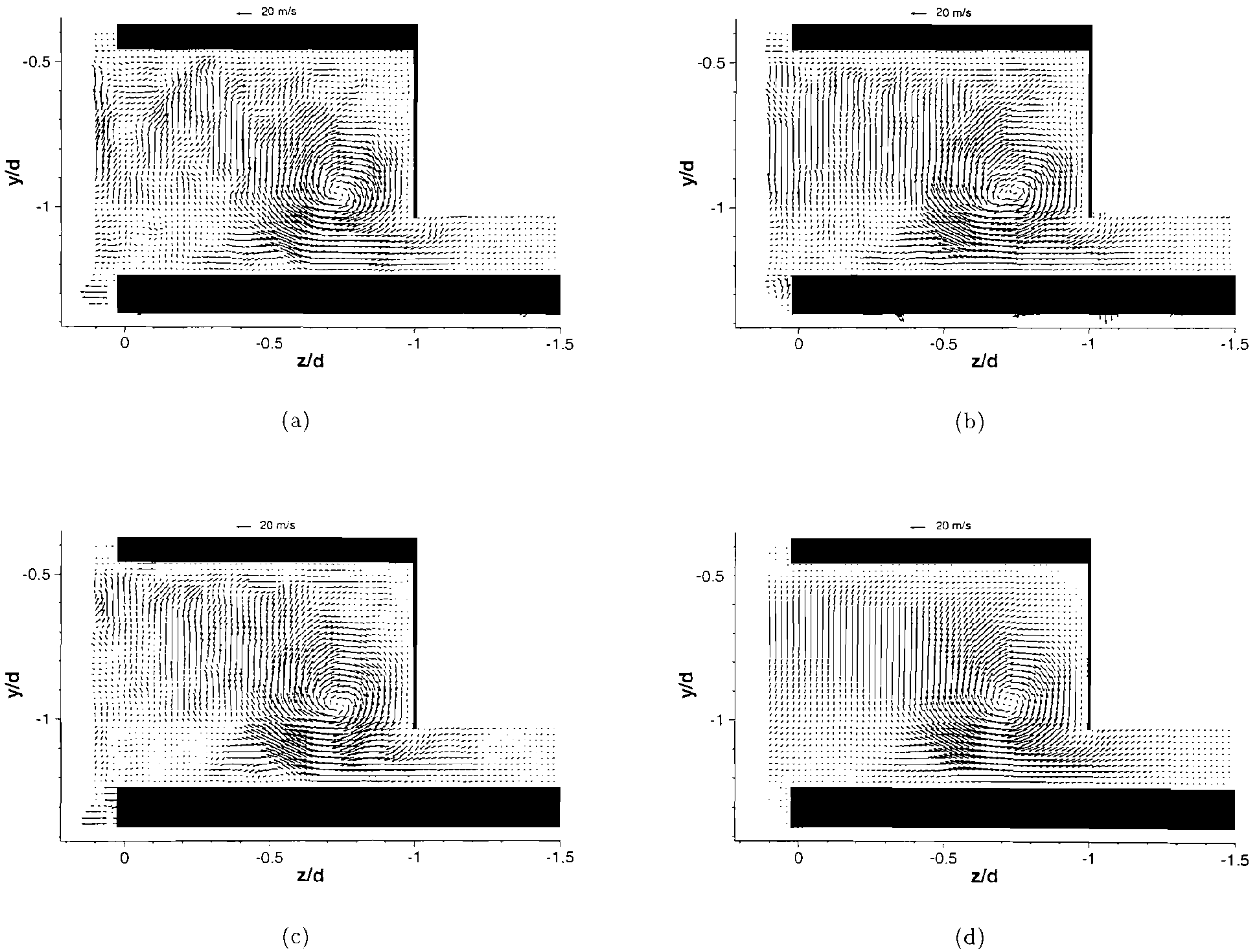

(a)

(b)

(c)

(d)

Figure 56: Instantaneous velocity vectors at x/d =6.83 in a Type C flow. h_r/d=0.204 (PIV).

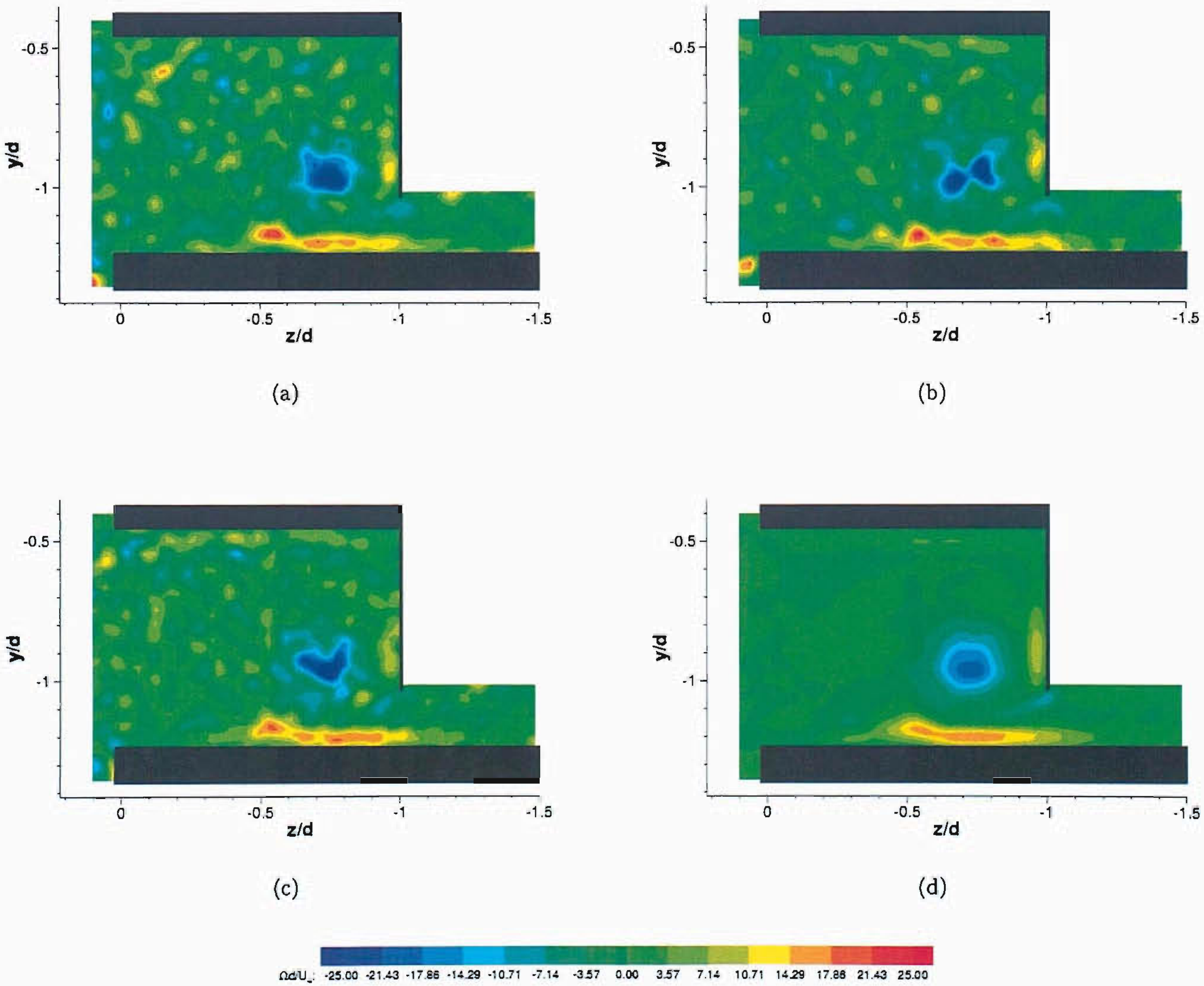

Figure 57: Instantaneous vorticity contours at x/d =6.83 in a Type C flow, h_r/d=0.204 (PIV).

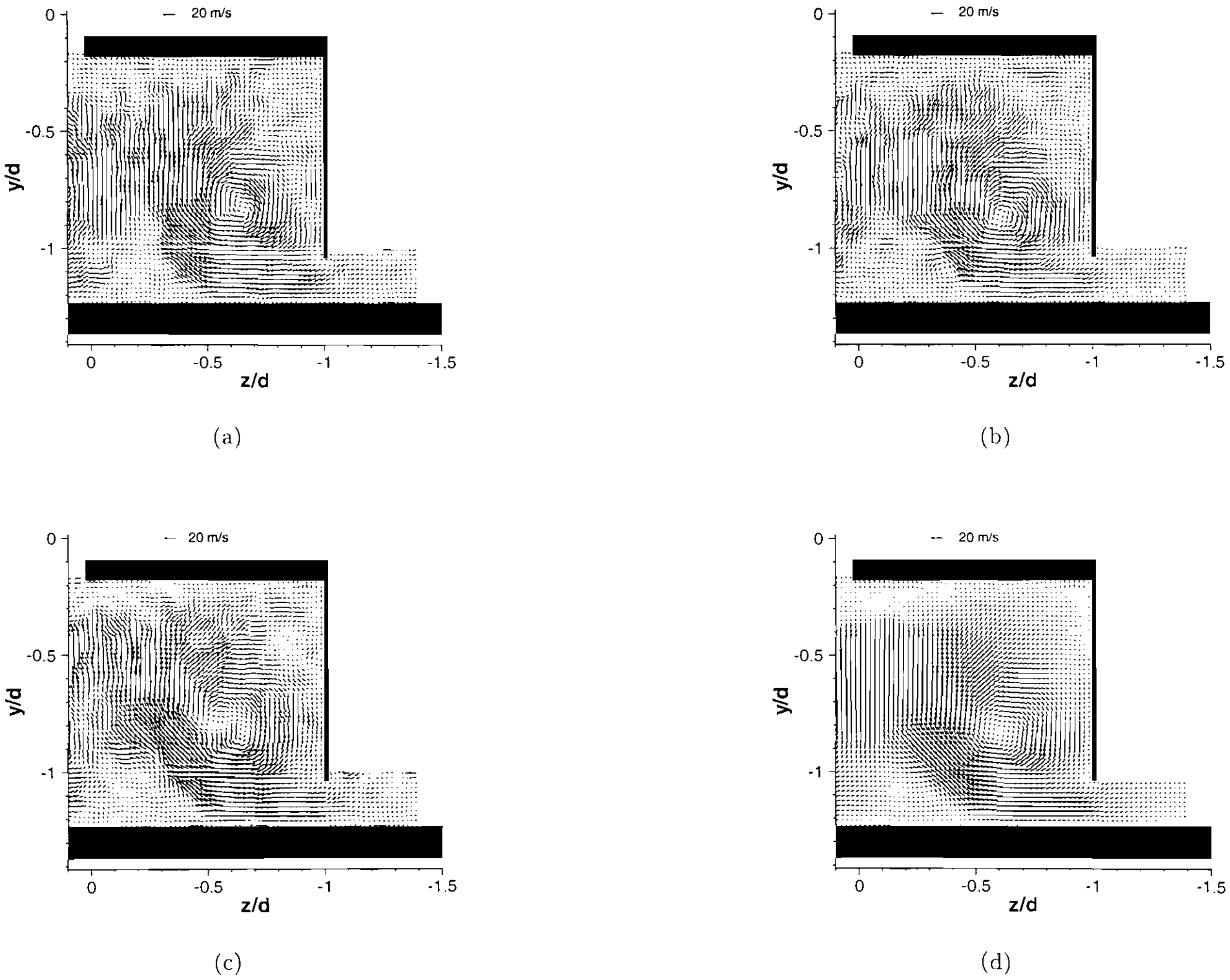

(a) (b) (c) (d)

Figure 58: Instantaneous velocity vectors at x/d =7.74 in a Type C flow, h_r/d=0.204 (PIV).

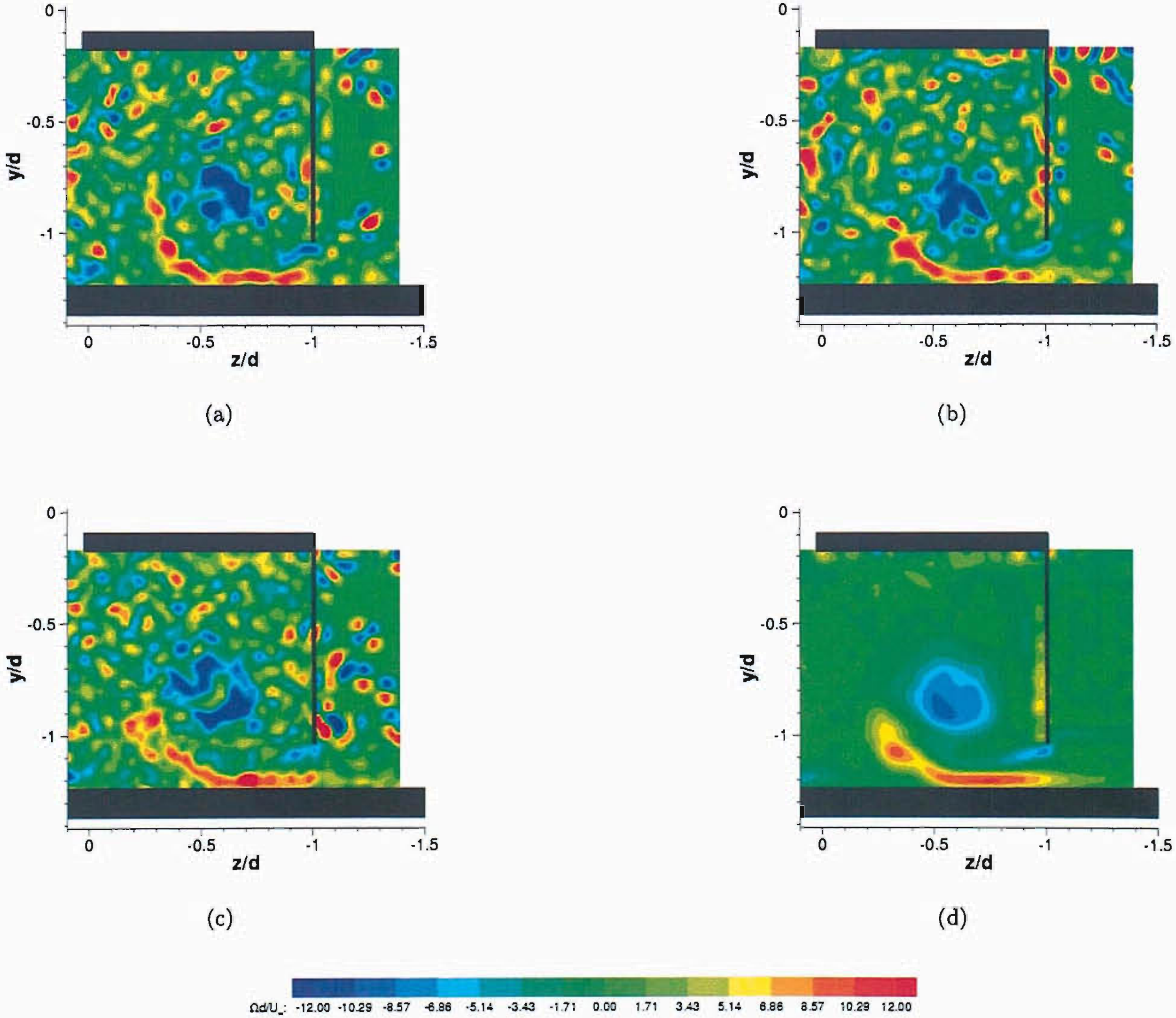

(a) (b)

(c) (d)

Figure 59: Instantaneous vorticity contours at x/d =7.74 in a Type C flow, h_r/d=0.204 (PIV).

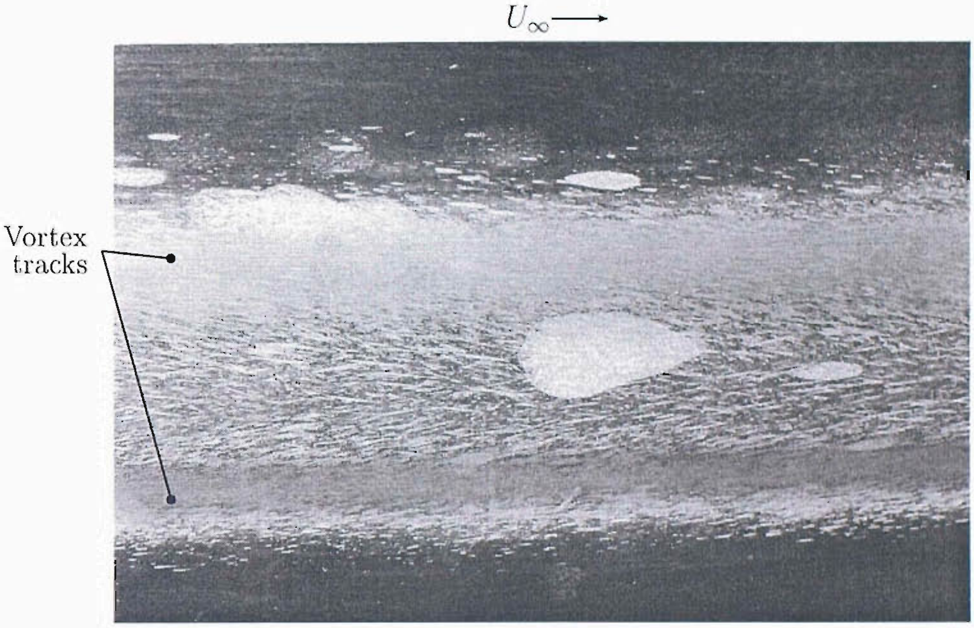

Figure 60: Oil flow visualisation on ground: h_r/d=0.255. Flow direction from left to right.

Chapter 6

Wake/Vortex Flow Development Behind the Diffuser

The evolution of the vortex pair exiting the diffuser was investigated by taking LDA measurements at four ride heights representative of each flow type, in spanwise planes downstream of the model at x_1/d =1.051 and x_1/d =2.006. In addition to these measurements, data were taken for three other ride heights at x_1/d =1.051. In measuring the properties of the vortex flow in the near wake of the diffuser, the potential effects of the wake upon any vehicle trailing behind the diffuser may be deduced.

6.1 Wake/Vortex Flow Development: Type A

The wake of the model at h_r/d=0.382, x_1/d =1.051 is illustrated in Figure 61. Only the left side vortex was measured in detail. Immediately, it may be seen that the flow at the vortex core was not measured, for the same reasons that it could not be measured for this ride height at x_1/d =0.096. The fact that the cores still contain no seeding particles at this measurement plane strongly suggests that the vortices remain concentrated and strong in the model near-wake. Although the core flow could not be measured, the cross-stream velocities in the flow surrounding the core are high, see Figure 61 (a). Once again, caution must be employed in interpreting the results in this part of the flow as there is a possibility that centrifugal effects could increase the seeding particle velocities beyond their true value. The vortex position has moved inboard and upwards. Although the true vortex core could not be measured, the core position given in Table 16 has been interpolated from the measurements surrounding the core and as such is an approximation to the true core position that has been calculated for the purpose of tracing the vortex trajectory (Figure 69). Though the model side-plates do not feature at this measurement plane, flow from the freestream is drawn in from the sides by the strong vortex flow, and is entrained around the outside of the vortex and upwards through the gap between the vortices at the centre-plane. The induced vortex at the ground is clear. Figure 61 (b) shows the streamwise velocity contours, u/U_∞. Around the vortex is a large pocket of high speed flow, just below the freestream speed. The boundary layer structure at the top of the diffuser and in the corners is still prevalent. Towards the centre-plane z/d =0, and towards the ground, the flow speed is slightly slower. In the absence of side-plates, there is no real sign of the vortex shear layer, however in general, the structure of the flow remains similar to that at x_1/d =0.096. The vorticity contours of Figure 61 (c) reveal that the vortex strength has diminished considerably, however the vortex shape retains a compact and distinct roundness, the size of which has not significantly increased from the previous measurement plane at x_1/d =0.096. The ground shear layer is not visible in the measurements due to the coarse nature of the measurement grid in this area, however the inducement of the ground boundary layer upwards toward the vortex is clearly apparent. The entrainment is stronger than at the diffuser exit, in reflection of the maintenance of the vortex strength and concentration.

Levels of TKE have increased around the vortex core, in the vicinity of the induced ground shear layer, and also at the top of the measurement grid corresponding to the flow that has exited from the top of the diffuser (Figure 61 (d)). In the majority of the vortex flow however, TKE remains low, in accordance with the well defined, strong vortex.

At two model widths downstream of the model, the vortices have moved further inboard and upwards (Figure 62). Both vortices were measured for this measurement plane, and the measurements indicate that the symmetry between the two is breaking down. Whilst the right side vortex core could not be measured, the left side vortex could (Figure 62 (a)). Thus it appears that the left side vortex is being affected by viscous diffusion/dissipation earlier than the right side vortex which persists in its coherent character. The asymmetry between the two vortex cores is not a consequence of the positions of the measurement points; several traverses were made across both of the vortices to ensure that there was no hole in the left side of the flow and that the right side flow was as shown. The cross stream velocities at the core of the left side vortex are lower than at previous measurement planes, however a comparison of corresponding vectors at the left and right side of the flow shows that there is little difference in the speeds from left to right. This instills more confidence in the measurements surrounding the hole in the data at the right side of the flow, that they are perhaps not so exaggerated by centrifugal effects. Air continues to be entrained from outside the model vicinity to flow around the vortices. The shape of each vortex is strongly oval as the low pressure influence persists in the top corners of the wake flow, drawing the vortex into the corners. Figure 62 (b) presents streamwise velocity contours which illustrate how much the wake flow has decelerated since exiting the diffuser, and in which direction it is moving; the wake is moving upwards as the slower moving flow that exited from the roof of the diffuser is now mostly above the plane of measurement. As this happens, higher speed flow replaces the flow underneath the vortices. The vorticity contours show that the vortices have still yet to lose their compactness and strength (Figure 62 (c)). The levels of vorticity outside of the vortex cores remains low, emphasising the definite coherence of the vortex flow in the wake. The vorticity level at the left side vortex core remains high. The area of induced vorticity at the ground has increased in size, reaching further towards the main vortices and it is very likely that the ground boundary layer thickness has also increased. It appears likely that further downstream the vortex flow and the ground boundary layer flow will merge at this ride height [5].

The TKE distribution at this plane is asymmetric, reflecting the differing stages of dissipation of the two vortices (Figure 62 (d)). The left side vortex has a higher turbulent kinetic energy level than the left. The remainder of the flow shows relatively low TKE levels.

6.2 Wake/Vortex Flow Development: Type B

The Type B wake flow was measured at h_r/d=0.255. The results for x_1/d =1.051, in which both vortices were measured, are given in Figure 63. Figure 63 (a) shows a vortex pair of equal size and position. Cross-flow speeds are significantly lower than at h_r/d=0.382. The vortices have moved in-board toward the model centre-plane, and are deflected upwards quite significantly in the absence of the regulatory influence of the side-plates upon the vortex position. The pressure gradient at the ground beneath the vortices is still large enough to induce cross-flow separation in the ground shear layer, and the vortex deflection is thought to be caused by the presence of the secondary vortices at the ground, which induce a vertical displacement of the main vortices [43]. The vortices have increased slightly in size from h_r/d=0.255, x_1/d =0.096, and are more of an oval shape; although the cores have moved in-board, the remainder of the vortex has expanded into the top corner regions of the wake flow. The u/U_∞ contours of Figure 63 (b) reveal that although there remains high speed flow around the outer part of the wake, the axial velocity of the vortex is decreasing. The velocity at the core appears to have increased from that at x_1/d =0.096, most likely due to diffusion. The streamwise vorticity has weakened, and the regions of concentrated vorticity at the core are smaller. The vortex cores are highly turbulent and diffuse (Figure 63 (d)), and the region of flow downstream of the centre of the diffuser exit is a concentrated region of TKE. TKE levels in the central region of the diffuser exit are reduced slightly from the levels at x_1/d =0.096 as the vortex travels downstream from the vicinity of the breakdown.

At x_1/d =2.006, the vortices are vertically displaced even further and are slightly further in-board than at the previous measurement plane (Figure 64 and Table 16), however a considerable upwash remains between the vortex cores. The vortices are more diffused and less concentrated than at x_1/d =1.051. The streamwise velocity gradient across the vortices is becoming less as the diffusion process continues. Vortex concentration has reduced slightly

(Figure 64 (c)) due to dissipation of the vortex. TKE levels have fallen and the concentration has been displaced to one side. The TKE concentration is also moving away from the ground plane in accordance with the overall trend of the upward displacement of the wake.

6.3 Wake/Vortex Flow Development: Type C

The type C flow continues to be asymmetric downstream of the model. The vortex has deflected upwards whilst the weaker re-circulating flow lies close to the ground (Figure 65 (a)). The cross-flow velocities across the diffuser have fallen slightly from x_1/d =0.096. A noticeable feature of the vortex is that the streamwise velocities at its core have increased since the diffuser exit plane ((Figure 65 (b), Table 16). Thus it appears that vortex breakdown does not occur in this vortex downstream of the diffuser. The region of reversed fluid has moved inboard toward the centreline (z/d =0) as has the vortex. The result is that the streamwise flow is starting to become more homogenised, streamwise velocity gradients across the span of the diffuser exit are decreasing. The vortex is rapidly losing concentration and the vorticity across the diffuser is dissipating to low levels (Figure 65 (c)). High TKE dominates the flow in the area surrounding the re-circulating/reversed flow whilst levels are much lower at the weaker vortex core and in the vicinity of the vortex (Figure 65 (d)). Overall, TKE levels are lower than in the type B flow at this measurement plane. This is probably as a result of the type C vortex not breaking down inside the diffuser.

At x_1/d =2.006 the distinction between the vortex and the circulating flow is less clear. The streamwise velocity is now less than freestream across the whole diffuser span, and is highest at the sides, decreasing gradually to the almost stagnated fluid towards the centreline (Figure 66 (b)). The wake has deflected further away from the ground, the vortex core is now at the roof of the diffuser area (Table 16, Figure 66 (b)). Reverse flow is no longer a feature of the flow as measured, however it is possible that a small region exists above y/d =0 and as such was not captured by the measurements. Dissipation of the vortex flow has resulted in low vorticity levels across the flow (Figure 66 (c)). High TKE exists in the decelerating fluid flowing towards the centreline (Figure 65 (d)). Levels in the remainder of the flow are low.

6.4 Wake/Vortex Flow Development: Type D

Low speed flow dominates the wake at h_r/d=0.064, x_1/d =1.051. The lack of flow entering the diffuser inlet affects the flow downstream of the model also. The streamwise flow is largely reversed or nearing stagnation at the centre of the exit area. The cross-flow velocity field is almost featureless excepting a small eddy at the ground at z/d =-0.5. This is also a region of weak vorticity (Figure 67 (c)). TKE levels throughout the wake are low, approaching zero in places. At x_1/d =2.006, cross-stream velocities have decreased further and the region of reversed flow is larger (Figure 68 (a) and (b)). Curiously, two small counter-rotating eddies were measured near the ground plane rather than one, reinstating a degree of symmetry to the flow. It is possible that the flow flipped sides during the course of the run, which took approximately three hours to measure. Attempts to reproduce the symmetric eddies in the PIV data were unsuccessful. Vorticity levels remain low ((Figure 68 (c)), however TKE levels have increased slightly (Figure 68 (d)). Type D flow creates a weak near-wake flow that would be unlikely to cause great difficulty to a trailing vehicle.

6.5 Discussion

Figure 69 charts the development of the vortex core locations throughout the diffuser and in the near wake flow for flow Types A, B and C. Figure 69 (a) shows how the cores are displaced vertically as the flow progresses through the diffuser, and Figure 69 (b) illustrates the spanwise translation of the cores. Values for the vortex core locations are given in Tables 14 and 16. Striking differences in position and strength between the type A and type B flows indicate that the two types of flow will affect any trailing aerodynamic vehicle in different ways. A predominant characteristic determining the effect of the vortex flow on a trailing aerodynamic vehicle is the strength of the vortex downstream of the model. At h_r/d=0.382, x_1/d =2.006 the vorticity at the vortex core is 16.4, which although a significant reduction in concentration compared to its concentration at the diffuser exit, remains a coherent and strong vortex. This is in contrast to the vortex at the same measurement plane at h_r/d=0.217, the vorticity of which is $\Omega_c d/U_\infty$ =1.7.

A second factor is in the extent of vertical displacement of the vortices; whereas the vortex core at h_r/d=0.382, x_1/d =2.006 is displaced to y/d =-0.410, at h_r/d=0.217, x_1/d =2.006 the core lies at y/d =-0.148. The more down-force that is generated by the diffuser, the more vertically displaced are the vortices. In type C flow the stronger vortex is displaced upwards to a slightly lesser degree than the type B vortices. The weaker vortex may deflect upwards or remain close to the ground as at h_r/d=0.159, x_1/d =1.051 (Table 16).

The combination of highly concentrated vortices and low TKE vortex core in the type A flow ensures that the vortices remain concentrated without dilating quickly downstream. In practice, their existence can exert an adverse effect on the aerodynamic characteristics of trailing vehicles, and could be a safety issue. The vortices could retain their coherence far enough downstream to locally interfere with the aerodynamic set up of the front wing for example. The aerodynamic balance can be sensitive to external influences and if too much air entered underneath the front wing the car could pitch nose upwards and become airborne. Alternatively, the vortex could suddenly interfere with another aerodynamic component such as one of the sidepods, and the aerodynamics may become unbalanced enough to cause partial loss of down-force on the trailing vehicle, which could result in loss of aerodynamic grip at the track surface. The broken down type B vortices move away from the ground as they travel downstream. The highly turbulent vortex cores would lead to a rapid dilation of the vortices as the turbulent diffusion and dissipation are much higher. These features would make type B flow a slightly different concern for a following vehicle. Turbulent air will prevent the aerodynamic components from performing as well as they would in clean air. In some cases this would make the car difficult to control, which is particularly hazardous at race car speeds.

An asymmetric wake flow is an obvious problem to a vehicle travelling in its influence, in that it would probably have an asymmetric effect on the following vehicle. For the ride height measured, the wake deflects upwards quickly on exiting the diffuser, leaving low speed, low vorticity fluid near the ground. However, the flow is now a concentration of high TKE, which would adversely affect the aerodynamic characteristics of a vehicle travelling closely to it.

6.6 Summary

- The vortex flow downstream of the model differs for each of the flow types.
- Type A vortices remain concentrated and retain a significant amount of strength. The flow has low TKE. The flow has the potential to locally interfere with the aerodynamics of a trailing vehicle posing serious handling and therefore safety problems.
- Type B vortices are larger and more diffuse. Low axial velocity and high TKE levels result in turbulent air that would significantly decrease the aerodynamic performance of a trailing vehicle.
- The asymmetric and turbulent Type C flow has the potential to unbalance the aerodynamics of a trailing vehicle.

h/d	x_1/d	u_c/U_∞		TKE_c/U_∞^2		y_c/d		z_c/d		$\Omega_c d/U_\infty$	
		ls	rs	ls	rs	ls	rs	ls	rs		
0.064	1.051		0.154		0.032		-0.925		0.534		-2.575
0.064	2.006	0.159	0.241	0.034	0.032	-0.914	-0.884	0.348	-0.513	0.956	-1.247
0.159	1.051	0.506	-0.098	0.064	0.056	-0.288	-0.835	0.711	-0.387	1.929	-0.756
0.159	2.006	0.088	0.452	0.074	0.045	-0.065	-0.192	0.285	-0.691	1.209	-1.327
0.204	2.006	0.474	0.145	0.066	0.076	-0.319	-0.099	0.594	-0.286	2.706	-1.84
0.217	2.006	0.391	0.302	0.067	0.052	-0.148	-0.273	0.524	-0.463	1.683	-1.802
0.255	1.051	0.215	0.193	0.093	0.098	-0.526	-0.540	0.485	-0.480	2.995	-2.994
0.255	2.006	0.354	0.350	0.061	0.0738	-0.303	-0.293	0.459	-0.492	2.359	-2.916
0.318	2.006	0.276	-	0.070	-	-0.314	-	0.415	-	3.942	-
0.382	1.051	-	-	-	-	-	-	-	-	-	-
0.382	2.006	0.385	-	0.043	-	-0.410	-	0.342	-	16.360	-

Table 16: LDA Cross-plane vortex flow in near wake of diffuser.

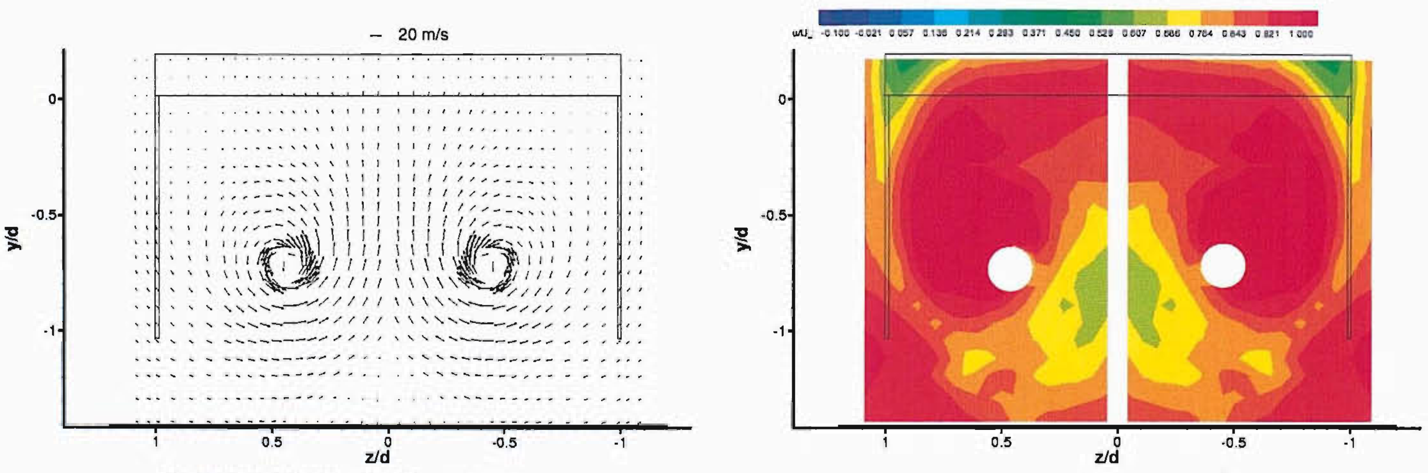

(a) Cross stream velocity vectors

(b) u/U_∞

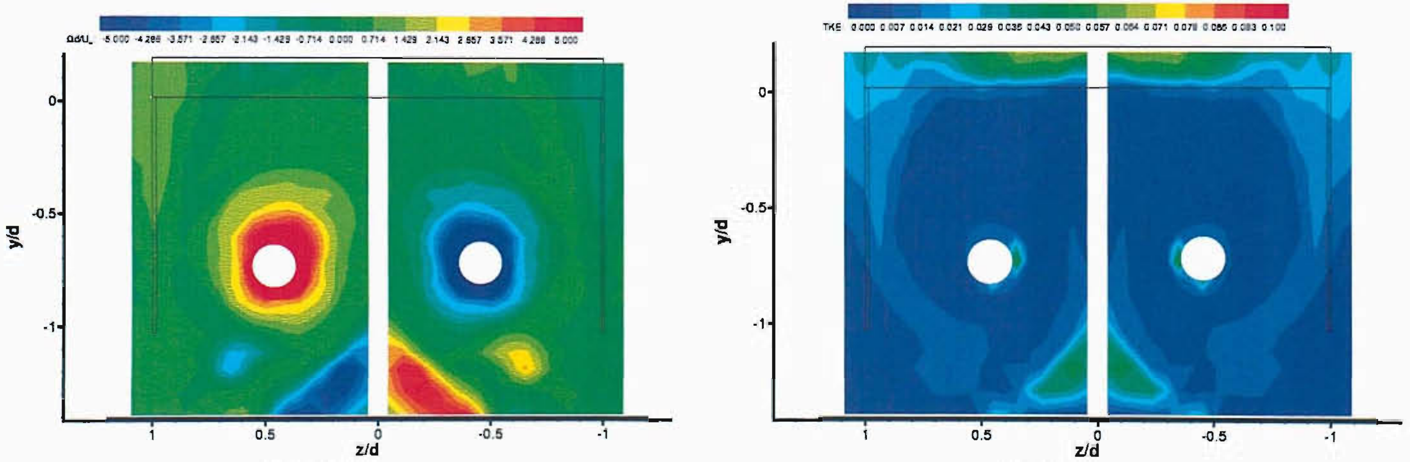

(c) $\Omega d/U_\infty$

(d) TKE

Figure 61: Near wake diffuser flow, Type A: x_1/d =1.051, h_r/d=0.382 (LDA).

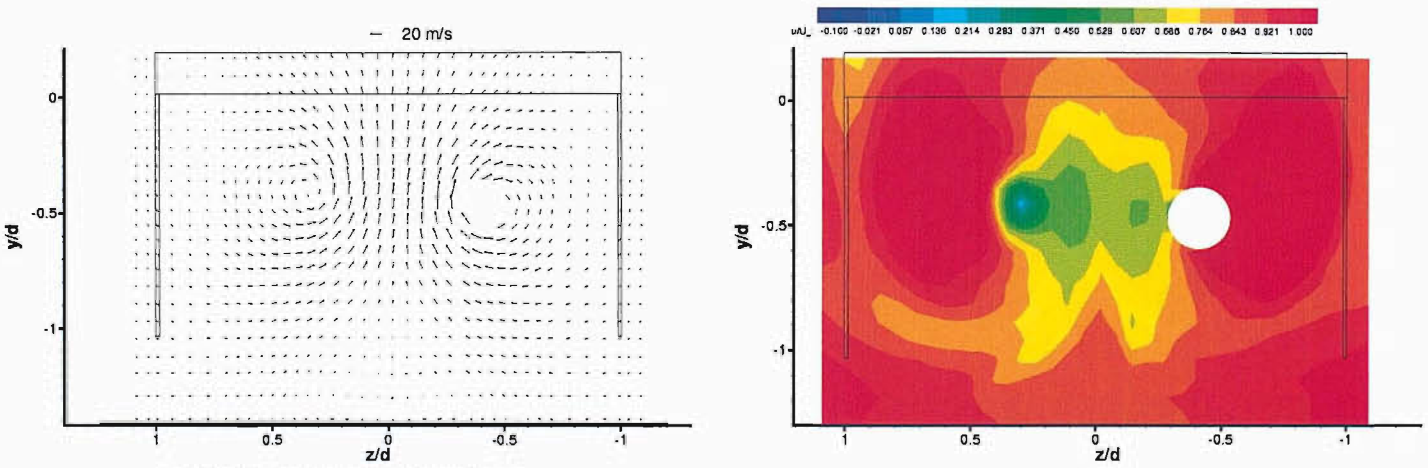

(a) Cross stream velocity vectors

(b) u/U_∞

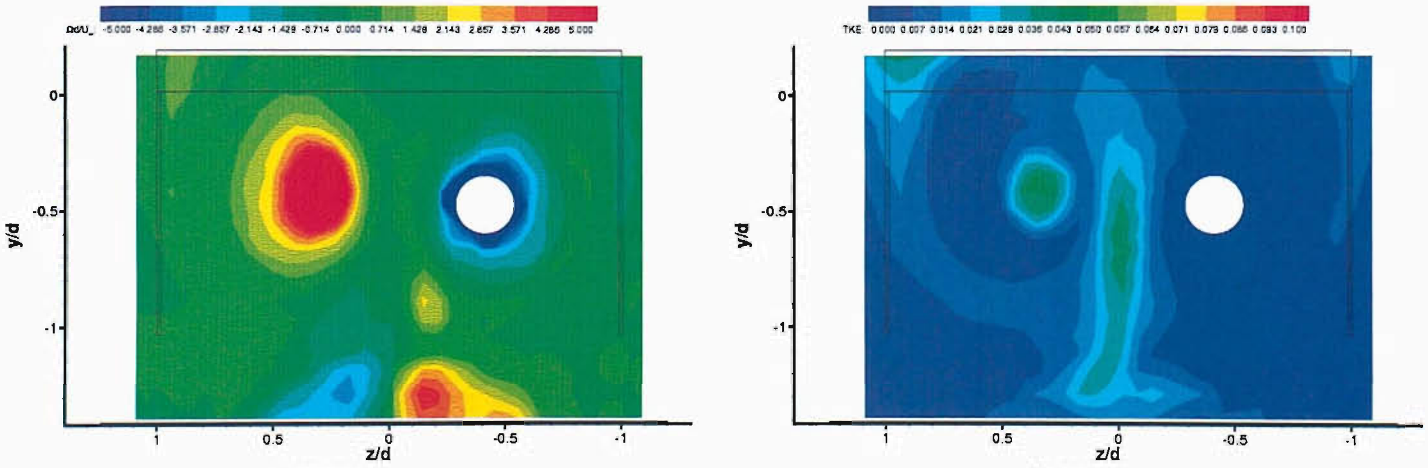

(c) $\Omega d/U_\infty$

(d) TKE

Figure 62: Near wake diffuser flow, Type A: x_1/d =2.006, h_r/d=0.382 (LDA).

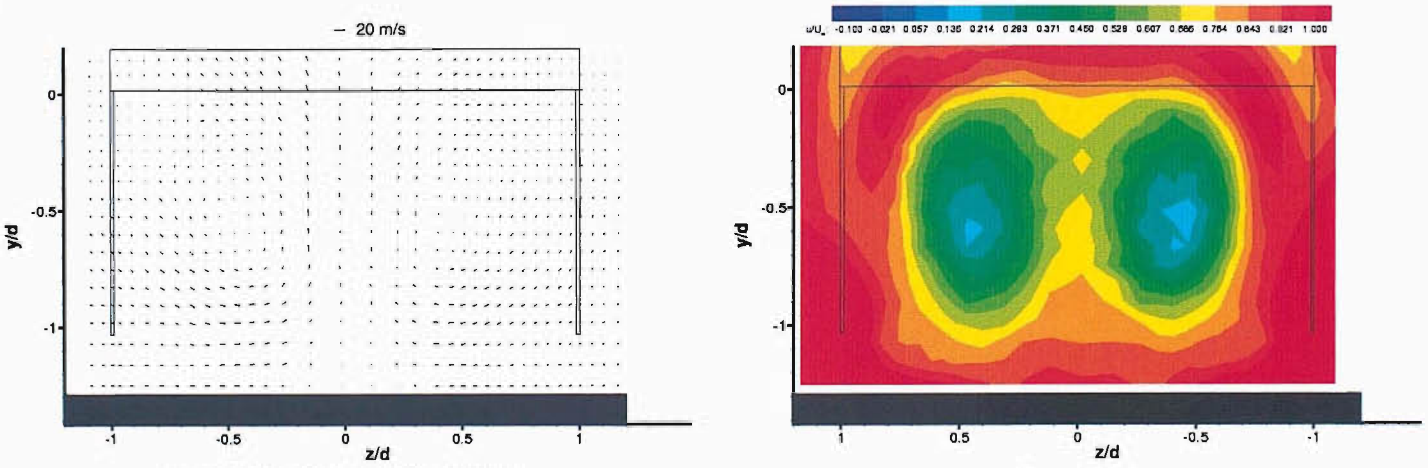

(a) Cross stream velocity vectors

(b) u/U_∞

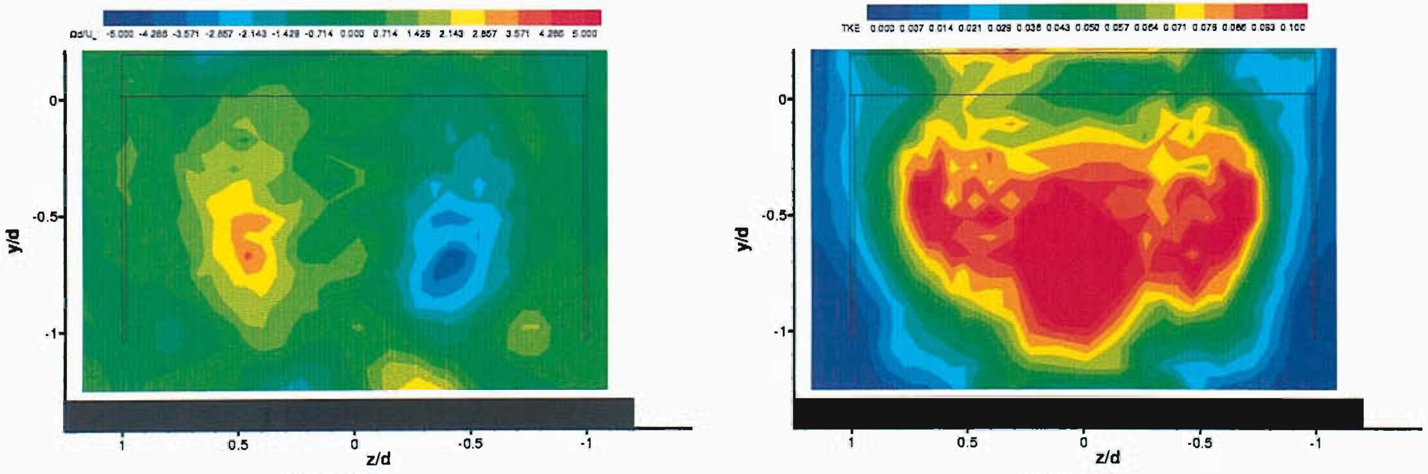

(c) $\Omega d/U_\infty$

(d) TKE

Figure 63: Near wake diffuser flow, Type B: x_1/d =1.051, h_r/d=0.255 (LDA).

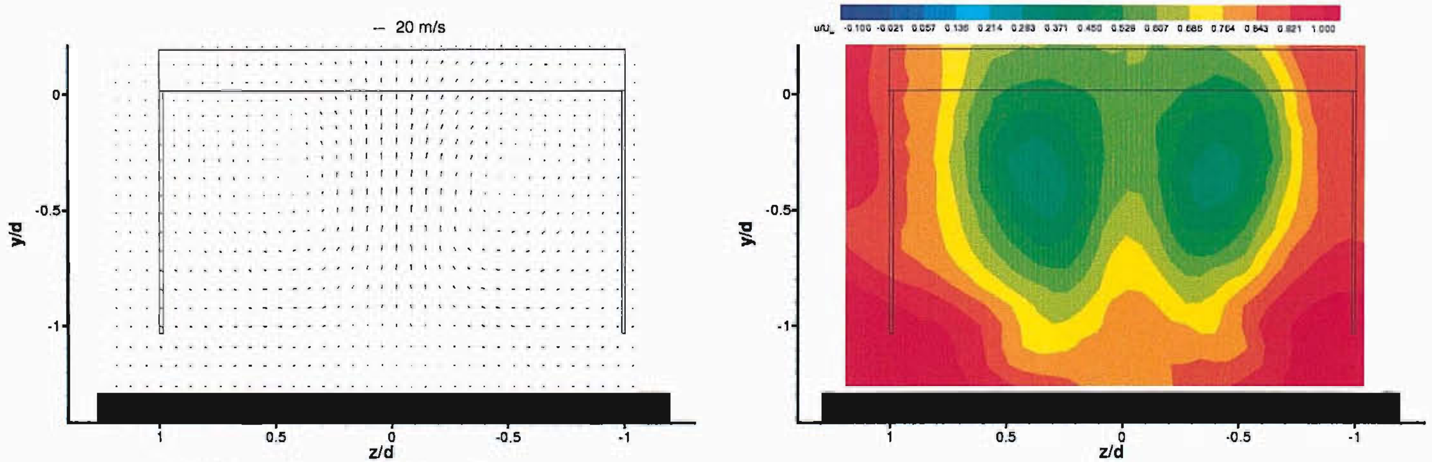

(a) Cross stream velocity vectors

(b) u/U_∞

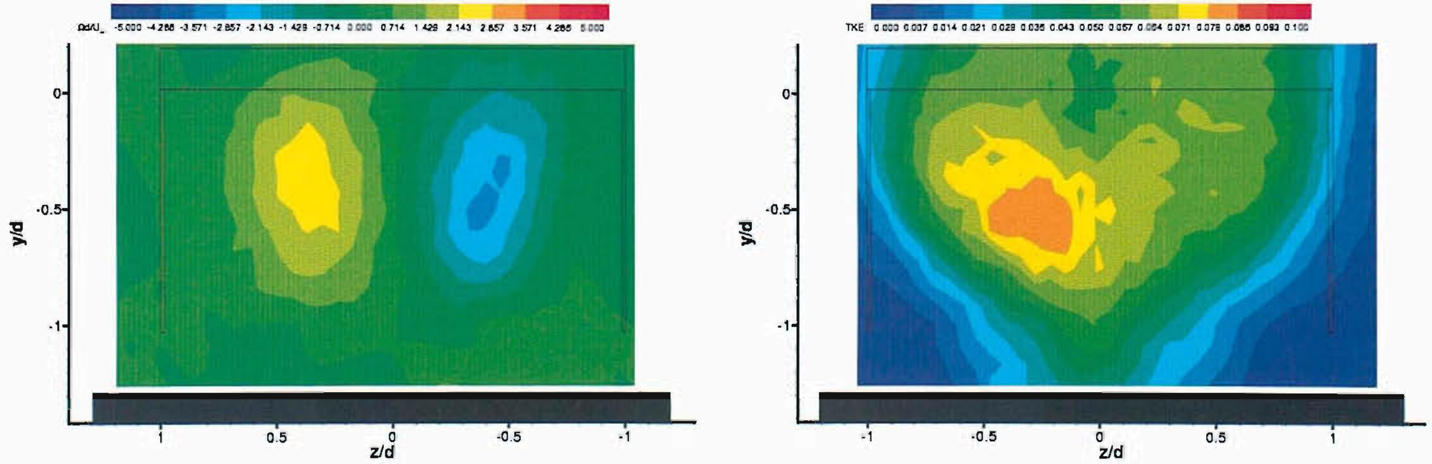

(c) $\Omega d/U_\infty$

(d) TKE

Figure 64: Near wake diffuser flow, Type B: x_1/d =2.006, h_r/d=0.255 (LDA) .

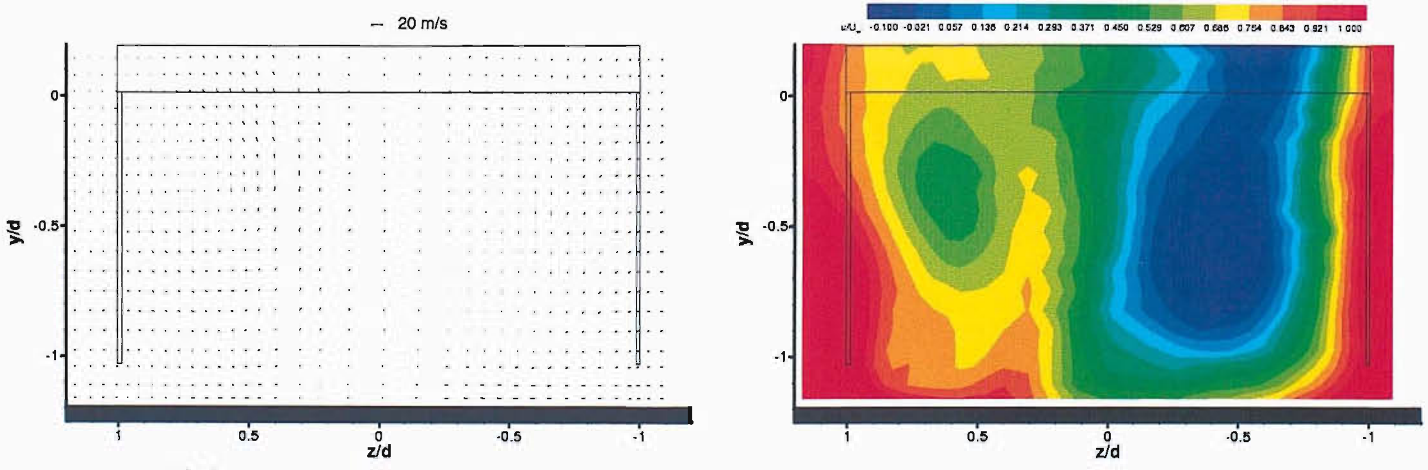

(a) Cross stream velocity vectors

(b) u/U_∞

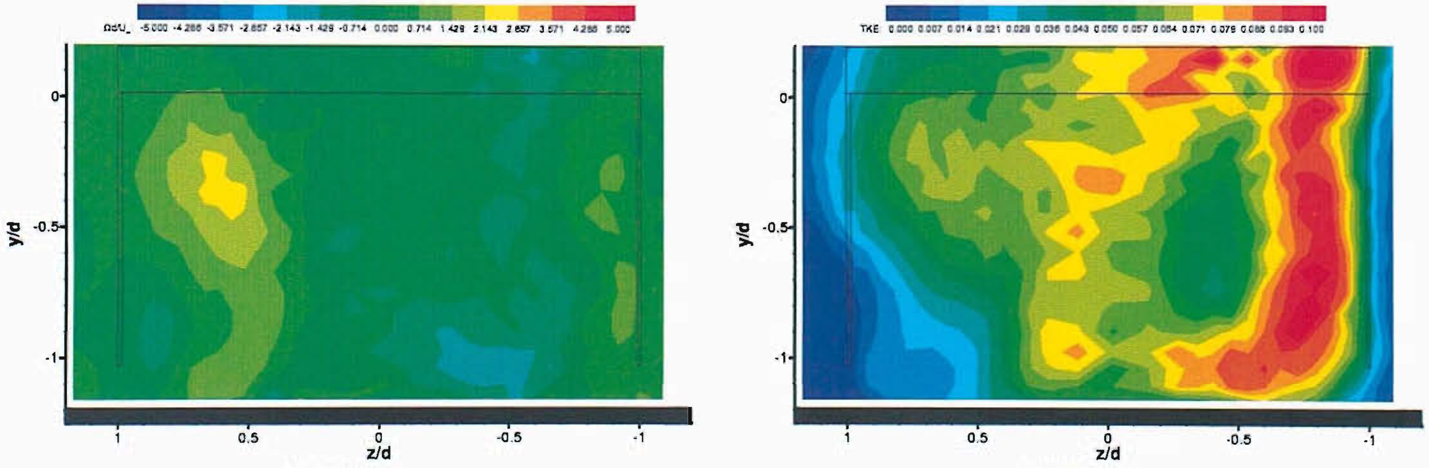

(c) $\Omega d/U_\infty$

(d) TKE

Figure 65: Near wake diffuser flow, Type C: $x_1/d = 1.051$, $h_r/d = 0.159$ (LDA) .

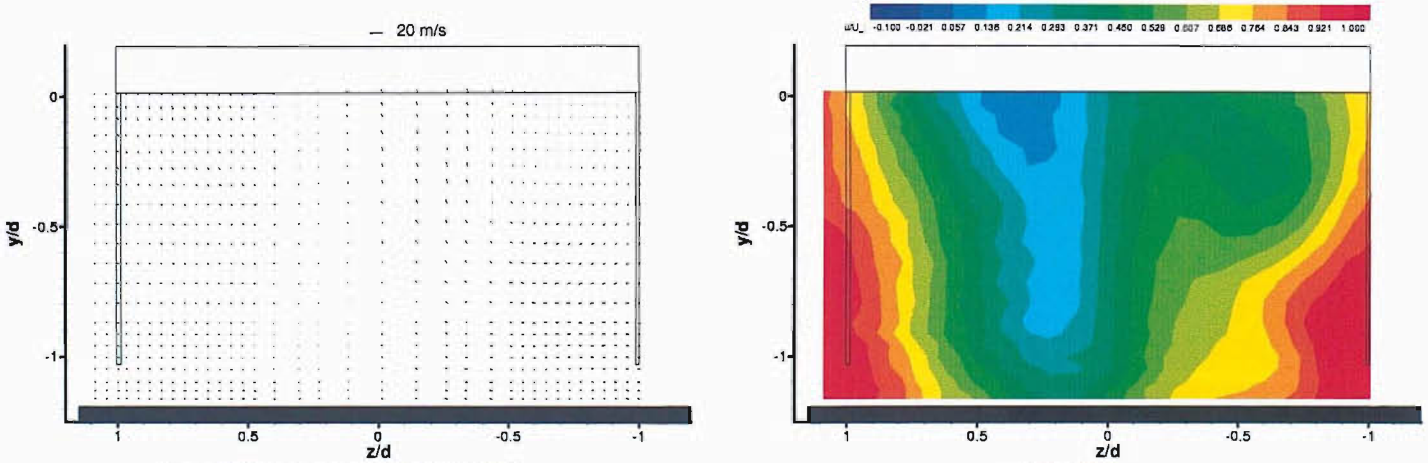

(a) Cross stream velocity vectors

(b) u/U_∞

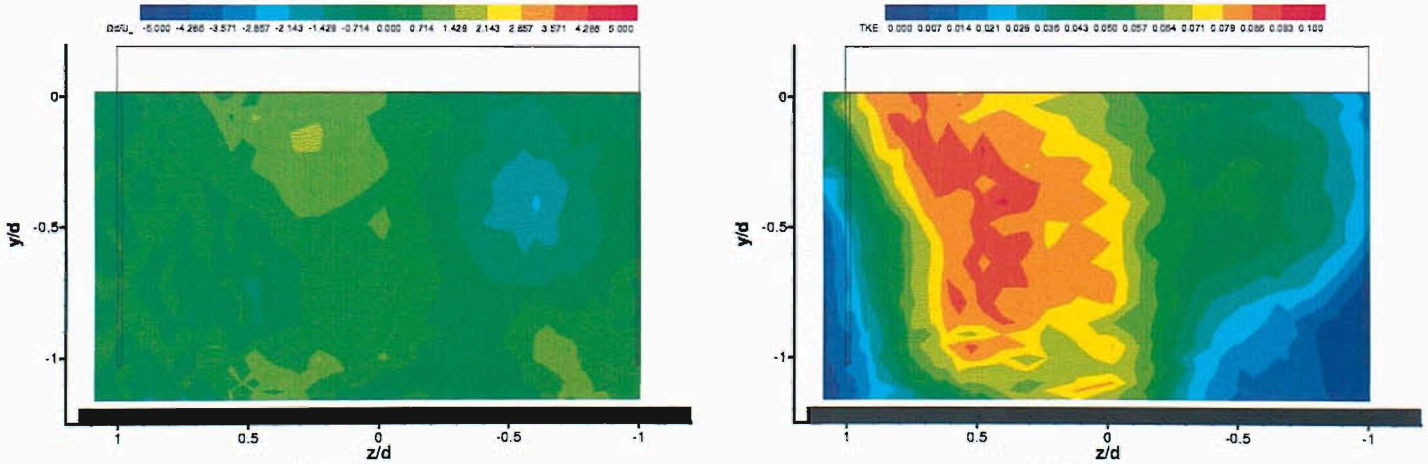

(c) $\Omega d/U_\infty$

(d) TKE

Figure 66: Near wake diffuser flow, Type C: x_1/d =2.006, h_r/d=0.159 (LDA).

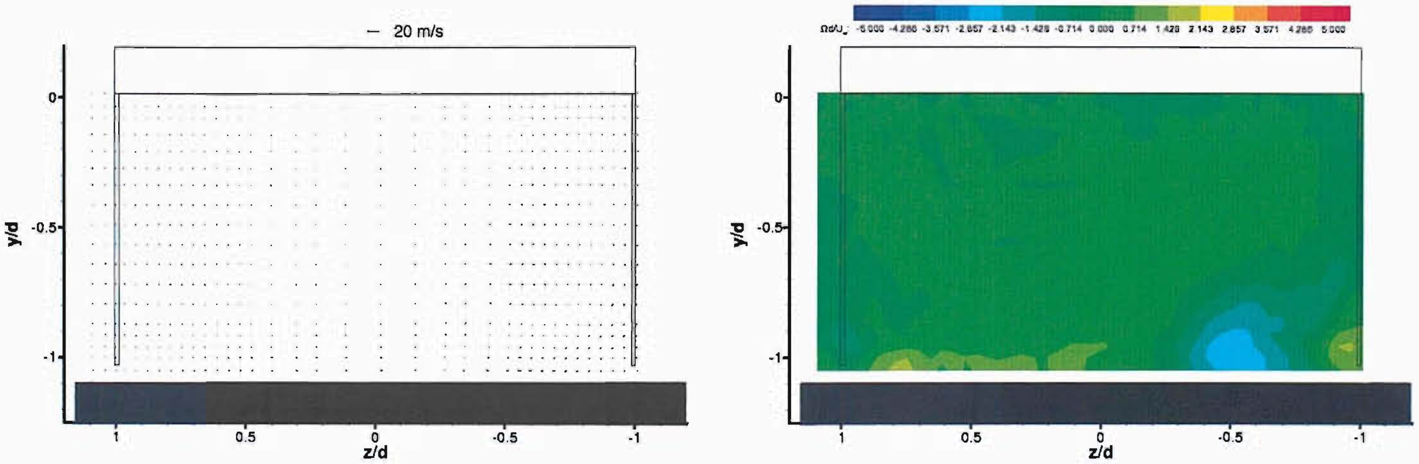

(a) Cross stream velocity vectors (b) u/U_∞

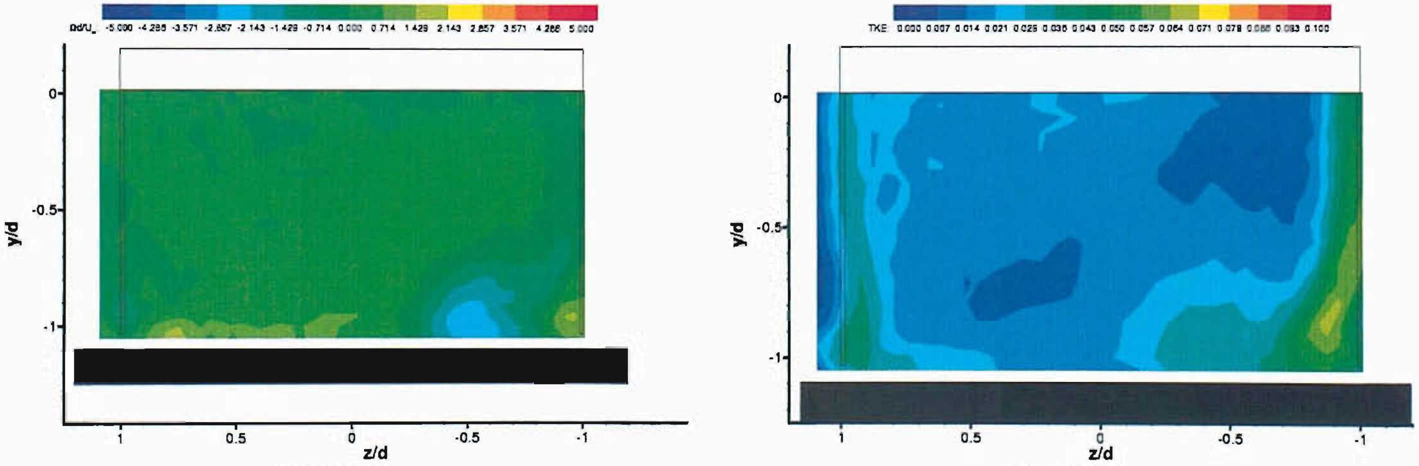

(c) $\Omega d/U_\infty$ (d) TKE

Figure 67: Near wake diffuser flow, Type D: x_1/d =1.051, h_r/d=0.064 (LDA).

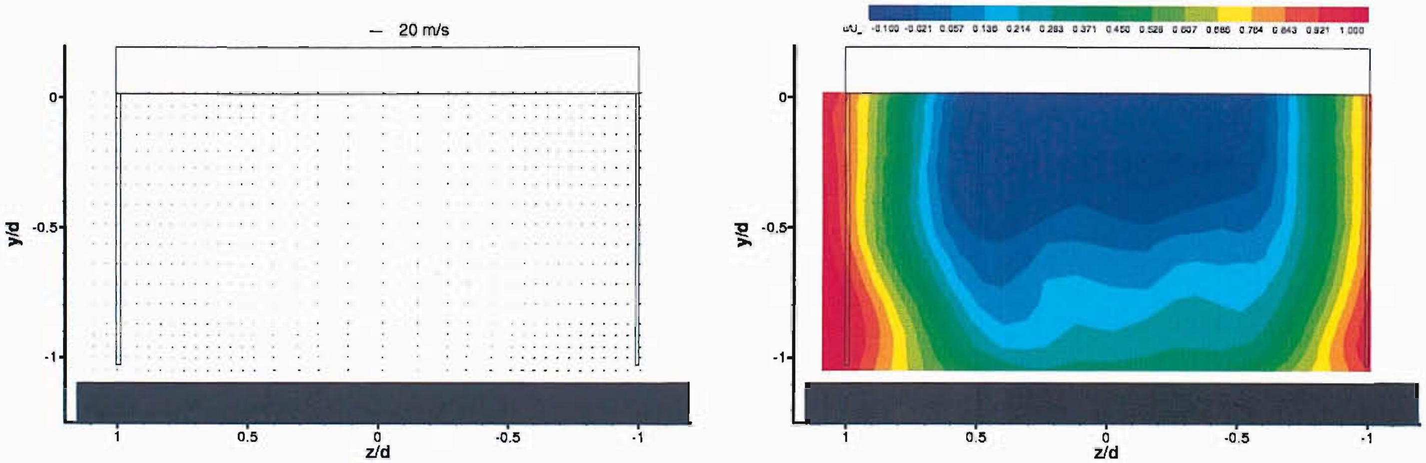

(a) Cross stream velocity vectors

(b) u/U_∞

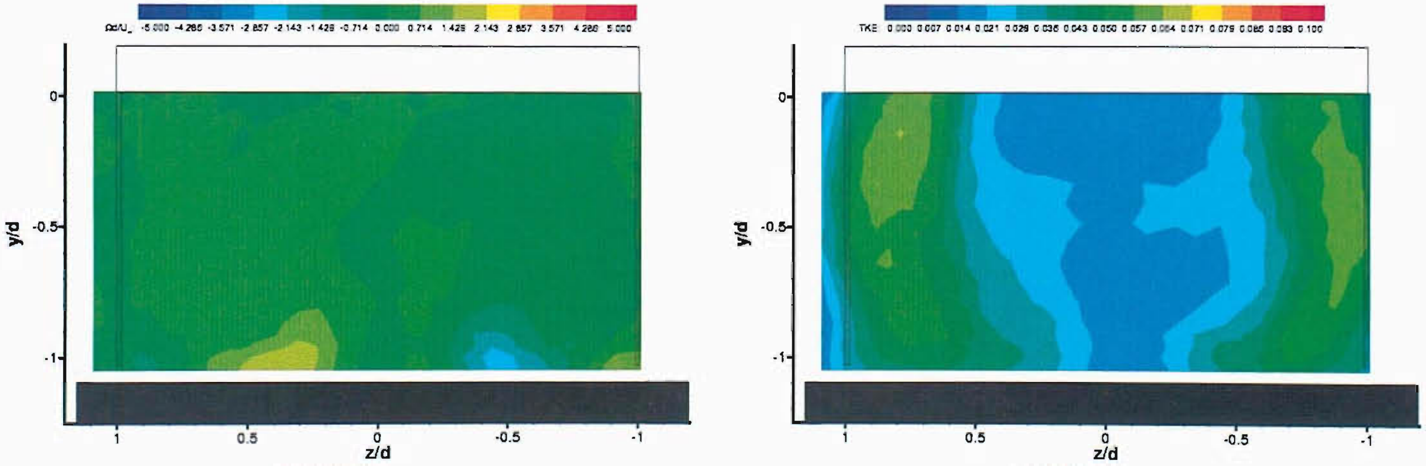

(c) $\Omega d/U_\infty$

(d) TKE

Figure 68: Near wake diffuser flow, Type D: x_1/d =2.006, h_r/d=0.064 (LDA).

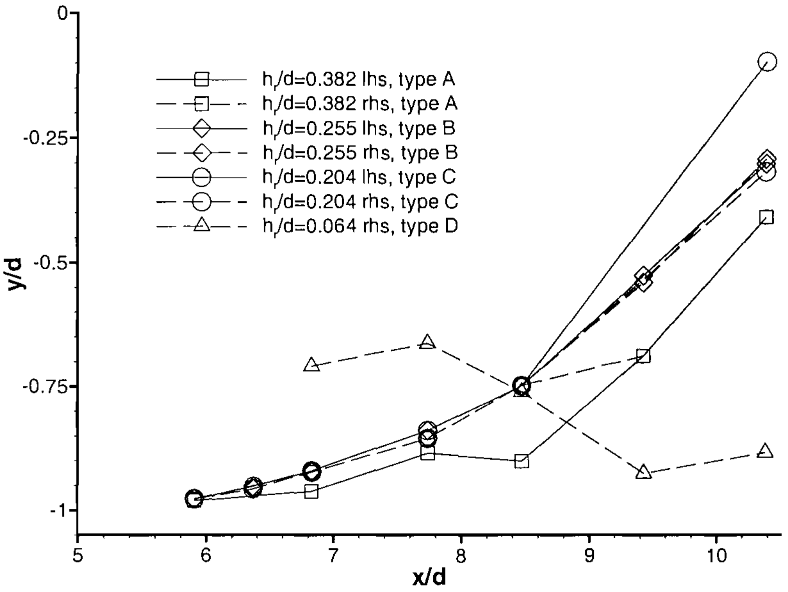

(a) $x/d - y/d$ vortex development

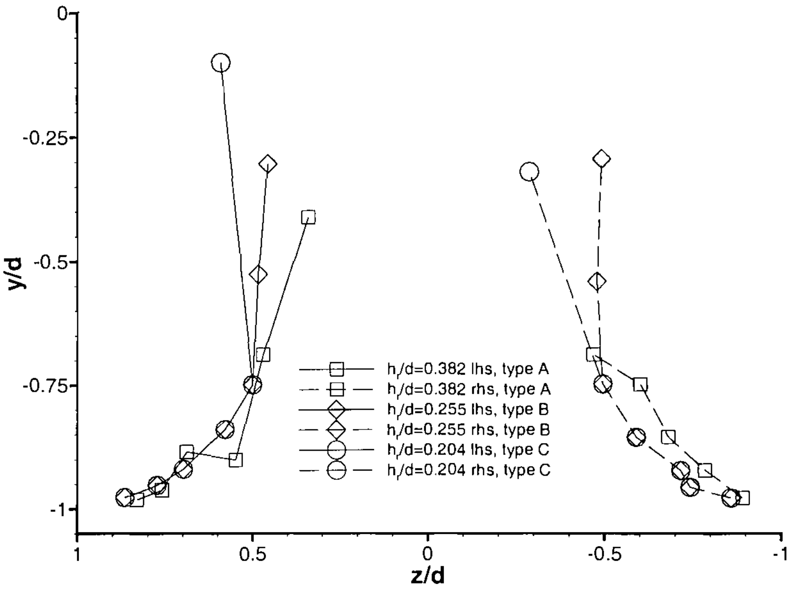

(b) $z/d - y/d$ vortex development

Figure 69: Vortex development inside the diffuser and in the near wake flow.

Chapter 7

A Computational Fluid Dynamics Model of the Diffuser Equipped Bluff Body

In this Chapter, the modelling of the Type A flow using computational fluid dynamics (CFD) is described. A brief statement of the motivation for this work is followed by a detailed description of the models used and the techniques employed in constructing the model. Results are presented in comparison with the experimental data and also in their own right as new insight into the fluid flow characteristics.

7.1 Motivation for the Computational Simulation

The experimental results have shown that the flow in and around the diffuser is complex and that its characteristics are different at different ride heights. Thus the task of replicating each of these flows is set. The diffuser in ground effect Type A flow has been modelled using the FLUENT computational fluid dynamics software to produce a more detailed flow solution than can be obtained with experimental techniques. The aim of the model is firstly to replicate experimental results and to use the more detailed solution to assist understanding of the flow. As the type A flow is less complex than the other flow types, it was considered to be the most sensible choice of flow to model for the purpose of establishing the requirements of the simulation techniques. Ultimately, simulations for necessary configurations of the model would provide a basis for developing the diffuser design.

The 3D diffuser model flow field is simulated using the FLUENT 5.2 computational fluid dynamics solver. Grids are generated using the FLUENT Geomesh 4.0 and TGrid 3.1.1 grid generation packages.

Type A flow has been modelled with a good degree of success. Modelling of the type B and C flows required computational resources above those of the workstation allocated for the calculations at the time.

7.2 Governing Equations and Models

The FLUENT software solves conservation equations for mass and momentum, with additional transport equations for modelling the effect of turbulence.

The equation for mass conservation, or the Continuity Equation, is written as in Cartesian tensor form as follows:

$$\frac{\partial \rho}{\partial t} + \frac{\partial}{\partial x_i}(\rho U_i) = 0 \tag{7.1}$$

Conservation of momentum in a fluid flow is governed by the Navier-Stokes equations. The Reynolds Averaged Navier-Stokes (RANS) equations are a time-averaged approximation to the exact Navier-Stokes equations and are written in Cartesian tensor form as follows

$$\rho \frac{du_i}{dt} = -\frac{\partial p}{\partial x_i} + \frac{\partial}{\partial x_j}\left[\mu\left(\frac{\partial u_i}{\partial x_j} + \frac{\partial u_j}{\partial x_i} - \frac{2}{3}\delta_{ij}\frac{\partial u_l}{\partial x_l}\right)\right] + \frac{\partial}{\partial x_j}(-\rho \overline{u\prime_i u\prime_j}) \tag{7.2}$$

where ρ is the air density, μ is the dynamic viscosity, u_i is the mean velocity where subscript i denotes the ith component of velocity, and subscript j denotes the next component from i, thus if the ith velocity component is to denote the u direction, then j denotes the v component. x_i is the directional tensor, and subscript i denotes the ith direction, hence if the ith direction is the y direction, then the jth direction is z. Subscript l denotes a summation over all three components of velocity or all three directions. $u\prime_i$ is the fluctuating velocity of the ith component of velocity.

The left side of the equation is the time rate of change of velocity of a fluid element as it moves through a point in space. The right hand side consists of force terms; the first term of the right hand side is the pressure gradient term, the second term is the viscous stresses expressed in terms of the rate of deformation of the velocity field. This term includes the bulk viscosity $-\frac{2}{3}\mu$, which is present in the definitions of the normal stresses. The term is facilitated in the equation by use of the Kronecker delta δ_{ij}. The final term is the Reynolds stress term introduced by the Reynolds averaging process.

7.3 Solution Process

Type A flow is steady and as such the modelled type A flow was solved as a steady flow case. Closure of the governing equations was realized using the one-equation Spalart-Allmaras turbulence model [86] with a wall function. The turbulence model was chosen as being computationally inexpensive yet having a reasonably good reputation in solving flows subject to an adverse pressure gradient [28]. The use of a wall-function was necessary in order to keep the number of grid cells to within the limits of the workstation resources. The convective terms in the governing equations were discretized using a second-order upwind scheme [6], and the SIMPLE pressure-correction algorithm was used for pressure-velocity coupling.

7.4 Grid Strategy

Type A flow was modelled at a ride height of h_r/d=0.764 (120 mm). Due to symmetry of the flow field and to the steady nature of the flow at this ride height, a symmetry-model about the z =0 axis was employed. The intention of this was to reduce the number of grid cells needed to model the flow. Experimental results show that for this diffuser model configuration, a symmetry model may only be used for higher ride heights where the flow field is steady. Future computations of flows in Regions B-D would require a full model.

The model was placed in a 'wind tunnel', in a test section of constant cross-sectional area equal to that of the 3.5 m × 2.6 m wind tunnel test section. The domain is 47.6 m in length, with the inlet approximately 15 model lengths upstream of the model, and the exit approximately 20 model lengths downstream.

Perspective views of the model surface mesh are shown in Figure 70. The detail of the hybrid mesh at the juncture of the side-plate and the diffuser inlet is given in Figure 71. A view of the hybrid mesh at the plane of symmetry around the model is shown in Figure 72. The hybrid mesh consisted of a zone of structured cells around the model, a structured cell block in the wake region and a zone of unstructured cells to complete the domain. Due to the acuteness of the diffuser angle, pyramids could not be grown to bridge the structured and unstructured cells at the side of the model, and so a non-conformal interface [28] was used to join the two meshes together at this location. In using a non-conformal interface, the grid node locations at the boundary at which two grid zones meet need not be identical. The solver creates an interior interface comprising the intersection of the faces at the boundary of the two zones to be interfaced. Fluxes across the zonal interface are calculated at the faces of this additional interface rather than at the faces at the boundaries of the two zones. The non-conformal interface was placed sufficiently far away from the model vicinity so as to minimize any effect it may have on the flow calculation. The hybrid mesh contains approximately 650,000 cells. This was approaching the maximum number of cells for the workstation. It is acknowledged that in computational studies a grid independence study should be performed to obtain an optimum grid. However in the present research, the grid was already close to the limiting number of grid cells that could be managed by the workstation, and because of this reason and due to time constraints a grid independence study was not conducted. With this situation in mind, the grid was carefully considered in order to minimize unnecessary cell distributions; the use of a symmetry model halved the cell requirements, and the boundary layer mesh was constructed to ensure that the first cell height was within the specified tolerance for the turbulence model. The grid outside of the boundary layer was also carefully controlled to ensure a smooth graduation of the cell sizes away from the model. Spanwise cell distributions were more concentrated within the diffuser and beneath the model than at the top and sides. Downstream of the model, structured mesh cells were interspersed with unstructured cells so as not to use unnecessarily large numbers of cells within the diffuser wake. It was, however, considered to be beneficial to the quality of the simulation to retain a structured mesh between the model and the ground plane.

$y^+ = \rho U_T y/\mu$ is a commonly used non-dimensional unit of distance from a wall that is used to determine the preferred distance of wall-adjacent cells from the wall. U_T is the fluid turbulent viscosity, y is the distance of the first cell from the wall and μ is the fluid dynamic viscosity. The y^+ values at the model wall were kept between 12 and 100 as recommended for use of the turbulence model with a wall function. y^+ at the tunnel floor was between 12 and 100 in the vicinity of the model. The majority of wall adjacent cells, including those underneath the model and in the vicinity of the diffuser had a y^+ of between 30 and 60.

Boundary conditions were imposed upon the computational domain, shown schematically in Figure 73. The walls of the test section were given a solid wall boundary condition except the floor, which was given a velocity of 20 m/s to simulate the moving ground condition. The inflow was specified by a velocity of 20 m/s and a turbulence intensity of 0.3% to match that in the 3.5 m × 2.6 m wind tunnel.

7.5 Results and Discussion

The simulation ran for 15 hours. During this time the mass-continuity residual reduced by between two and three orders of magnitude and remained at this value for several hundred iterations (Figure 74). The simulation was judged to have reached convergence.

The results of the simulation were assessed by the accuracy of predicted values in comparison to certain measured quantities. Specifically, these were the down-force and drag on the model, surface pressure coefficients along the model underbody centreline, spanwise pressure coefficients across the diffuser ramp and the vortex flow field at intervals along and downstream of the model.

On reaching convergence, the predicted forces on the model were C_L=-0.878 (measured value C_L=-0.983) and C_D=0.311 (measured value 0.314).

7.5.1 Surface Pressures

Comparisons were made of the measured and predicted surface pressures (Figure 75). Figure 75 (a) shows that the computational results upstream of the diffuser inlet agree reasonably well with the measured values. The predicted suction at the diffuser inlet is less than the measured value; C_p=-1.369 compared with C_p=-1.529, a percentage error of 10.5%. The predicted pressure gradient at the diffuser ramp closely matches that measured from the tappings. Figure 75 (b) is a comparison of the measured and predicted spanwise surface pressures across the diffuser ramp. At each location on the ramp the prediction agrees with the measurement to a good degree of accuracy. Suction peaks in the prediction very close to the sides of the ramp at $x/d = 5.44$ confirm that the vortex axis lies beyond the tapping at this location.

Flow stagnates at the model nose tip, where the C_p=0.997 (Figure 76). The pressure decreases from the nose tip to the beginning of the model shoulders, where the longitudinal curvature of the model decreases. The pressure increases again at the transition zone between the rounded nose and the square mid-section. Over the top and side surfaces of the model mid-section (upstream of the ramp) the pressures are negative, rising to atmospheric pressure towards the model rear. The underside surface pressures decrease from the nose towards the flat bottom, and also from the sides toward the model centre line. Upstream of the diffuser inlet the pressures become more negative, particularly so at the centre line with pressures at the more exposed sides trailing behind. Suction across the inlet is uniform, excepting local concentrations of high suction at the sides. The concentrations of suction are limited to the inlet, to small zones at the sides of the diffuser ramp in the first part of the diffuser, and along the edges of the side-plates. Elsewhere on the ramp the pressure increases quickly to slightly below atmospheric pressure at the model base.

Predicted base pressures are plotted in comparison with experimental data in Figure 77. The data is taken in a horizontal line across one half of the diffuser base, at y/d =0.508. It may be seen that the prediction agrees well with the experiment between z/d =0 and z/d =-0.65, however further outboard the prediction does not follow the trend of the experimental data. Where the experimental data indicates a suction peak, identified in Chapter 3 as being associated with the strong vortex lying beneath the base, the predicted base pressure continues to reduce toward the outboard edge of the base, and reaches a strong suction at the base edge. This predicted low pressure zone is present at the rear edge of the model sides as well as at the edges of the base. Thus the predicted flow remains attached as it flows around the sharp corner from the side to the base, accelerating as it does so and creating the low pressure. This is believed to be incorrect, and indicates that perhaps the wake strength is being underpredicted as it does not draw the flow rearwards away from the model. In the oil flow visualisation, streaklines are not seen at the corners of the base, indicating that the flow separates at the rear of the model rather than remaining attached at the base corner.

7.5.2 Off Surface Flow

The flow upstream of the model begins to decelerate from the freestream velocity at approximately 0.6 m upstream of the nose, reaching zero velocity at the nose tip. Figure 78 presents contours of streamwise velocity in the structured mesh at the symmetry plane; the gap at x/d =11 consists of unstructured mesh cells, which for ease of presentation have been omitted. A thin boundary layer surrounds the model centreline, increasing in thickness towards the model rear. A large re-circulation bubble occupies the space immediately behind the base, and the flow from the top and ramp surfaces extends downstream, deflected upwards at an angle marginally shallower than the diffuser angle. At the ground the adverse pressure gradient inside the diffuser causes the ground flow to decelerate, and the flow is induced upwards by the low pressure inside the diffuser. From later Figures 79-82 it becomes clear that this induction is overpredicted. A large zone of high speed flow through the centre of the diffuser decelerates to below freestream velocity upon its exit from the diffuser. This high speed flow follows the angle of the diffuser and flows upwards, eventually meeting the base flow wake.

At the inlet to the diffuser the through-flow maintains a high velocity across the diffuser, reaching 27.96 m/s (u/U_∞ = 1.40)(Figure 79 (a)). A thin boundary layer at the model underside increases in thickness at the corners as the streamwise flow begins to be sucked underneath the model by the diffuser. The grid at the inlet corners consists of tetrahedrons and as a result the contours are less smooth than they are elsewhere in the boundary layer. The ground boundary layer reaches freestream speed at 6 mm above the ground, although the streamwise velocity continues to rise to above u/U_∞ =1.3 at the centreplane.

At x/d =5.91 (Figure 79 (b)), the vortex pair have rolled up and are positioned towards the lower end of the side-plates, and the vortex centre is at z/d =0.92, y/d =-0.97. The streamwise velocity at the vortex centre is above the freestream (u/U_∞ =1.13). The boundary layers at the diffuser ramp and at the ground have both thickened, reducing the area of high speed flow through the diffuser. At the ramp surface, the boundary layer is thickest at the model centreline z/d =0, yet has decreased in the corner under the influence of the vortex lying beneath it. The ground boundary layer is beginning to become thicker at the centre than at the sides.

By x/d =6.83 (Figure 79 (c)) the through-flow has decelerated to the freestream velocity, with faster fluid squeezing through the gap between the diffuser ramp and the top of the vortex. The cross-flow at the centre of the vortex appears to be low speed, however the streamwise flow remains high at u/U_∞ =1.104. The vortex has moved inboard and upwards, the centre now at z/d =0.86, y/d =-0.93. It is becoming apparent that the induction of the ground boundary layer upwards into the diffuser is being overpredicted, as the ground boundary layer at the centreline is now almost 50 mm thick. This level of unseparated boundary layer thickness does not appear in the LDA contours of streamwise flow in Type A at either h_r/d=0.764 or h_r/d=0.382 (Figure 26 (a) and (b)), and is considered to be unrealistic. Figure 80 presents a comparison between the predicted streamwise vorticity at x/d =6.83 and corresponding PIV measurements. The two figures are broadly similar, and the position of the vortex core is well predicted. The centre of the predicted vortex is within 0.4% of the y/d position and 5.2% of the z/d position. However, the prediction fails to capture the finer detail of the vortex flow. For example, the predicted vortex has a larger diameter than the measured vortex and although its centre is predicted well in comparison with that of the measured vortex, the vortex lies much closer to the side-plate than the measured vortex. This is thought to be a consequence of the failure of the simulation to predict a boundary layer at the lower end of the inner side-plate. The boundary layer is a feature of the flow in Figure 80 (b) as well as in LDA measurements at the diffuser exit (Figure 26 (a)). Although the accuracy of the measurements must be analysed with caution due to the level of resolution of the measurement grid near the side-plate, the boundary layer is believed to be present. The computational grid resolution at the inner side-plate is not fine enough to capture this detail. The predicted vortex extends further toward the side-plate in the absence of any boundary layer there. The shear layer instability is not captured. The predicted vortex appears to be more diffuse than the measured vortex; its diameter is visibly larger and its concentration at the centre is $\Omega d/U_\infty$ =13.44, compared to the measured $\Omega d/U_\infty$ =38.46.

Predicted data extracted for a cross-plane at x_1/d =0.096 were compared with corresponding LDA measurements (Figure 81). The predicted vortex flow again broadly agrees well with the measured data. The position of the concentrated vortex near the bottom of the side-plate is very close to the position of the measured vortex (Figure 81 (a)). The centre of the vortex at h_r/d=0.764 could not be measured by the LDA as explained in Chapter 4, however extrapolation from the surrounding vectors gives a centre of y/d=-0.873, z/d=-0.737. The predicted vortex centre is at y/d=-0.810 z/d=-0.780, giving a positional accuracy of within 7.2% and 5.8% in the y/d and z/d directions respectively of the extrapolated vortex centre.

However, the predicted vortex flow characteristics are not so accurately predicted. The vortex is larger and more diffuse than the measured vortex. The streamwise velocity u/U_∞ at the vortex core was measured to be 1.259 (extrapolated from neighbouring velocity vectors), whilst the predicted value is 0.861. The induced boundary layer near to the ground in the centre of Figure 81(a) is now clearly non-physical. The simulation fails to deal with steep pressure gradients and separation. This could be due to the use of a wall function to predict the boundary layer flow at the ground plane. Resolution of the boundary layer to the ground could be necessary to predict the flow behaviour at the ground correctly. These problems could also be associated with the performance of the turbulence model.

7.5.3 Wake Behind Model

The predicted near wake flow at x_1/d =2.006 is compared with LDA measurements in Figure 82. Whilst the prediction in Figure 82 (a) extends to the ground plane, the LDA measurements in Figure 82 (b) were curtailed at y/d =-1.38 due to time constraints. The LDA measurements show a streamwise velocity of above u/U_∞ =1 except at the vortex shear layer which continues to persist downstream of the diffuser exit. The simulation does not predict a clearly discernible shear layer downstream of the model, however the vortices remain apparent. The streamwise flow is of freestream velocity or above except in the vicinity of the vortex, where the streamwise velocity decreases, and at the centreline of the flow where the unseparated ground boundary layer continues to expand unrealistically into the vortex flow.

7.6 Discussion

The drag force and surface pressures of the type A diffuser flow are predicted successfully. Therefore, the discrepancy in the predicted lift coefficient compared with the measured lift coefficient is thought to be mainly a consequence of the error in predicting the vortex flow characteristics. The most notable difference between the predicted flow field and the experimental measurements is the occurrence of a low axial speed vortex core in the prediction, compared with a high speed core observed in the experiments. The low speed vortex core is thought to be associated with the fact that the predicted flow seems to be diffuse, that the vortex strength is diffused by the turbulence model and/or the grid too early.

Flow separation is not well predicted, as seen in the induced boundary layer flow at the ground which was found in experiments to be separated. This could be due to a lack of boundary layer resolution at the ground. Inherent to wall functions is a constant value of κ (von Karman's constant) which is not true in a flow under an adverse pressure gradient [89]. The turbulence model may also contribute to the error. The Spalart Allmaras turbulence model utilises the Boussinesq hypothesis [45] to relate the Reynolds stresses to the mean velocity gradients. Although the hypothesis is computationally inexpensive, it assumes isotropic turbulent viscosity (μ_T) in each component of flow direction, an assumption that is not strictly true.

For successful modelling of type B flow where separation occurs on the ramp, resolution of the boundary layer to the wall is believed to be required at least inside the diffuser. Processing power limited the present runs to using a wall function, which produces satisfactory results for flow with no ramp separation. Also, a full model is probably needed to correctly predict separation at lower ride heights, since the symmetry plane could dampen out the unsteadiness of these flows.

Flow in the inviscid vortex core region should not be greatly affected by near wall flow, therefore it should be independent of the turbulence model used. However, in the case of the Spalart-Allmaras turbulence model, the turbulent viscosity is calculated based upon vorticity. Thus a high vorticity could result in an over prediction of μ_T, slowing the vortex core. Indeed, the turbulence model has a tendency to overpredict μ_T [28].

7.7 Summary

The aerodynamic parameters of the type A diffuser flow are predicted successfully. A discrepancy in the predicted and measured lift coefficients is believed to be associated with errors in prediction of the vortex flow. Surface pressure contours reveal that low pressure zones at the model surface are confined to localized zones at the diffuser inlet and at the sides of the early part of the diffuser ramp. Low pressure zones also appear near the lower edges of the inner side-plates. The predicted vortex core has a low axial speed. This could be a consequence of the way in which the turbulence model calculates turbulent viscosity. The simulation fails to predict areas of flow separation. It is believed that a full model and boundary layer resolution to the walls would be necessary to resolve the detail of the vortex flow and separation, especially at lower ride heights.

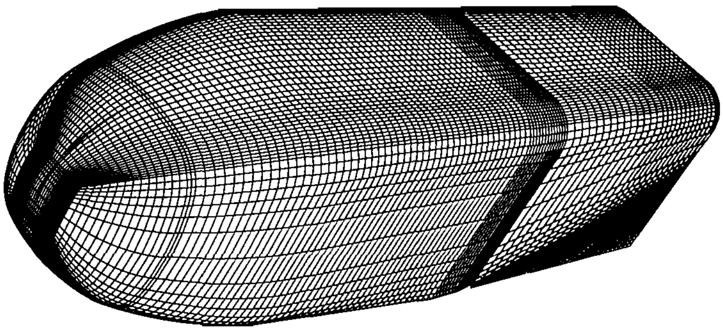

(a) Surface mesh

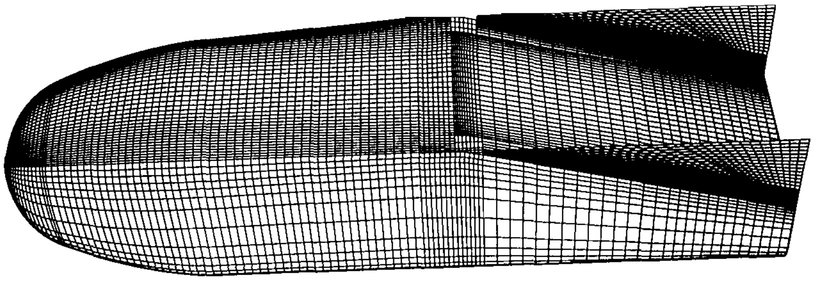

(b) Mesh from underneath

Figure 70: Model surface mesh (reflected about x-axis.)

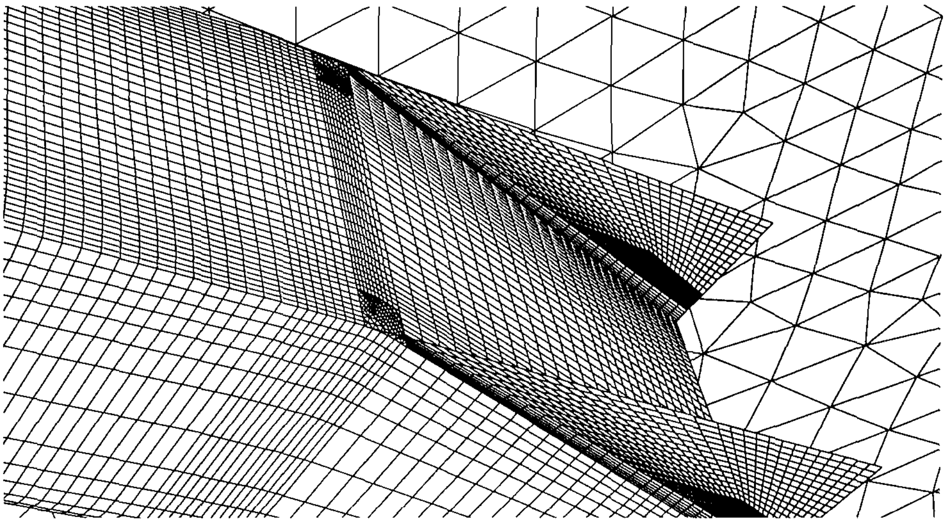

(a) Mesh at diffuser ramp

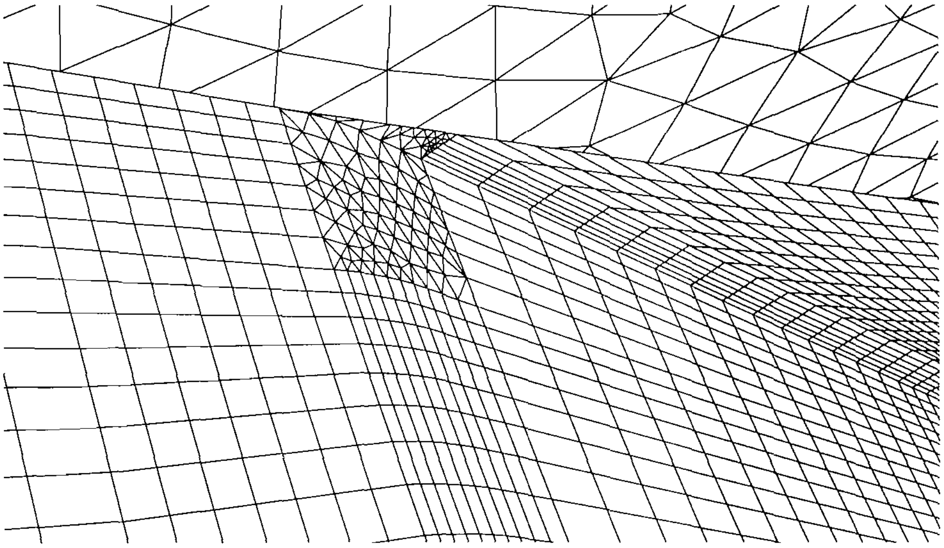

(b) Hybrid mesh at the diffuser inlet and side-plate corner

Figure 71: Further detail of model surface mesh.

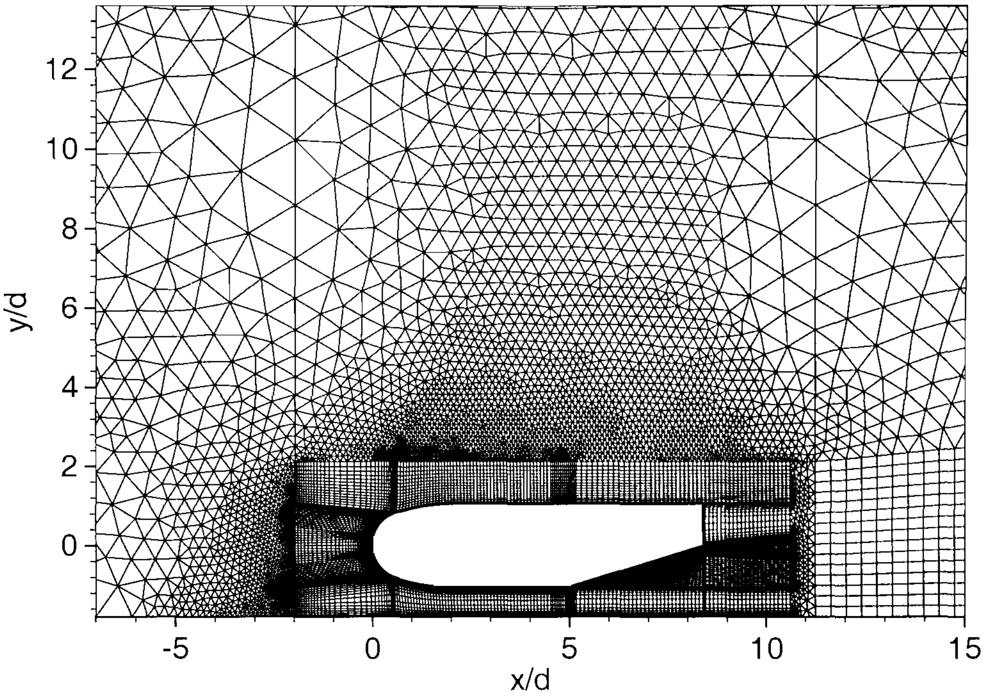

Figure 72: Hybrid mesh for a Type A flow at the symmetry plane.

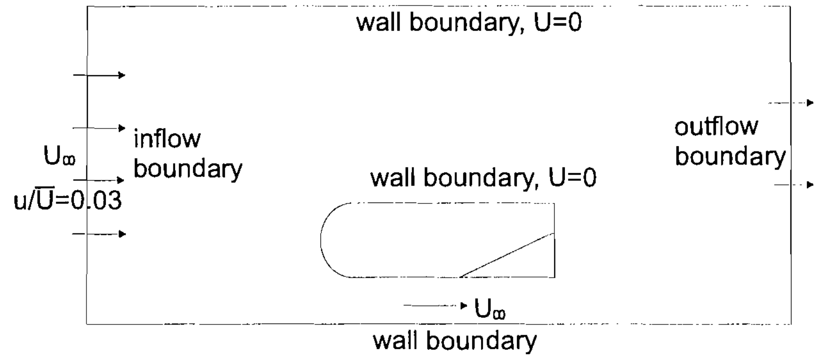

Figure 73: Schematic of computational boundary conditions.

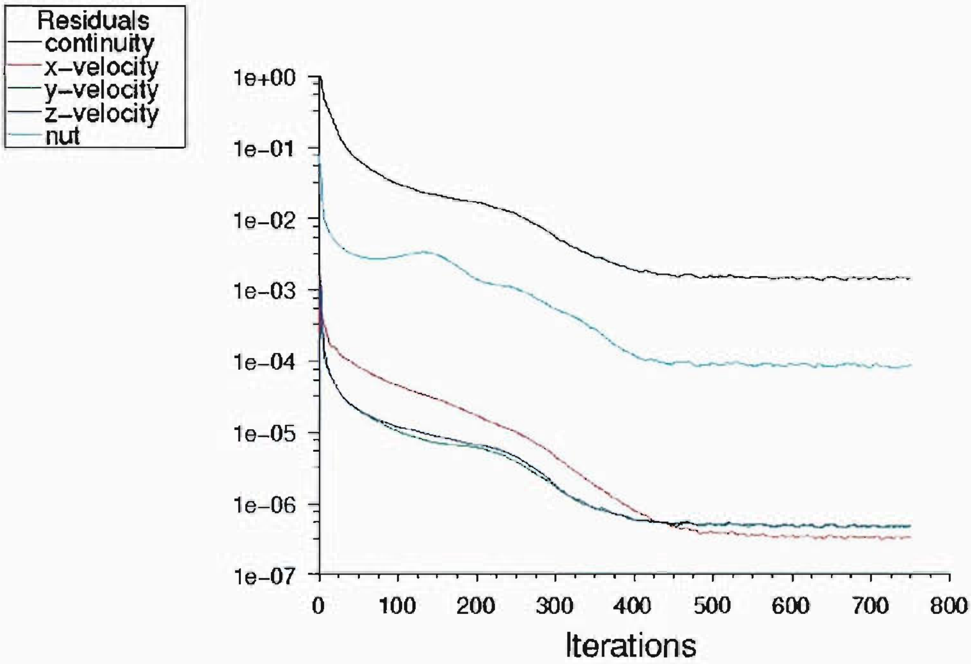

Figure 74: Residuals for the type A flow simulation.

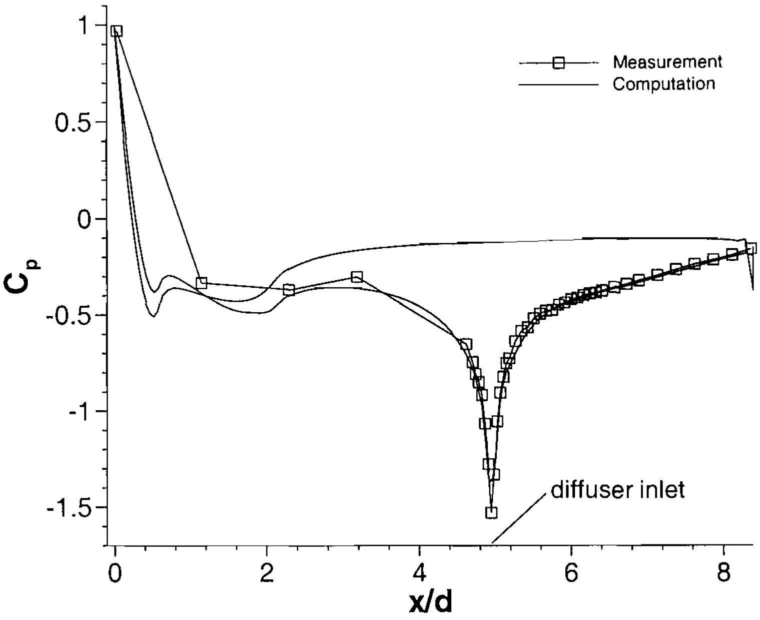

(a) Underbody centreline pressures

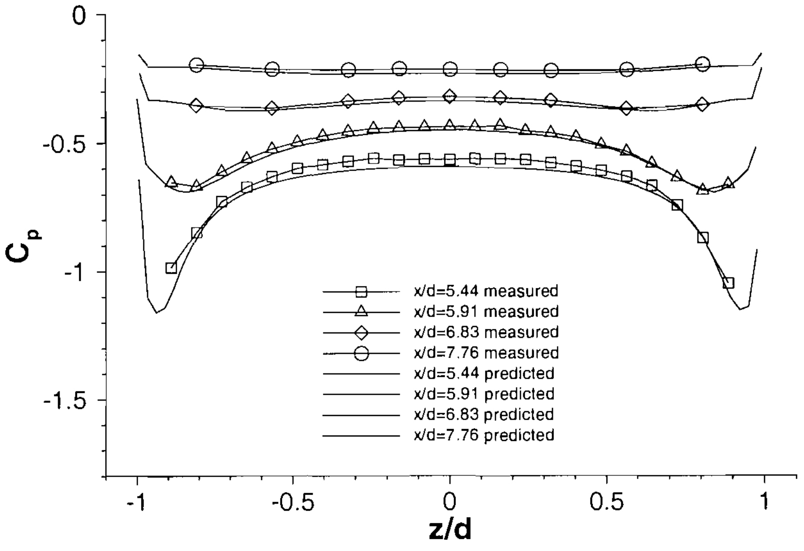

(b) Spanwise pressures

Figure 75: Computational and measured surface pressures at h_r/d=0.764 (Type A).

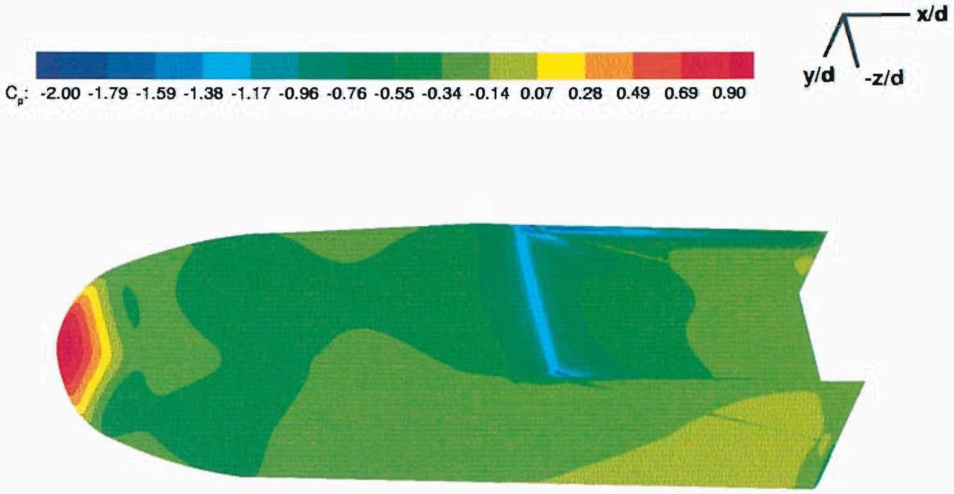

Figure 76: Predicted surface pressure contours, h_r/d=0.764 (Type A).

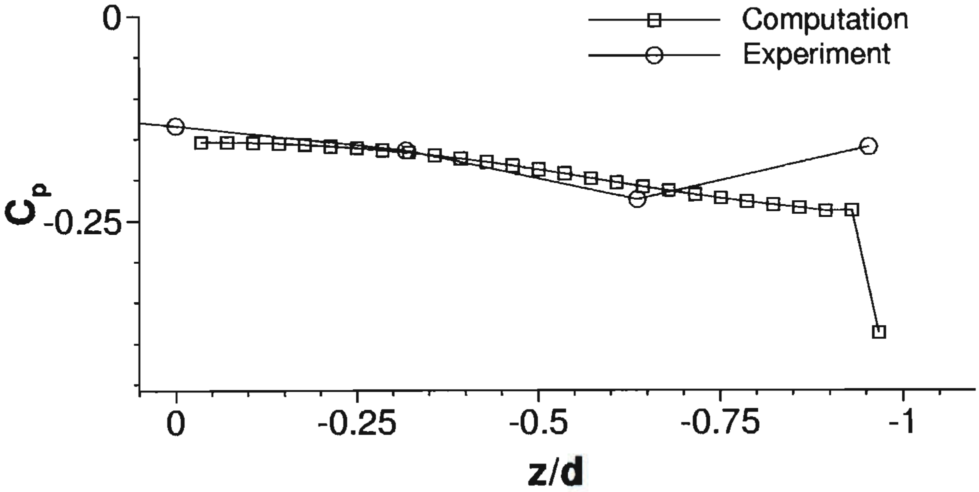

Figure 77: Predicted and experimental base pressures, h_r/d=0.764 (Type A).

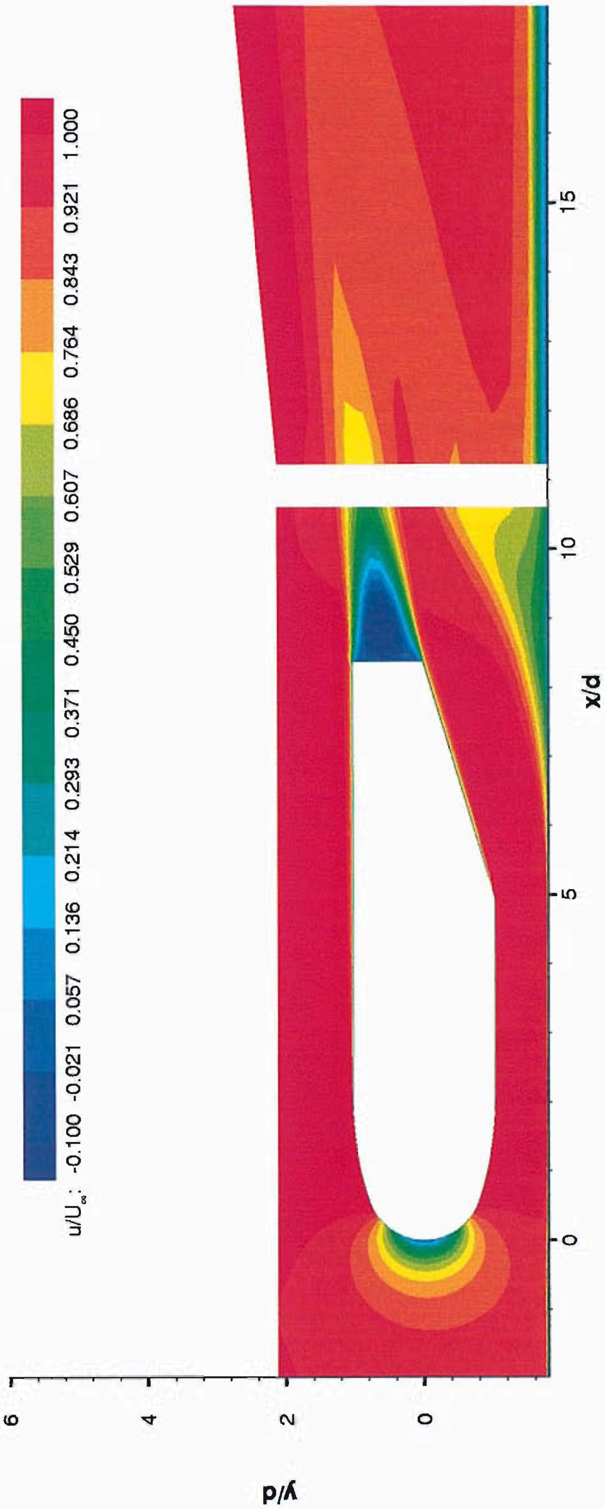

Figure 78: Contours of u/U_∞ at model symmetry plane.

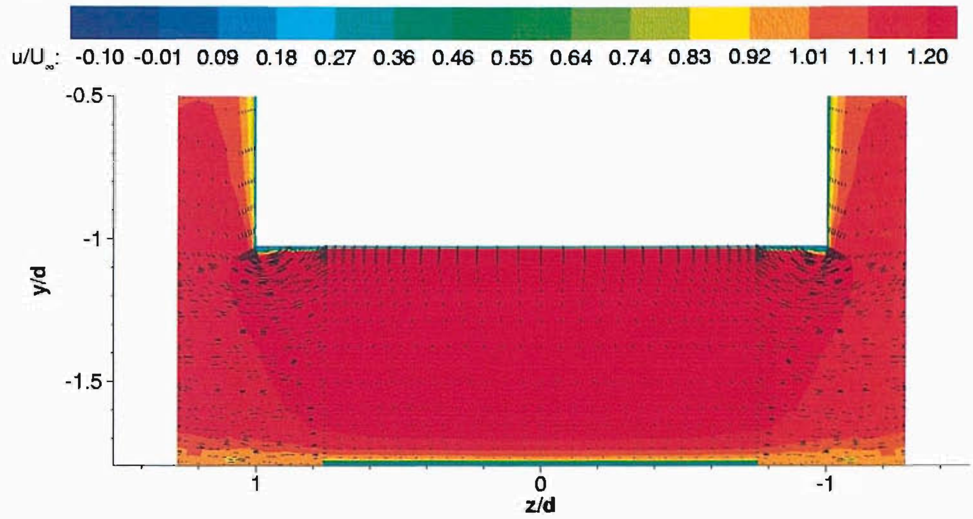

(a) x/d=4.95

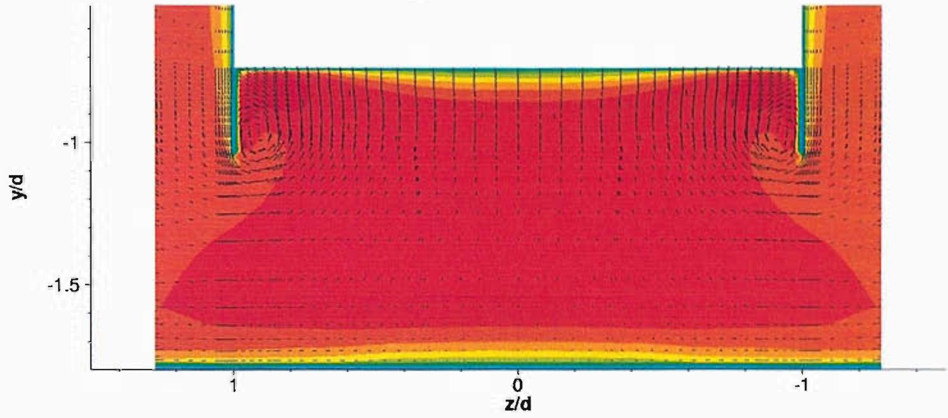

(b) x/d=5.91

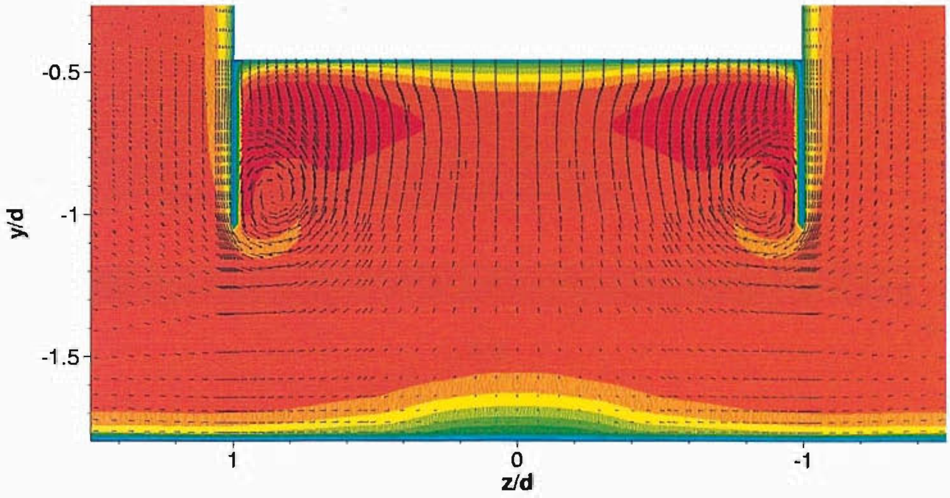

(c) x/d=6.83

Figure 79: Predicted cross-plane velocity vectors and contours of u/U_∞ at h_r/d=0.764 (Type A).

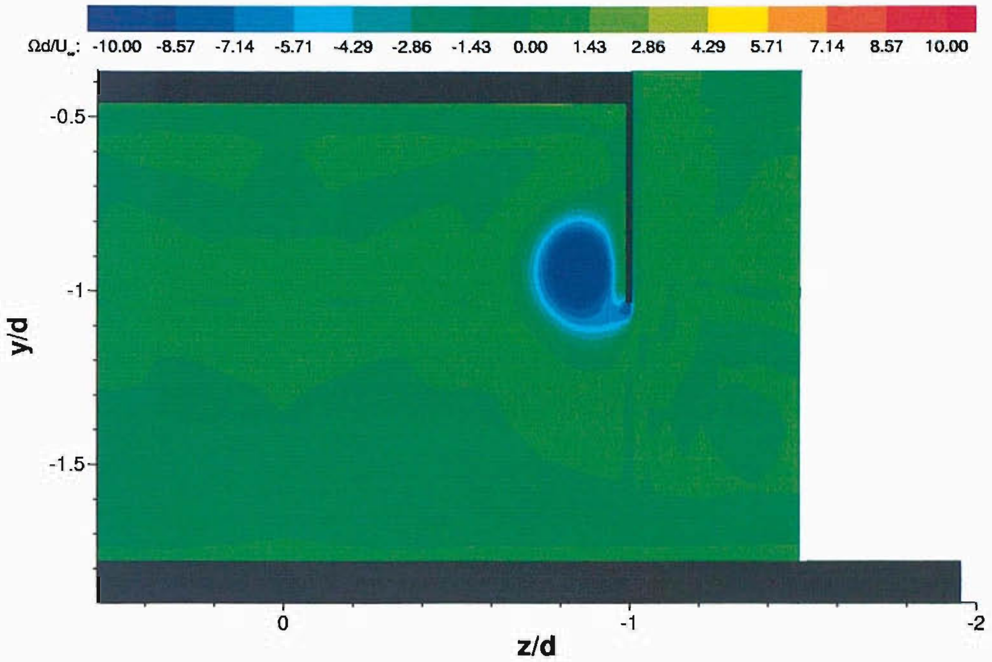

(a) Computation

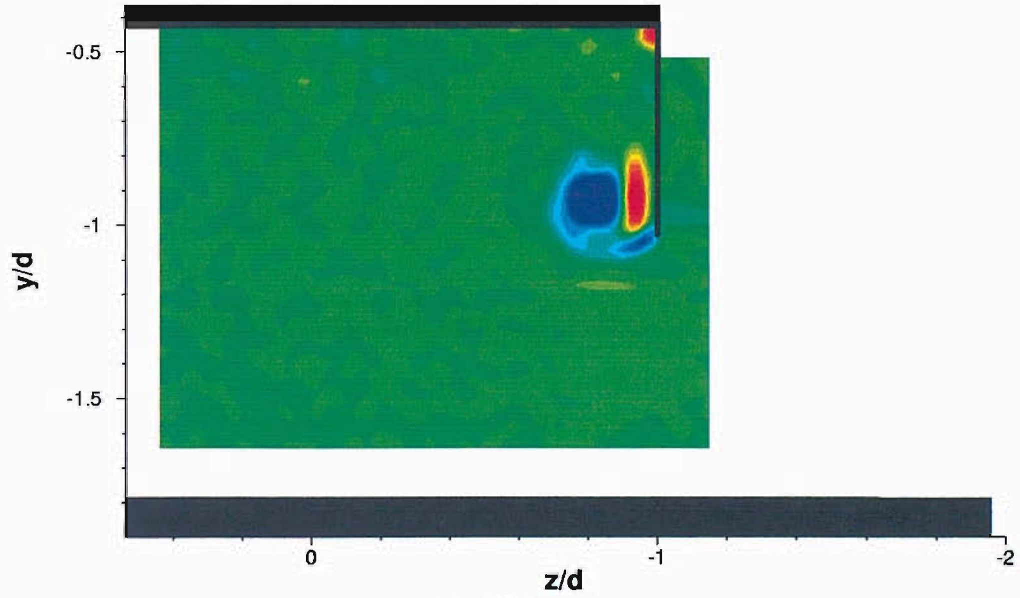

(b) PIV measurement

Figure 80: Vortex flow at x/d=6.83, h_r/d=0.764 (Type A).

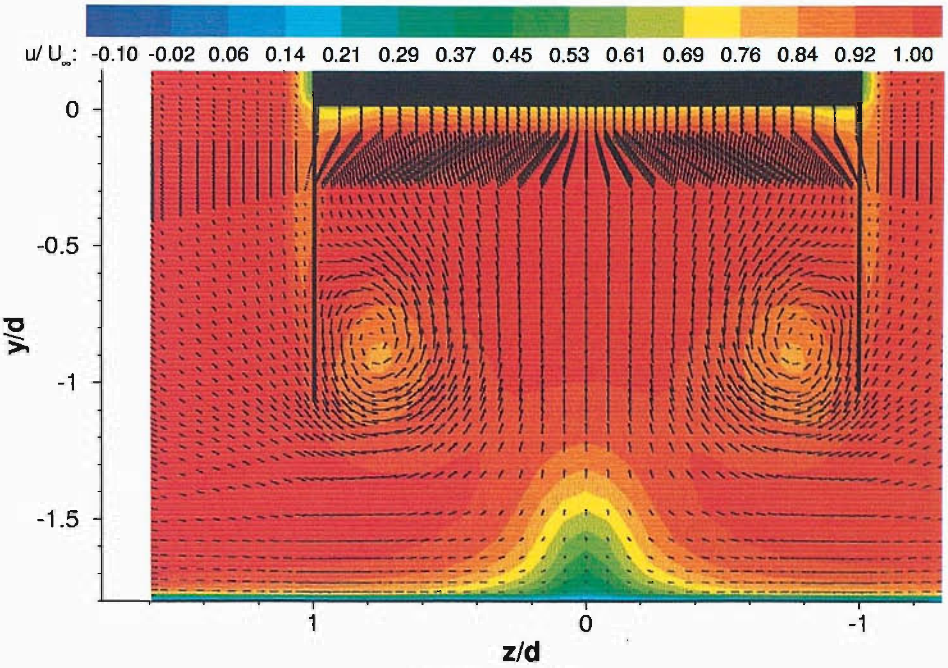

(a) Computation

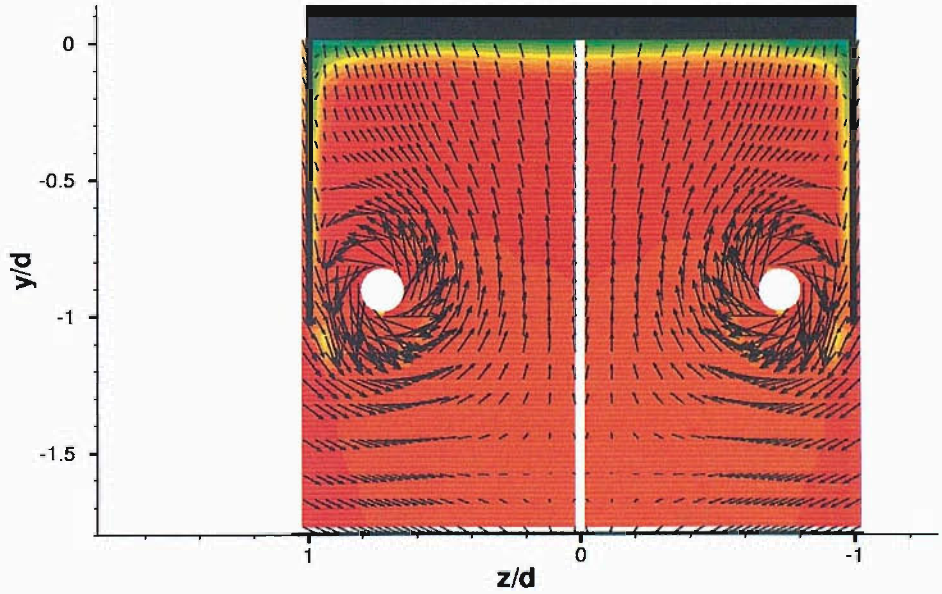

(b) LDA measurement

Figure 81: Vortex flow at x_1/d=0.096, h_r/d=0.764 (Type A).

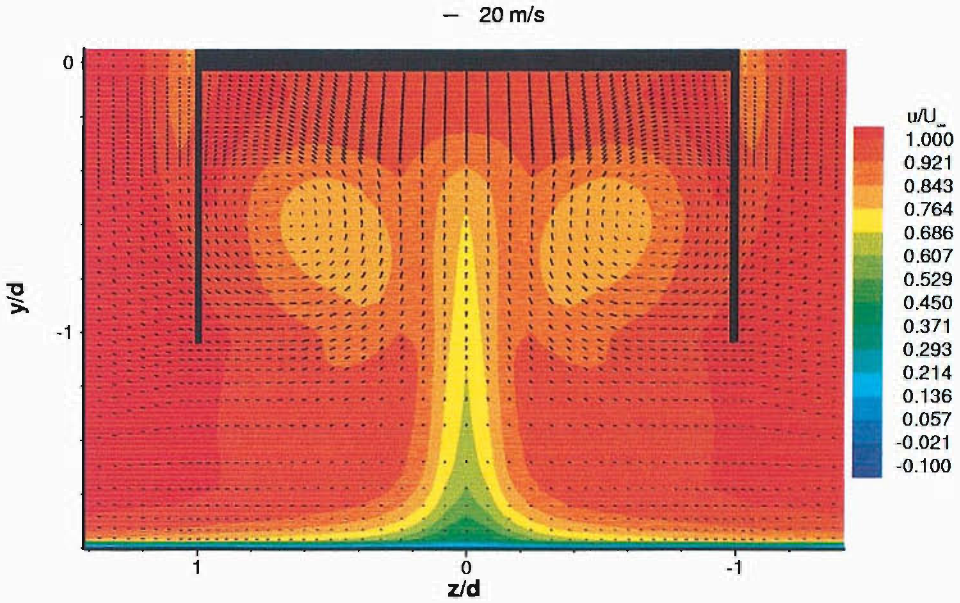

(a) Computational prediction

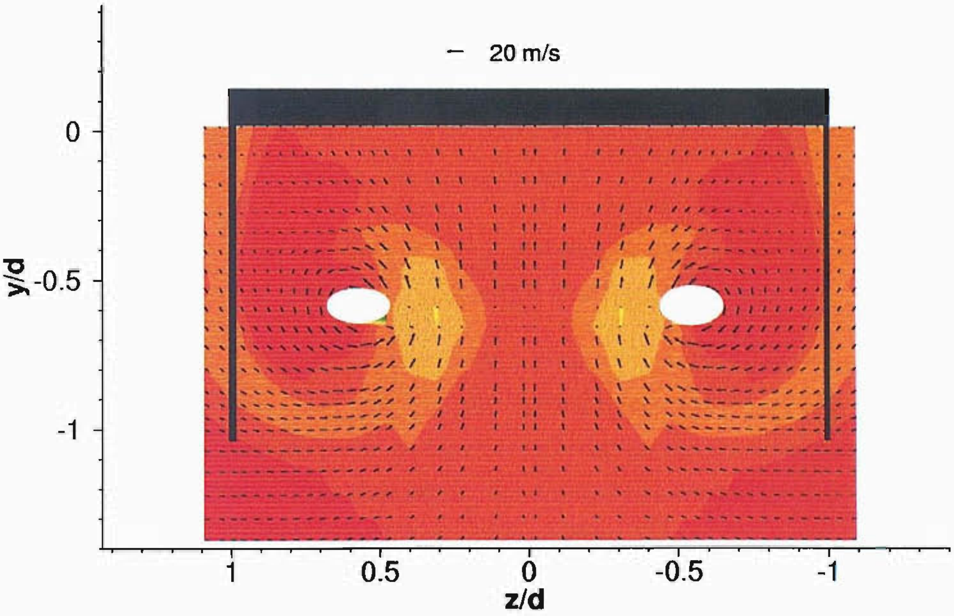

(b) LDA measurement

Figure 82: Vortex flow at x_1/d=2.006, h_r/d=0.764 (Type A).

Chapter 8

Conclusions

Model tests were performed on a bluff body equipped with a fixed steep-angle diffuser. During the course of the research it has been found that:

- The down-force curve consists of four distinct regions, A-D as the model ride height is altered.
- At larger ride heights, down-force on the model increases with reducing ride height (type A).

  The type A flow (down-force enhancement) is characterised by a steady, strong, counter-rotating vortex pair. The axial speed at the core is above freestream. No flow separation occurs on the ramp surface.

- The down-force increase is followed by a plateau in the down-force - ride height curve (type B), at the end of which the maximum down-force occurs.

  The type B flow is characterised by a counter-rotating vortex pair that is steady and strong in the early part of the diffuser, yet they become large, diffuse and unsteady. The axial speed at the core of the unsteady vortices is lower than the surrounding flow. The change in the vortex characteristics is caused by vortex breakdown of both vortices inside the diffuser.

  A separation bubble appears on the diffuser ramp in the type B flow.

- As the ride height is reduced to below the ride height of the maximum down-force, a sharp down-force reduction occurs (type C).

  The type C flow is characterised by a single vortex on one side of the flow and re-circulating flow/ flow reversal on the other. One vortex has completely broken down in this flow type. The remaining vortex is coherent, becoming unsteady towards the diffuser exit.

- A further reduction in the ride height will lead to the disappearance of the down-force contribution inside the diffuser (type D).

  The type D flow is characterised by a weak vortex, weak re-circulating flow and flow reversal.

- During the course of the PhD thesis research, it was found that boundary layer merging is not the cause of the down-force reduction phenomenon. The down-force reduction on the model is believed to be due to the break-down of one vortex at the diffuser inlet and the consequent blockage of the through-flow caused by the re-circulating and reversing flow inside the diffuser.
- The type A vortex exhibits a shear layer instability that is spatially steady.
- Cross-flow separation of the ground boundary layer occurs inside the diffuser in flow types A, B and C as a result of vortex induction and the subsequent cross-flow adverse pressure gradient.
- The wake characteristics downstream of the model differ for each flow type and hence each vortex type will have a different effect on a trailing aerodynamic vehicle.
- The results of the research provide a reliable experimental database for the validation of computational simulations of the experiment.
- The RANS simulation of the type A flow is successful in the prediction of forces and surface pressures. The main flow features are captured well.

As the thesis progressed, the experimental side of the research required completion and it became more apparent that a successful CFD model for the prediction of flow types B and C would require modelling of the full diffuser and with boundary layer resolution to the model wall. This would require more processing power than was available at the time. It was felt that time would be more usefully spent ensuring the experimental side of the research was completed.

The ultimate goal of the ongoing research is to control the diffuser flow to enhance the down-force characteristics and avoid a sharp stall. There was not sufficient time during the present study to explore flow control possibilities.

Chapter 9

Recommendations for Future Work

This has been a first study of the flow through the diffuser in ground effect. The thesis as it stands presents a comprehensive database for a single angle diffuser in ground effect, and the objective of significantly increasing current understanding of diffuser behaviour has been achieved. Due to the inherent nature of the research process there are a number of avenues which should now be explored. In order to further understand diffuser flow in ground effect the following are proposed:

- Three-component velocity measurements in streamwise planes inside the diffuser for verification of vortex breakdown. This would require a transparent side-plate. The vortex breakdown should be charted in relation to the down-force levels through type B flow. LDA measurements would ideally show this correlation, however cross-plane PIV measurements will give a good indication.
- Measurement of swirl velocities and axial velocities for investigation of breakdown criterion. This would require accurate LDA results, thus a non-refractive transparent medium to use for the side-plate would be necessary.
- Quantification of the reduction in area ratio due to the increased vortex size in type B flow, and also of the critical effective area ratio at which the maximum down-force occurs, could assist in the development of design criteria.
- The effect of a change in yaw or roll angle of the model is probably to accentuate asymmetry in the diffuser flow field, however the consequences for vortex breakdown and the down-force curve should be explored.
- Diffuser flow behaviour may differ with a change in angle. Experimental studies of various diffuser angles should be undertaken to investigate this possibility.
- An investigation of time dependent forces and pressures in type B and type C flow.

- Investigation of the effectiveness of flow control methods in alleviating the pressure gradient in the diffuser and in avoiding the sudden changes in down-force between ride heights. To conform with current F1 regulations, the form of control should be passive. Air jets are conceivable if they are powered passively, for instance by the exhaust air. The vortices are strong and large. It is anticipated that a significant amount of energy input will be required to avoid vortex breakdown, however carefully positioned solid vortex generators or strakes are worth investigation.
- Design improvements discovered in isolated diffuser tests could be incorporated onto the racing car diffuser. The ultimate test of the design will be its performance in conjunction with the whole car.
- Grid independence studies should be performed for the Type A flow simulation. A successful CFD model for prediction of flow types B and C will require modelling of the full diffuser model with boundary layer resolution up to the model wall. Boundary layer resolution will be necessary on the diffuser ramp at the least, and this approach is recommended for steady flow and unsteady RANS calculations. These calculations will be most effectively performed in parallel on a workstation or cluster having sufficient amounts of RAM (Random Access Memory) and processing power.

Bibliography

[1] Achenbach, E. Vortex shedding from spheres. *Journal of Fluid Mechanics*, 62:209–221, 1974.

[2] Ashjaee, J. & Johnston, J.P. Straight-walled, two-dimensional diffusers - transitory stall and peak pressure recovery. *J. Fluids Engineering*, 102:275–282, 1980.

[3] Baldwin, B., Barth, T.,J. A one equation turbulence transport modelfor high Reynolds number wall-bounded flows. *AIAA Paper 91-0610*, 1991.

[4] Bardina, J., Lyrio, A., Kline, S.J., Ferziger, J. H., Johnston, J. P. A prediction method for planar diffuser flows. *Journal of Fluids Engineering*, 103:315–321, 1981.

[5] Barlow, J.B., Rae, W.H. Jr, Pope, A. *Low-Speed Wind Tunnel Testing.* Wiley Interscience, 1999.

[6] Barth, T.J., Jespersen, D. The design and application of upwind schemes on unstructured meshes. *AIAA-89-0366*, 1989.

[7] Bearman, P. Review-Bluff body flows applicable to vehicle aerodynamics. *J. Fluids Engineering*, 102:265–274, 1980.

[8] Benedict, L.H. & Gould, R.D. Towards better uncertainty estimates for turbulence statistics. *Experiments in Fluids*, 22(2):129–136, 1996.

[9] Brundrett, E. & Baines, W. The production and diffusion of vorticity in duct flow. *J. Fluids Mechanics*, 19:375–394, 1964.

[10] Buice, C. Experimental investigation of flow through an asymmetric plane diffuser. *Stanford University, Centre for Turbulence Research, Annual Research Briefs*, 1996.

[11] Burgin, K., Adey, P.C. and Beatham, J.P. Wind tunnel tests on road vehicle models using a moving belt simulation of ground effect. *Journal of Wind Engineering and Industrial Aerodynamics*, 22:227–236, 1986.

[12] Campbell, J.F., Chambers, J.R. & Rumsey, C.L. Observation of airplane flow fields by natural condensation effects. *J. Aircraft*, 26:593-604, 1989.

[13] Carlson, J.J., Johnston, J.P. & Sagi, C.J. Effects of wall shape on flow regimes in straight two-dimensional diffusers. *J. Basic Engineering*, 89:151-160, 1967.

[14] Carr, G.,W. The aerodynamics of basic shapes for road vehicles. Part 2: saloon car bodies. *MIRA Report 1968/9*, 1968.

[15] Chien, K.Y. Predictions of channel and boundary layer flows with a low-Reynolds-number turbulence model. *AIAA Journal*, 20(1):33-38, 1982.

[16] Childs, R.E. & Ferziger, J.H. A computational method for subsonic compressible flow in diffusers. *AIAA Paper 83-0505*, 1983.

[17] Cho, N.H., Fletcher, C.A.J. Computation of turbulent conical diffuser flows using a non-orthogonal grid system. *Computers and Fluids*, 19(3-4):347-361, 1991.

[18] Cipolla, K.M., and Rockwell, D. Instantaneous crossflow topology on a delta wing in presence of vortex-breakdown. *Journal of Aircraft*, 35(2):218-223, 1998.

[19] Cooper, K.R., Bertenyi, T., Dutil, G., Syms, J., Sovran, G. The aerodynamic performance of automotive underbody diffusers. *SAE Paper 980030*, 1998.

[20] Cooper, K.R., Sovran, G. & Syms, J. Selecting automotive diffusers to maximise underbody performance. *SAE Paper 2000-01-0354*, 2000.

[21] Delery, J., Pagan,D., and Solignac, J-L. On the breakdown of the vortex induced by a delta wing. In *Second International Colloquim on Vortical Flows*, Baden, Switzerland, 6-7 April, 1987.

[22] Delery, J.M. Aspects of vortex breakdown. *Prog. Aerospace Sci.*, 30:1-59, 1994.

[23] Dighe, A.S. Effects of aspect ratio and low reynolds number on the pressure recovery and flow regime behaviour of plane wall diffusers . *PhD thesis, Purdue University, Indianapolis, U.S.*, 1973.

[24] Dudek, J.C., Georgiadis, N.J., Yoder, D.A. Calculation of turbulent subsonic diffuser flows using the NPARC Navier-Stokes code. *AIAA Paper 96-0497*, 1996.

[25] Ersoy, S. & Walker, J.D.A. Flow induced at a wall by a vortex pair. *AIAA Journal*, 24:1597-1605, 1986.

[26] Faler, J.H., Leibovich, S.L. An experimental map of the internal structure of a vortex-breakdown. *Journal of Fluid Mechanics*, 86(2):313-355, 1978.

[27] Fattica, M. & Mittal, R. Progress in the large-eddy simulation of an asymmetric plane diffuser. *Stanford University CTR Annual Research Briefs*, pages 249–254, 1996.

[28] FLUENT. User's Guide, version 5, 1998.

[29] Frost, R.L.L. Experimental investigations of the base pressures found on a bluff body in ground effect. *Aeronautical Journal*, 85:63–70, 1981.

[30] Gad-el-Hak, M., Blackwelder, R.F.,. The Discrete Vortices from a Delta Wing. *AIAA Journal*, 23:961–962, 1985.

[31] Gan, G.H., Riffat, S.B. Measurement and CFD prediction of diffuser pressure loss coefficient. *Applied Energy*, 54(2):287–300, 1995.

[32] Garry, K.P. Some effects of ground clearance and ground plane boundary layer thickness on the mean base pressure of a bluff vehicle type body. *Journal of Wind Engineering and Industrial Aerodynamics*, 62:1–10, 1996.

[33] George, A.R. Aerodynamic effects of shape, camber, pitch, and ground proximity on idealized ground-vehicle shapes. *ASME, Journal of Fluids Engineering*, 103:631–638, 1981.

[34] George, A.R., Donis, J.E. Flow patterns, pressures, and forces on the underside of idealized ground effect vehicles. *Aerodynamics of Transportation-II, Fluids Engineering Division, ASME, FEO*, 7:69–79, 1983.

[35] Gessner, F.B., Chan, Y.L. Flow in a rectangular diffuser with local flow detachment in the corner region. *Journal of Fluids Engineering, Transactions of the ASME*, 105(2):204–211, 1983.

[36] Ghose, L., Kline, S.J. The computation of optimum pressure recovery in 2D diffusers. *Journal of Fluids Engineering*, 103:419–426, 1978.

[37] Gibson, A.H. On the flow of water through pipes having converging or diverging boundaries. In *Proceedings. Roy. Soc. Aeronautics*, pages 366–378, 1910.

[38] Gibson, A.H. On the resistance to flow of water through pipes or passages having divergent boundaries. In *Transactions. Roy. Soc. Aeronautics. Edinburgh*, 1913.

[39] Gursul, I. & Xie, W. Origin of vortex wandering over delta wings. *J. Aircraft*, 37(2):348–350, 1999.

[40] Hah, C. Calculation of various diffuser flows with inlet swirl and inlet distortion effects. *AIAA Journal*, 21(8):1127–1133, 1983.

[41] Hanjalic, K., Launder, B.E. Sensitizing the dissipation equation to irrotational strains. *Journal of Fluids Engineering*, 102(34), 1980.

[42] Harvey, J.K. Some observations of the vortex-breakdown phenomenon. *Journal of Fluid Mechanics*, 14:585–592, 1978.

[43] Harvey, J.K., Perry, F.J. Flowfield produced by trailing vortices in the vicinity of the ground. *AIAA Journal*, 9(8):1659–1660, 1971.

[44] Herchel, C. *The two books on water supply of the city of Rome of Sextus Julius Frontinius.* Dana Estes, Boston, 1899.

[45] Hinze, J.O. *Turbulence.* McGraw-Hill Publishing Co., New York, 1975.

[46] Howell, J.P. The influence of ground simulation on the aerodynamics of simple car shapes with an underfoor diffuser. In *RAes Conference on Vehicle Aerodynamics*, pages 36.1–36.11, Loughborough University, Leics., U.K., 1994.

[47] Jeffrey, D. The Aerodynamics of the Gurney Flap . *PhD thesis, Southampton University*, 1998.

[48] Johnston, J.P. Review: diffuser design and performance analysis by a Unified Integral Method. *J. Fluids Engineering*, 120:6–18, 1998.

[49] Johnston, J.P. & Powars, C.A. Effects of aspect ratio on the performance of straight-walled, two-dimensional diffusers. *J. Basic Engineering*, 91(D):549–551, 1969.

[50] Kaltenbach, H-J., Fatica, M., Mittal, R., Lund, T.S., Moin, P. Study of flow in a planar asymmetric diffuser using large-eddy simulation. *J. Fluid Mechanics*, 390:151–185, 1999.

[51] Klein, A. Effects of inlet conditions on conical diffuser performance. *J. Fluids Engineering*, 103:250–257, 1981.

[52] Kline, S.J. On the nature of stall. *J. Basic Engineering*, September:305–320, 1959.

[53] Kline, S.J., Abbott, D.E. & Fox, R.W. Optimum design of straight-walled diffusers. *Journal of Basic Engineering*, September 1959.

[54] Lai, Y.G., So, R.M.C., Hwang, B.C. Calculation of planar and conical diffuser flows. *AIAA Journal*, 27(5):542–548, 1989.

[55] Lambourne, N.C., and Bryer, D.W. The bursting of leading edge vortices - some observations and discussion of the phenomenon. *ARC R&M No.3282*, 1961.

[56] Launder, B.E., Spalding, D.G. The numerical computation of turbulent flow. *Computational Mechanics in Applied Mechanical Engineering*, 3:269–289, 1974.

[57] Leibovich, S.L. The structure of vortex breakdown. *Annual Review of Fluid Mechanics*, 10:221–246, 1978.

[58] Leibovich, S.L. Aerodynamics of vortical type flows in three dimensions. *AGARD, CPP-342*, 1983.

[59] Lowson, M.V., Riley, A.J. & Swales, C. Flow structure over delta wings. *AIAA Paper 95-0586*, 1995.

[60] Maltby, R. & Keating, R. *Flow visualisation in windtunnels using indicators*, pages 29–38. AGARDograph, 1962.

[61] McDonald, A.T. & Fox, R.W. An experimental investigation of incompressible flow in conical diffusers. *Int. J. Mech. Sci.*, 8:125–139, 1966.

[62] McKnight, N. *Technology of the F1 Car.* Hazelton, 1998.

[63] McMillan, O.J., Johnston, J.P. Performance of low-aspect ratio diffusers with fully developed turbulent inlet flows: Part 1: Some experimental results. *Journal of Fluids Engineering*, 1973.

[64] Menke, M., Gursul, I. Nonlinear Response of Vortex Breakdown over a Pitching Delta Wing. *Journal of Aircraft*, 36(3):496–500, 1999.

[65] Mobarak, A., Fouad, M.A., Metwally, M.A. Turbulence measurements in a straight walled 2D diffuser. *ASME Paper 86-GT-60*, 1986.

[66] Moffat, R.J. Describing the uncertainties in experimental results. *Experimental Thermal and Fluid Science*, 1:3–17, 1988.

[67] Moore, C.A. & Kline, S.J. Some effects of vanes and of turbulence in two-dimensional wide-angle subsonic diffusers. *NACA TN 4080*, 1958.

[68] T. Morel. The effect of base slant on the flow pattern and drag of three-dimensional bodies with blunt ends. In *Aerodynamic drag mechanisms of bluff bodies and road vehicles*. Plenum Press, New York, 1978.

[69] Morkovin, M.V. Flow round a circular cylinder-a kaliedoscope of challenging fluid phenomena. In *ASME Symposium on Fully Separated Flows*, 1964.

[70] Obi, S., Aoki, K., Masuda, S. Experimental and computational study of turbulent separating flow in an asymmetric plane diffuser. In *Ninth Symposium on Turbulent Shear Flows*, Kyoto, Japan, August 16-18, 1993.

[71] Okwuobi, P.A.C. & Azad, R.S. Turbulence in a conical diffuser with fully developed flow at entry. *J. Fluid Mechanics*, 57(3):603–622, 1973.

[72] Patterson, G.N. Modern diffuser design. *Aircraft Engineering*, 10:267–273, 1938.

[73] Payne, F.M. The structure of leading edge vortex flows including vortex breakdown. *PhD thesis, University of Notre Dame, U.S.*, 1987.

[74] Payne F.M., Ng, T.T., Nelson, R.C., Schiff, L.B. Visualisation and wake surveys of vortical flow over a delta wing. *AIAA Journal*, 26(2):137–143, 1988.

[75] Reichert, B.A., Wendt, B.J. An experimental investigation of S-duct flow control using arrays of low-profile vortex generators. *AIAA Paper 93-0018*, 1993.

[76] Reid, E.G. Performance characteristics of plane-wall two-dimensional diffusers . *NACA TN 2888*, 1953.

[77] Reneau, L.R., Johnston, J.P., Kline, S.J. Performance and design of straight two-dimensional diffusers. *J. Basic Engineering, Trans. ASME*, 89(1):141–150, 1967.

[78] Reynolds, G.A. & Abtahi, A.A. Three dimensional vortex development, breakdown and control. *AIAA Paper 89-0998*, 1989.

[79] Riley, A.J. & Lowson, M.V. Development of a three-dimensional free shear layer. *J. Fluid Mechanics*, 369:49–89, 1998.

[80] Rothe, P.H., Barry, J.J., Johnston, J.P. & Pulliam, T. CFD assessment with diffuser data. In *ASME Fluids Engineering Division Summer Meeting*, pages FEDSM 3026, 1997.

[81] Runstadler, P.W., Dolan, F.X. & Dean, R.C. Diffuser data book. *Creare Inc.*, 1975.

[82] Sarpkaya, T. On Stationary and Travelling Vortex Breakdowns. *Journal of Fluid Mechanics*, 45(3):585, 1971.

[83] Sarpkaya, T. Effect of the adverse pressure gradient on vortex breakdown. *AIAA Journal*, 12(5):602–607, 1974.

[84] Sovran, G. The kinematic and fluid-mechanic boundary conditions in underbody flow simulation. In *CNR-Pininfarina workshop on wind tunnel simulation of ground effect*, Turin, Italy, 1994.

[85] Sovran, G. & Klomp, E.D. Experimentally determined optimum geometries for rectilinear diffusers with rectangular, conical or annular cross-section. In *Symposium on fluid mechanics of internal flow*. Elsevier Publishing, Amsterdam, 1967.

[86] Spalart, P. , Allmaras, S. A one-equation turbulence model for aerodynamic flows. *AIAA-92-0439*, 1992.

[87] Sprenger, H. Experimental investigation of straight and curved diffusers. *Ministry of Aviation Report TIL/TS134*. 1959.

[88] Strawn, R.C., Ferziger, J.H., Kline, S.J. A new technique for for computing viscous-inviscid interactions in internal flows. *Journal of Fluids Engineering*, 106:79–84, 1984.

[89] Trupp, A.C., Azad, R.S. & Kassab, S.Z. Near wall velocity distributions within a straight conical diffuser. *Experiments in Fluids*, 4:319–331, 1986.

[90] Tults, H. Flow expansion and pressure recovery in fluids. *Proc. American Soc. Civil Engineers*, 80(3):567–1–567–26, 1954.

[91] Visbal, M.R., Gordnier, R.E. Crossflow topology of vortical flows. *AIAA Journal*, 32:1085–1087, 1994.

[92] Waitman, B.A., Reneau, L.R. & Kline, S.J. Effects of inlet conditions on performance and design of two-dimensional diffusers. *J. Basic Engineering*, 39(3):349–360, 1961.

[93] Washburn, A.E. & Visser, K.D. Evolution of the vortical structures in the shear layrer of delta wings. *AIAA Paper 94-2317*, 1994.

[94] Wentz, W.H., Kohlman, D.L. Vortex breakdown on slender sharp-edged wings. *Journal of Aircraft*, 8(3):156–161, 1984.

[95] Wilcox, D.C. Simulation of transition with a two-equation turbulence model. *AIAA Journal*, 32(2), 1994.

[96] Winternitz, F.A.L. & Ramsay, W.J. Effects of inlet boundary layer on pressure recovery, energy conversion and losses in conical diffusers. *J. Roy. Aero. Soc.*, 61:116–124, 1957.

[97] Xu, D., Leschziner, M.A., Khoo, B.C., Shu, C. Numerical prediction of separation and reattachment of turbulent flow in axisymmetric diffuser. *Computers and Fluids*, 26(4):417–423, 1997.

[98] Yeung, A.F.K. & lee, B.H.K. Particle image velocimetry study of wing-tip vortices. *J. Aircraft*, 36(2):482–484, 1999.

[99] Zhang,X. Turbulence measurements of a longitudinal vortex generated by an inclined jet in a turbulent boundary layer. *ASME Journal of Fluids Engineering*, 120:765–771, 1998.

Appendix A

Uncertainties in Measured Values

A.1 Uncertainty in Force Measurements

The data from the force balance was sampled by a computer program which computes the mean force based on 75 samples. 8 runs were made for each ride height, and the uncertainty estimate is calculated from the average force computed from these data. Figures quoted here are for a lift coefficient of C_L =-2 and a drag coefficient of C_D =0.5, and as such represents data having among the worst levels of uncertainty.

It is estimated that the model ride height was set to an accuracy of ±0.25 mm using metal spacers to set the height. This resulted in uncertainties of C_L =0.0140 and C_D =0.0035. During the test runs no lifting of the moving ground belt was observed.

The dynamic pressure in the test section was maintained at 25 mmH_20 to an accuracy of ±0.05 mmH_20. The variation in dynamic pressure is proportional to the uncertainty of the down-force measured, and results in an uncertainty of C_L =0.0040 and C_D =0.001.

Due to changes in the ambient temperature and pressure of the test section, the Reynolds Number altered over the course of a test. A log was kept of these variations during the tests. In addition, the effect was extrapolated from tests at higher and lower Reynolds Numbers. The effect of Reynolds Number on the measurements was estimated to be C_L =0.000607 and C_D =0.0016.

The overhead balance system outputs the data in terms of steps, where 59.903 steps equates to $1N$ of lift force. The data output is accurate to one step, however before and after each run the output was monitored to ensure that the balance was reading zero steps before a run and returned to within 10 steps at the end of the run. Sometimes a run was repeated in order to ensure the residual was within this limit. Occasionally a residual of 20 steps or more was recorded. This usually indicated a problem with the measurement system, such as the pitch rod making contact with the tunnel roof. On these occasions the problem was addressed and the run discarded. The contribution of the residual to the uncertainty was

C_L =0.0033 and C_D =0.0033.

The total uncertainty was evaluated using the procedure described by Moffat [66] in which the squares of each individual component of uncertainty are summed and then square rooted to give the figure quoted. The uncertainties in C_L and C_D measurements were calculated as ±0.0280 and ±0.0038 respectively.

A.2 Uncertainty in Pressure Measurements

The uncertainty in the surface pressure coefficients has been estimated for a pressure coefficient of C_p =-2. This is representative of typical pressure coefficients measured inside the diffuser. The model height was set to an accuracy of 0.25 mm, corresponding to an uncertainty of C_p =0.0140. The dynamic pressure in the test section was maintained within 0.05 mmH_20 resulting in an uncertainty of C_p =0.004. The quoted accuracy of the ZOC transducer was ±0.8 mm, which results in a contribution of C_L =0.064. The output was given to an accuracy of 3 d.p., corresponding to an uncertainty of C_p =0.0005. The total uncertainty was calculated using the method of Moffat [66] as C_p =0.0656, where the largest contribution was due to the quoted accuracy of the ZOC transducer.

A.3 Uncertainty in LDA Measurements

The positional accuracy of the LDA traverse mechanism was ±0.01 mm. However, the uncertainties in determining x, y, z were estimated at ±0.15 mm taking into account the gear backlash. The LDA beam measurement volume had a cross-section diameter of 0.326 mm. It was concluded that the 95% confidence level uncertainties in the x, y, z measurements were ±0.16 mm. Following the procedure given by Moffat[66], the uncertainties in the LDA velocities measurements were estimated at ±0.09 m/s, ±0.09 m/s, and ±0.31 m/s for u, v, w respectively at a freestream speed of 20 m/s.

For the turbulent stress measurements, an estimation of the 95% confidence interval was obtained following the procedures given by Benedict and Gould[8], using their jack-knife routine. Typical values for the normal stresses are: $\overline{uu}, \overline{vv}. \overline{ww} < \pm 8\%$.

A.4 Uncertainty in PIV Measurements

The mean flow PIV data presented in Chapter 4 are obtained by averaging over 500 instantaneous sets of data measured in a single run. These 500 sets were measured in batches of up to 100 sets at a time during the run. This is because the quality of the data was found to vary significantly during the time period of a run, and no more than 100 sets could be taken at once before deterioration of the data quality. Even so, during the time period of a run some instantaneous datasets contained little or no noise whilst others contained a large amount. This variation in the quality within the run is thought to depend upon the level of seeding present in the wind tunnel during the run. Too little or too much seeding could cause poor quality results, thus it was essential to take data at times when the seeding level was at an optimum. This involved adding short bursts of seeding at the start of a run and testing the conditions in the tunnel by taking one or two readings. Once the level of seeding yielded data containing low noise levels, up to 100 datasets were obtained. Any poor quality data from the end of the dataset were discarded.

The Dantec Flowmanager software contains options for processing the raw data captured during a test run. The quality of the results was also found to depend on the method of post-processing. Cross-correlation of each image pair of images was available at several levels of resolution; in descending order of resolution these are 16×16, 32×32 and 64×64 pixels. Processing at 16×16 pixels created too much noise in the results. Processing at 32×32 pixels yielded 79×63 vectors over the measurement plane, and is the resolution at which the majority of data are processed. Processing at 64×64 pixel resolution gave only 39×31 vectors over the measurement plane and consequently, some of the flow detail was lost. However the mean vorticity output by each process resolution agreed closely, giving $\Omega d/U_\infty$ =2.63 and 2.625 respectively.

During a test run it was found to be essential to eliminate all light sources or reflections within the test section and even outside in the control room. However, an unavoidable reflection from the laser deflected from the side-plate lower edge and produced a faint line across the images (Figure 36. The line appears in the PIV results as a slight discontinuity (Figure 34). Areas of the flow affected by reflection from the model are noticeable in the correlated vector maps as large vectors that are unfeasibly large. A velocity range validation filter was applied to the correlated vector map to remove these vectors, known as 'outliers'. Further processing options were available to smooth and filter the results, however they were not used as they tended to blur the flow features.

One method of assessing the accuracy of the PIV data is to compare it to LDA data measured at the same plane. Figure 83 shows both PIV and LDA measurements of w/U_∞ taken at h_r/d=0.255, x_1/d =0.096 in a vertical traverse in the vicinity of the vortex core. The maximum non-dimensionalised spanwise velocity measured by the LDA is 0.432. At the same measurement point, the PIV records w/U_∞ =0.401. The percentage difference between the two is 7.6%. The minimum velocity measured by the LDA is -0.672, whereas the PIV measured -0.604. The percentage difference between these measurements is 10.1%. However, most of the results are of a smaller percentage difference for the same measurement co-ordinates.

Thus, although the accuracy of the PIV data is difficult to assess in isolation, it may be concluded that PIV produces reasonable accuracy when compared to the LDA results.

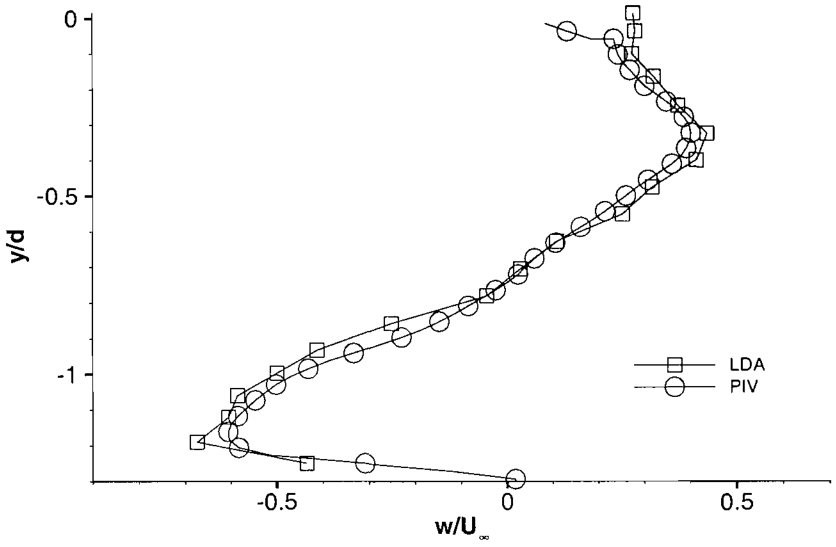

Figure 83: Comparison between LDA and PIV measurements, type B flow.

Appendix B

Measurement Repeatability

B.1 Repeatability of Force Measurements

Figure 84 (a) shows the repeatability of down-force measurements taken in different wind tunnel sessions for the 17 degrees diffuser angle model. It may be seen that the down-force coefficient repeats very well in flow types A and B, excepting a single measurement point at h_r/d=0.318. This ride height is the first height measured at which the separation bubble and flow unsteadiness appears, which may account for this discrepancy. Agreement between sessions in flow types C and D is not as good. This could be a consequence of slightly different ambient conditions inside the tunnel between the two sets of data which could alter the breakdown characteristics of the vortices.

B.2 Repeatability of Pressure Measurements

The short term and long term repeatability of the surface pressure measurements was assessed by taking multiple readings within a run, and then by repeating the runs in separate test sessions. Short term repeatability was assessed using the tapping giving the maximum spanwise suction at a model ride height of 34 *mm*, which lies at x/d =5.440, z/d =0.890. Over 9 non-consecutive runs taken on the same day, the following readings were taken; -2.534, -2.585, -2.564, -2.550, -2.510, -2.540, -2.48, -2.475, -2.463. The average of these is 2.251 with a standard deviation of σ =0.264. Figure 84 (b) shows the long term repeatability of data recorded for a model ride height of 34 *mm*. The agreement in the data from the two test sessions is good over the whole diffuser ramp, with only a few exceptional points falling outside of the measurement uncertainty.

B.3 Repeatability of LDA measurements

Due to time constraints, no repeatability of the LDA data was assessed.

B.4 Repeatability of PIV Measurements

PIV measurements were all taken during a two week test session. Thus long term repeatability of the results is unavailable. During the session, a run of 500 datasets was taken in batches of 100 datasets. Short term repeatability of the data is assessed by calculating the mean vorticity at the vortex core of each set of 100 and comparing it with the total average over 500 datasets. The measurements at h_r/d=0.255, x_1/d =0.096 were used for the calculation, as the run is representative of the unsteady flow field. The vortex centres for each set of 100 datasets were 0.509,-0.764, 0.501,-0.7495, 0.509,-0.756,0.494,-0.74,0.500,-0.755. This compared to the average over 500 data sets of 0.501,-0.749. The respective mean vorticities at each of these locations was 2.49, 2.78, 2.57, 3.32 and 2.41 compared to the mean over 500 of 2.625. The mean vorticity for each data set is within 8.2% of the mean measured over the full set with the exception of the fourth set which is significantly above the mean. On further inspection, this relatively high vorticity is apparently due to the region of maximum vorticity occurring more centrally in the vortex in this data set than is found in the other datasets.

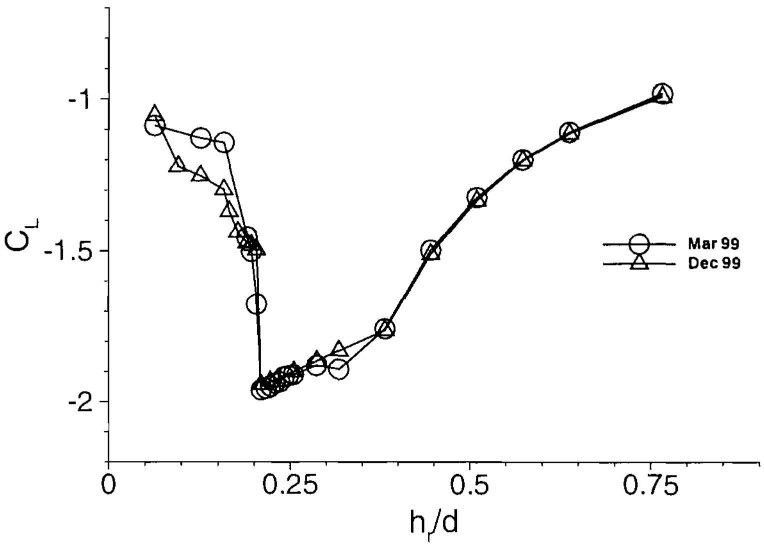

(a) Down-force measurements

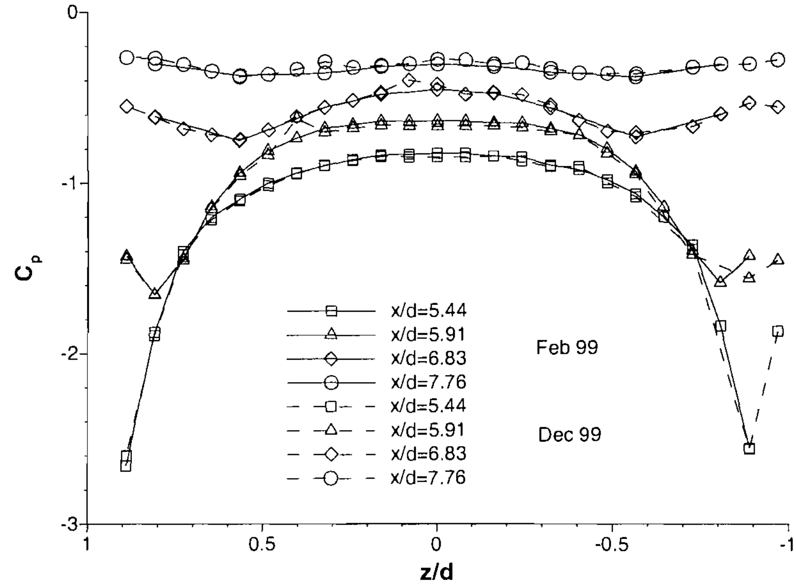

(b) Surface pressure measurements

Figure 84: Long term repeatability of experimental measurements.